WASHINGTON UNIVERSITY
DEPARTMENT OF PHYSICS
LABORATORY FOR ULTRASONICS
St. Louis, Missouri 63130

"Ultrasonic Nondestructive Evaluation Techniques Applied to the Quantitative Characterization of Textile Composite Materials"

Final Progress Report: July 24, 1998

NASA Grant Number: NAG1-1848

Principal Investigator:

Dr. James G. Miller
Professor of Physics

The NASA Technical Officer for this grant is:

Dr. William P. Winfree
NASA Langley Research Center
Hampton, Virginia

Ultrasonic Nondestructive Evaluation Techniques Applied to the Quantitative Characterization of Textile Composite Materials

I. Introduction

Development of woven, knitted, braided and stitched materials and structures for application on primary structures of commercial transport aircraft has been conducted by NASA during the period from 1985 to 1997. Different composite types have been identified for use in particular parts of airframe structures.[1] Because of these new advanced materials and structures, as well as the application of advanced processing methods, there is a need to develop new nondestructive evaluation (NDE) methods to address the new demands. Nondestructive evaluation methods applicable to post-production inspection of component integrity as well as methods applicable to process control in manufacturing are important to successful implementation of these materials. The successful development and implementation of quantitative ultrasonic nondestructive evaluation techniques applied to the characterization of advanced materials requires a methodic investigation of many important questions. The interaction of an interrogating ultrasonic field with the inherent physical properties of these advanced materials needs to be addressed. Textile composites with through-the-thickness reinforcement offer a challange to the NDE community. By their very nature these composites represent a phase distorting anisotropic medium. Investigations focused on whether ultrasonic NDE methods which work well with more conventional composite materials can be applied to the new, more complex, material systems are essential.

In this final report we summarize our recent developments of advanced ultrasonic nondestructive evaluation methods applied to the characterization of anisotropic materials. An electronic version of this report has been included on the accompanying CD-ROM in the Adobe™ Portable Document Format (PDF).

A. References

1. Marvin B. Dow and H. Benson Dexter, "Development of Stitched, Braided and Woven Composite Structures in the ACT Program and at Langley Research Center (1985 to 1997)", NASA, Technical Publication, Report Number: TP-97-206234, (November 1997, 1997).

II. Ultrasonic Field Parameters (June 1996 to December 1996)

The use of an ultrasonic wave propagation model in conjunction with measured data is investigated to enhance the understanding of the physics underlying the interaction of ultrasound with anisotropic materials, such as multiaxial warp-knit composites and other fiber-reinforced specimens. We present images obtained from experimental measurements and simulations of ultrasonic fields in water. Furthermore, the simulation is extended to produce images of ultrasonic field propagation through a woven fiber composite material with values of the anisotropy of the attenuation coefficient based on knowledge of previous work by our group.[1] For reasons of image resolution, all images have been included on the accompanying CD-ROM in Adobe™ Portable Document Format (PDF).

In Section II.A we describe the implementation of the ultrasonic wave propagation model we employed. In addition, we briefly address concerns related to the ultrasonic beam, such as diffraction and phase cancellation across the face of a finite-aperture, phase-sensitive receiving transducer. Section II.B describes the experimental arrangement and methods for acquiring the ultrasonic diffraction patterns. Following the description of the data acquisition technique, Section II.C details the analysis of the experimental data and the methods of the simulations. In Section II.D, the resulting images of the ultrasonic diffraction patterns derived from experimental data are compared with model simulations (See CD-ROM for images). A discussion of the observations and conclusions are found in Section II.E.

A. Background

The overall goal of this research is to enhance the understanding of the scientific principles necessary to successfully develop advanced ultrasonic materials characterization methods required for the inspection of complex fiber-reinforced material structures. A specific goal of our proposed research is to understand the fundamental physics underlying the interaction of ultrasonic fields

with the inherent physical properties of these complex material structures. This includes developing an understanding of how ultrasonic fields propagate in these materials by examining the propagation of the phase-fronts and energy of the ultrasound in these inherently anisotropic materials.

In order to develop a robust measurement method for nondestructive evaluation of anisotropic materials, it is necessary to have an understanding of the diffraction of the ultrasonic field within the media. Diffraction of the ultrasonic field can occur for a variety of reasons, including the intrinsic nature of a specific sample (specific intrinsic textile composite parameters, i.e., tow sizes, layup configuration, etc.), surface roughness (both random and periodic), external stitching, and inhomogeneities. In addition, the experimental sampling of the ultrasonic field may be compromised due to phase cancellation effects across the face of the receiving transducer[2,3]. Computer simulations can be utilized in developing a more fundamental understanding of the effects that phase-distorting anisotropic materials can have on the diffraction pattern and propagation characteristics of the interrogating ultrasonic wave.

There are a number of ultrasonic wave propagation models available for numerical implementation, such as the Measurement Model[4], the Wisconsin Method[5,6] and the Angular Spectral Decomposition method[7-12], to name a few. Each model has its advantages. The Angular Spectral Decomposition method offers a numerically efficient algorithm. For this reason, as a first step we have chosen to employ the Angular Spectral Decomposition method as a tool for modeling our experimental arrangements.

A.1 Approach

Our approach toward understanding the diffraction of ultrasound within anisotropic materials is to progress systematically from structurally simple specimens to more complex structured composite specimens. This systematic approach facilitates the understanding of how increasing

structural complexity affects the ultrasonic diffraction pattern. Initial investigations of ultrasonic diffraction patterns were conducted in water only. Subsequent investigations modeled the effects of inserting a woven fiber composite specimen into the ultrasonic field.

B. Experimental Arrangement and Method

All measurements in this study were performed in an immersion tank using a 0.5" diameter, spherically-focused (2" focal length), piezoelectric transducer of a nominal center frequency of 10 MHz (Panametrics V311) as the transmitting transducer. A 1 mm diameter PVDF, broadband, needle hydrophone (Force Institute) was used as the receiving transducer. The receiving hydrophone was scanned in a series of planes (32 sites by 32 sites with 0.5 mm separation between sites, 15.5 mm by 15.5 mm area total) at axial positions of 1", 2", and 3" from the transmitting transducer. These positions permitted measuring the ultrasonic field before the focal zone, within the focal zone, and after the focal zone of the transmitting transducer.

Figure 1 is a schematic diagram showing the data acquisition system used in this investigation. The ultrasonic signal sent to the transmitting transducer was a broadband pulse generated by a Metrotek MP215 pulser. The ultrasonic signal received by the hydrophone was initially sent through a unity-gain preamplifier (Force Institute) matched specifically to the hydrophone, providing 50 Ω coupling to the receive-side electronic equipment. The signal was then sent through a pair of step attenuators (HP 355 series) that permitted a more precise adjustment of the signal amplitude to prevent saturation of the input stage of the receiving electronic equipment. Further amplification was achieved by sending the received signal through a Metrotek MR106 rf amplifier. The rf signal was digitized with a Tektronix 2430A digital oscilloscope. An Apple Macintosh II computer was used to read the rf time traces and store them for off-line analysis.

At each site of the pseudo-array, 64 time traces were acquired and averaged off-line before being stored to disk. Each rf time trace consisted of 1024 points sampled at 250 MegaSamples/s (0.004 μs sampling period). The digital oscilloscope was externally triggered by the

synchronization pulse provided by the MP215 pulser. The data acquisition delay time (relative to the trigger signal) was set manually such that the received trace was localized within the acquisition window.

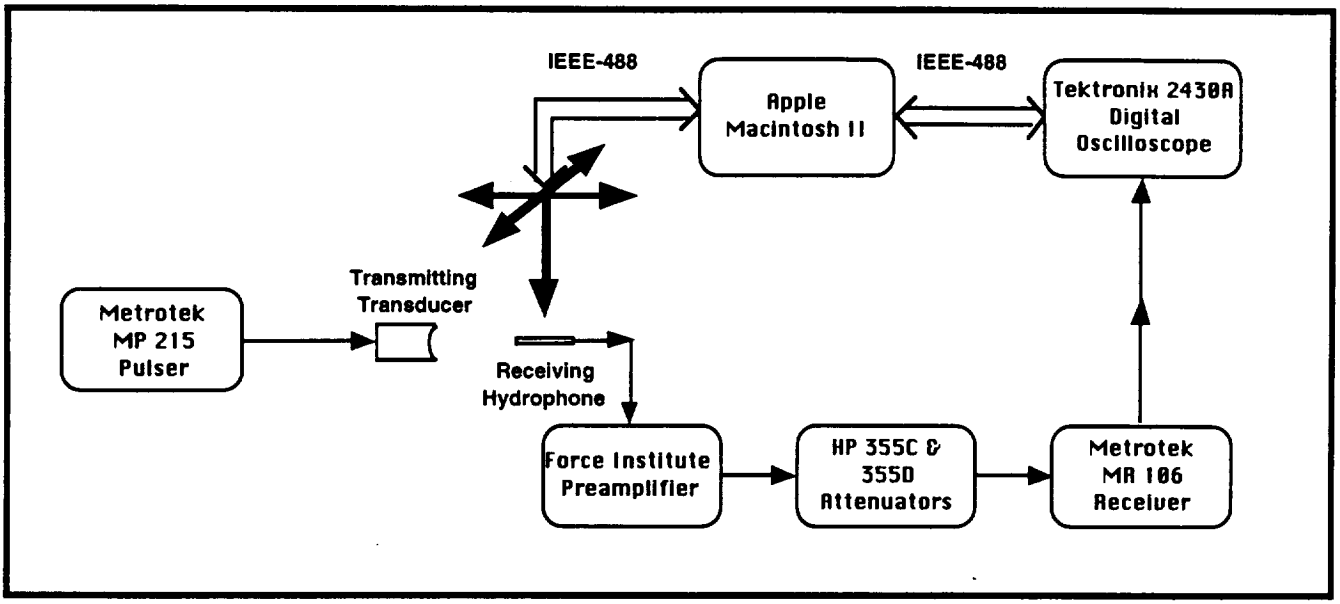

Figure 1: Experimental arrangement of data acquisition equipment

C. Data Analysis and Modeling

Data analyses and computer modeling were performed using in-house custom software written in the C programming language on a Power Macintosh. These routines performed all the necessary tasks to calculate and visualize the simulated ultrasonic diffraction patterns, based on either the simulated or experimentally measured ultrasonic fields, using the method of Angular Spectral Decomposition. In order to construct images of continuous-wave ultrasonic fields, it was necessary to calculate the in-phase and quadrature parts of the pressure field measured at each pseudo-array scan site. The averaged rf time trace acquired at each pseudo-array site was Fast Fourier Transformed. The real and imaginary parts of the Fourier transform corresponded to the in-phase and quadrature parts, respectively, of the received pressure field spectra. In order to use

data from the broadband measurements in the continuous-wave based method of Angular Spectral Decomposition, single-frequency data was extracted from the in-phase and quadrature calculations providing narrow-band in-phase and quadrature representations of the field measured with the pseudo-array. These narrow-band representations were then imported into the in-house custom-designed software program to permit visualization of the propagated pressure fields.

C.1 Propagations from Experimentally Measured Field

For the experimental water path data, we imported the in-phase and quadrature parts of the experimentally measured pressure field at single frequencies (5.13 MHz, 7.08 MHz, and 11.2 MHz) at the receiver plane for each of the positions from the transmitting transducer (1", 2", and 3"). We zero-padded our 32 x 32 single-frequency in-phase and quadrature parts of the pressure field to 64 x 64 in order to minimize boundary effects (which can occur in the Fourier projection technique if array size is too small) as the fields were propagated. We applied a radial (from the center of the pseudo-array) Hanning window to the zero-padded in-phase and quadrature parts of the pressure field so as to prevent sharp discontinuities due to the padding. The measured ultrasonic pressure field was back-propagated to the transmitting transducer plane. Furthermore, the measured ultrasonic pressure field was forward-propagated to a distance of 4" from the transmitter transducer plane. (See Figure 2 on CD-ROM for an illustration of this procedure.) The distance between planes of propagation was 1 mm. The resulting diffraction patterns for the meridian plane views and the receiver plane views were constructed.

C.2 Propagations from Simulated Field

For visualizations of the simulated ultrasonic fields through water, we modeled our ultrasonic source as a 0.5" diameter, spherically-focused piston. Similar to our experimental data analysis, we used a 64 by 64 array with a 0.5 mm between sites. The distance between planes of propagation was 1 mm. We then propagated a single-frequency (5.13 MHz, 7.08 MHz, or 11.2

MHz) ultrasonic field for comparison to the experimental measurement. We simulated the ultrasonic pressure field that the hydrophone pseudo-array would see at distances of 1", 2", and 3" from the source plane. We also simulated the magnitude of the pressure fields in the meridian plane for a distance of up to 4" from the source plane.

C.3 Propagations from Experimentally Measured Field through Woven Composite Model

In order to build intuition of the diffraction effects due to anisotropic media, we simulated ultrasonic wave propagations through woven fiber composites. A woven fiber composite would diffract the ultrasonic field for several reasons, including: attenuation anisotropy, phase velocity anisotropy, and refraction at the woven layers due to non-normal incidence of ultrasound onto the warp and fill. As a first step in modeling an anisotropic material, our composite model consisted of a five-harness biaxial weave pattern, with the visible warp regions having 50% of the attenuation of the visible fill regions. The relative attenuations of the woven composite were chosen based on experimental measurements from previous work by this group[1]. An image of our composite model is shown in Figure 13 (see CD-ROM), with darker regions corresponding to the fill and the lighter regions corresponding to the warp of the weave pattern.

We imported the narrow-band (5.13 MHz) in-phase and quadrature parts of the pressure field measured by the hydrophone pseudo-array positioned 2" from the transmitting transducer. We again zero-padded our 32 x 32 narrow-band in-phase and quadrature parts of the pressure field to 64 x 64 in order to avoid boundary effects as the fields were propagated. Similarly, we applied a radial (from the center of the pseudo-array) Hanning window to the zero-padded in-phase and quadrature parts of the pressure field so as to prevent sharp discontinuities due to the padding. To simulate the attenuation of a thin woven fiber composite coupon, we propagated the ultrasonic pressure field through the composite model, positioned at the focal plane of the transmitting transducer, to a distance 10 mm past the composite model. We generated images of the diffraction

patterns for the receiver plane views of the magnitude, in-phase, and quadrature parts of the pressure field. The inclusion of the in-phase and quadrature images for the woven fiber composite investigation permits insight into the nature of phase cancellation across the face of the receiver transducer.

The experimental and simulated propagated fields were saved to disk and imported into a commercial imaging software package (Transform 3.3, Fortner Research LLC, Sterling, VA) for final production of the ultrasonic pressure field images. In the pressure magnitude images (receiver plane view image and meridian plane view two-dimensional image and surface plot), darker regions correspond to larger relative pressure magnitudes and lighter regions correspond to smaller relative pressure magnitudes. However, for the in-phase and quadrature parts of the pressure field, a blue to white to red color table has been used. Blue regions correspond to negative values, red regions correspond to positive values, and white regions are neutral. We chose to crop the receiver plane views of the ultrasonic in-phase, quadrature, and magnitude fields so that only the original 32 by 32 grid was shown. Cropping the images permitted zooming the region of interest and displaying the image on a scale exhibiting finer resolution.

D. Results

In this Section we discuss the images of the pressure magnitudes of the ultrasonic field in a meridian plane view and the receiver plane view, and images of the in-phase and quadrature parts of the pressure field in the receiver plane view. The images discussed here are for a single frequency (5.13 MHz) extracted from the broadband measurements. Two-dimensional images are shown of the magnitude of the pressure field at the receiver plane view for the water-path simulations and experimental data. We also include two-dimensional images and surface plots of a meridian plane view of the water-path simulations and experimental measurements. For the woven fiber composite simulation, we include two-dimensional images of the magnitude, in-phase, and

quadrature parts of the pressure field in the receiver plane view. Please see CD-ROM for all the images discussed in this Section.

The meridian plane views have dimensions of ~1.5 inches by 4.0 inches. (Please note the aspect ratio of 2.25:1.) The receiver plane views represent dimensions of ~0.75 inches by ~0.75 inches. In Figures 3 to 5 and Figures 7 to 12, the simulated images are constructed using the same uniformly-excited spherically-focused piston source parameters, and are provided in each figure for direct comparison to the different experimental situations.

Figure 3 compares the ultrasonic diffraction pattern in a meridian plane of the water-path only simulation and that obtained based on the field measurements of the receiving hydrophone 1" from the transmitting transducer. Figures 4 and 5 show similar images, with the position of the receiving hydrophone now at 2" and 3", respectively, from the transmitting transducer. Figure 2 shows the positioning of the transmitting transducer in relation to the propagated field in the meridian plane. In Figures 3 to 5 there are good qualitative agreement between simulation source and experimentally measured source in the depth and width of the focal zone. We also see agreement in the initial convergence of the source to the focal zone and the subsequent spreading of the ultrasonic field, as one would expect from a focused transducer.

Figures 7 to 9 are surface plots of the pressure magnitudes in the meridian plane. These figures present information about the pressure magnitude of the source across its face, in addition to the focal zone information of the ultrasonic field. Figure 6 shows a cartoon that identifies the position of the transmitting transducer relative to the surface plot of the ultrasonic field. In the upper left side of each surface plot, the transmitting transducer radiates downward to the right. In addition to the grayscale coding of the relative pressure magnitudes, the height of the surface plot corresponds to the relative pressure magnitude. (Please note the 2.67:1 aspect ratio in the plane normal to pressure magnitude.) We can make the same qualitative comments regarding the focal zone as we did for Figures 3 to 5. In addition, the back-propagation of the experimentally received ultrasonic fields to the source plane shows the departure from our model of a uniformly excited piston source. We observe a gradual decline in pressure magnitude as we move to the edge of the

transducer for the back-propagated experimentally measured fields. This raises the concern of the validity of modeling our source as being uniformly excited, or of the validity of the back-propagation model itself. We will address this further in Section II.E.

Figures 10 to 12 compare the ultrasonic diffraction patterns in the receiver plane of the simulation and the water-path only experimental data at 1", 2", and 3", respectively. Again, we find good agreement between simulation and experimental measurement for the relative pressure magnitudes and the 3 dB-down regions (as noted by the red dashed circle) from the peak pressure.

Figure 13 shows an image of the attenuation mask of the woven fiber specimen model. As mentioned previously, the darker regions in the image correspond to regions of more attenuation, and the lighter regions corresponding to regions of less attenuation. Figures 14 to 22 contain images of the in-phase part, quadrature part, and magnitude of the pressure fields of the ultrasonic diffraction pattern in the receiver plane 10 mm beyond focal plane. Figures 14 to 17 compare the in-phase parts of the pressure fields of water-path only and through the composite model using different color tables and data ranges. By modifying the range of data imaged and adjusting the color table, we are able to emphasize different features of the images. Figures 14 and 15 use a linear color table. Figures 16 and 17, however, use a non-linear color table which emphasizes changes in the sign of the in-phase part of the pressure field. Similarly, Figures 18 to 21 compare the quadrature parts of the pressure fields of water-path only and through the composite model using different color tables and data ranges. We recognize a slight distortion of the in-phase and quadrature parts of the pressure field through the composite specimen model as compared to the in-phase and quadrature parts of the pressure field of the water-path only by comparing the shape of the central positive (red) region. However, in the images of the magnitude of the pressure field it is more difficult to discern changes between through water-path only and through the composite model, as evidenced in Figure 22. (Please note similarity of 3 dB-down regions highlighted by the red dashed lines.)

E. Discussion

We have implemented a systematic approach to enhance the understanding of the physics underlying the interaction of ultrasound with anisotropic materials. Initial investigations were performed to validate our technique of using an Angular Spectral Decomposition method to simulate experimental situations. In Figures 7 to 9, we compared the simulated source to the source predicted from back-propagation of the measured ultrasonic field. In future work, it may be advantageous to simulate a source with a smooth pressure variation out to the edge in contrast to a uniformly-excited piston source.

We extended our use of the Angular Spectral Decomposition method to model the possible effects that would occur in an anisotropic woven fiber composite. As a first step, we have considered only the magnitude attenuation effects, neglecting other pertinent effects, including phase velocity anisotropy and refraction at the surface that may occur. We observed in Figures 14 to 21 phase alterations, as compared to a water-path only signal, which could possibly produce phase cancellation across the face of the interrogating phase-sensitive transducer, thus underestimating the signal strength. Furthermore, knowledge of the diffraction effects of the anisotropy of the material will aid in linear, 1.5, and two-dimensional array beam forming.

These observations lead to several issues of concern for further investigation. In our model of a woven fiber composite, we have chosen a small tow size. It is worth investigating how adjusting tow size can affect the received signal. Furthermore, we have shown images constructed for 5.13 MHz. Increasing frequency will permit finer resolution of the constructed images. However, in the pursuit of a robust measurement technique, it is worth considering the issue of focal spot size versus spatial averaging.

F. References

1. T.D. Lhermitte, S.M. Handley, M.R. Holland, and J.G. Miller, "Anisotropy of the Frequency-Dependent Ultrasonic Attenuation in Unidirectional Graphite/Epoxy Composite Material", *Proc. IEEE Ultrasonics Symposium*, (Orlando, Published 1992), Vol. 91CH3079-1, pp. 819-823, (1991).

2. L. J. Busse, et al., "Phase Cancellation Effects: A Source of Attenuation Artifact Eliminated by a CdS Acoustoelectric Receiver", *Ultrasound in Medicine*, Vol. 3, pp. 1519-1535, (1977).

3. Patrick H. Johnston and J.G. Miller, "Phase-Insensitive Detection for Measurement of Backscattered Ultrasound", *IEEE Transactions on Ultrasonics, Ferroelectrics, and Frequency Control*, Vol. UFFC-33, pp. 713-721, (1986).

4. F. J. Margetan and R. B. Thompson, "The Use of Axial Pressure Field Scans to Characterize Spherically-Focussed Ultrasonic Transducers, and Results for Three Nominally Identical 5-MHz Probes", Center for Nondestructive Evaluation, Report Number: ISU/ETC-5, (June, 1994).

5. Mitchell M. Goodsitt, Ernest L. Madsen, and James A. Zagzebski, "Field patterns of pulsed, focused, ultrasonic radiators in attenuating and nonattenuating media", *J Acoust Soc Am*, Vol. 71, pp. 318-329, (1982).

6. Ernest L. Madsen, Mitchell M. Goodsitt, and James A. Zagzebski, "Continuous waves generated by focused radiators", *J Acoust Soc Am*, Vol. 70, pp. 1508-1517, (1981).

7. C. J. Bouwkamp, "Diffraction Theory", *Reports on Progress in Physics*, Vol. 17, pp. 35-92, (1954).

8. M. Forbes, S. Letcher, and P. Stepanishen, "A Wave Vector, Time-Domain Method of Forward Projecting Time-Dependent Pressure Fields", *J Acoust Soc Am*, Vol. 90, pp. 2782-2793, (1991).

9. Mark E. Schafer and Peter A. Lewin, "Transducer Characterization Using the Angular Spectrum Method", *J Acoust Soc Am*, Vol. 85, pp. 2202-2214, (1989).

10. Peter R. Stepanishen and Kim C. Benjamin, "Forward and Backward Projection of Acoustic Fields Using FFT Methods", *J Acoust Soc Am*, Vol. 71, pp. 803-812, (1982).

11. Christopher J. Vecchio and Peter A. Lewin, "Finite Amplitude Acoustic Propagation Modeling Using the Extended Angular Spectrum Method", *J Acoust Soc Am*, Vol. 95, pp. 2399-2408, (1994).

12. Robert C. Waag, James A. Campbell, Jan Ridder, and Peter R. Mesdag, "Cross-Sectional Measurements and Extrapolations of Ultrasonic Fields", *J Acoust Soc Am*, Vol. 32, pp. 26-35, (1985).

III. Dependence of Pressure Magnitude on Frequency for Ultrasonic Measurements of a Woven Cloth (December 1996 to June 1997)

Previously[1], we proposed a simple model to simulate the effect of a thin woven composite on an insonifying ultrasonic pressure field. This initial approach provided an avenue to begin development of a robust measurement method for nondestructive evaluation of anisotropic materials. We extend that work by performing experimental measurements on a single layer of a five-harness biaxial woven composite to investigate how a thin, yet architecturally complex, material interacts with the insonifying ultrasonic field.

In Section III.A of this Progress Report we describe the experimental arrangement and methods for data acquisition of the ultrasonic diffraction patterns upon transmission through a thin woven composite. We also briefly describe the thin composite specimen investigated. Section III.B details the analysis of the experimental data followed by the experimental results in Section III.C. Finally, a discussion of the observations and conclusions is found in Section III.D.

A. Experimental Arrangement and Methods

All measurements in this study were performed in an immersion tank using a set of 0.5" diameter, spherically-focused (4" focal length), piezoelectric transducers with nominal center frequencies of 5 MHz, 10 MHz, and 15 MHz (Panametrics V309, V311, and V319, respectively) as the transmitting transducer. For notational purposes, we refer to the different transducers by their nominal center frequency (i.e., the 5 MHz transmitting transducer). The thin woven composite was positioned in the focal plane of the transmitting transducer and oriented normal to the beam axis of the transducer. The thin composite, as mentioned above, is a single layer (less than 1 mm thick) of a five-harness biaxial weave. A 1 mm diameter PVDF, broadband, needle hydrophone (Force Institute, Type MH28-10) was used as the receiving transducer. The receiving hydrophone was positioned 120 mm from the transmitting transducer (approximately 20 mm from

the back side of the specimen). In the receiving plane, the hydrophone sampled the ultrasonic pressure field in a two-dimensional pseudo-array manner[2]. The pseudo-array was composed of 64 sites by 64 sites (4096 total sites) with 0.5 mm separation between adjacent sites for a total sampled area of 31.5 mm by 31.5 mm.

Figure 1 is a schematic diagram showing the data acquisition system used in this investigation. The transmitting transducer was excited with a broadband pulse generated by a Panametrics 5800 pulser/receiver. The ultrasonic signal received by the hydrophone was initially sent through a unity-gain preamplifier (Force Institute, Type BAS) matched specifically to the hydrophone, providing 50 Ω coupling to the receive-side electronic equipment. The signal was then sent through a pair of programmable attenuators (HP 8494G and 8496G) that permitted precise adjustment of the signal amplitude to prevent saturation of the input stage of the receiving electronic equipment and to maximize the dynamic range of the oscilloscope. From the attenuators, the received signal went to the receiving stage of the Panametrics 5800 pulser/receiver, and finally on to a Tektronix 2430 digital oscilloscope for digitization. An Apple Macintosh IIfx computer utilized in-house custom software written in the C programming language to acquire the rf time traces and store them for off-line analysis.

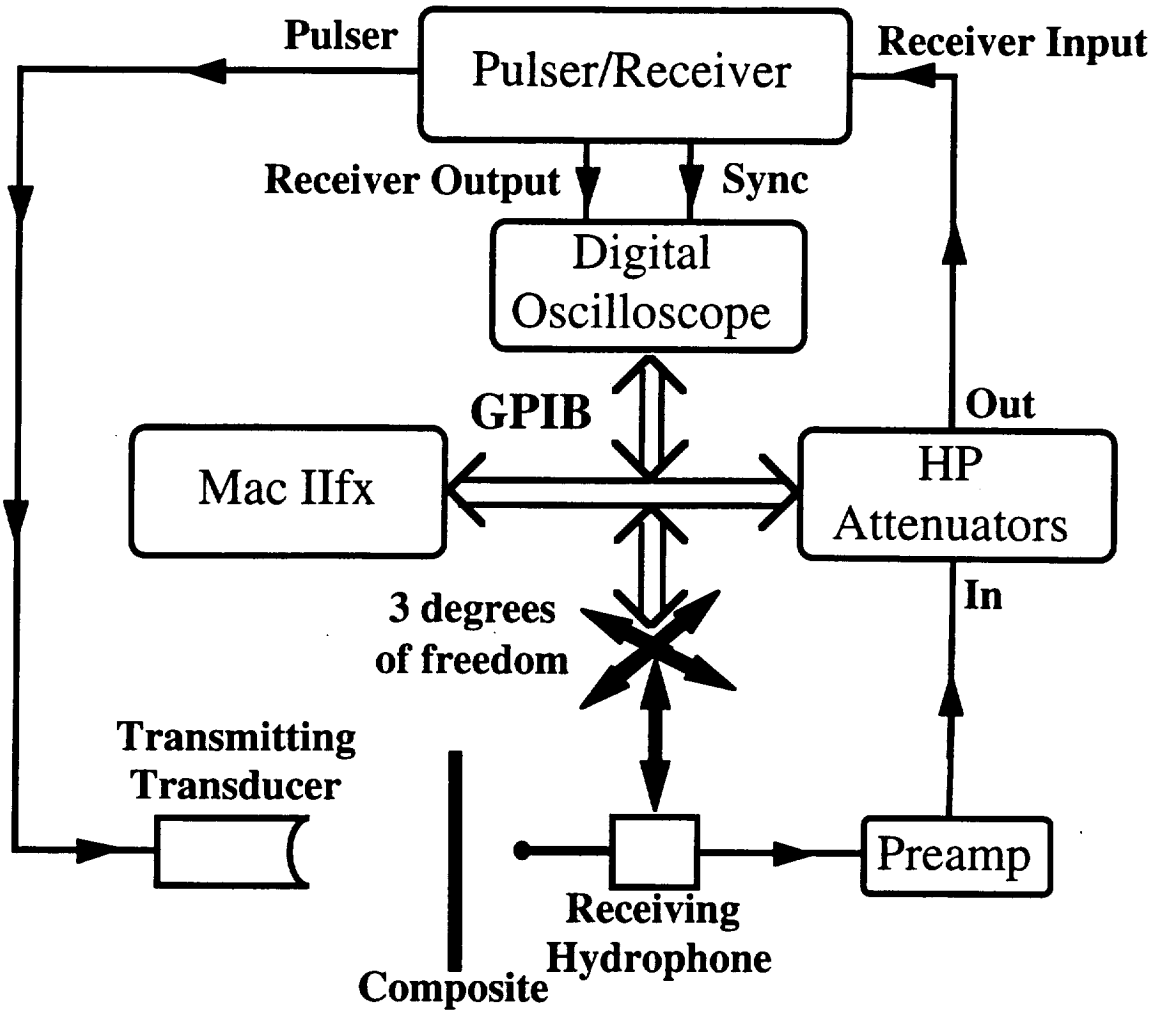

Figure 1: Experimental Setup.

It is a goal of this experimental research to understand how systematic variations of the acquisition system, as well as changes in the materials investigated, affect the quantitative evaluation of these materials. The first physical parameter we chose to vary systematically was the nominal center frequency of the transmitting transducer. Three transmitting transducers were employed for the acquisition of the experimental data discussed within this report.

Prior to pseudo-array scanning of the ultrasonic beam through the thin composite, dynamic range measurements of the experimental system with the thin composite inserted were performed for each transmitting transducer. At the origin of the pseudo-array, a series of rf traces were

acquired with the insertion of a range of attenuations (0 dB to 60 dB in 5 dB steps). At each attenuation setting, 64 rf time traces were acquired and averaged off-line before being stored to disk. The voltage scale of the digital oscilloscope was adjusted in order to maximize the dynamic range of the oscilloscope. Each rf time trace acquired throughout this study consisted of 1024 points sampled in the interleave mode at 250 MegaSamples/s (0.004 μs sampling period). (The stability of the rf time trace at all sites insured there would be no averaging problems with the oscilloscope operating in the interleave mode.) The digital oscilloscope was externally triggered by a synchronization pulse provided by the Panametrics 5800. The data acquisition delay time (relative to the trigger signal) was set manually such that the received trace was localized within the acquisition window.

Following the measurement of the dynamic range of the experimental system with the thin composite inserted, the transmitted beam through the thin composite was scanned in a pseudo-array manner, as described above. In addition to maximizing the dynamic range of the oscilloscope at the pseudo-array origin site, the programmable attenuators were adjusted to maximize the dynamic range of the receive-side electronics. At each site of the pseudo-array, 64 rf time traces were acquired and averaged off-line before being stored to disk.

To investigate how the spatial variation of the weave pattern for the thin woven composite affects the phase fronts of the ultrasonic signal, we conducted four pseudo-array scans with each transducer. Figure 2 illustrates the relative positioning of the four different scan regions with respect to the thin composite. The center of each pseudo-array scan was linearly separated by 3 mm from the previous pseudo-array scan. These four regions provide a fair representation of the different types of regions that would be encountered in subsequent studies of this thin composite.

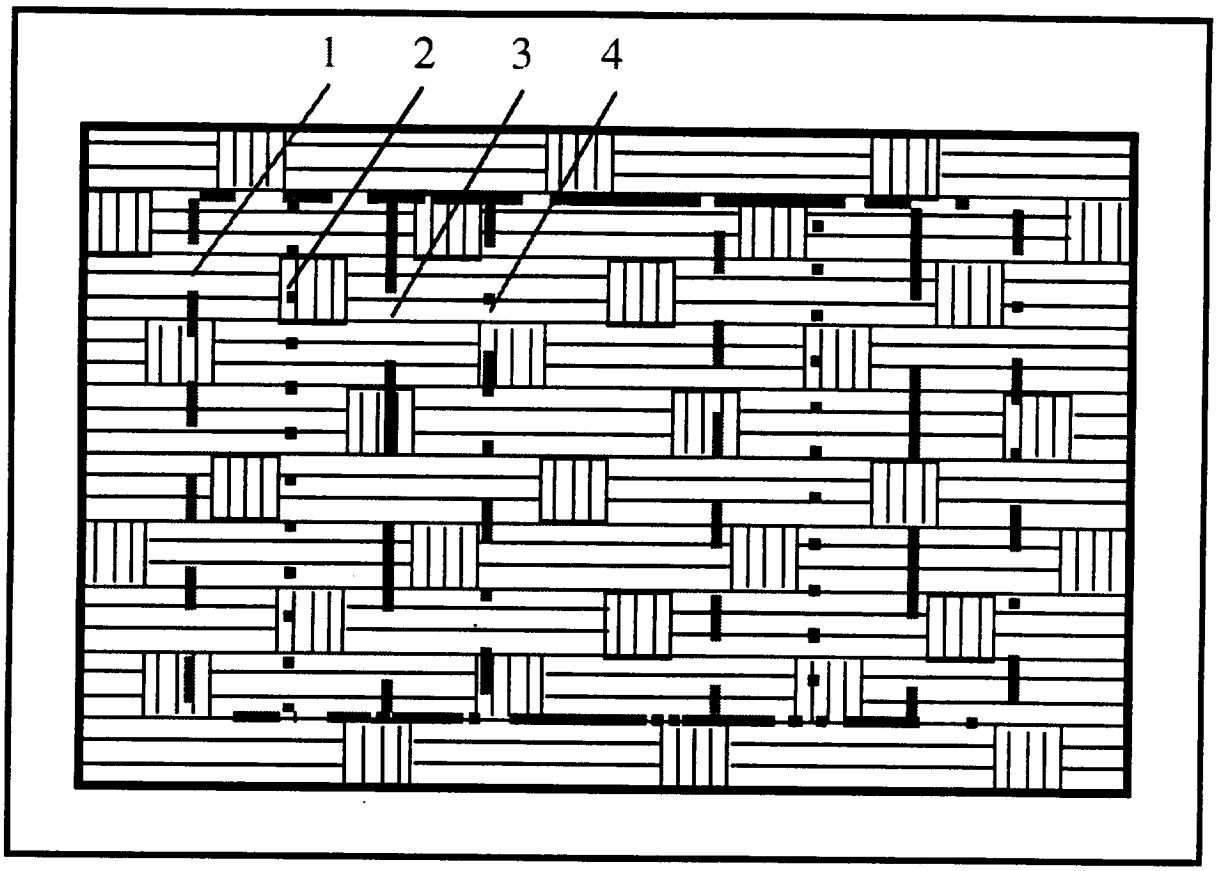

Figure 2: Relative positioning of different scanned regions of the thin woven composite.

B. Data Analysis

B.1 Software

Data analyses and visualization were performed on a Power Macintosh using in-house custom software written in the C programming language, in conjunction with a commercial graphing package (DeltaGraph® Pro 3.5, DeltaPoint, Inc., Monterey, CA) and an imaging software package (Transform 3.3, Fortner Research LLC, Sterling, VA).

B.2 Dynamic Range Measurement Analysis

For the dynamic range measurements, each averaged rf time trace was Fast Fourier Transformed. The magnitude of the Fast Fourier Transform was then squared to provide the power spectrum. In addition, for each transducer, the differences in power spectra were calculated by subtracting the power spectrum resulting from the insertion of 10 dB of attenuation from each power spectrum. The dynamic range power spectra and relative power spectra for each transmitting transducer were then plotted.

B.3 Pseudo-Array Measurement Analysis

For the pseudo-array scans, the time-averaged rf trace acquired at each pseudo-array site was Fast Fourier Transformed and the magnitude of the Fast Fourier Transform was calculated. To provide a more robust approach for material evaluation, we performed a narrowband averaging analysis on the data. Discrete frequency data within a 1 MHz bandwidth was extracted from the broadband pressure magnitude spectra, and subsequently averaged to provide a narrowband magnitude representation of the measured pressure field. The 1 MHz bandwidth typically corresponded to 5 or 6 data points, dependent upon where the 1 MHz bandwidth fell on the discretely sampled pressure magnitude spectrum. Averaging over frequencies offered the advantage of reducing susceptibility to unrepresentative single frequency events (outliers).

For each of the three transmitting transducers, we acquired five sets of data (one water path and four composite paths). For each data set, narrowband analysis was performed over three distinct frequency ranges (see Table 1). For the 5 MHz transmitting transducer, we calculated narrowband magnitudes of the pressure field for 2.5 MHz to 3.5 MHz, 4.5 MHz to 5.5 MHz, and 6.5 MHz to 7.5 MHz. For the 10 MHz transmitting transducer, we calculated narrowband magnitudes of the pressure field for 7.5 MHz to 8.5 MHz, 9.5 MHz to 10.5 MHz, and 11.5 MHz to 12.5 MHz. Finally, for the 15 MHz transmitting transducer, we calculated the narrowband

magnitudes of the pressure field for 10.5 MHz to 11.5 MHz, 12.5 MHz to 13.5 MHz, and 14.5 MHz to 15.5 MHz.

B.3a Magnitude Image Construction

Image construction of the experimentally measured narrowband magnitude of the ultrasonic pressure field was performed using Transform 3.3. For all images, only the central region (central 32 sites by 32 sites, i.e., 15.5 mm by 15.5 mm) of the pseudo array appears. Cropping the images permitted zooming the region where effects due to changes in physical parameters (i.e., water path versus composite path, insonifying frequency, and composite position) were most significant. All magnitude of the pressure field images are presented using grayscale mappings. Darker regions correspond to larger relative pressure magnitudes and lighter regions correspond to smaller relative pressure magnitudes. For purposes of presentation, the images were interpolated to present smooth transitions across the receiving pseudo-array aperture. A bilinear interpolation method (row then column) calculates the grayscale for each pixel of the image.

Transducer	Narrowband Ranges
5 MHz	2.5 MHz to 3.5 MHz
	4.5 MHz to 5.5 MHz
	6.5 MHz to 7.5 MHz
10 MHz	7.5 MHz to 8.5 MHz
	9.5 MHz to 10.5 MHz
	11.5 MHz to 12.5 MHz
15 MHz	10.5 MHz to 11.5 MHz
	12.5 MHz to 13.5 MHz
	14.5 MHz to 15.5 MHz

Table 1: Narrowband ranges for the transducers.

Figure 3 shows a representative pressure magnitude field overlaid with a cartoon of the composite weave pattern. It also provides relevant dimensions for the images.

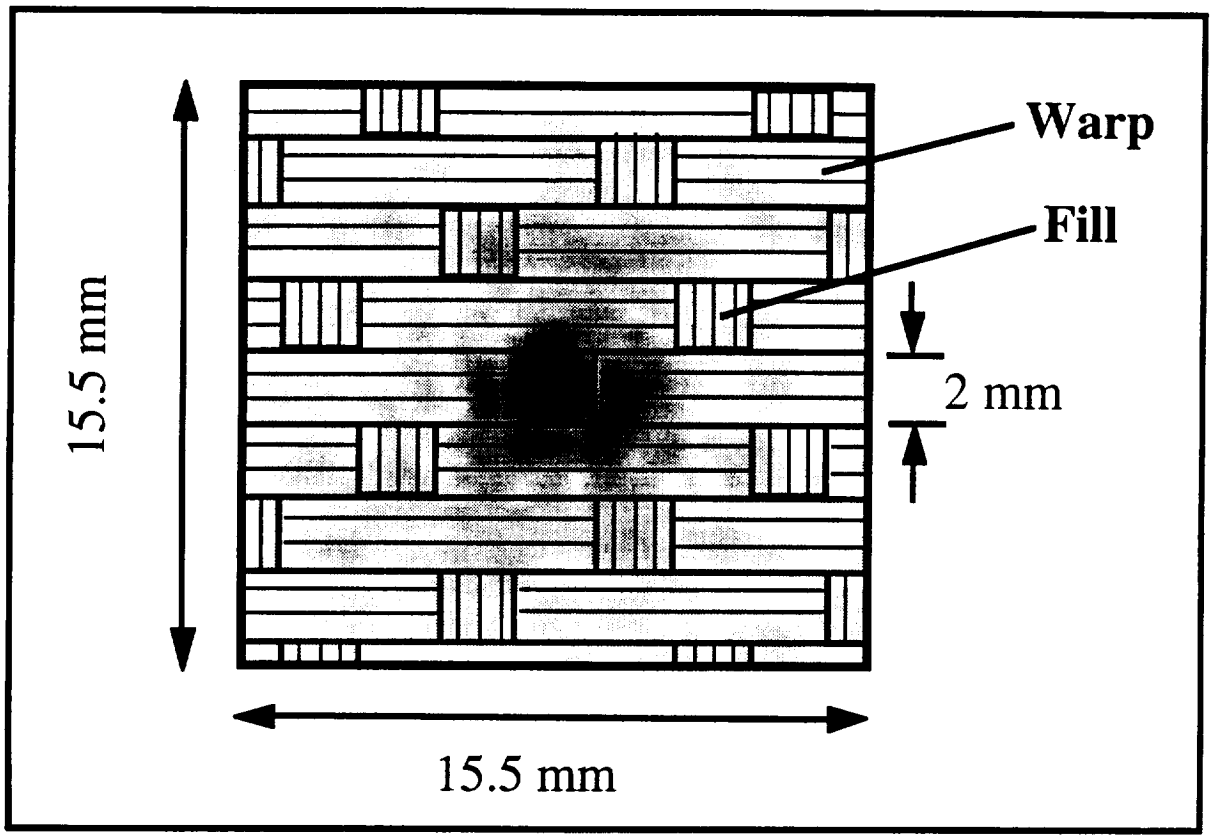

Figure 3: Representative pressure magnitude image with a cartoon of the thin woven composite overlaid.

For each series of scans (1 water path and 4 composite paths) for a particular transmitting transducer, a set of images was constructed (3 sets total) consisting of 3 sections. All the images of this report employ grayscale mapping. However, within each section, images are displayed using a data floor and data ceiling specific to that section to calculate the bin size. Therefore, the same data ranges are mapped to the same gray value for the images within each section (i.e., bin sizes are the same). The use of this grayscale mapping technique permits direct comparison of images *within* each image section. We do not provide direct comparison for images from different transducers because system effects have not been completely deconvolved for the use of different

transducers. However, we can still make some general observations between these sets as will be discussed later.

The first section of an image set compares pressure magnitude measurements for water path only to pressure magnitude measurements with the thin composite inserted. The second section compares magnitude measurements from different scanned regions of the thin woven composite for a particular narrowband frequency. The third and final section of an image set for a given transducer compares the pressure magnitudes for a given thin composite position at different insonifying frequencies. Table 2 provides the organization to the sets of the images constructed.

C. Results

In this Section we discuss the dynamic range measurement results and the receiver plane images of the experimentally measured narrowband magnitude of the pressure field through water path only and through the thin woven composite. Please see either the hardcopy images included with this report or the accompanying CD-ROM for viewing of images discussed in this Section.

Figures 4, 6, and 8 show representative power spectra for the 5 MHz, 10 MHz, and 15 MHz transmitting transducers, respectively, for different electronic attenuation settings with the thin composite inserted in the signal path. Figures 5, 7, and 9 show representative difference power spectra (with respect to the power spectrum obtained for 10 dB of attenuation) for the 5 MHz, 10 MHz, and 15 MHz transmitting transducers, respectively. The vertical dashed lines in each figure demarcate the 10 dB-down region for the power spectrum. These figures provide confidence that all experimental data acquired for this report were within the usable bandwidth of the acquisition system, in addition to being well above the noise floor and below the saturation ceiling.

Table 2 offers an index to the figures of the images constructed. As described above, each of the 3 sets are organized into 3 sections (see Chart 1). Each set is composed of 10 figures. The first section of each set consists of three pairs of images: the narrowband magnitudes for water

path and composite path at three narrowband ranges. The second section has three subsections of four images: the narrowband magnitudes of the four different composite positions at three narrowband ranges. The third section of each set has four subsections of three images: the narrowband magnitudes for the three narrowband ranges at the four composite positions.

Figures	Transducer	Description
10 to 12	5 MHz	Compare water path to composite path
13 to 15		Compare different composite positions
16 to 19		Compare different frequencies
20 to 22	10 MHz	Compare water path to composite path
23 to 25		Compare different composite positions
26 to 29		Compare different frequencies
30 to 32	15 MHz	Compare water path to composite path
33 to 35		Compare different composite positions
36 to 39		Compare different frequencies

Table 2: Pressure magnitude image figures.

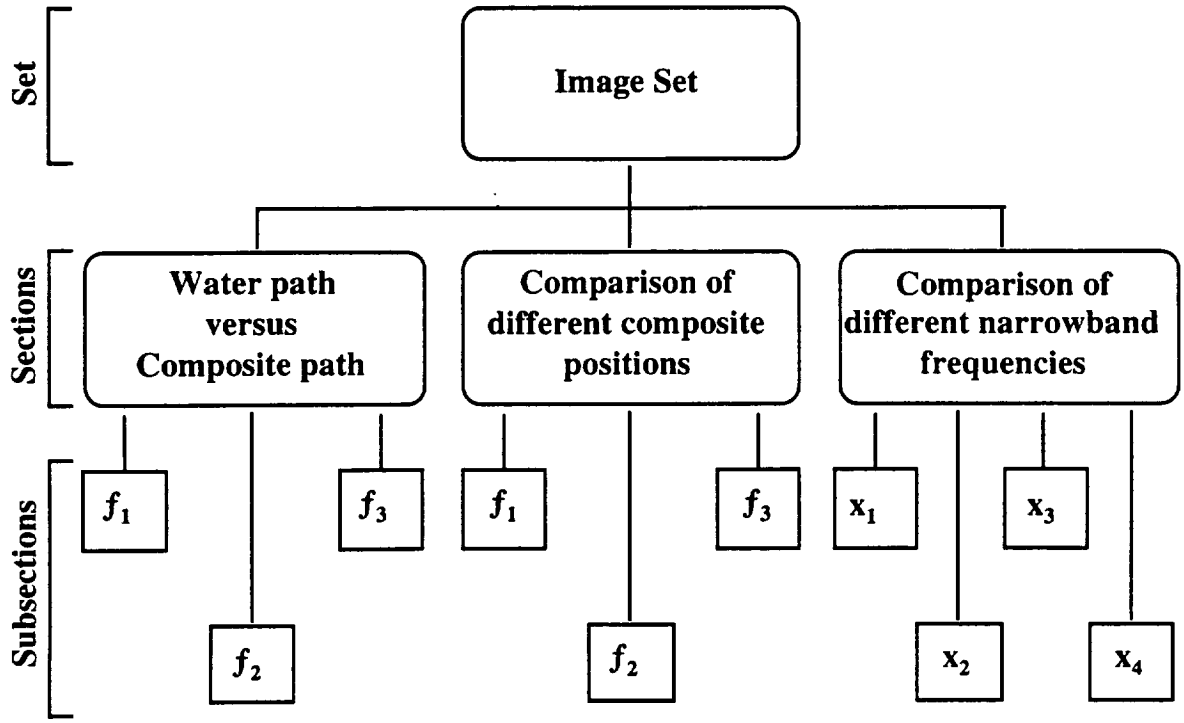

Chart 1: Organizational chart of an image set. Each image set is divided into 3 sections. The f's represent the narrowband frequency ranges and the x's represent the composite positions.

D. Discussion

D.1 Comparison of Water Path versus Thin Composite Path

Inspection of the images comparing the pressure magnitude for water path and composite path provides several general observations (see Figures 10 to 12, 20 to 22, 30 to 32). First, there is an apparent decrease in pressure magnitude for the ultrasonic signal which passes through the thin composite. This decrease is expected due to the reflection losses at the water-composite interfaces, in addition to the attenuation encountered from propagation through the thin composite as compared to water path only. Second, the disruption of the circular symmetry of the ultrasonic beam due to the insertion of the composite is evident. A contribution to the observed loss of symmetry of the ultrasonic pressure magnitude may be due to a very slight non-normal incidence

of the ultrasonic beam with respect to the fill orientation of the thin composite (see Figure 40)[3,4]. As the ultrasonic beam interrogates different regions of the thin woven composite, the fill orientation with respect to the ultrasonic beam will change. It is this anisotropy of the fill orientation with respect to axis of the ultrasonic beam that can contribute to the distortion of the ultrasonic beam, and, in turn produce a mottled and distorted pressure magnitude field[5]. In addition, there will be a wavelength dependence to the interaction of the ultrasonic field with the fill. We could imagine that another thin composite of a different weave pattern would result in a different distortion of the ultrasonic signal. For both the water paths and the composite paths it is apparent that as frequency increases (wavelength decreases) the cross-sectional area of the ultrasonic beam decreases, thus decreasing the area (volume) of insonification. This is discussed further in the following subsection.

D.2 Comparison of Insonifying Frequencies

As we increase the frequency of insonification, the diameter of our ultrasonic beam decreases (see Figures 16 to 19, 26 to 29, and 36 to 39). This decrease in the ultrasonic beam diameter, most notable for the higher frequencies, is of importance when the main beam diameter is on the order of or smaller than features of the composite (i.e., the fiber bundle size). In this case, the pressure magnitude images can be highly dependent upon the region of the composite insonified and the wavelength of the insonifying beam. For instance, the ultrasonic beam diameter could be contained within one fiber bundle or it may overlay the edge of a fiber bundle (see Figure 41). These two situations can produce distinctly different results.

For frequencies of 10 MHz and greater we are able to view the finer details of the thin composite, such as the fiber bundle size. Rough measurements from the images show the fiber bundle dimensions to be approximately 2 mm which agrees well with measurement of the fiber bundle size of the thin composite.

Knowledge of the insonifying volume as a function of frequency becomes increasingly important if one wishes to extend these observations to the use of true two-dimensional transmitting and receiving arrays. With available digital technologies, dynamic focusing of a two-dimensional array will permit customized focusing of the ultrasonic field.

D.3 Comparison of Thin Composite Positions

At lower frequencies (longer wavelengths), the main beam diameter is large enough that on average approximately the same type of region is insonified (see Figures 13 to 15). This reduces the amount of pressure magnitude variation that we observe between the different composite regions for a given frequency. In contrast, as mentioned above, the pressure magnitude images for the different scanned regions are more sensitive at higher frequencies (see Figures 23 to 25 and 33 to 35).

E. References

1. James G. Miller, "Ultrasonic Nondestructive Evaluation Techniques Applied to Quantitative Characterization of Textile Composite Materials", NASA, Progress Report, Report Number: NAG 1-1848, (December, 1996).

2. Mark R. Holland and J.G. Miller, "Phase-Insensitive and Phase-Sensitive Quantitative Imaging of Scattered Ultrasound Using a Two-Dimensional Pseudo-Array", 1989, (Chicago, Published 1988), Vol. 88 CH 2578-3, pp. 815-819.

3. Brian N. Cox and Gerry Flanagan, "Handbook of Analytical Methods for Textile Composites", NASA, Report Number: Contractor Report 4750, (March, 1997).

4. K.K. Shung and J.M. Dzierzanowski, "Effects of Phase-Cancellation on Scattering Measurements", *Ultrasonic Imaging*, Vol. 4, pp. 56-70, (1982).

5. Peter W. Marcus and Edwin L. Carstensen, "Problems with Absorption Measurements of Inhomogeneous Solids", *J. Acoust. Soc. Am.*, Vol. 58, pp. 1334-1335, (1975).

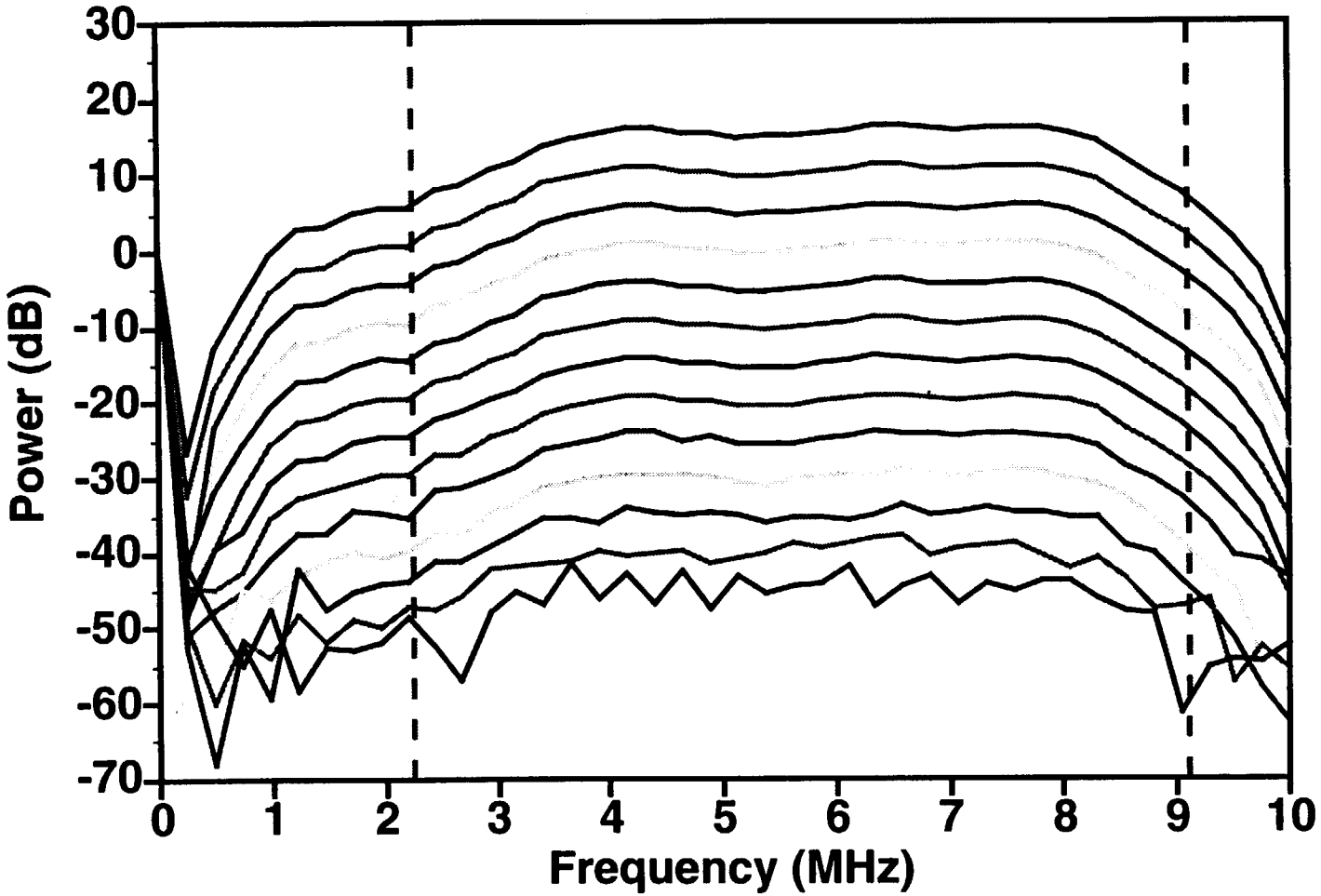

Figure 4: Power spectra of the thin woven composite for the 5 MHz transmitting transducer resulting from the insertion of attenuation in 5 dB steps. The vertical dashed lines demarcate the 10 dB-down region ($\approx$ 2 to 9 MHz).

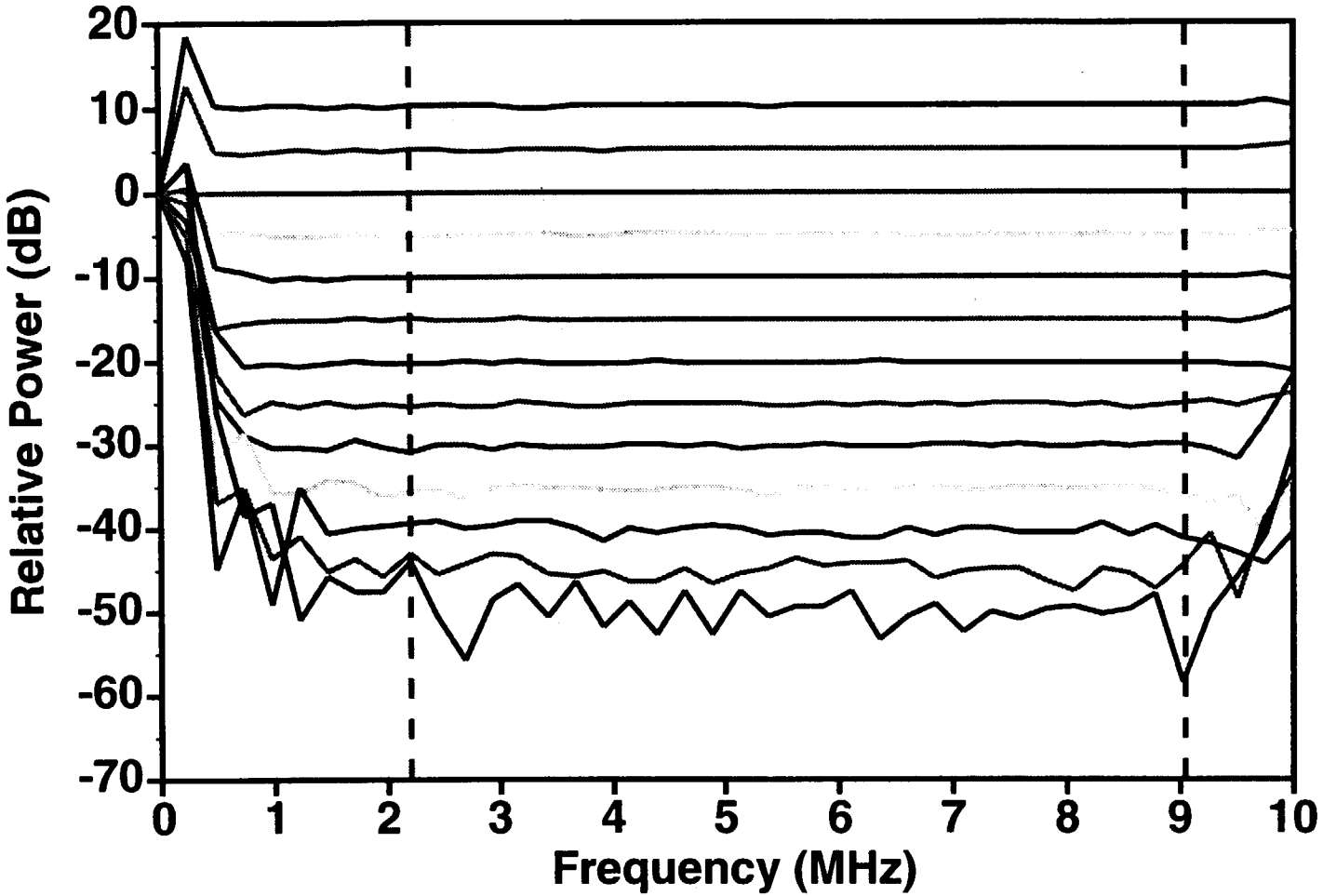

Figure 5: Relative power spectra of the thin woven composite for 5 MHz transmitting transducer resulting from the insertion of attenuation in 5 dB steps. The vertical dashed lines demarcate the 10 dB-down region ($\approx$ 2 to 9 MHz).

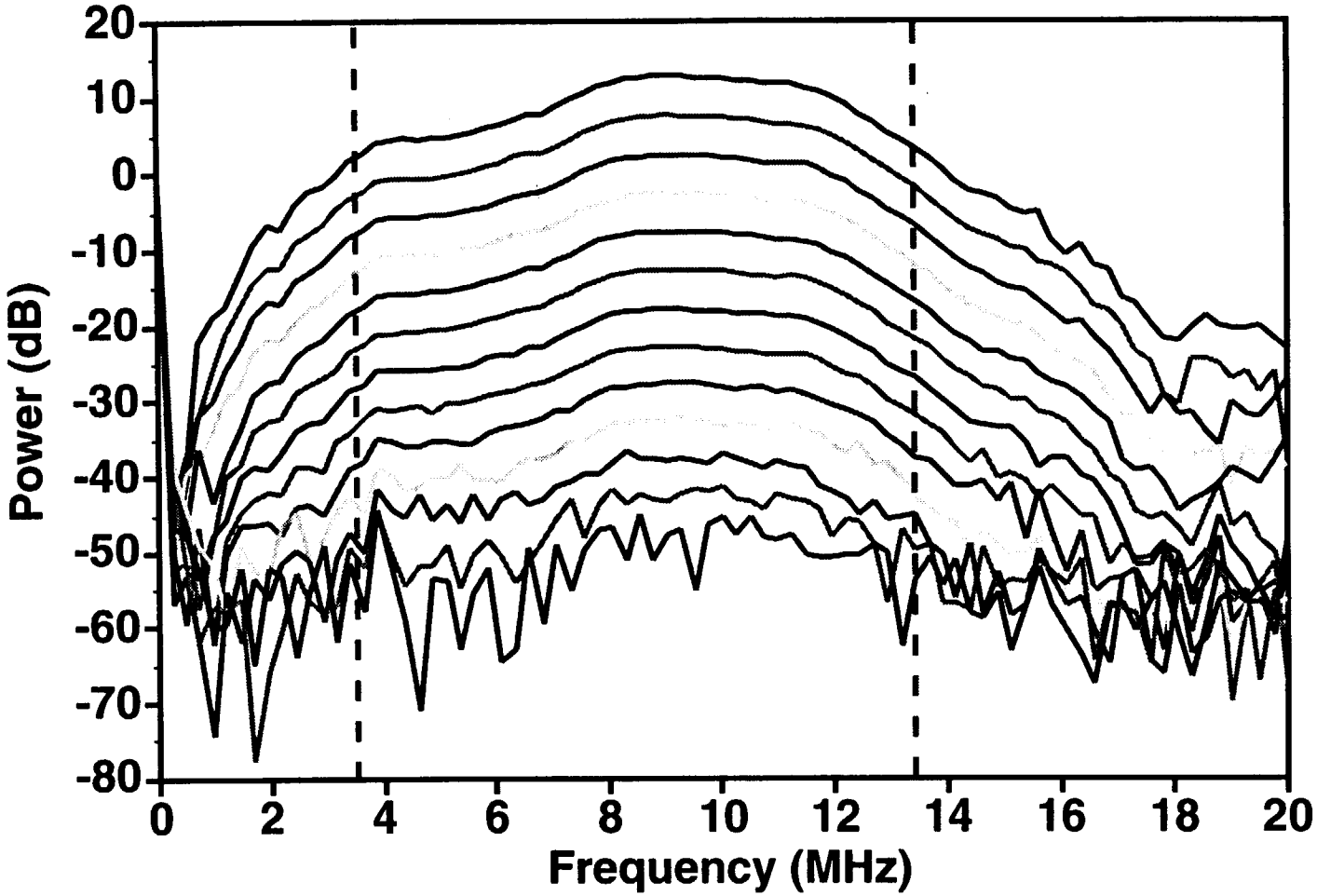

Figure 6: Power spectra of the thin woven composite for the 10 MHz transmitting transducer resulting from the insertion of attenuation in 5 dB steps. The vertical dashed lines demarcate the 10 dB-down region (≈ 3.5 to 13.5 MHz).

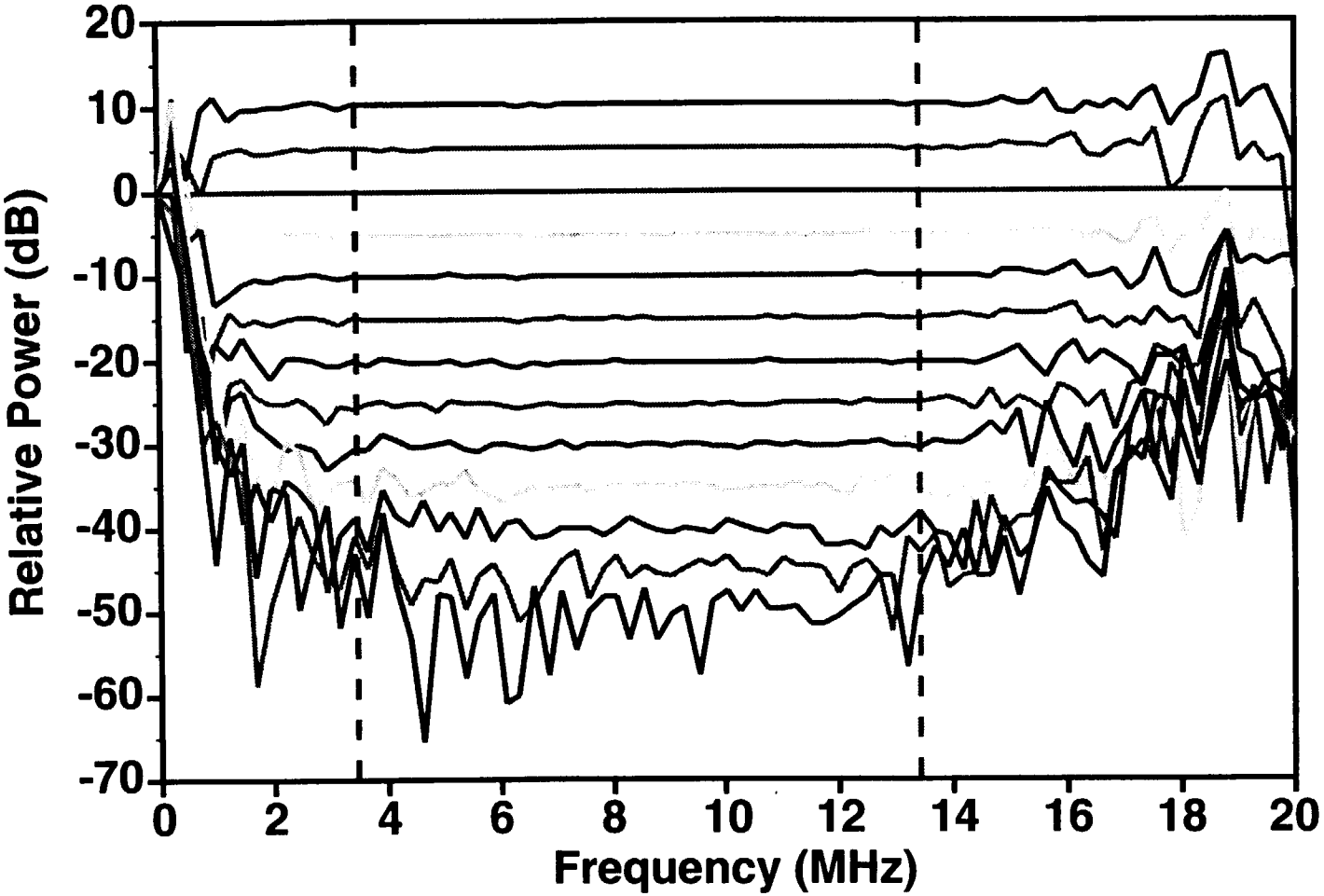

Figure 7: Relative power spectra of the thin woven composite for 10 MHz transmitting transducer resulting from the insertion of attenuation in 5 dB steps. The vertical dashed lines demarcate the 10 dB-down region (≈ 3.5 to 13.5 MHz).

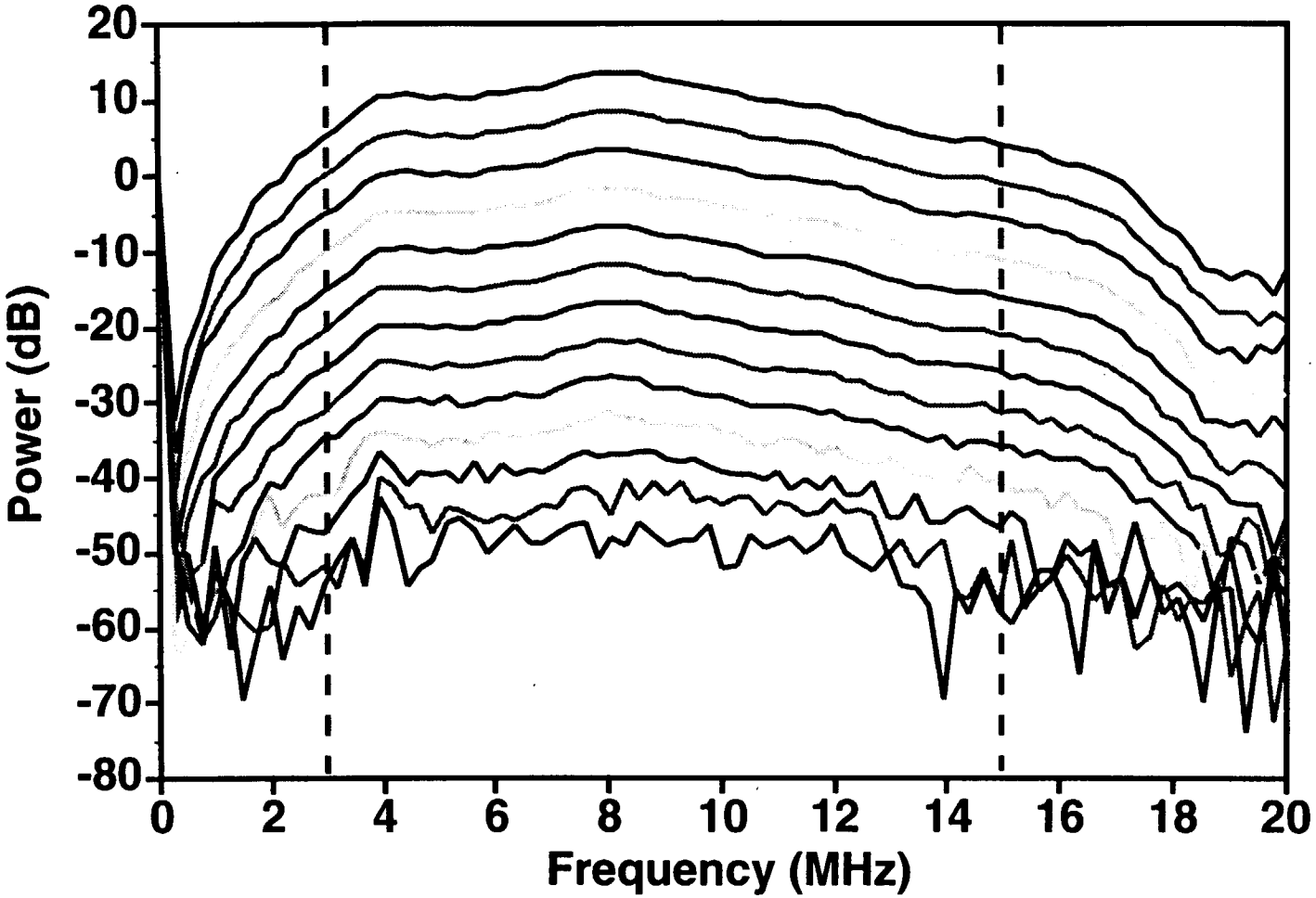

Figure 8: Power spectra of the thin woven composite for the 15 MHz transmitting transducer resulting from the insertion of attenuation in 5 dB steps. The vertical dashed lines demarcate the 10 dB-down region (≈ 3 to 15 MHz).

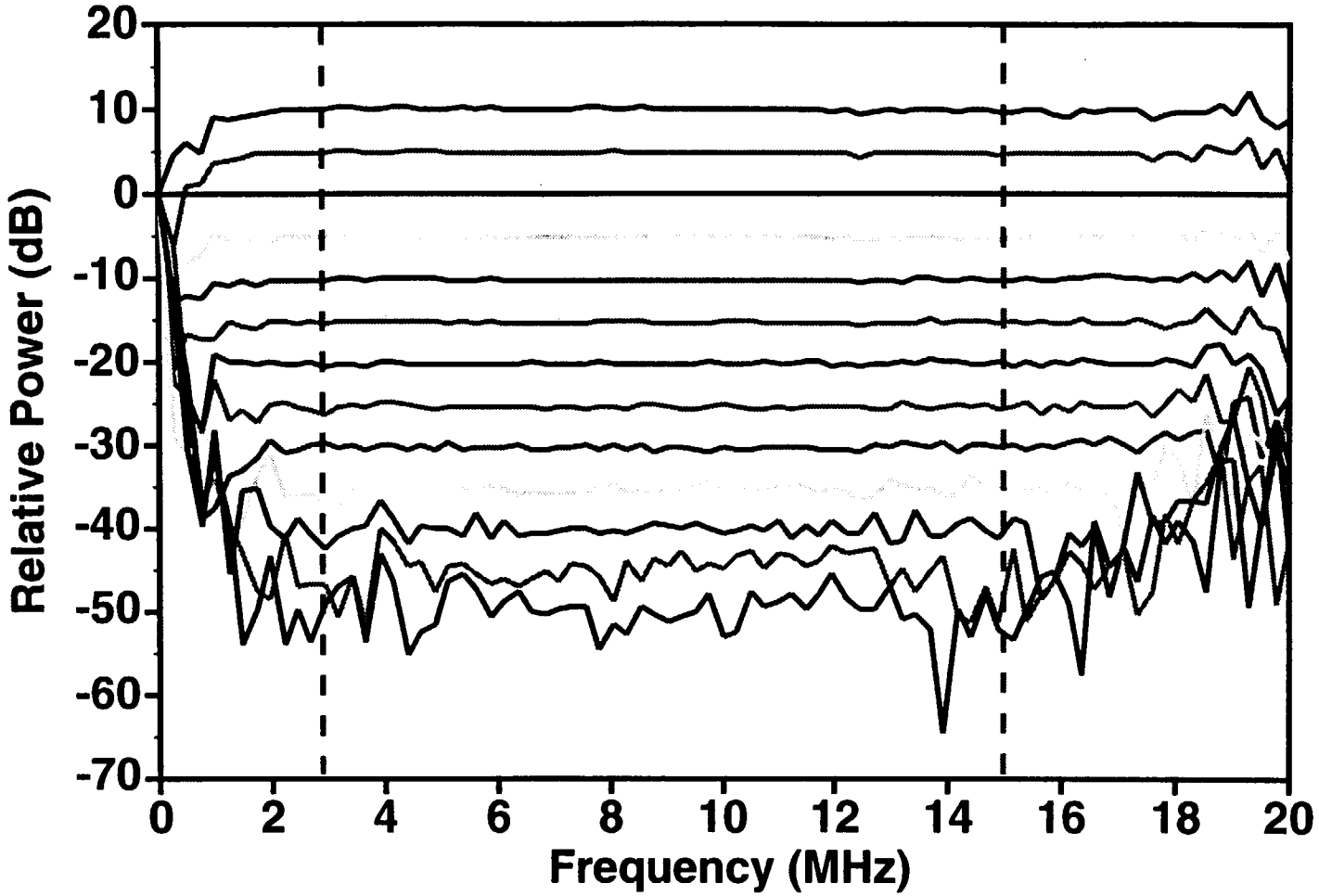

Figure 9: Relative power spectra of the thin woven composite for 15 MHz transmitting transducer resulting from the insertion of attenuation in 5 dB steps. The vertical dashed lines demarcate the 10 dB-down region (≈3 to 15 MHz).

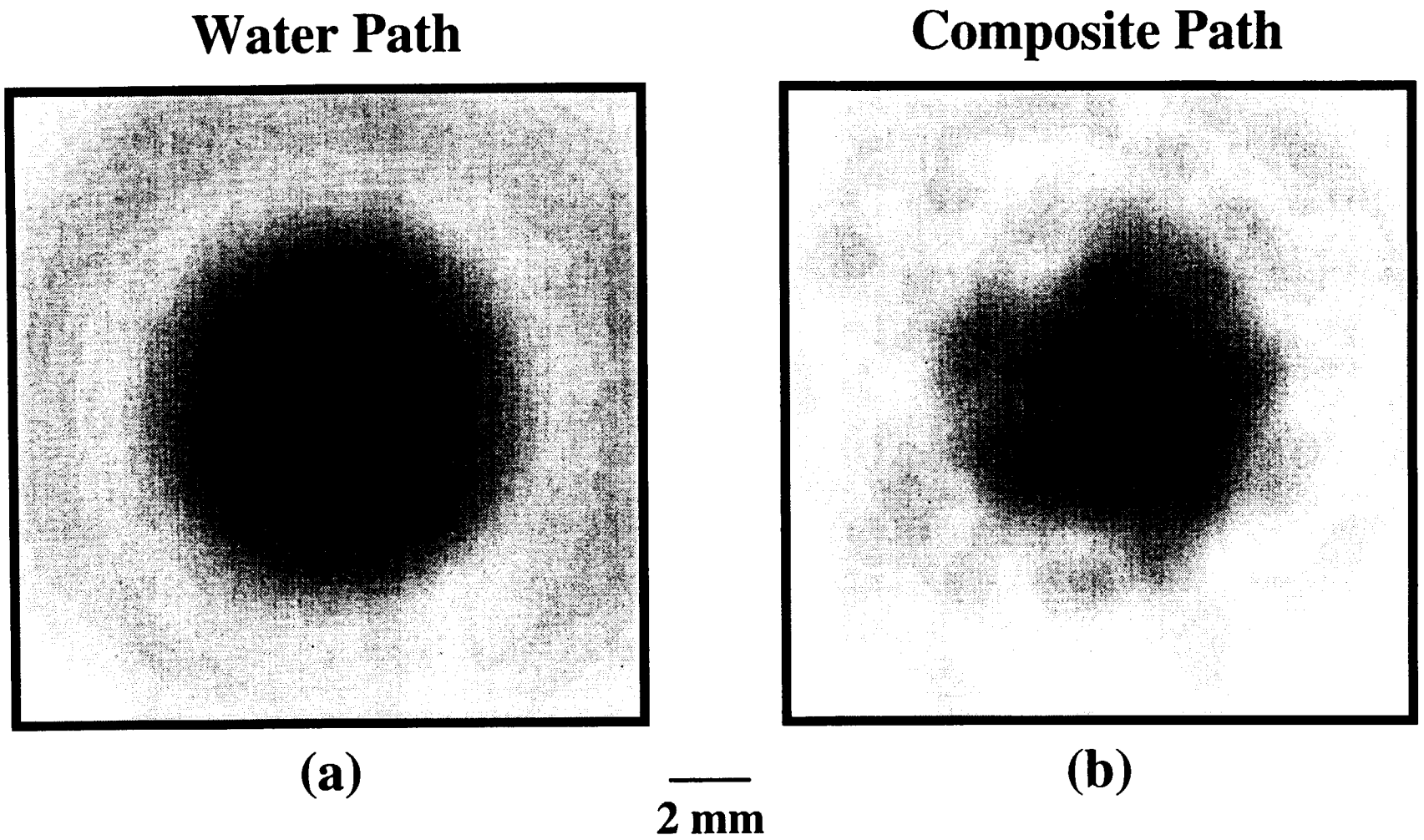

Figure 10: Water path versus composite path for 2.5 MHz to 3.5 MHz. Receiver plane images for (a) narrowband pressure magnitude for water path only and (b) narrowband pressure magnitude for composite path using the 5 MHz transducer.

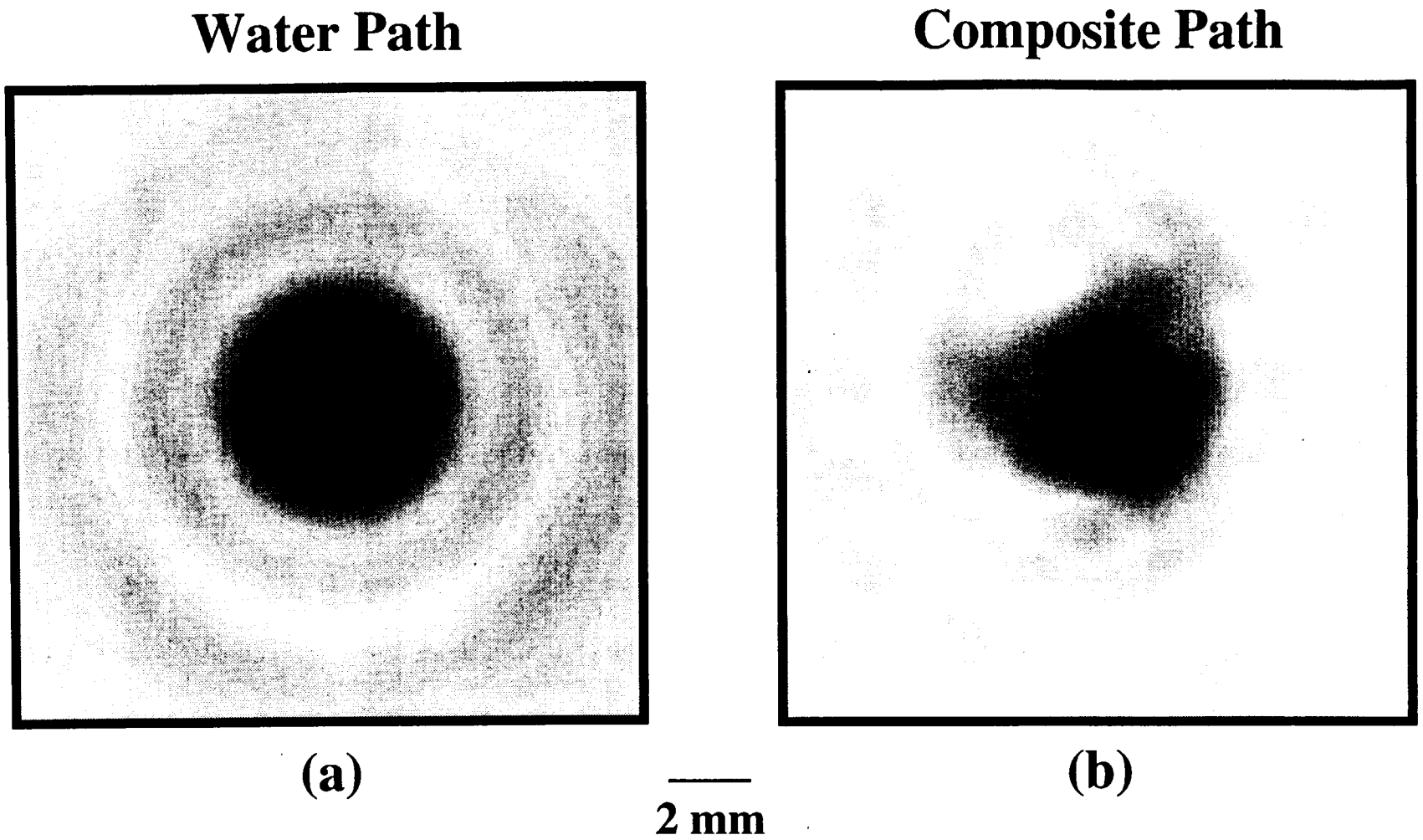

Figure 11: Water path versus composite path for 4.5 MHz to 5.5 MHz. Receiver plane images for (a) narrowband pressure magnitude for water path only and (b) narrowband pressure magnitude for composite path using the 5 MHz transducer.

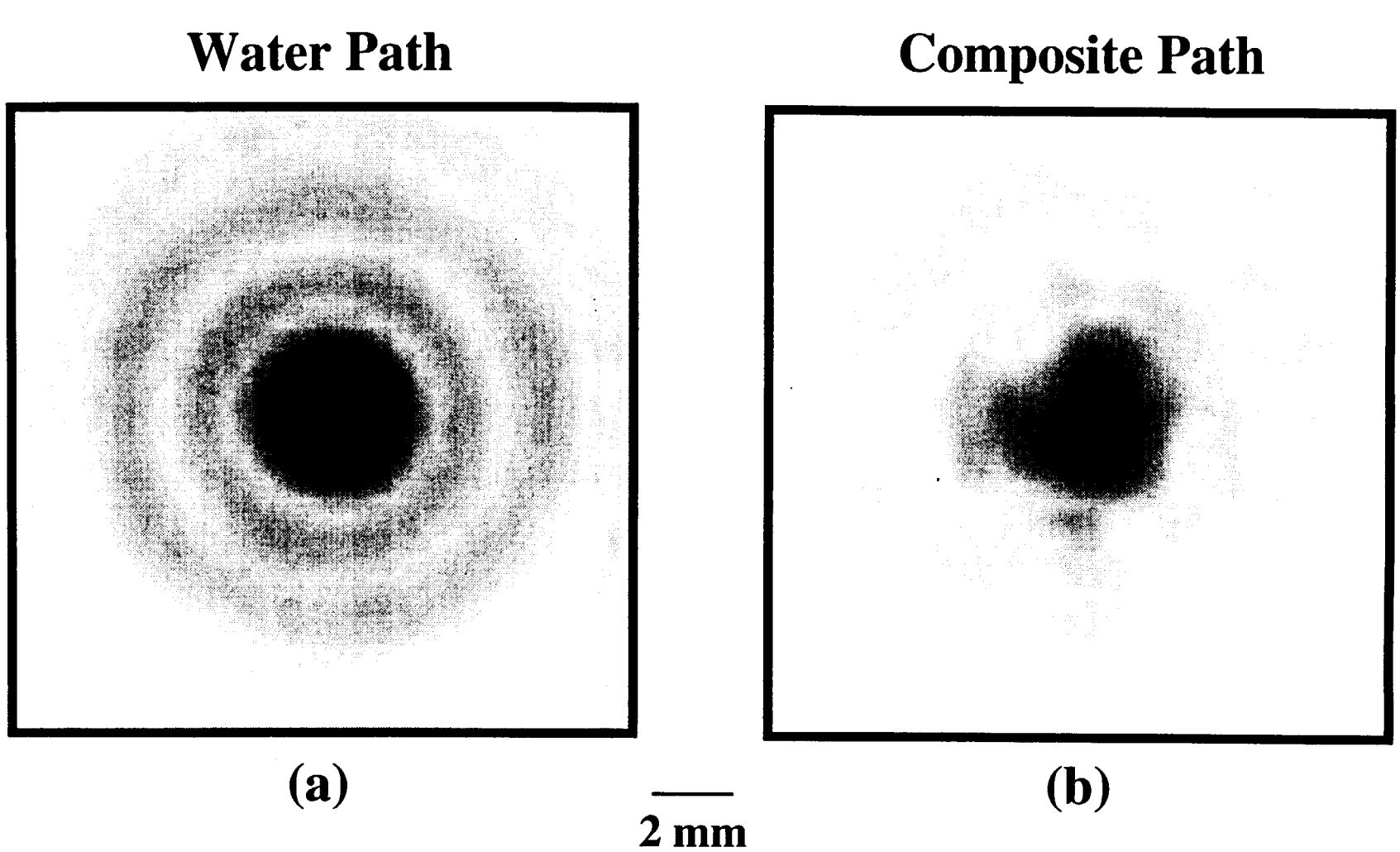

Figure 12: Water path versus composite path for 6.5 MHz to 7.5 MHz. Receiver plane images for (a) narrowband pressure magnitude for water path only and (b) narrowband pressure magnitude for composite path using the 5 MHz transducer.

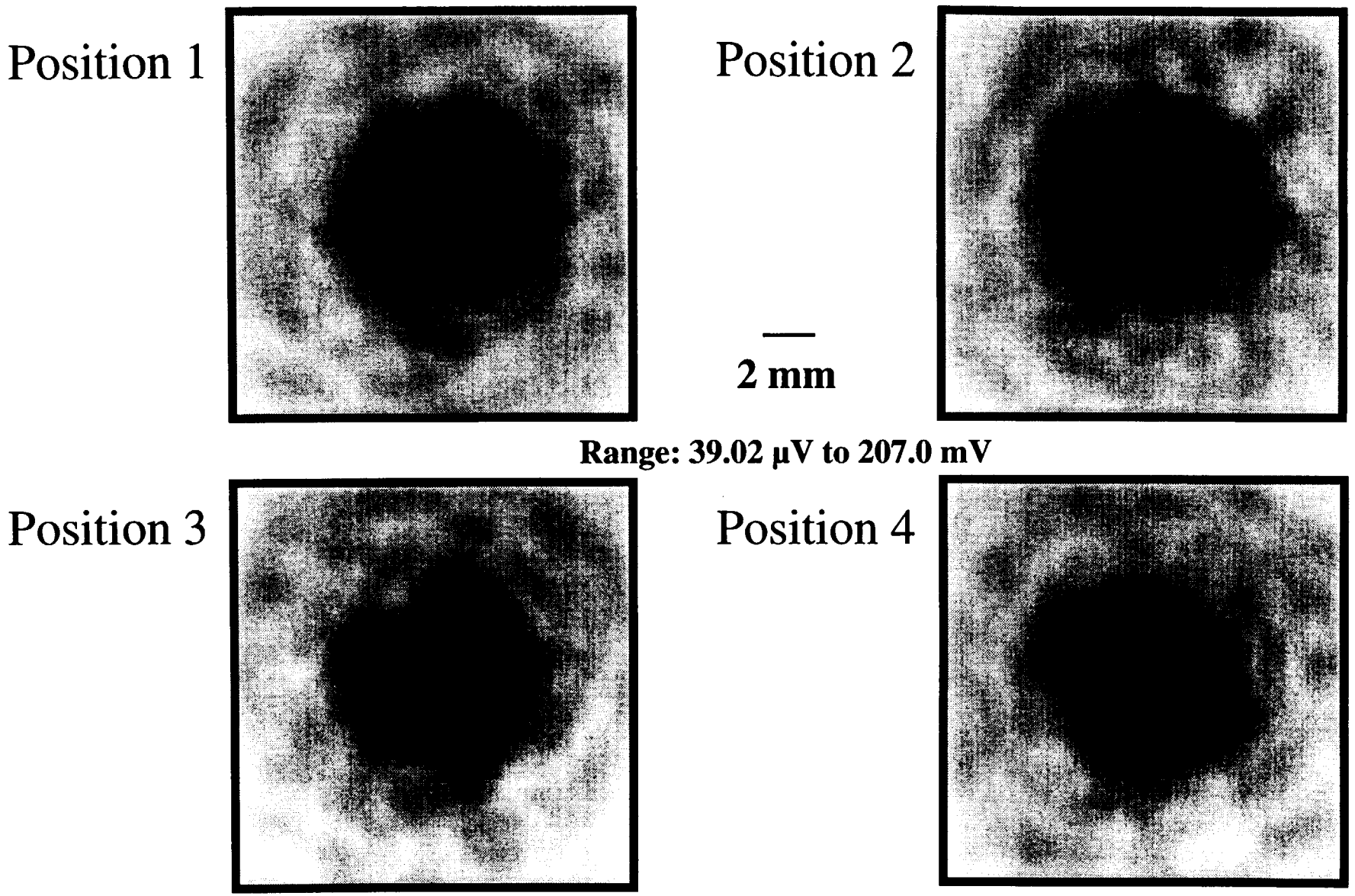

Figure 13: Comparison of positions for 2.5 MHz to 3.5 MHz. Receiver plane images of the narrowband pressure magnitude are shown for the different scanned regions of the thin composite using the 5 MHz transducer.

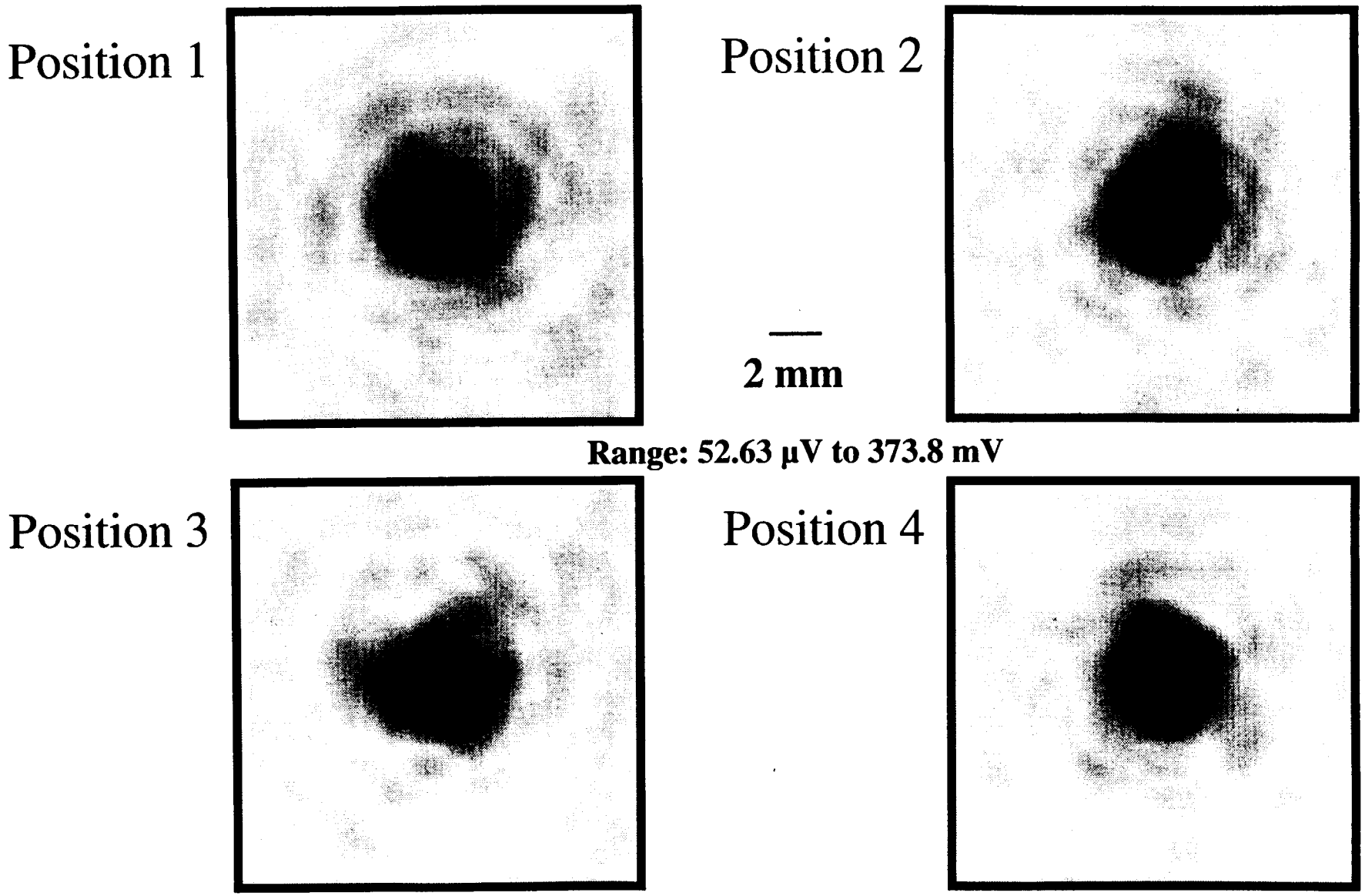

Figure 14: Comparison of positions for 4.5 MHz to 5.5 MHz. Receiver plane images of the narrowband pressure magnitude are shown for the different scanned regions of the thin composite using the 5 MHz transducer.

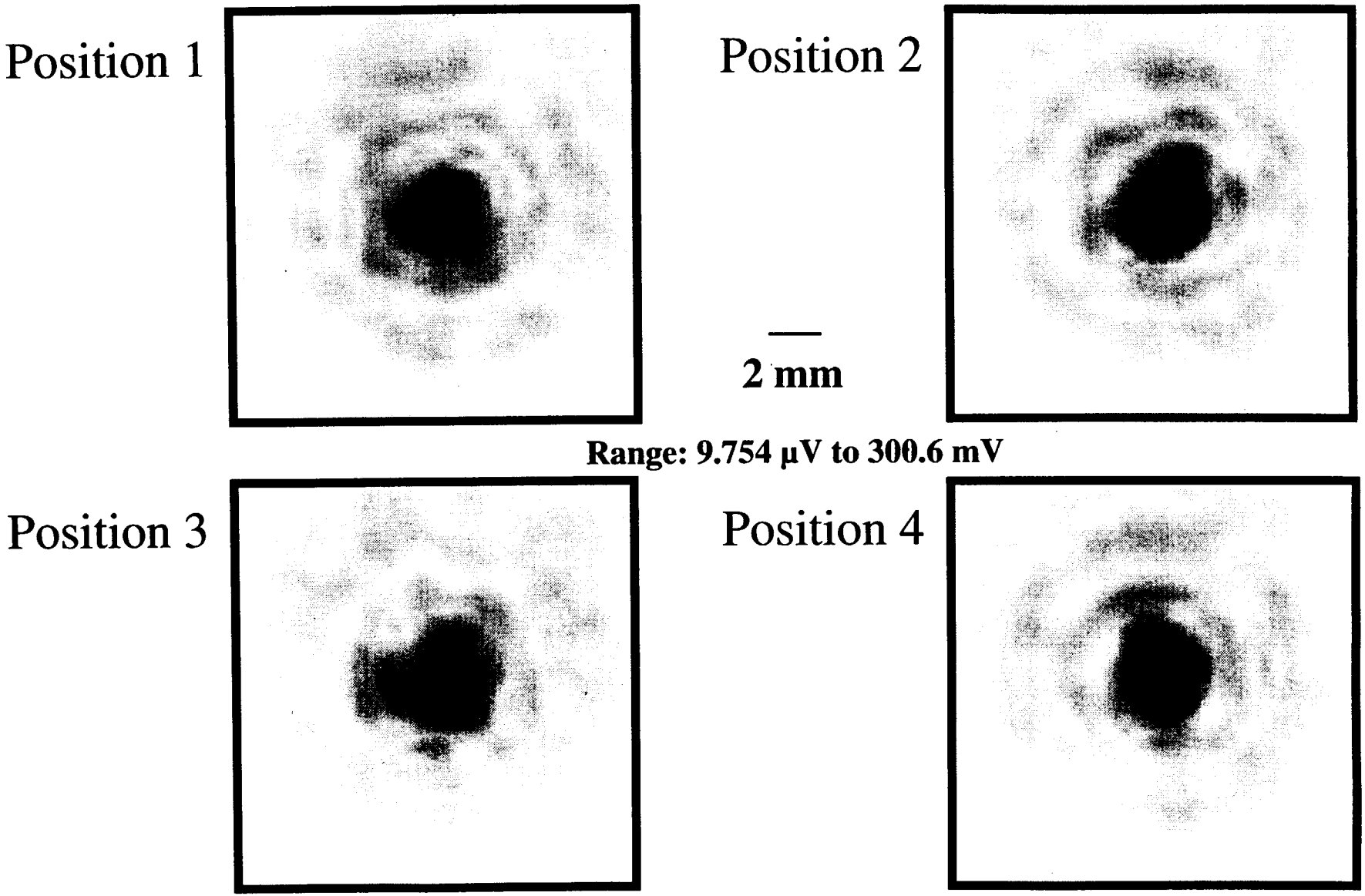

Figure 15: Comparison of positions for 6.5 MHz to 7.5 MHz. Receiver plane images of the narrowband pressure magnitude are shown for the different scanned regions of the thin composite using the 5 MHz transducer.

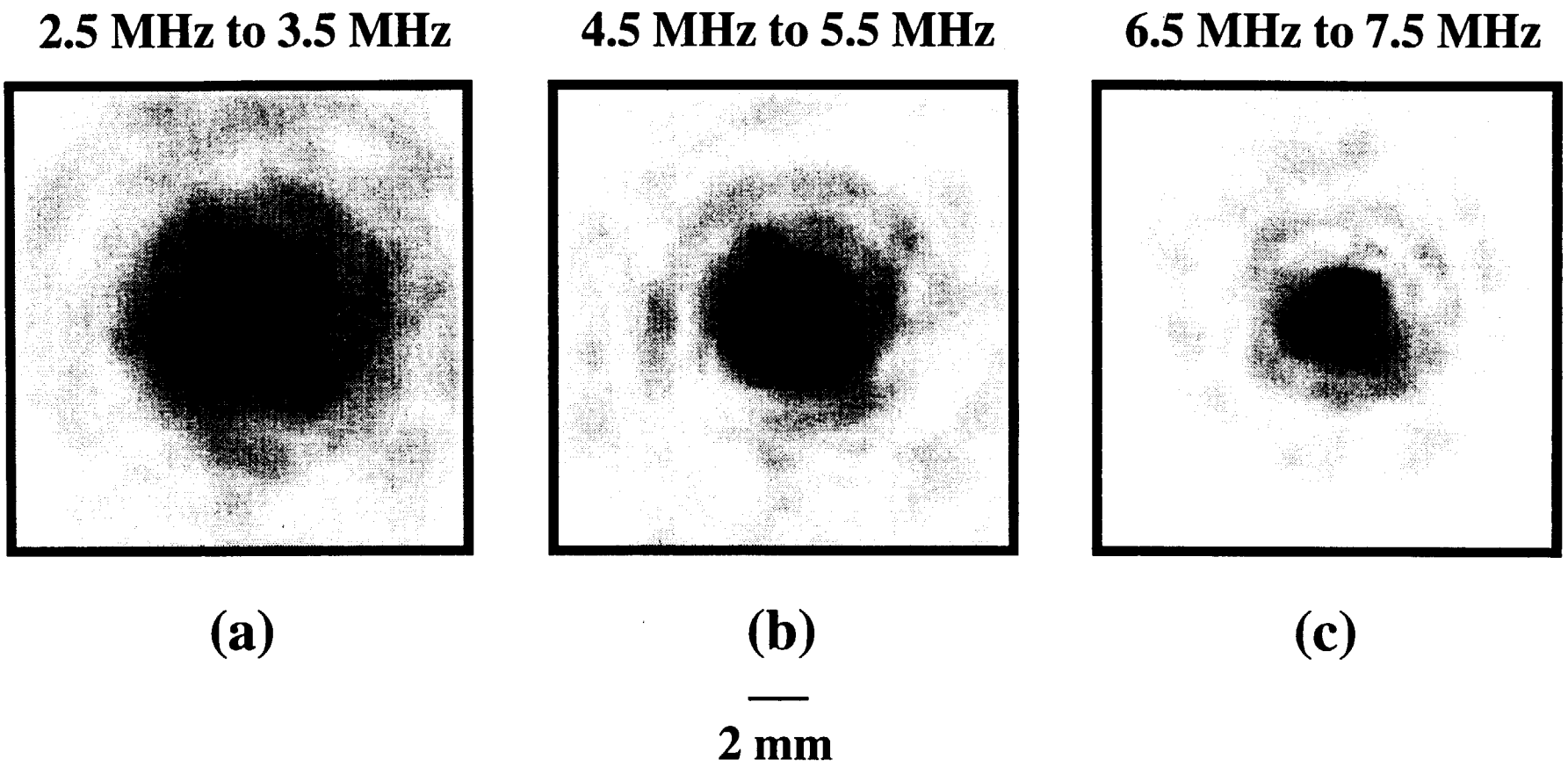

Figure 16: Comparison of insonifying frequencies at Position 1 with 5 MHz transducer. Receiver plane images of the narrowband pressure magnitudes at Position 1 of the thin composite are shown for the different frequency ranges for the 5 MHz transducer.

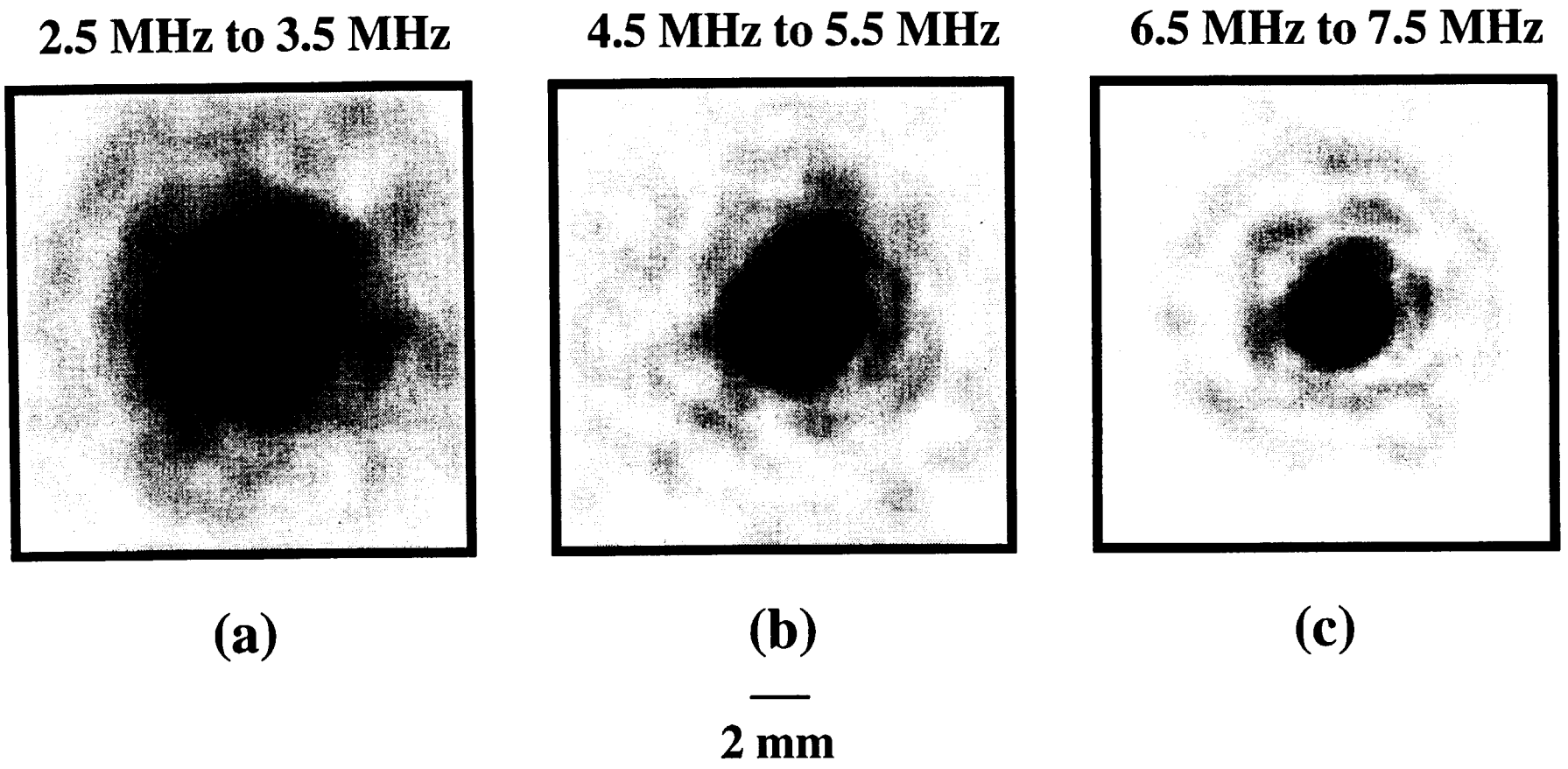

Figure 17: Comparison of insonifying frequencies at Position 2 with 5 MHz transducer. Receiver plane images of the narrowband pressure magnitudes at Position 2 of the thin composite are shown for the different frequency ranges for the 5 MHz transducer.

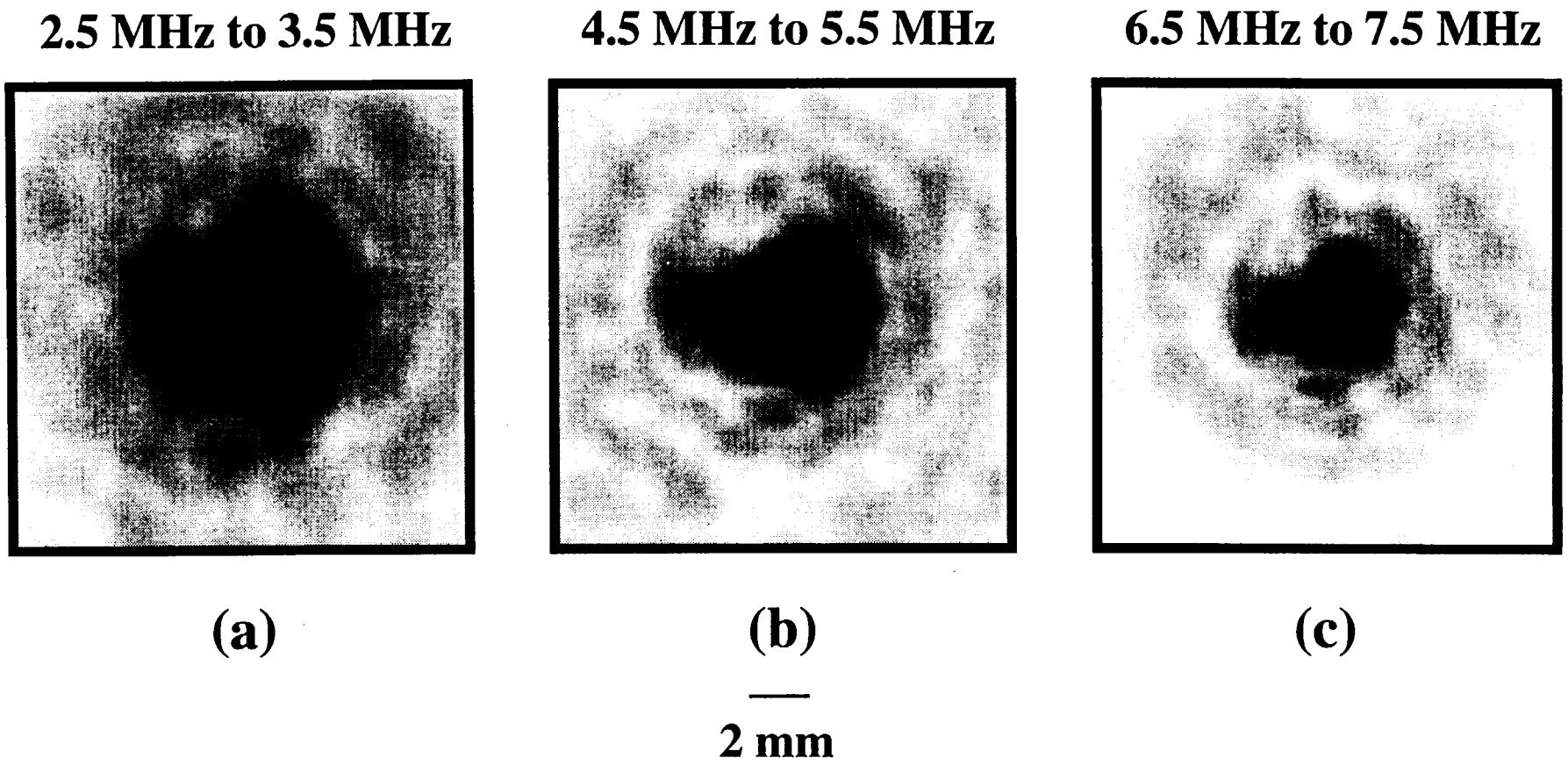

Figure 18: Comparison of insonifying frequencies at Position 3 with 5 MHz transducer. Receiver plane images of the narrowband pressure magnitudes at Position 3 of the thin composite are shown for the different frequency ranges for the 5 MHz transducer.

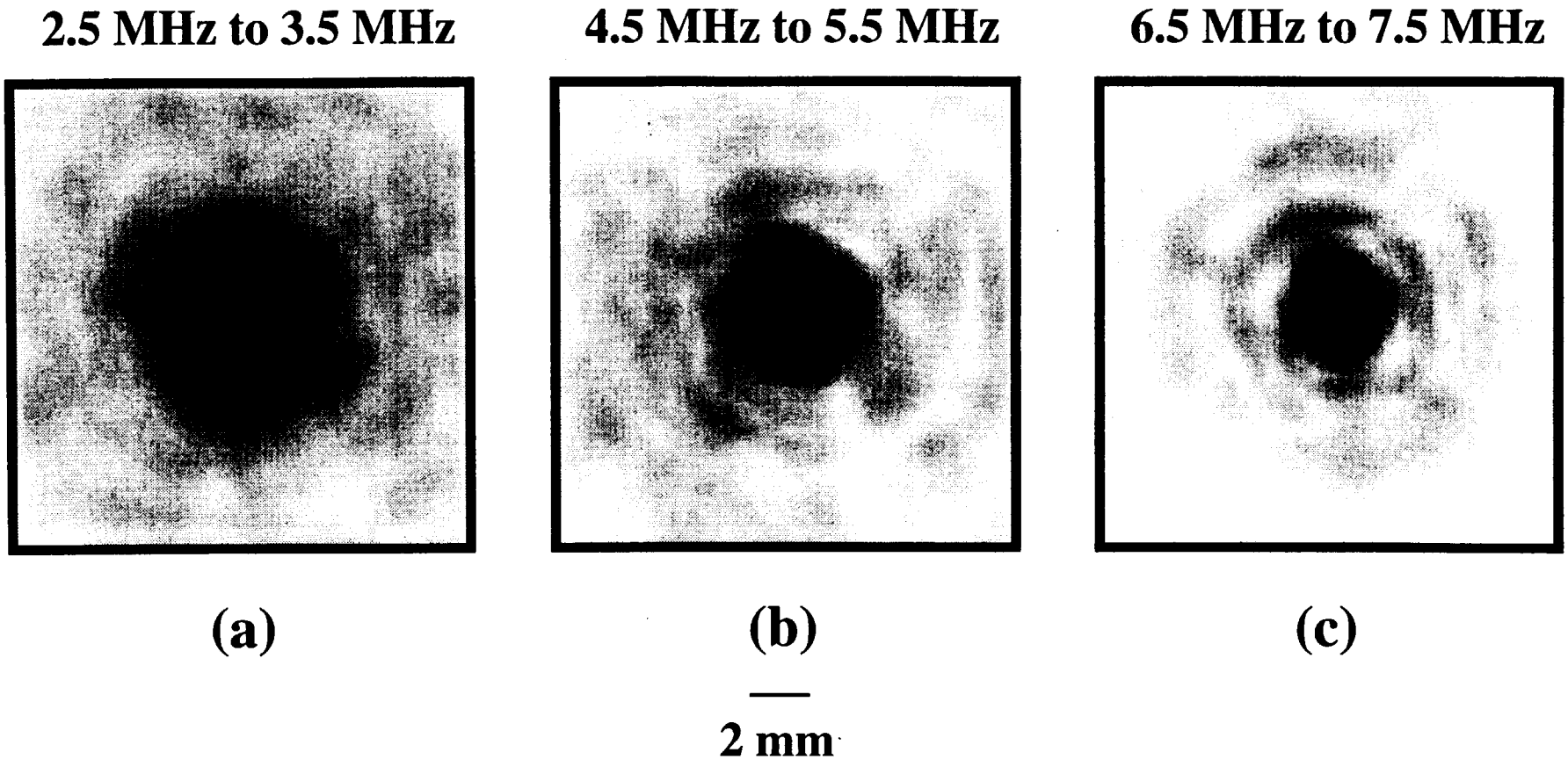

Figure 19: Comparison of insonifying frequencies at Position 4 with 5 MHz transducer. Receiver plane images of the narrowband pressure magnitudes at Position 4 of the thin composite are shown for the different frequency ranges for the 5 MHz transducer.

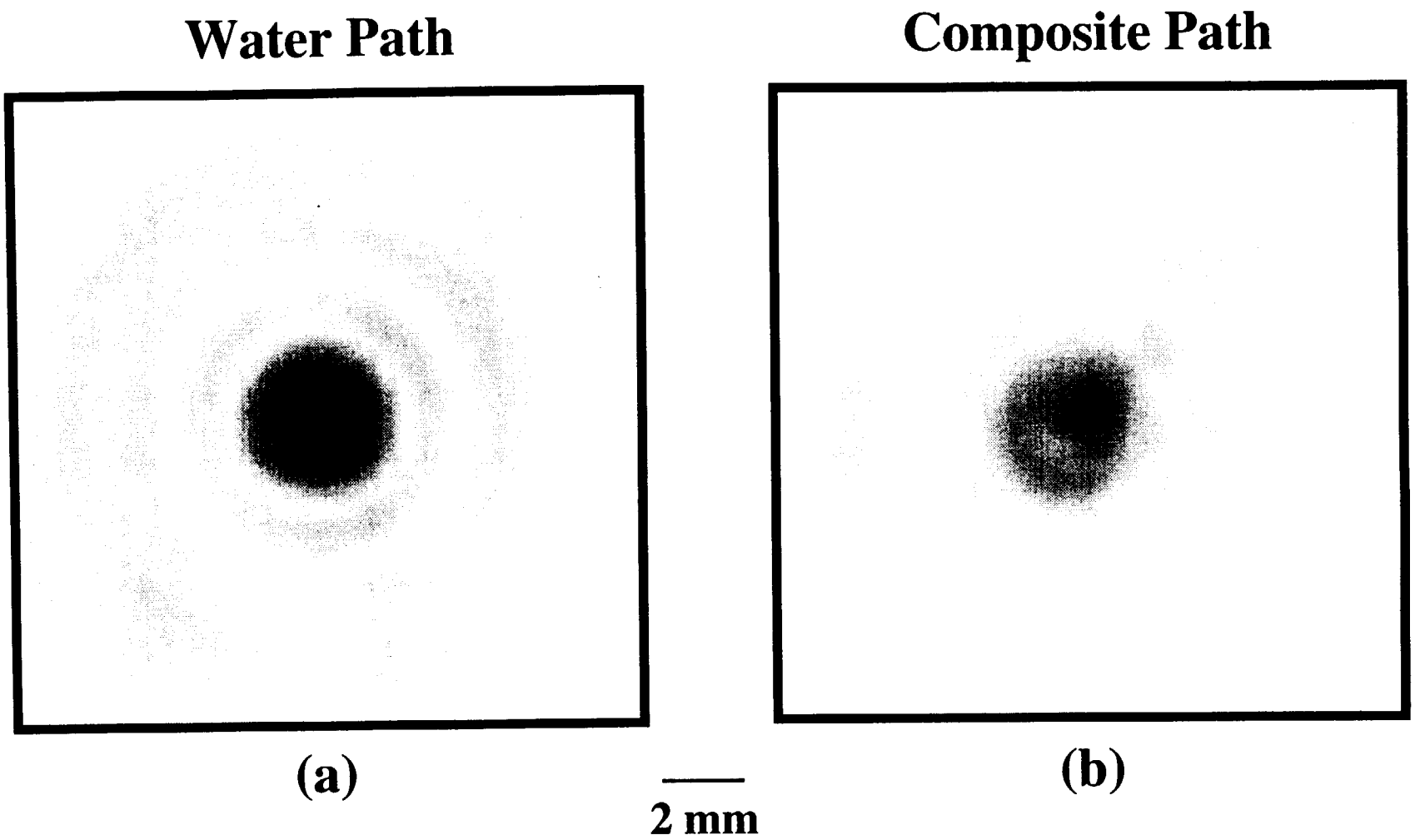

Figure 20: Water path versus composite path for 7.5 MHz to 8.5 MHz. Receiver plane images for (a) narrowband pressure magnitude for water path only and (b) narrowband pressure magnitude for composite path using the 10 MHz transducer.

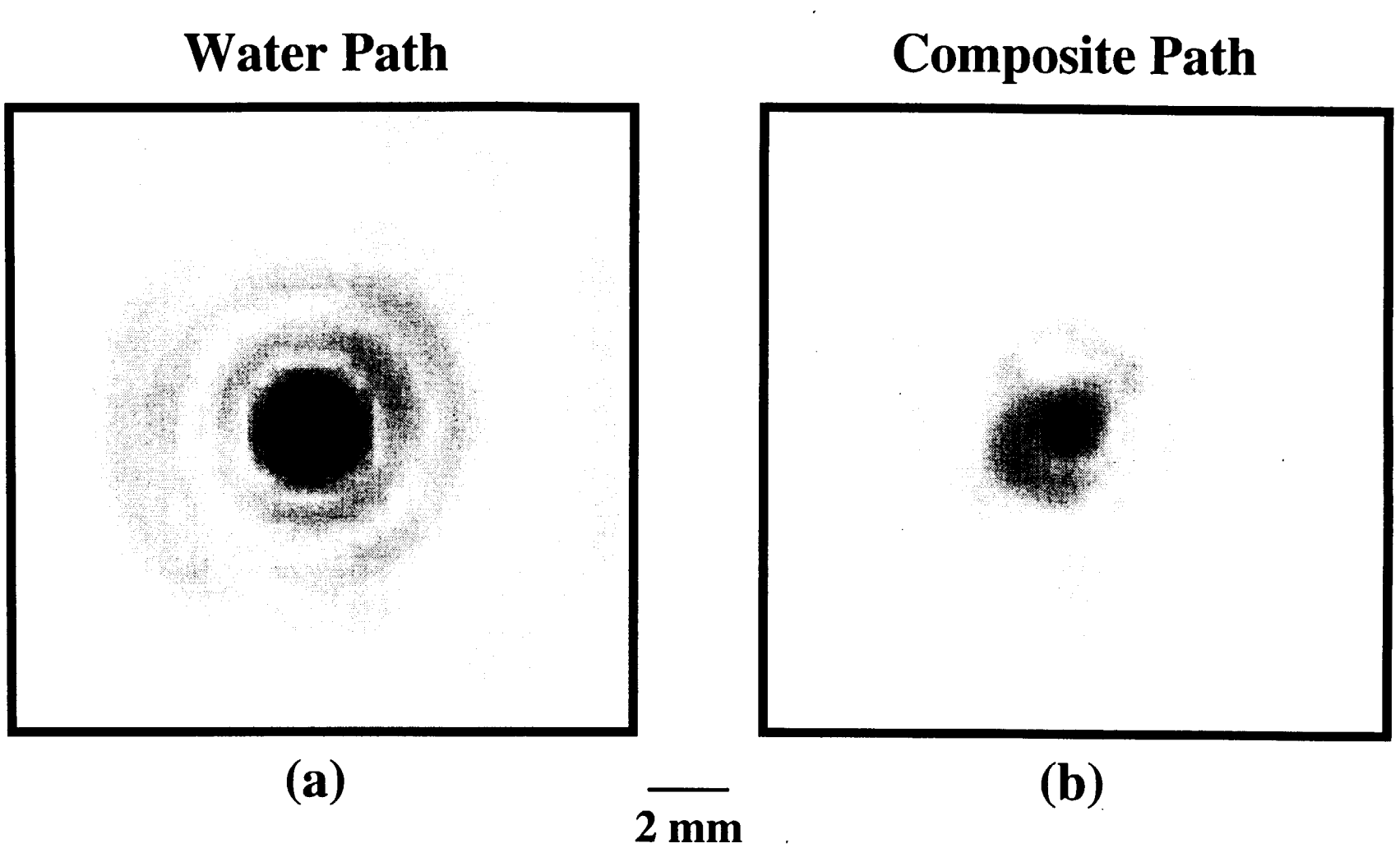

Figure 21: Water path versus composite path for 9.5 MHz to 10.5 MHz. Receiver plane images for (a) narrowband pressure magnitude for water path only and (b) narrowband pressure magnitude for composite path using the 10 MHz transducer.

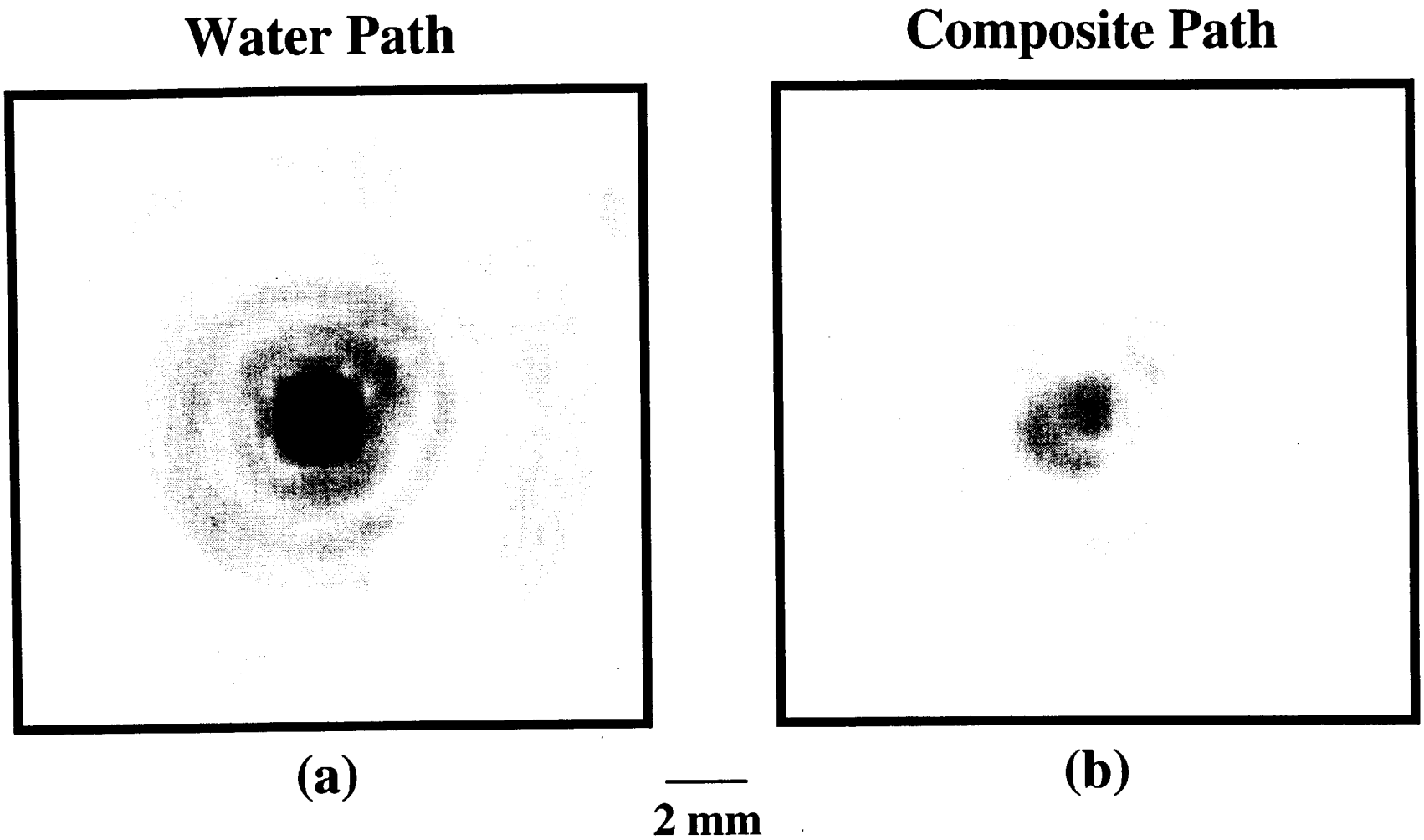

Figure 22: Water path versus composite path for 11.5 MHz to 12.5 MHz. Receiver plane images for (a) narrowband pressure magnitude for water path only and (b) narrowband pressure magnitude for composite path using the 10 MHz transducer.

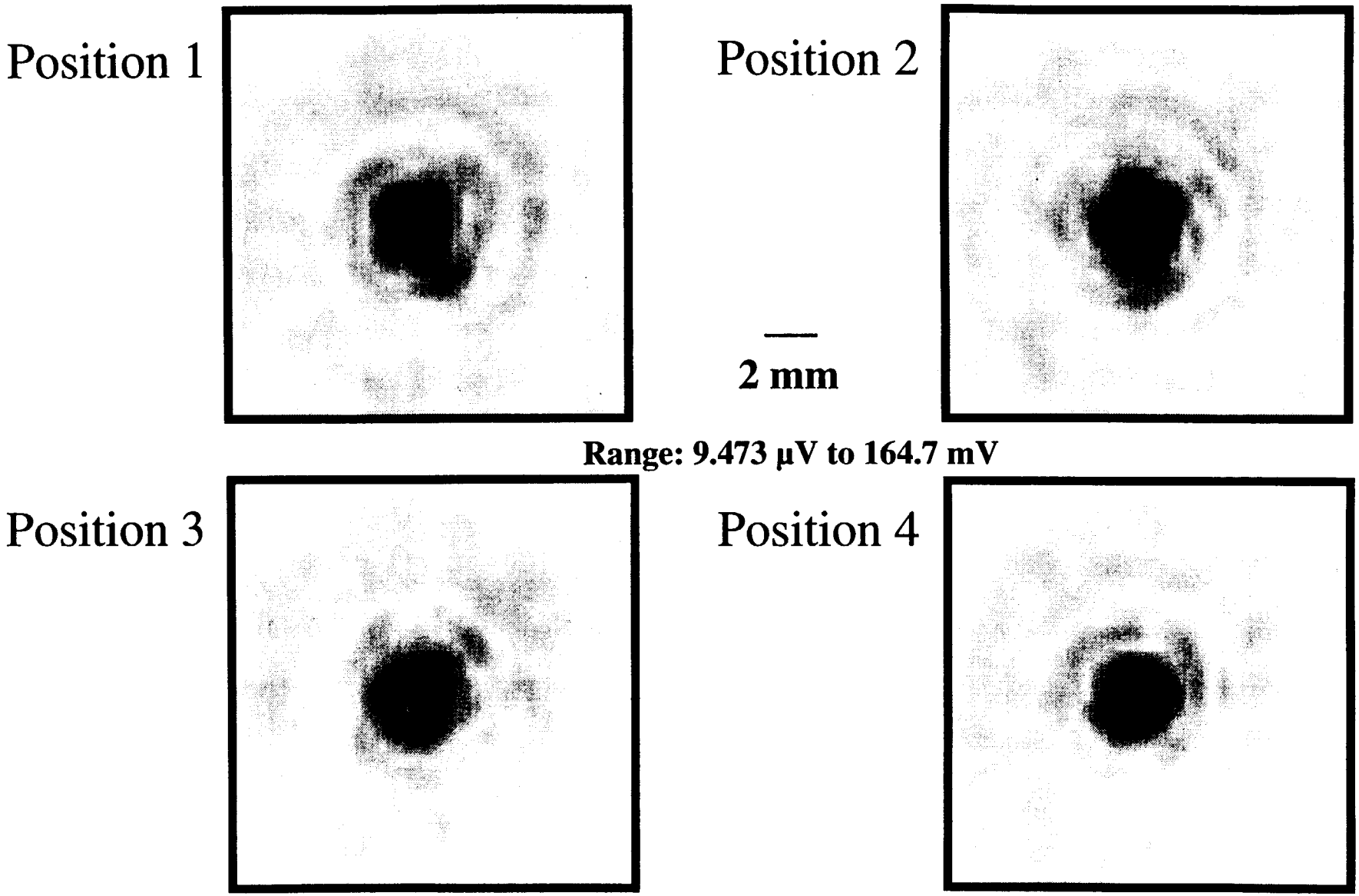

Figure 23: Comparison of positions for 7.5 MHz to 8.5 MHz. Receiver plane images of the narrowband pressure magnitude are shown for the different scanned regions of the thin composite using the 10 MHz transducer.

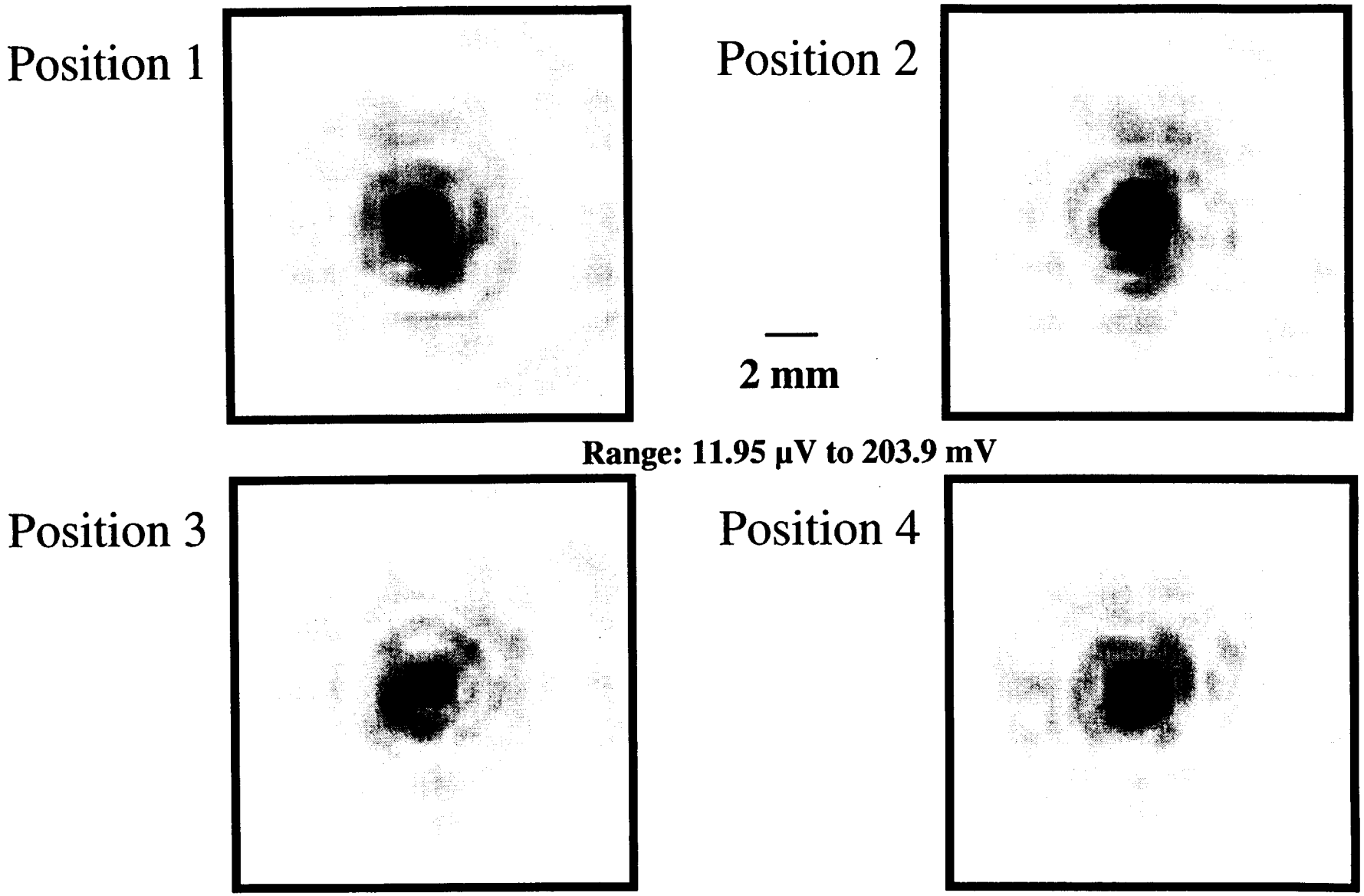

Figure 24: Comparison of positions for 9.5 MHz to 10.5 MHz. Receiver plane images of the narrowband pressure magnitude are shown for the different scanned regions of the thin composite using the 10 MHz transducer.

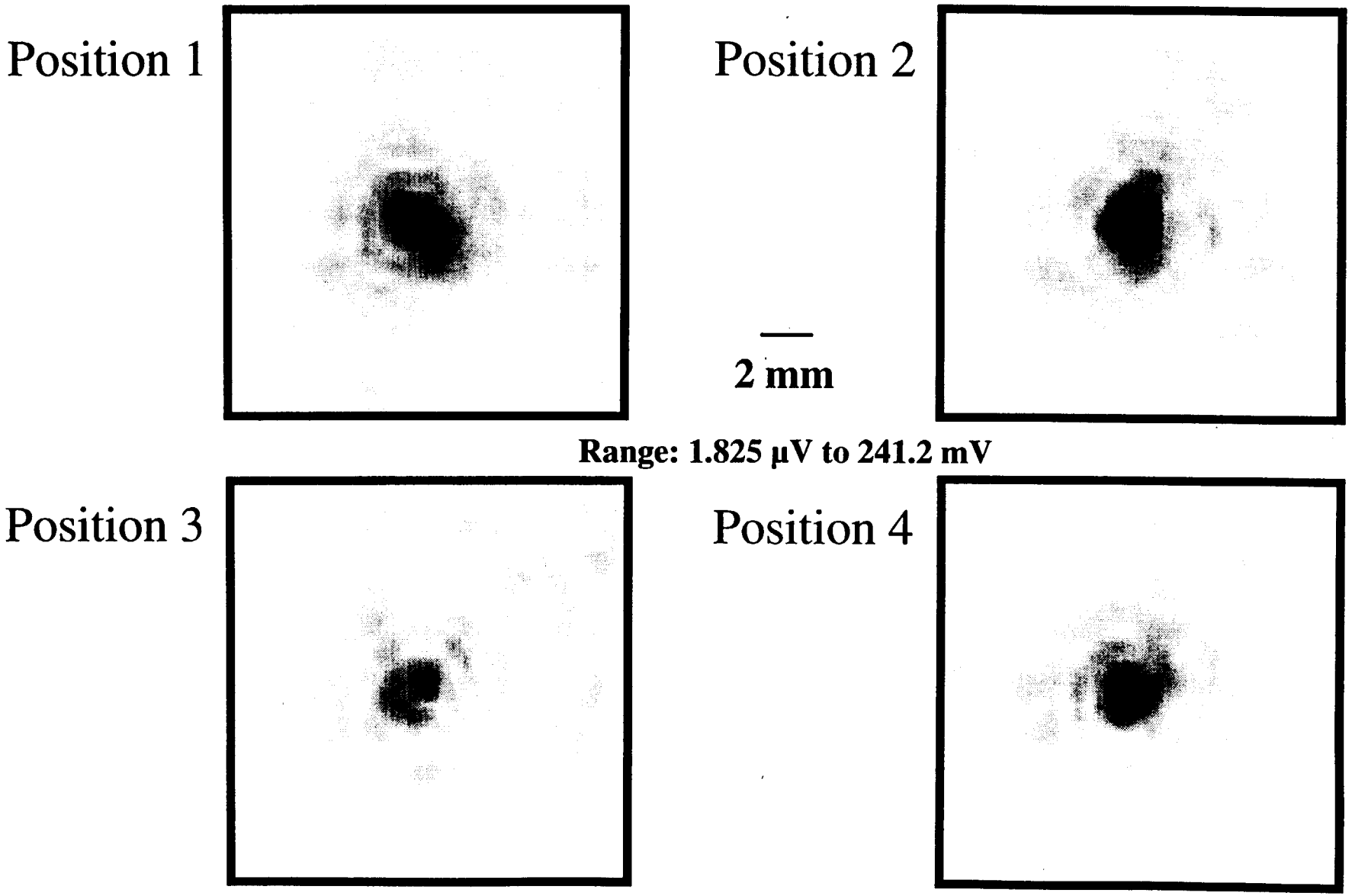

Figure 25: Comparison of positions for 11.5 MHz to 12.5 MHz. Receiver plane images of the narrowband pressure magnitude are shown for the different scanned regions of the thin composite using the 10 MHz transducer.

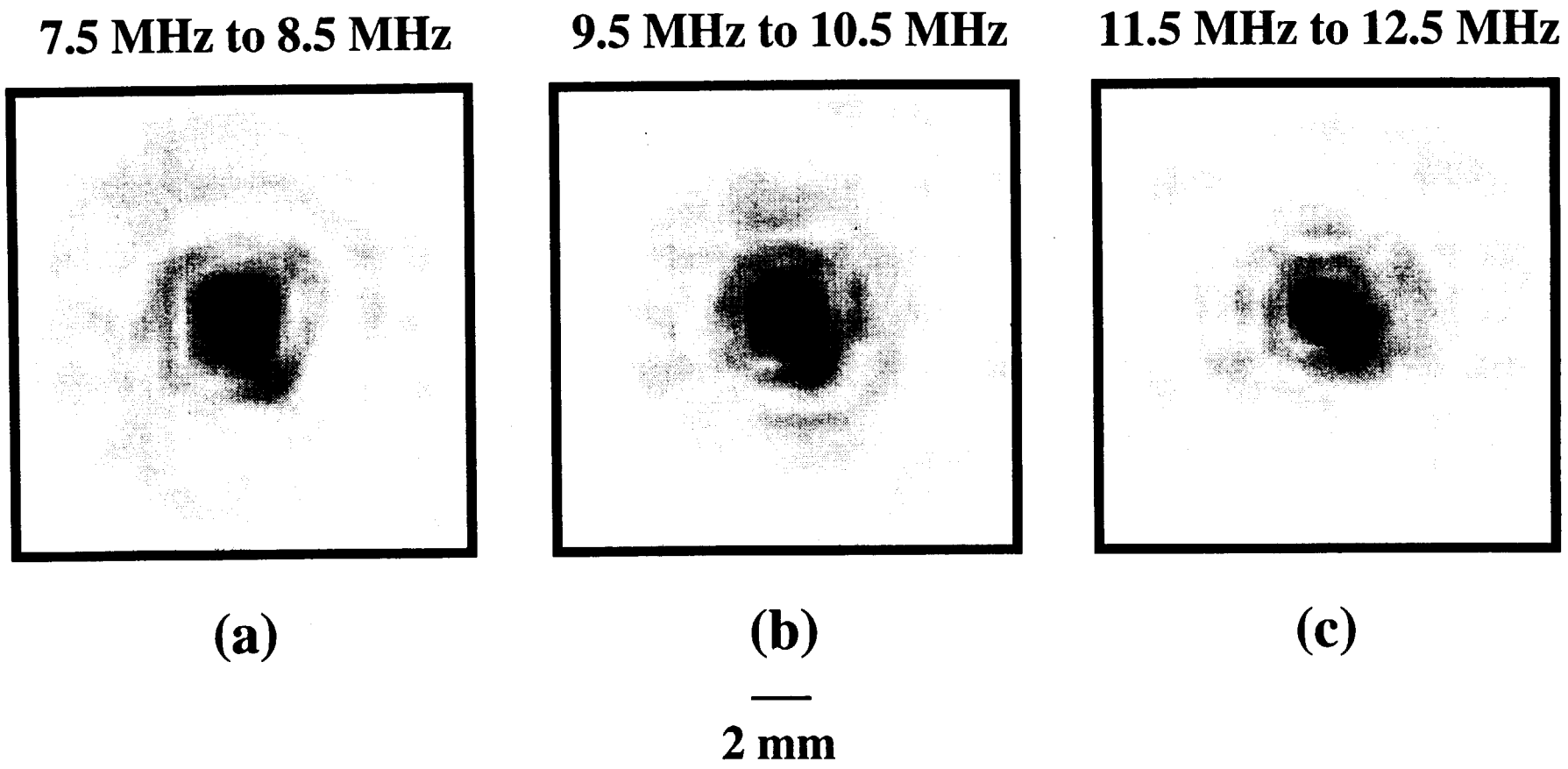

Figure 26: Comparison of insonifying frequencies at Position 1 with 10 MHz transducer. Receiver plane images of the narrowband pressure magnitudes at Position 1 of the thin composite are shown for the different frequency ranges for the 10 MHz transducer.

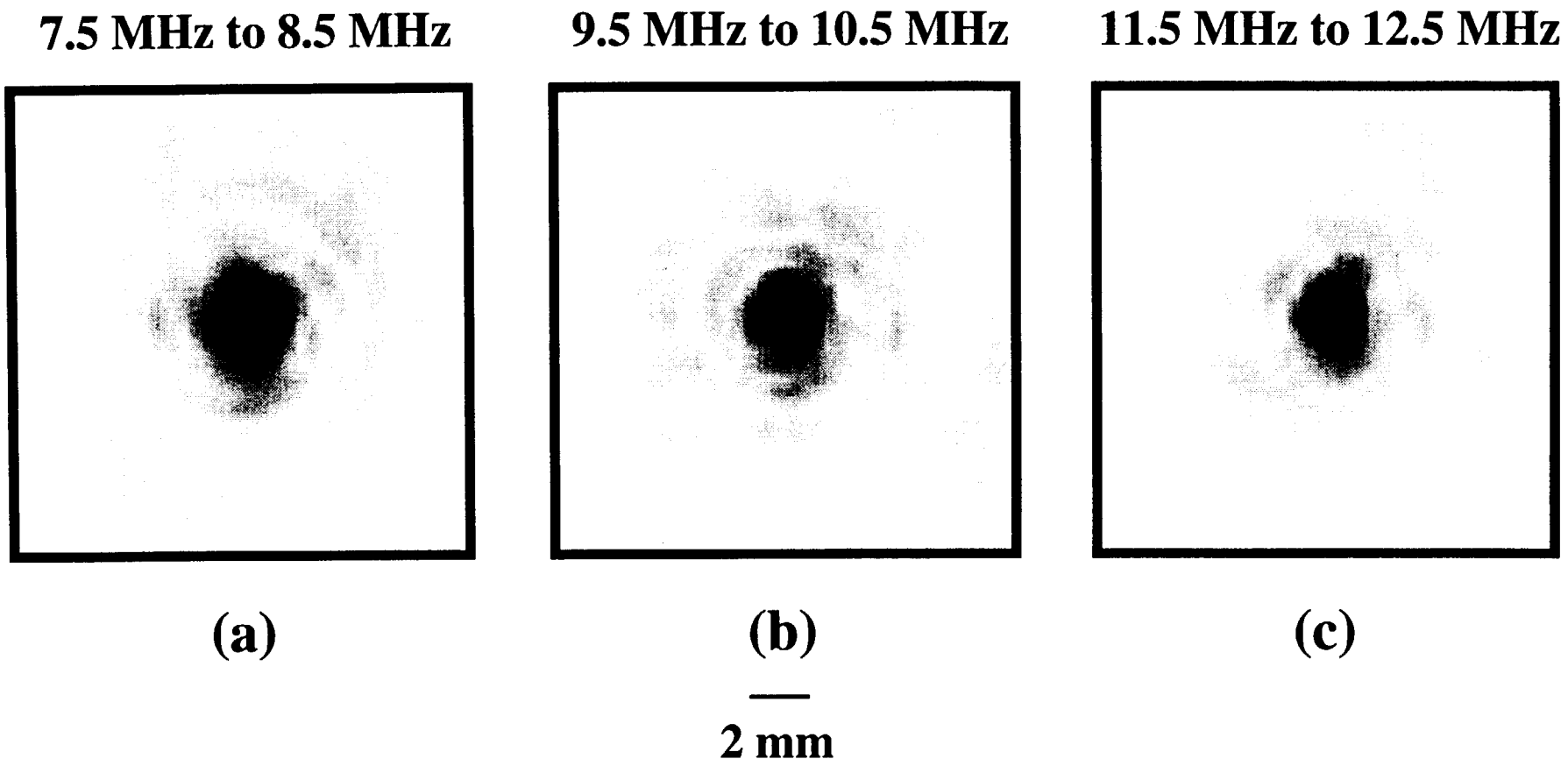

Figure 27: Comparison of insonifying frequencies at Position 2 with 10 MHz transducer. Receiver plane images of the narrowband pressure magnitudes at Position 2 of the thin composite are shown for the different frequency ranges for the 10 MHz transducer.

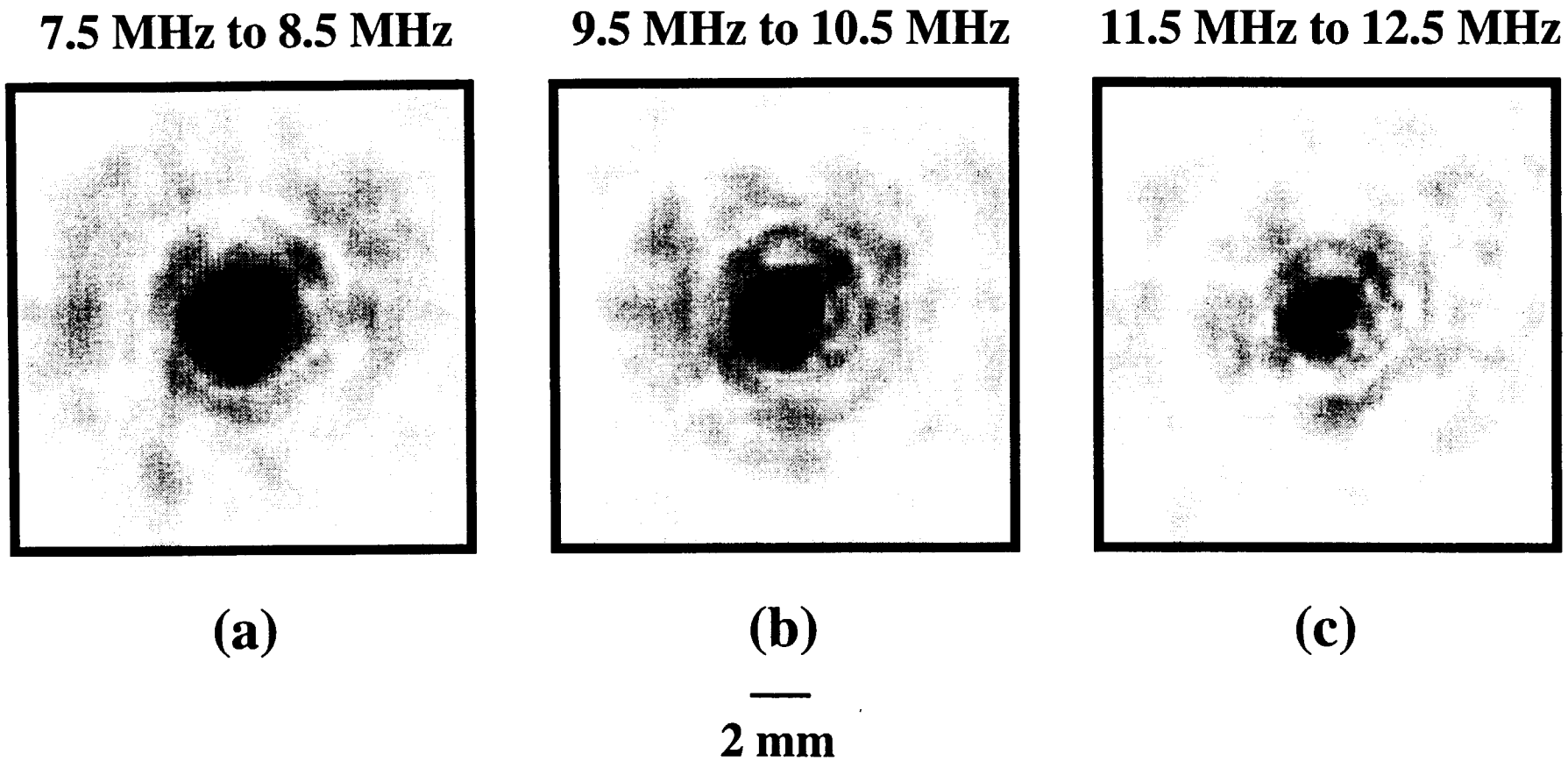

Figure 28: Comparison of insonifying frequencies at Position 3 with 10 MHz transducer. Receiver plane images of the narrowband pressure magnitudes at Position 3 of the thin composite are shown for the different frequency ranges for the 10 MHz transducer.

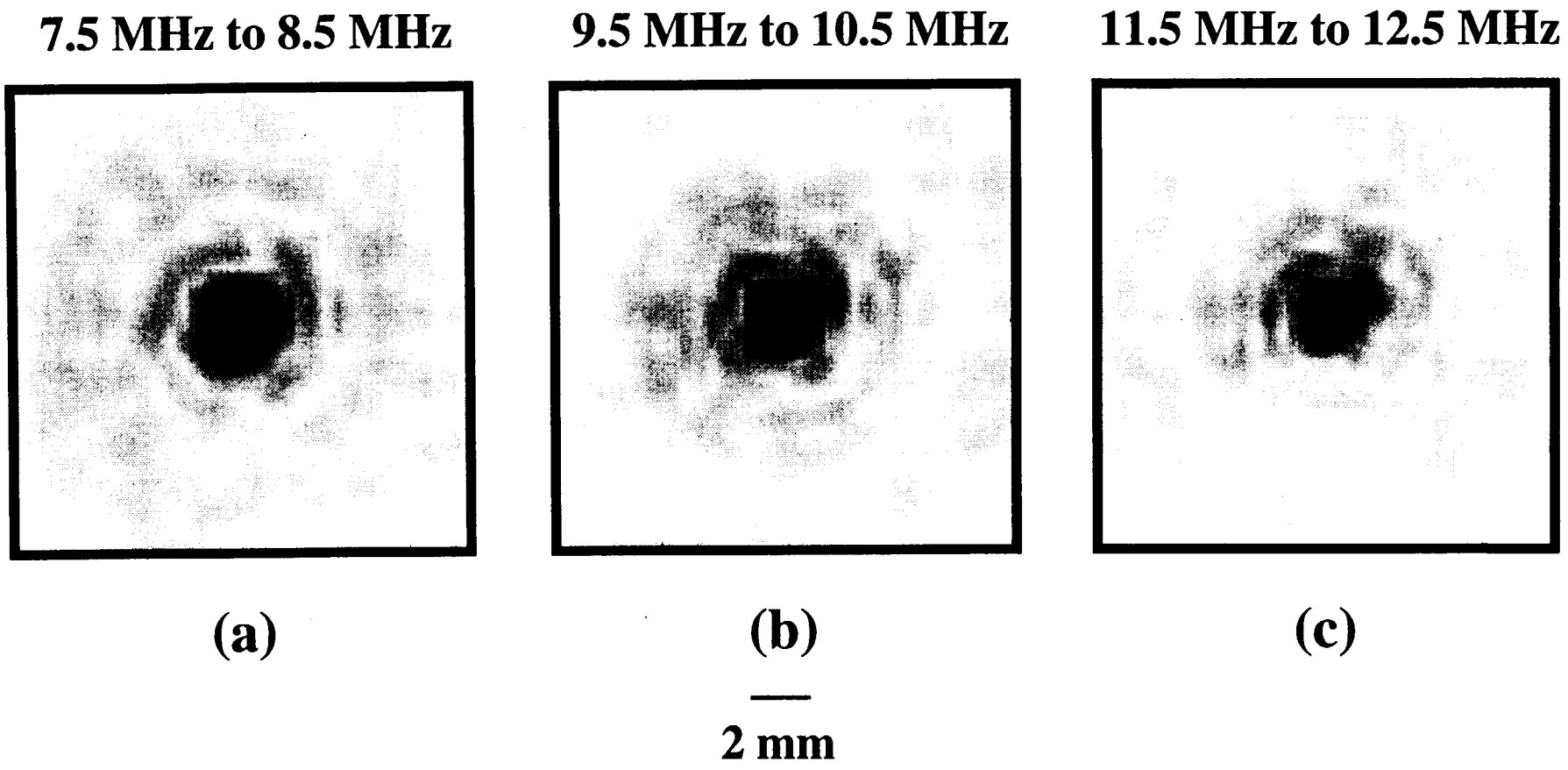

Figure 29: Comparison of insonifying frequencies at Position 4 with 10 MHz transducer. Receiver plane images of the narrowband pressure magnitudes at Position 4 of the thin composite are shown for the different frequency ranges for the 10 MHz transducer.

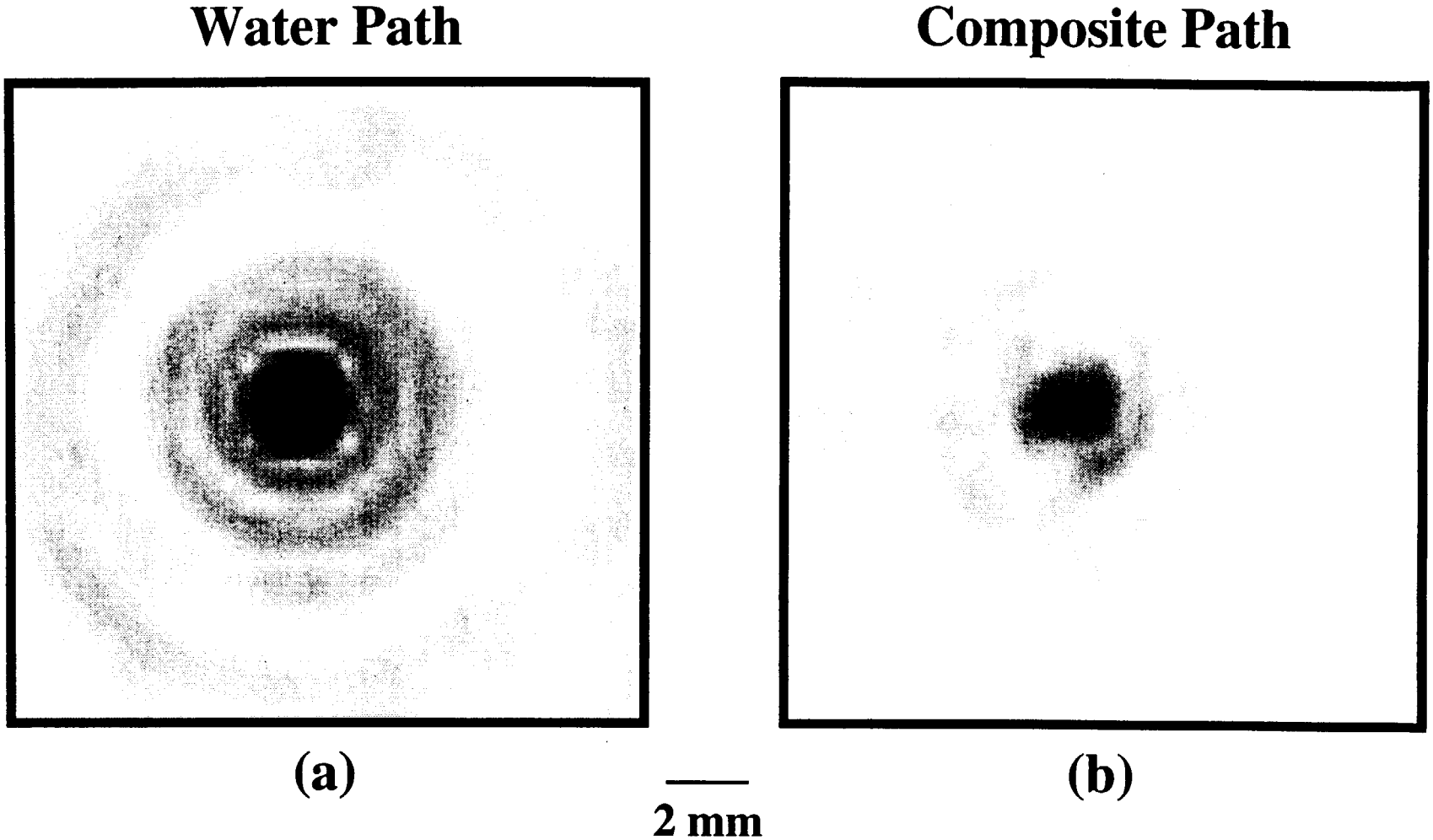

Figure 30: Water path versus composite path for 10.5 MHz to 11.5 MHz. Receiver plane images for (a) narrowband pressure magnitude for water path only and (b) narrowband pressure magnitude for composite path using the 15 MHz transducer.

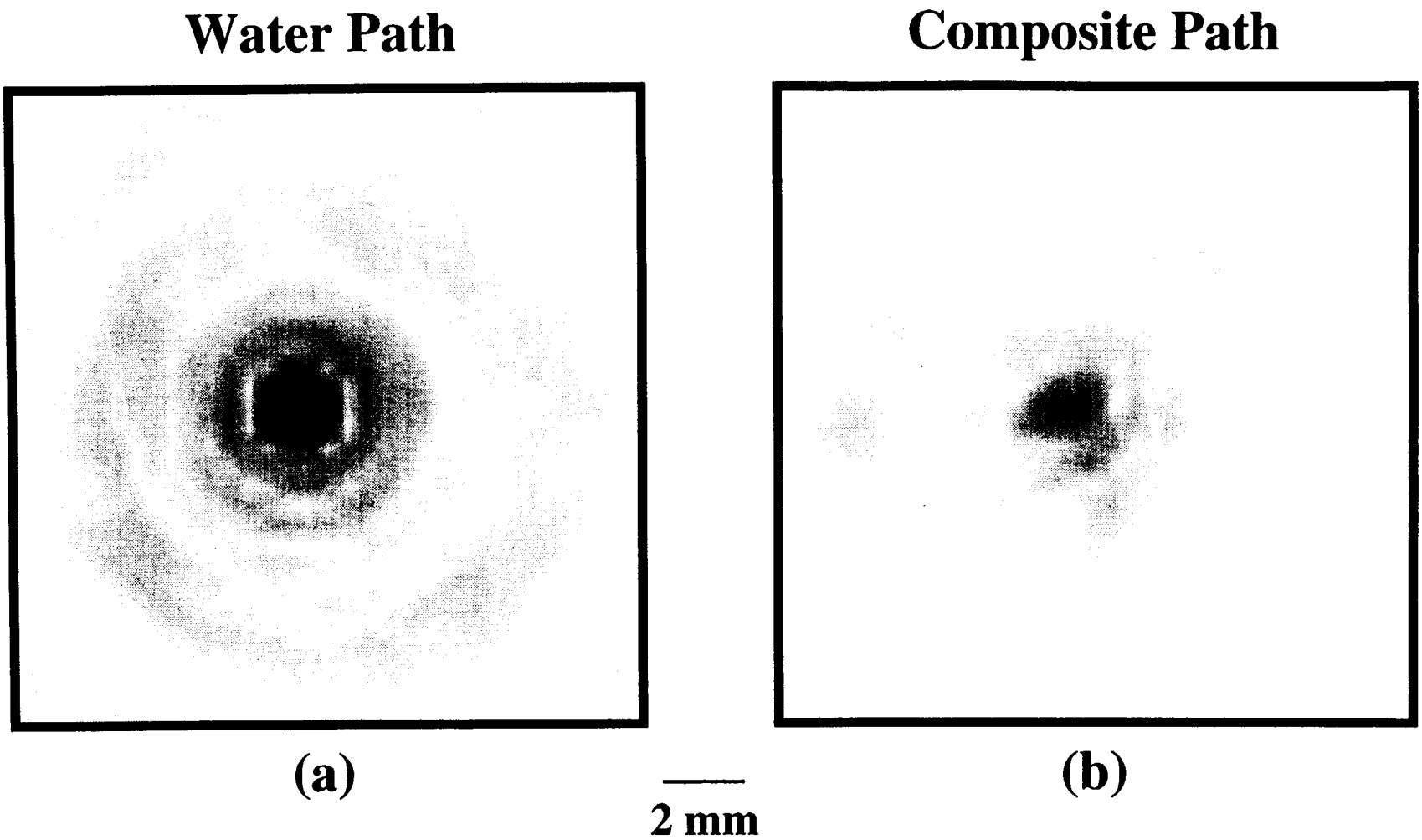

Figure 31: Water path versus composite path for 12.5 MHz to 13.5 MHz. Receiver plane images for (a) narrowband pressure magnitude for water path only and (b) narrowband pressure magnitude for composite path using the 15 MHz transducer.

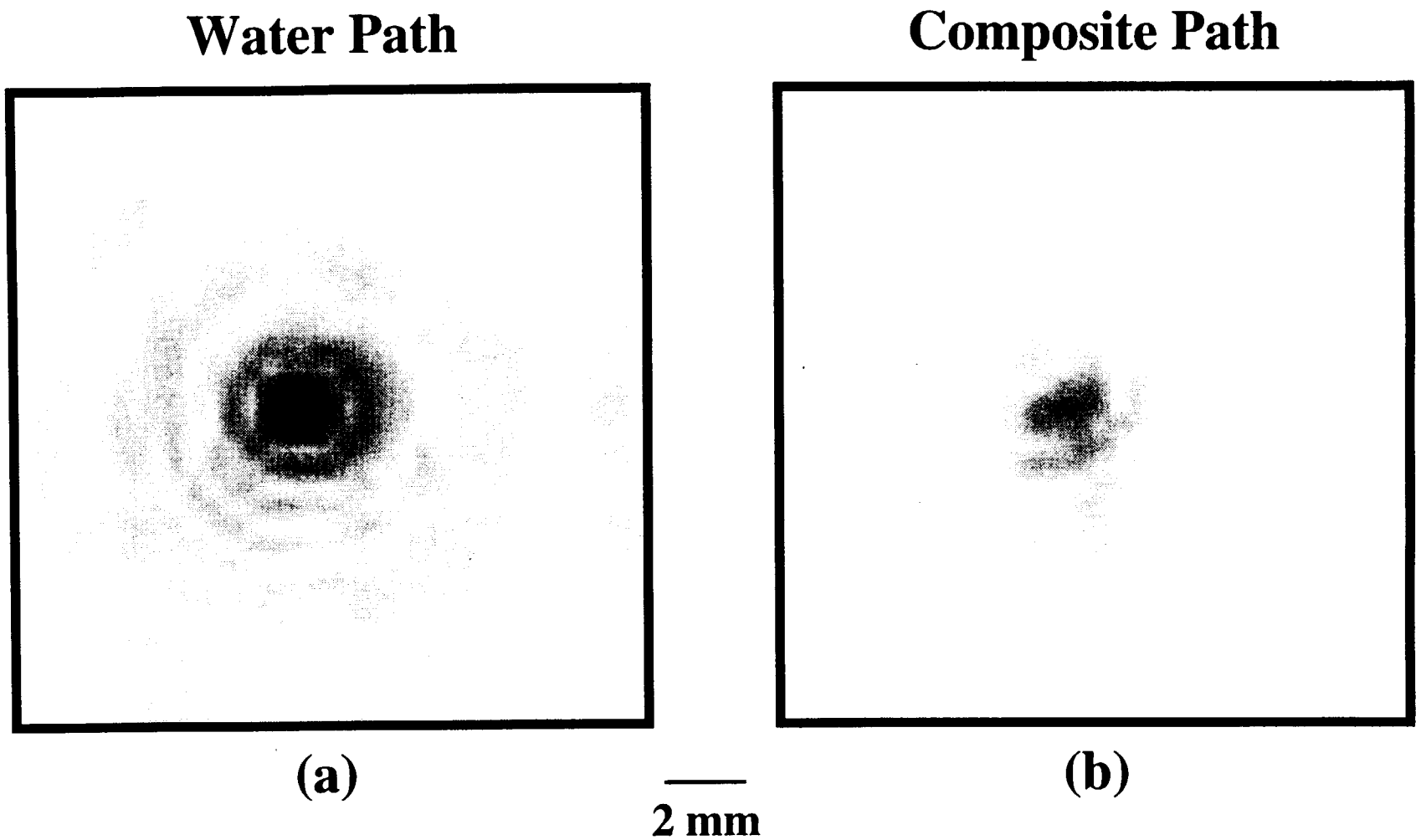

Figure 32: Water path versus composite path for 14.5 MHz to 15.5 MHz. Receiver plane images for (a) narrowband pressure magnitude for water path only and (b) narrowband pressure magnitude for composite path using the 15 MHz transducer.

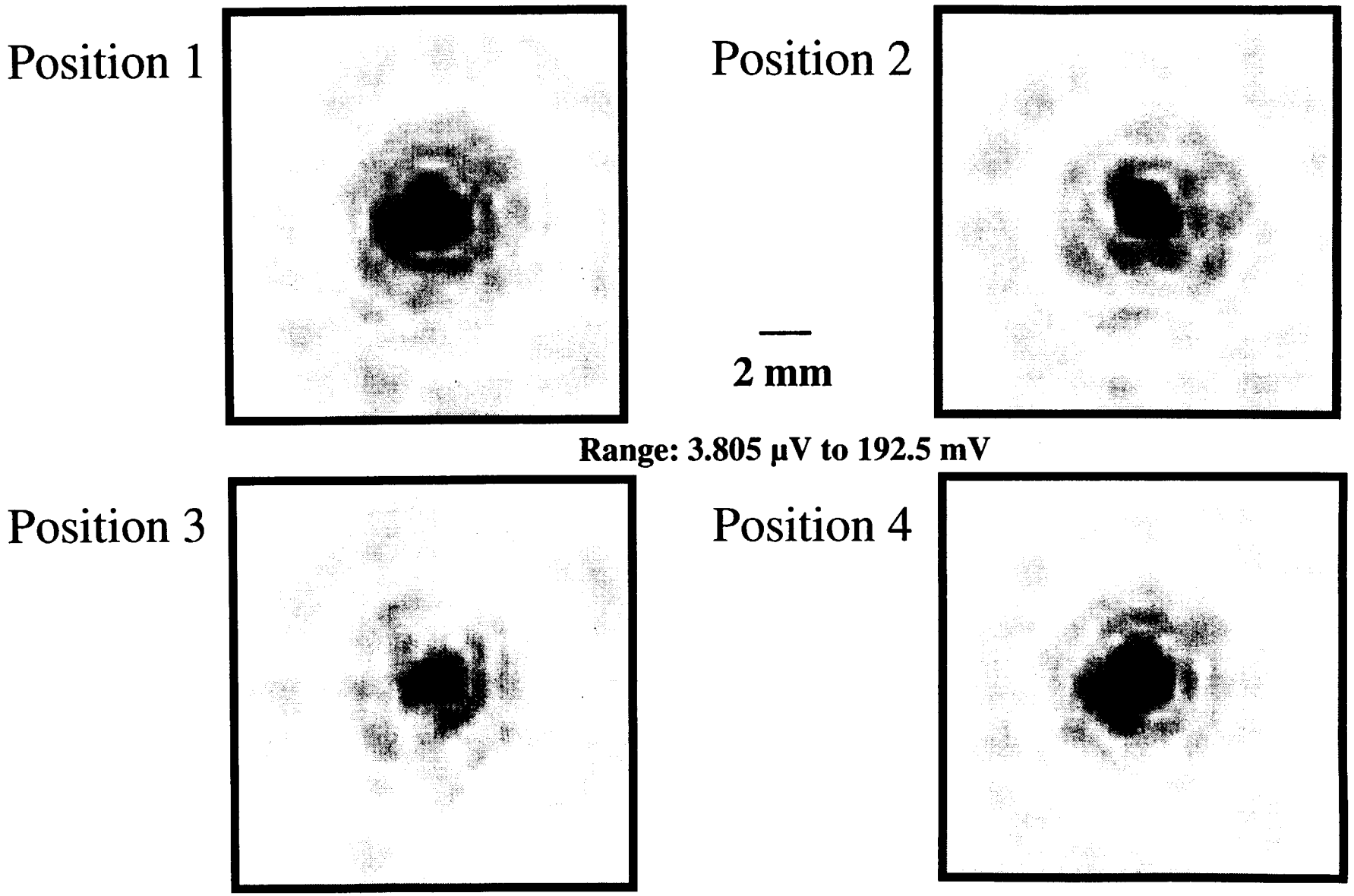

Figure 33: Comparison of positions for 10.5 MHz to 11.5 MHz. Receiver plane images of the narrowband pressure magnitude are shown for the different scanned regions of the thin composite using the 15 MHz transducer.

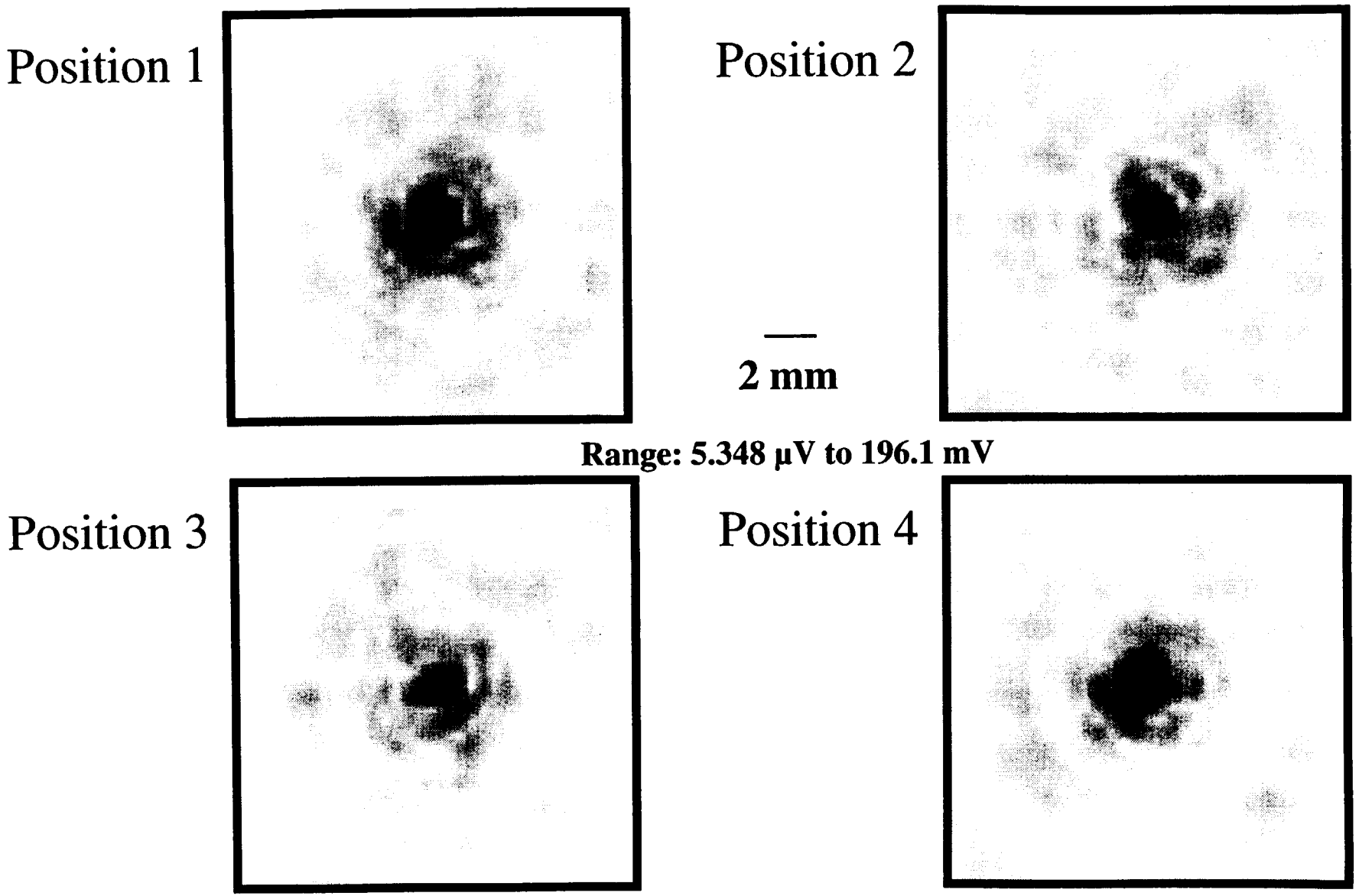

Figure 34: Comparison of positions for 12.5 MHz to 13.5 MHz. Receiver plane images of the narrowband pressure magnitude are shown for the different scanned regions of the thin composite using the 15 MHz transducer.

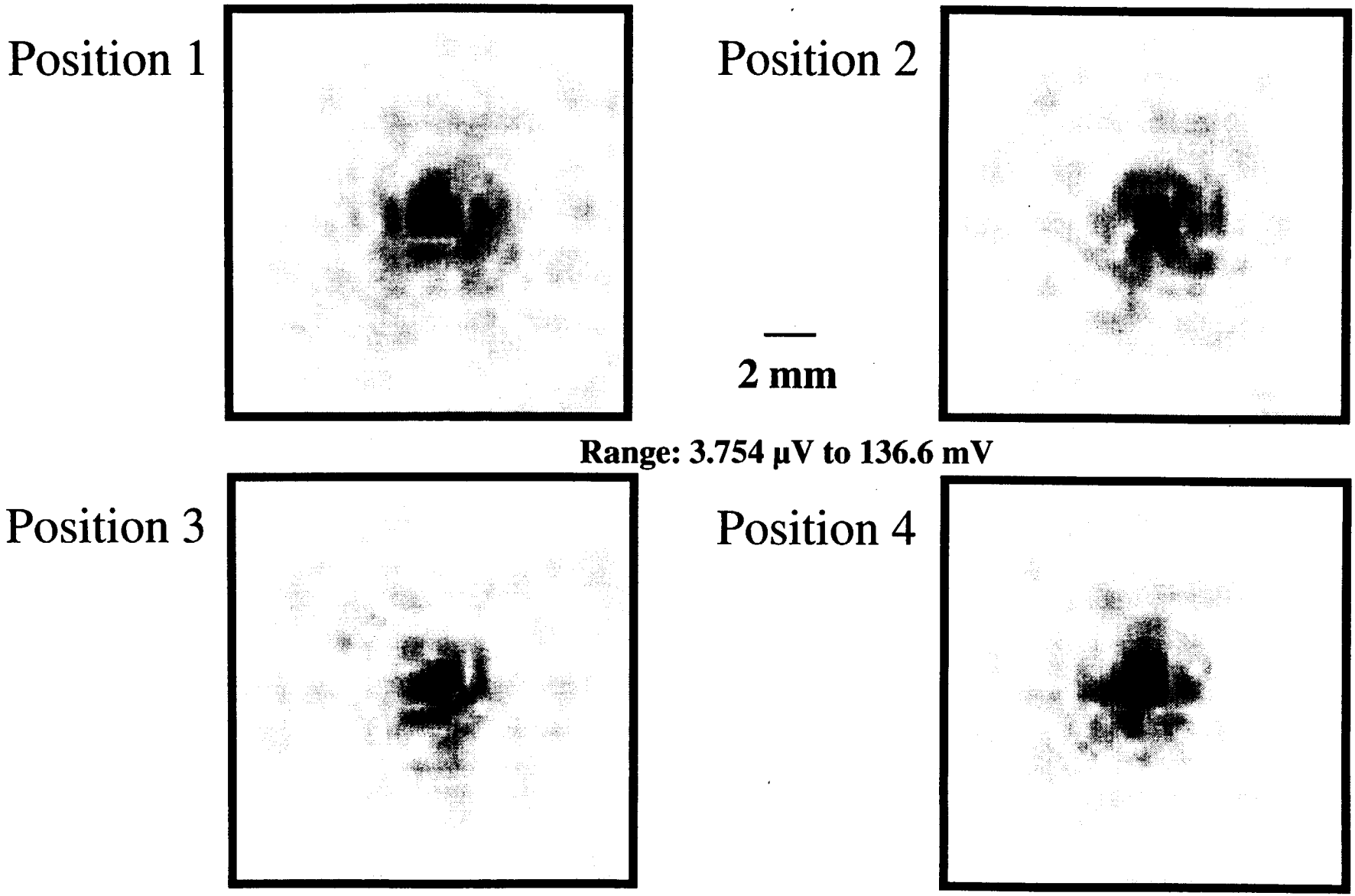

Figure 35: Comparison of positions for 14.5 MHz to 15.5 MHz. Receiver plane images of the narrowband pressure magnitude are shown for the different scanned regions of the thin composite using the 15 MHz transducer.

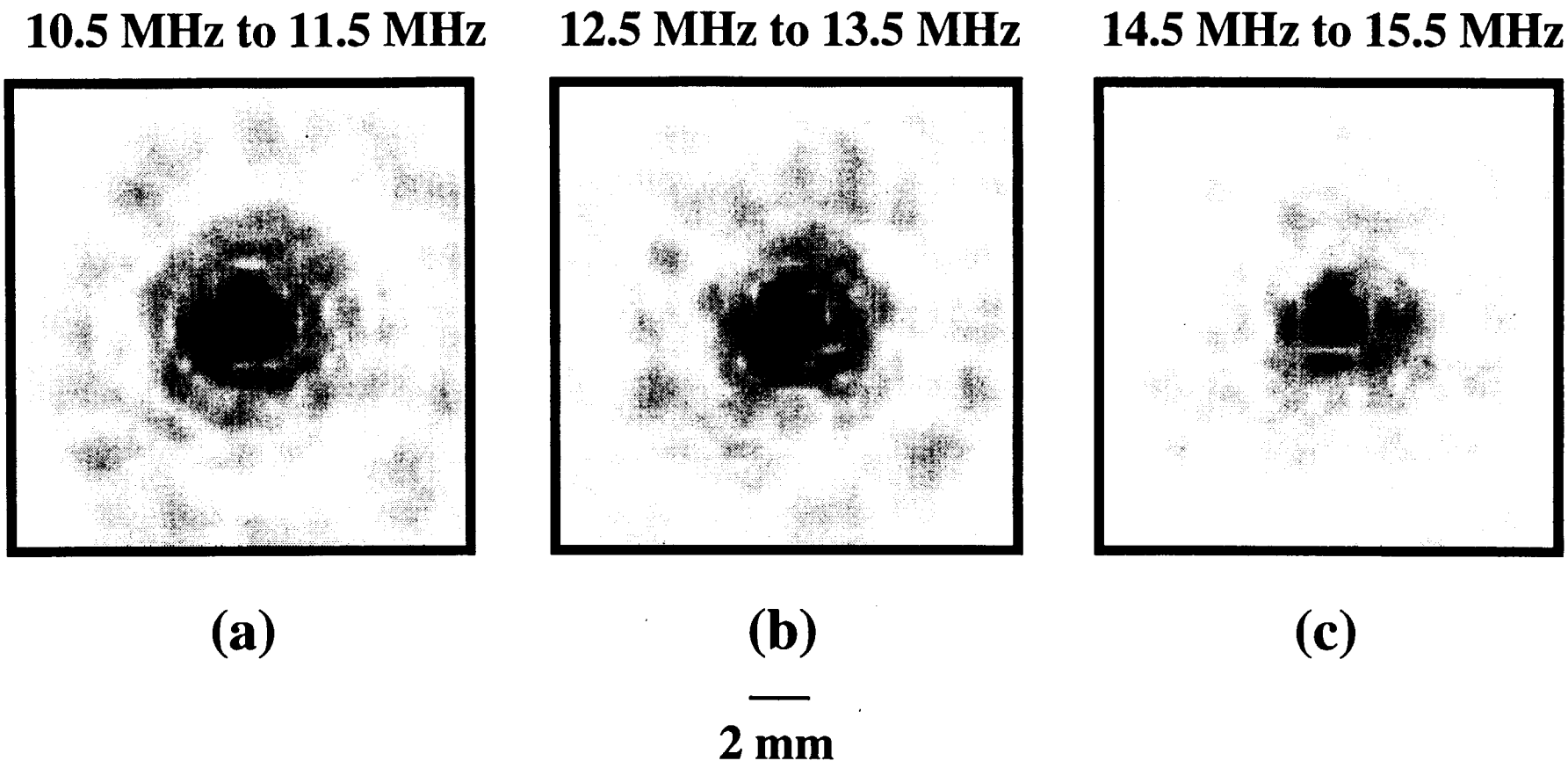

Figure 36: Comparison of insonifying frequencies at Position 1 with 15 MHz transducer. Receiver plane images of the narrowband pressure magnitudes at Position 1 of the thin composite are shown for the different frequency ranges for the 15 MHz transducer.

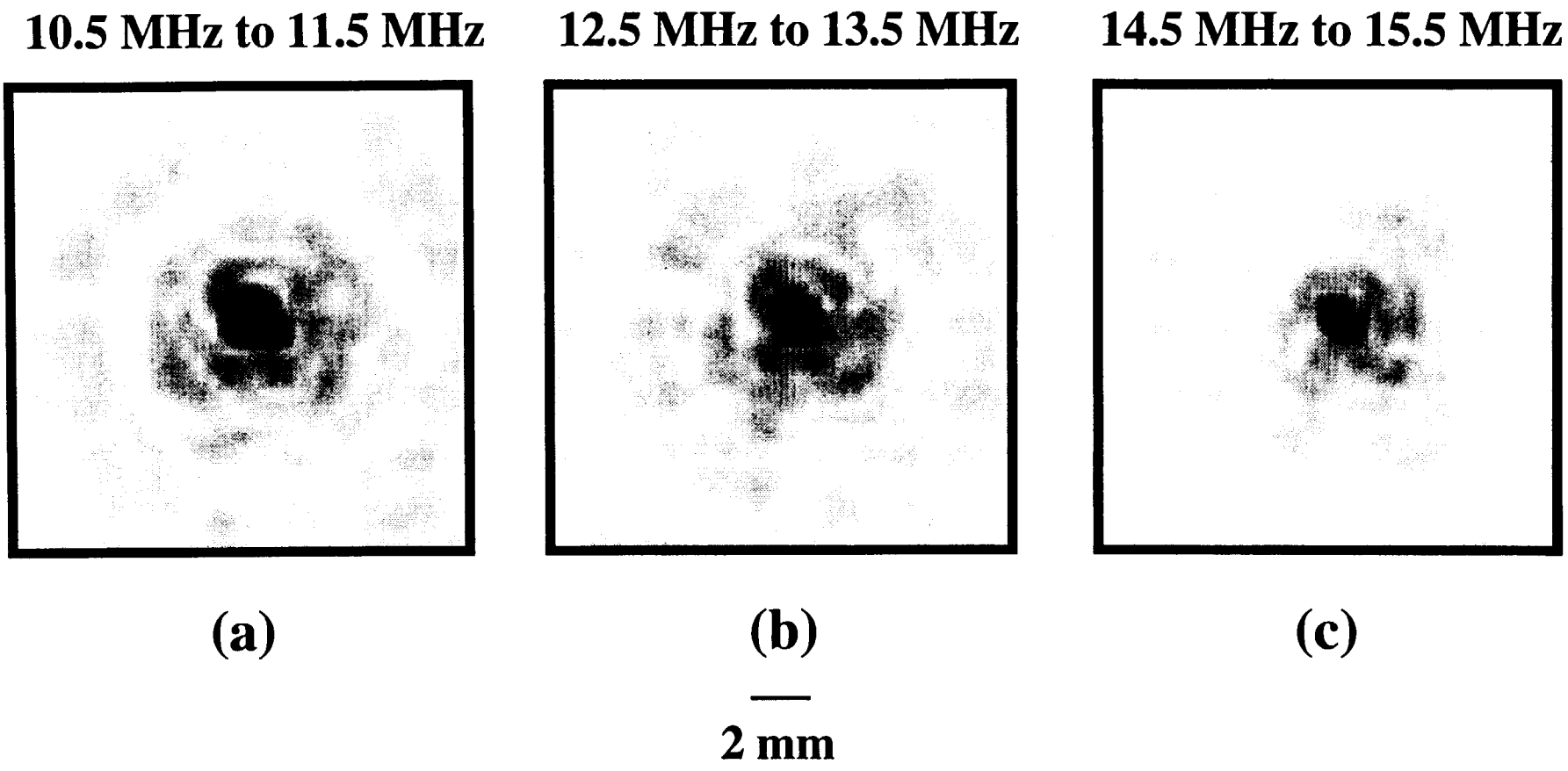

Figure 37: Comparison of insonifying frequencies at Position 2 with 15 MHz transducer. Receiver plane images of the narrowband pressure magnitudes at Position 2 of the thin composite are shown for the different frequency ranges for the 15 MHz transducer.

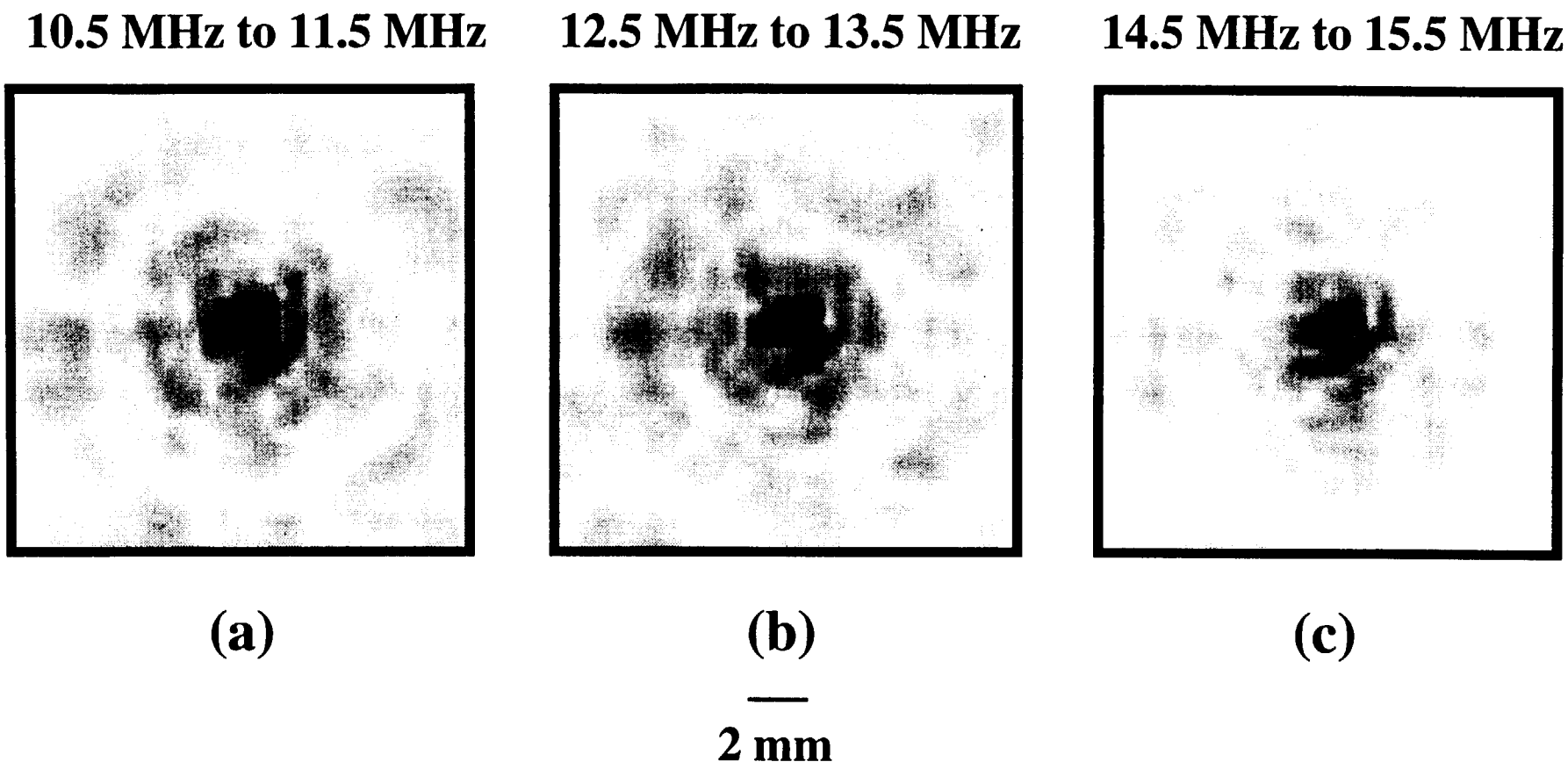

Figure 38: Comparison of insonifying frequencies at Position 3 with 15 MHz transducer. Receiver plane images of the narrowband pressure magnitudes at Position 3 of the thin composite are shown for the different frequency ranges for the 15 MHz transducer.

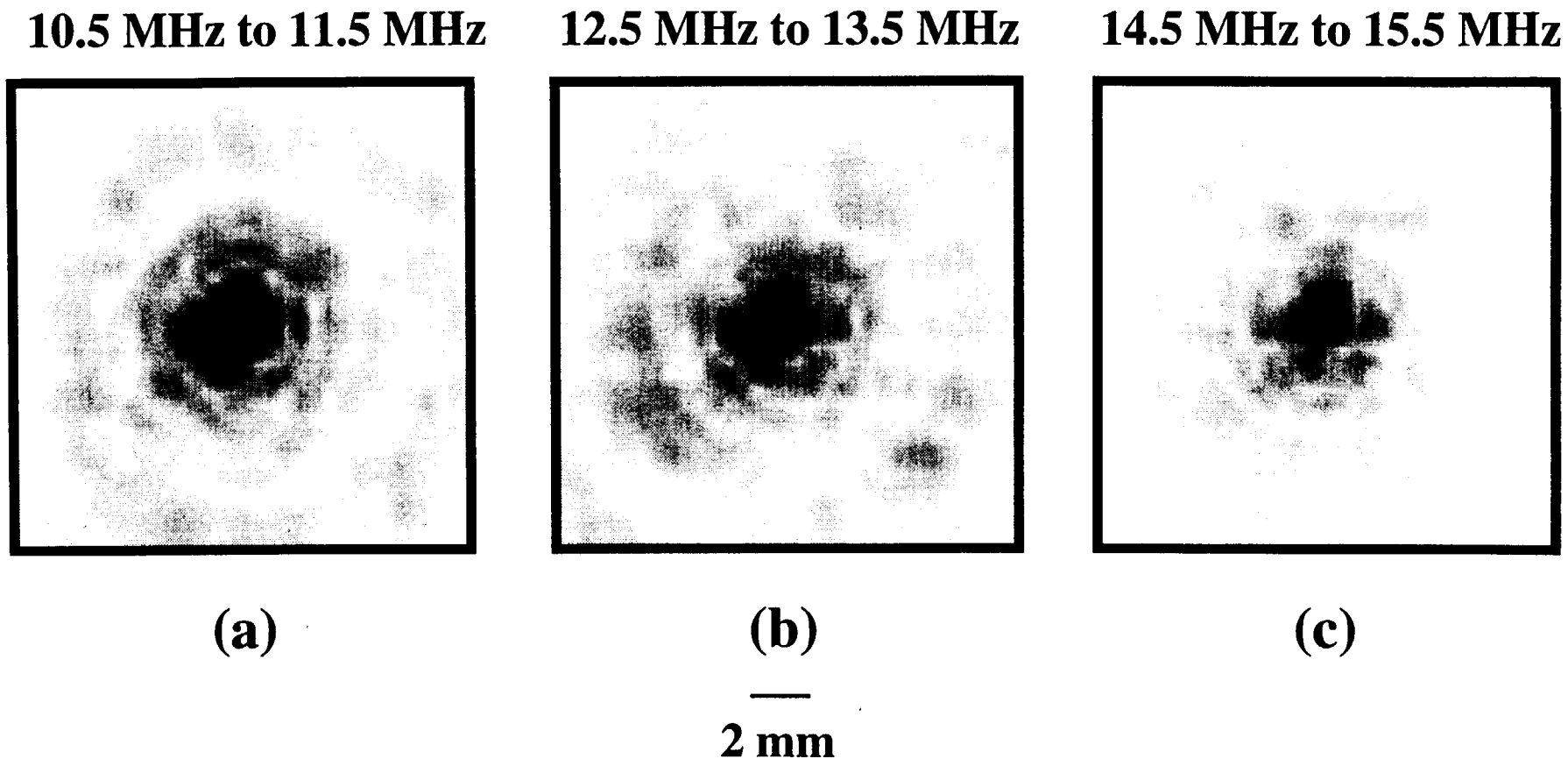

Figure 39: Comparison of insonifying frequencies at Position 4 with 15 MHz transducer. Receiver plane images of the narrowband pressure magnitudes at Position 4 of the thin composite are shown for the different frequency ranges for the 15 MHz transducer.

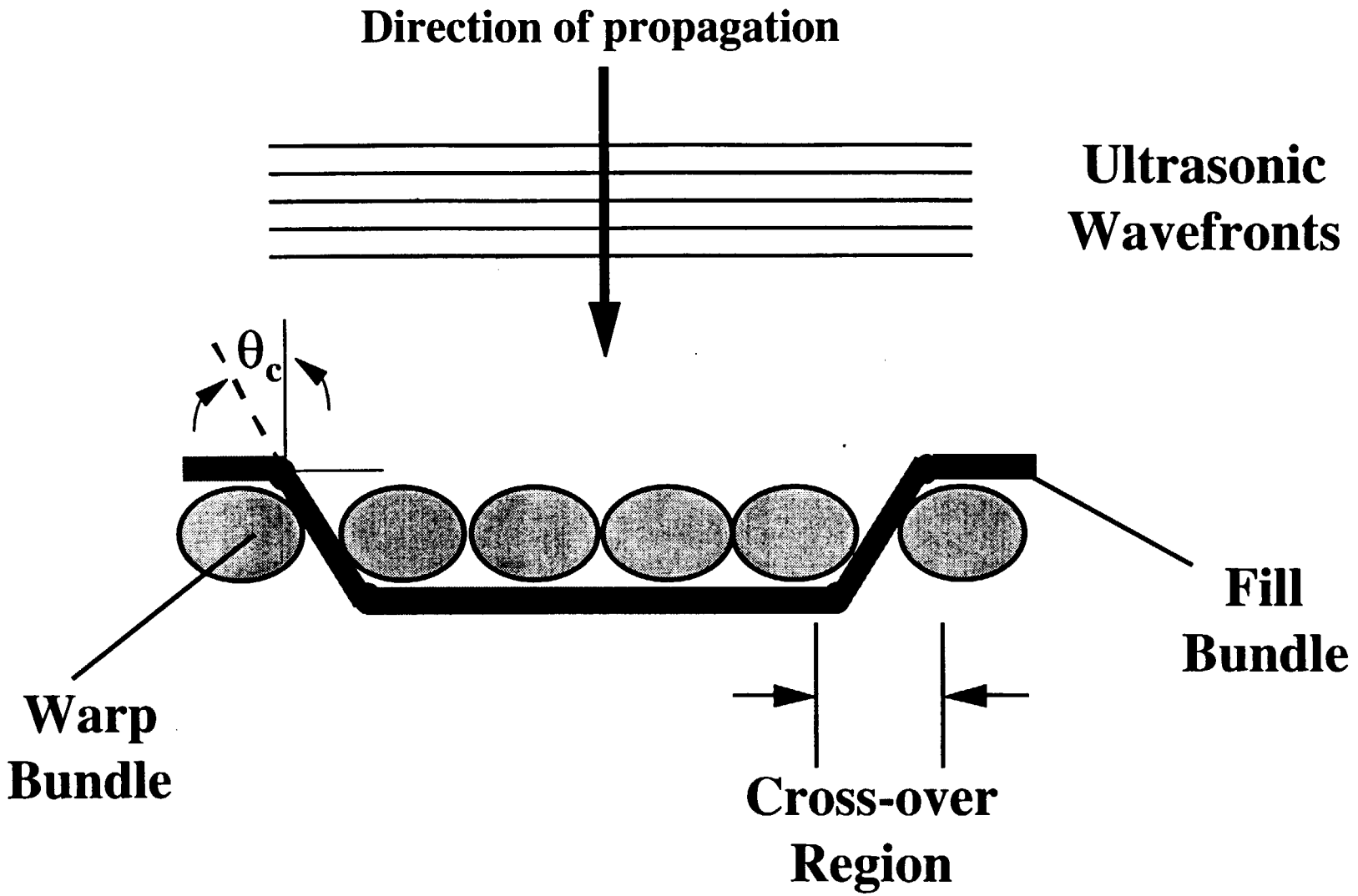

Figure 40: Cartoon of a sideview of the thin woven composite. The composite is shown in relation to an impinging ultrasonic pressure field. Note the direction of propagation of the ultrasonic wavefronts are normal with respect to the warp orientation and the ultrasonic wavefronts are at an angle θ_c with respect to the fill orientation.

IV. Dependence of Complex Pressure on Frequency for Ultrasonic Measurements of a Woven Cloth (June 1997 to December 1997)

In this section we consider issues relevant to the application of single-element, one-dimensional, and two-dimensional array technologies towards probing the mechanical properties of advanced engineering composites and structures. We provide comparisons between phase-sensitive and phase-insensitive detection methods for determination of textile composite structure parameters. We also compare phase-sensitive and phase-insensitive apparent signal loss measurements in an effort to study the phenomenon of phase cancellation at the face of a finite-aperture single-element receiver. Furthermore, we extend our work on ultrasonic beam profile issues through investigation of the phase fronts of the pressure field.

In Section IV.A we briefly describe the experimental arrangement and methods for data acquisition of the ultrasonic diffraction patterns upon transmission through a thin woven composite. Section IV.B details the analysis of the experimental data followed by the experimental results in Section IV.C. Finally, a discussion of the observations and conclusions is found in Section IV.D.

A. Experimental Arrangement and Methods

All measurements in this study were performed in a water tank using a set of 0.5"-diameter, spherically-focused (4" focal length), piezoelectric transducers with nominal center frequencies of 5 MHz, 10 MHz, and 15 MHz (Panametrics V309, V311, and V319, respectively) as the transmitting transducer. The thin woven composite was positioned in the focal plane of the transmitting transducer and oriented normal to the beam axis of the transducer. A 1 mm diameter PVDF, broadband, needle hydrophone (Force Institute, Type MH28-10) was used as the receiving transducer. The receiving hydrophone was positioned 120 mm from the transmitting transducer

(approximately 20 mm from the back side of the specimen). In the receiving plane, the hydrophone sampled the ultrasonic pressure field in a two-dimensional pseudo-array. The pseudo-array was composed of 64 sites by 64 sites (4096 total sites) with 0.5 mm separation between adjacent sites for a total sampled area of 31.5 mm by 31.5 mm. Figure 1 is a schematic diagram showing the data acquisition system used in this investigation. For further details regarding the experimental arrangement, the thin woven composite, and data acquisition protocol please refer to Section II of the previous Progress Report which is included in the CD-ROM version of this report.

A goal of this ongoing experimental research is to understand how systematic variations of the acquisition system, as well as changes in the materials investigated, affect the quantitative evaluation of these materials. The first physical parameter we chose to vary systematically was the nominal center frequency of the transmitting transducer. Three transmitting transducers, as mentioned above, were employed for the acquisition of the experimental data discussed within this report.

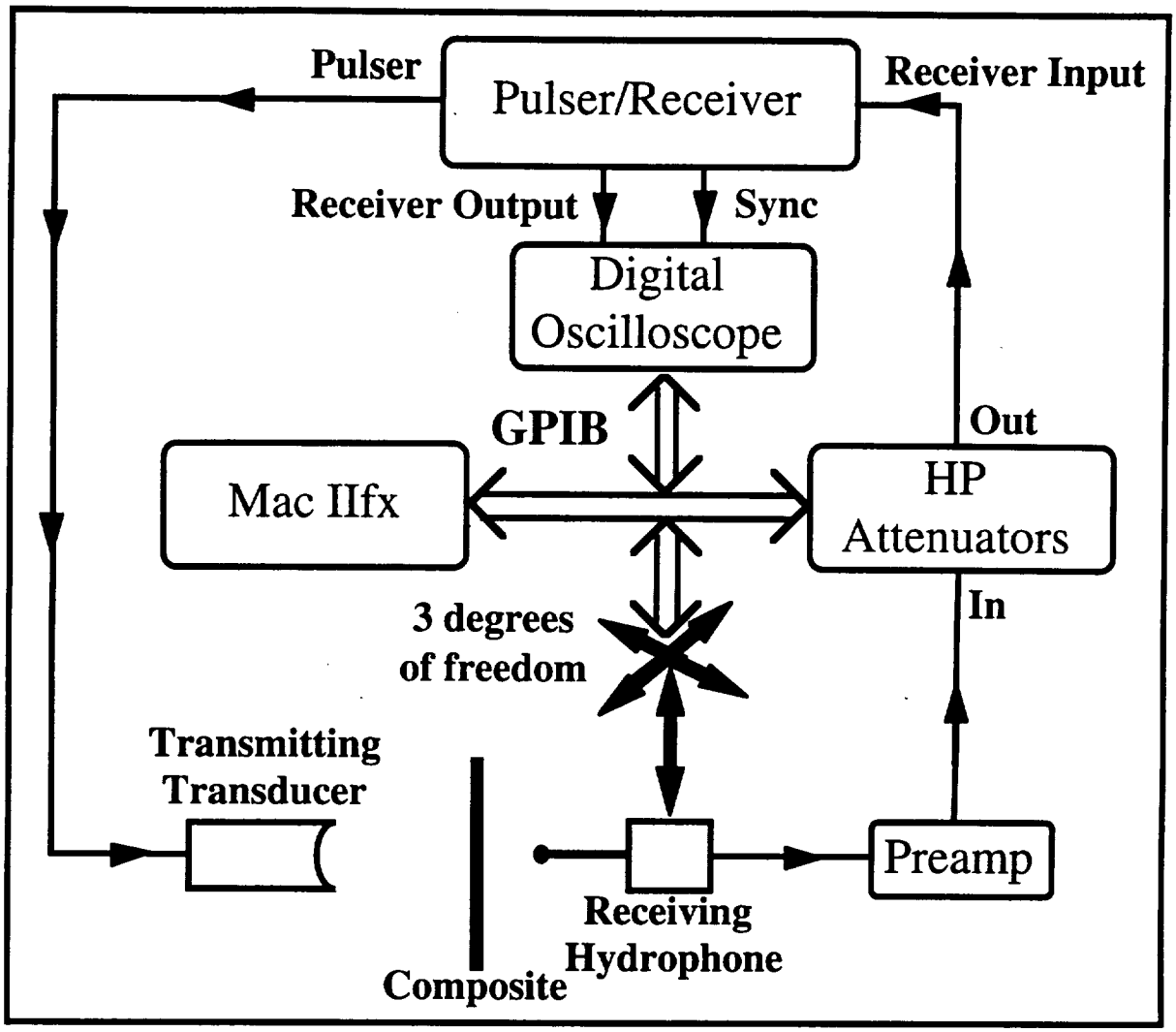

Figure 1. Experimental Setup.

In addition, we investigated how the spatial variation of the weave pattern of the thin woven composite affected the phase fronts of the ultrasonic signal. To that end we conducted pseudo-array scans over 4 different regions of the woven composite for each of the 3 transmitting transducers previously mentioned (5, 10, 15 MHz center frequencies). Figure 2 illustrates the relative positioning of the four different scan regions with respect to the thin woven composite. The center of each pseudo-array scan was linearly separated by 3 mm from the previous pseudo-

array scan. These four regions provide a fair representation of the different types of regions that would be encountered in subsequent studies of this composite.

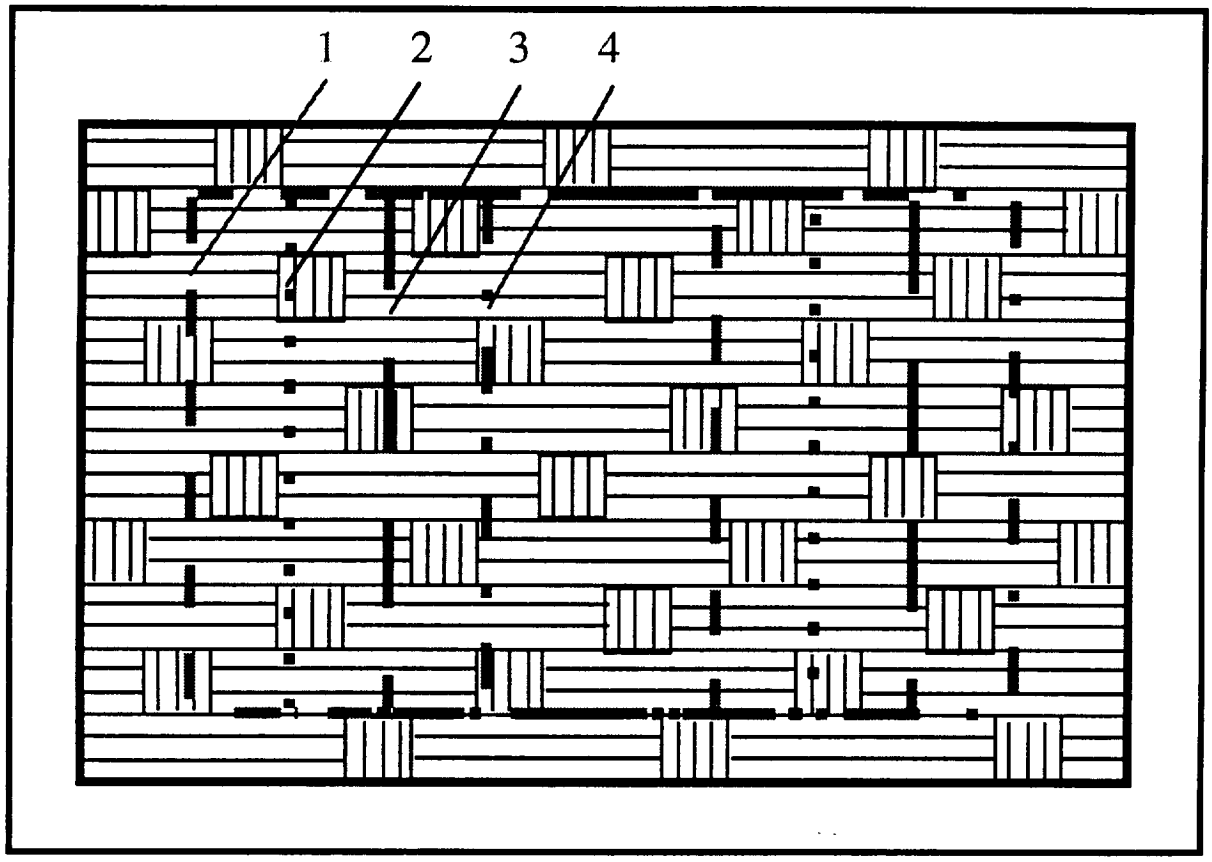

Figure 2. Relative positioning of the four different scanned regions of the thin woven composite.

B. Data Analysis

B.1 Software

Data analyses and visualization were performed on a Power Macintosh using in-house custom software written in the C programming language in conjunction with a commercial imaging software package (Transform 3.3, Fortner Software, Sterling, VA), a commercial spreadsheet

package (Excel 5.0, Microsoft, Redmond, WA), and a commercial graphing package (DeltaGraph® Pro 3.5, DeltaPoint, Inc., Monterey, CA).

B.2 Pseudo-Array Measurement Analysis

For the two-dimensional pseudo-array scans, the time-averaged rf trace acquired at each pseudo-array site was Fast Fourier Transformed to determine the spectral content of the time-domain rf trace. Discrete frequency data were extracted from the real and imaginary parts of Fourier transform of the broadband rf trace to provide a single-frequency representation of the respective parts of the pressure field. Throughout this report, we will refer to the real part of the Fourier transform as the in-phase part of the signal, and similarly, we will refer to the imaginary part of the Fourier transform as the quadrature part of the signal. This terminology is consistent with the terminology used is the electrical engineering community. (Please refer to Appendix A for a discussion of this choice of terminology.) The magnitude of the Fourier transform was calculated by taking the square root of the sum of the squares of the real and imaginary parts of the Fourier transform.

For each of the three transmitting transducers, we acquired five sets of data (one water path and four composite paths). For each transmitting transducer data set, single-frequency image analysis was performed at three distinct frequencies. For the 5 MHz transmitting transducer, we calculated the magnitude, in-phase, and quadrature parts of the pressure field near 3 MHz, 5 MHz, and 7 MHz. For the 10 MHz transmitting transducer, we calculated the magnitude, in-phase, and quadrature parts of the pressure field near 8 MHz, 10 MHz, and 12 MHz. Finally, for the 15 MHz transmitting transducer, we calculated the magnitude, in-phase, and quadrature parts of the pressure field near 11 MHz, 13 MHz, and 15 MHz.

B.2a Magnitude Image Construction

Image construction of the experimentally measured single-frequency magnitude of the ultrasonic pressure field was performed using Transform 3.3. For the magnitude images, the central region (central 32 sites by 32 sites, i.e., 15.5 mm by 15.5 mm) of the pseudo-array appears. Cropping the images permitted zooming the region where effects due to changes in physical parameters (i.e., water path versus composite path, insonifying frequency, and composite position) were most significant. All magnitude of the pressure field images are presented using the grayscale mapping shown in Figure 3. Darker regions correspond to larger relative pressure magnitudes and lighter regions correspond to smaller relative pressure magnitudes. For purposes of presentation, the images were interpolated to present smooth transitions across the receiving pseudo-array aperture. A bilinear interpolation method (row then column) calculates the grayscale for each pixel of the image. Figure 4 shows a representative pressure magnitude field overlaid with a cartoon of the composite weave pattern. It also provides relevant dimensions for the images.

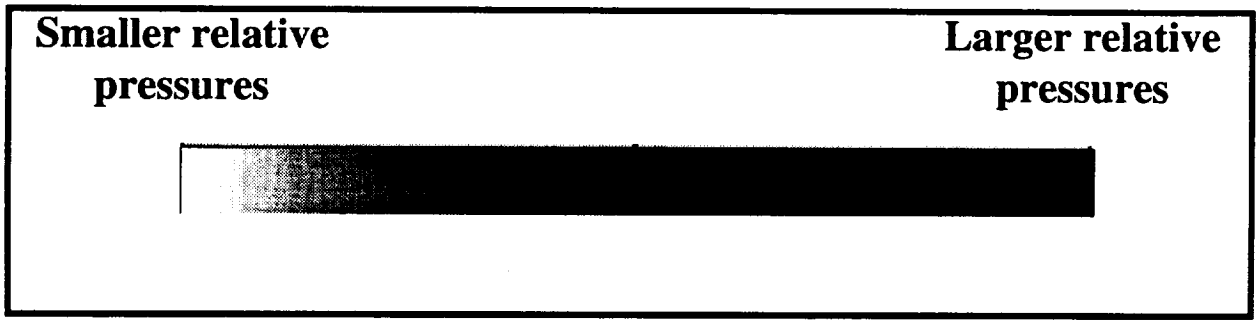

Figure 3. Grayscale mapping used for pressure magnitude images.

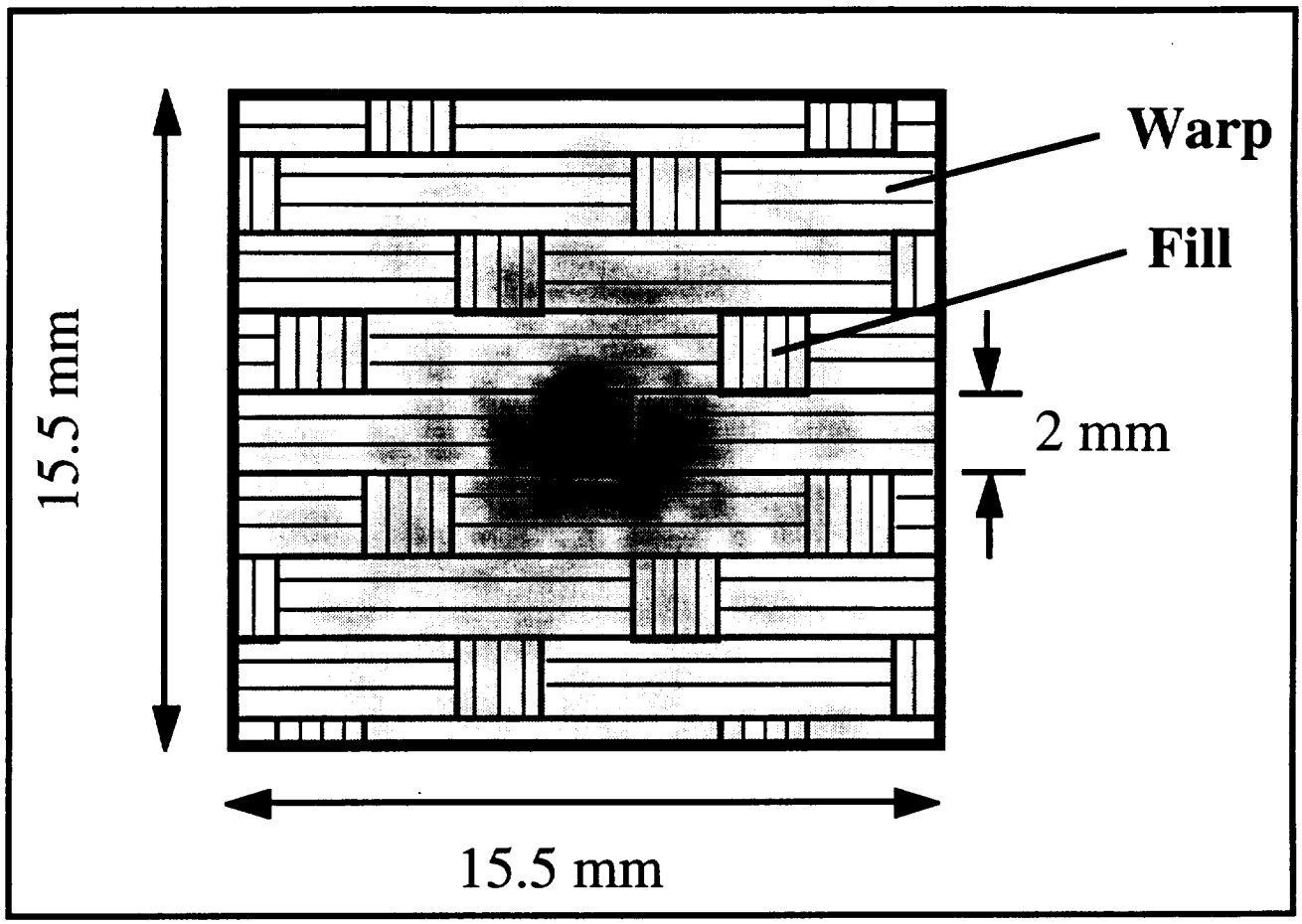

Figure 4. Representative pressure magnitude image with a cartoon of the thin woven composite overlaid.

B.2b In-Phase and Quadrature Image Construction

Image construction of the experimentally measured single-frequency in-phase and quadrature parts of the ultrasonic pressure field was also performed using Transform 3.3. All images of the in-phase and quadrature parts of the pressure field are presented using the color mapping shown in Figure 5. Red regions correspond to positive values, blue regions correspond to negative values, and white corresponds to neutral values. The particular mapping was chosen so as to emphasize the mixing of positive and negative values of in-phase or quadrature signals over a spatial region. Similar to the pressure magnitude images, the central region of the pseudo-array appears and a bilinear interpolation method (row then column) calculates the color for each

pixel of the image. Figure 6 shows representative in-phase and quadrature images for a reference path signal.

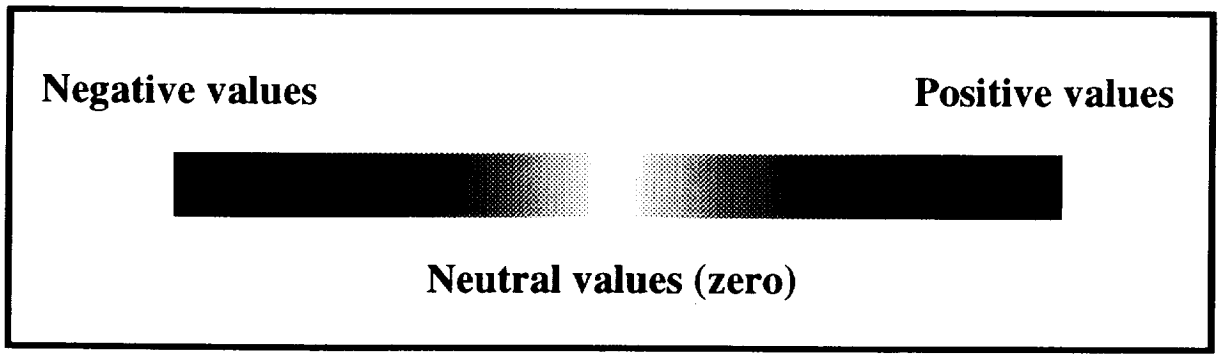

Figure 5. Colorscale mapping used for in-phase and quadrature images.

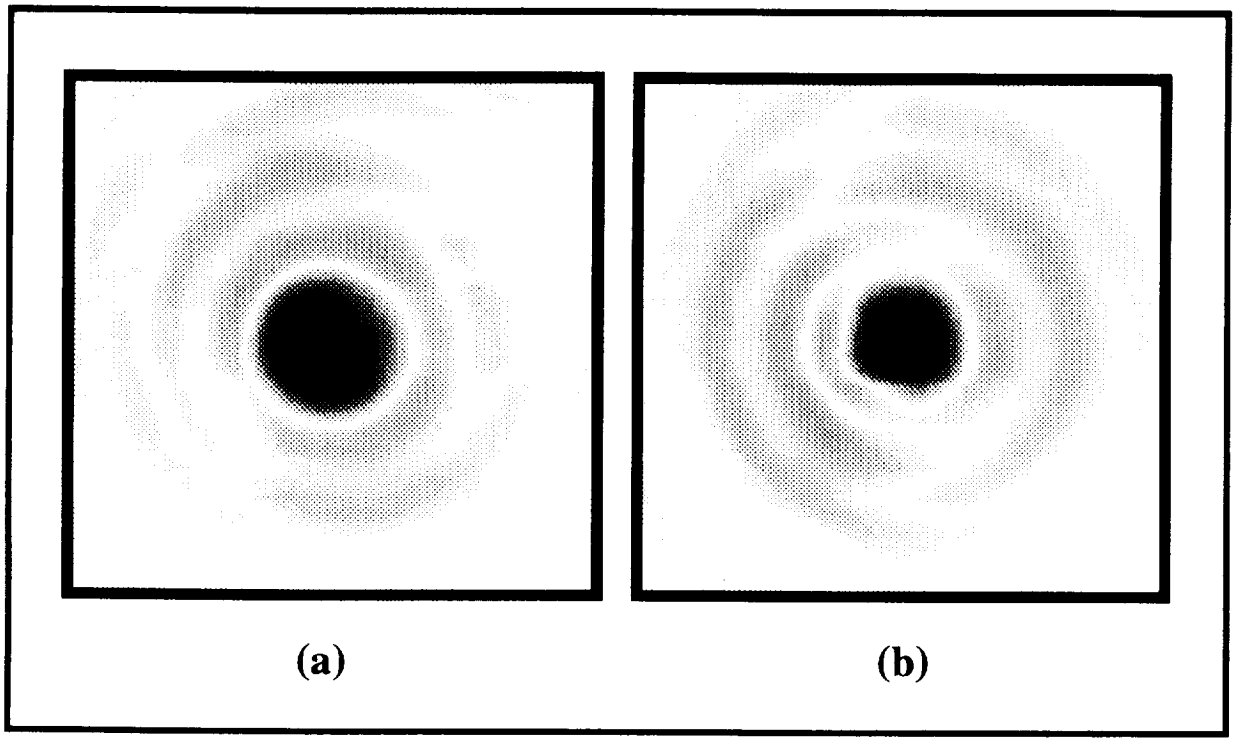

Figure 6. Representative (a) in-phase and (b) quadrature images of an ultrasonic pressure field transmitted through water only. Data ranges and color scales are the same for both images.

The organization of the in-phase and quadrature images (Figures 7 to 156) in the Results section is similar to the organization of the magnitude images of the previous report. For each series of scans (1 reference path and 4 composite paths) for a particular transmitting transducer, a set of images was constructed (1 set for each transducer for a total of 3 sets) consisting of 4 sections each. For each figure, images are displayed using a common data floor and data ceiling to calculate the colorscale bin size. Therefore, the same data values are mapped to the same color value for the images within each figure (i.e., bin sizes are the same). The use of this colorscale mapping technique permits direct comparison of images within each figure. Direct comparison for images from different transducers has not been performed at this stage of the analysis since system effects have not been completely deconvolved for the use of different transducers. However, we are still able to make some general observations between these sets as will be discussed below.

The first section of an image set compares in-phase pressure signals for the reference path to in-phase pressure signals with the thin woven composite inserted. Similar comparisons are also made for the quadrature signals. For each transducer, 4 regions of the composite were scanned and subsequently analyzed at 3 single frequencies. The second section compares in-phase and quadrature signals with the thin woven composite inserted for the 4 scanned regions at 3 single frequencies. The third section of an image set for a given transducer compares the in-phase (quadrature) pressure signals for a given thin woven composite region at 3 different insonifying frequencies. The fourth and final section compares the in-phase (quadrature) pressure signals at a given frequency for the 4 different scanned regions.

B.2c Apparent Signal Loss Analysis

Extending our qualitative analysis of the in-phase and quadrature images of this report and the magnitude images of the previous Progress Report, we calculate the apparent signal loss of the ultrasonic pressure field due to transmission through the thin woven composite. Initial analysis is

performed on the 5 MHz transducer data . The apparent signal loss calculations have not taken into account diffraction or insertion loss corrections. These compensations, as well as analysis of the 10 MHz and 15 MHz transducers data, are left for future work.

We calculate the apparent signal loss by two approaches.[3-6] The first method simulates the two-dimensional pseudo-array as a 0.5"-diameter *phase-sensitive* planar receiver. In this case, the receiver is sensitive to the phase of the pressure field. The second method uses the pseudo-array to simulate a 0.5"-diameter *phase-insensitive* planar receiver. In contrast to a phase-sensitive receiver, a phase-insensitive receiver is not sensitive to the phase of the pressure field but instead is sensitive to the magnitude or energy of the pressure field. For the present case, we will always be considering a phase-insensitive receiver that is sensitive to the energy (power) of the pressure field (i.e., an acoustoelectric-like receiver[7-9]). Figure 157 shows the footprint the 0.5"-diameter receiver with respect to the size of the in-phase and quadrature images.

In-house software in conjunction with Transform 3.3, Excel 5.0, and DeltaGraph Pro 3.5 was used to calculate the apparent signal loss. In general, the signal loss is calculated by the conventional log spectral subtraction technique for a reference power signal and a sample power signal. The phase-sensitive power was calculated as follows. Only those signals that the simulated receiver would measure were considered (i.e., those array sites under the footprint of the simulated receiver). As in the case of a single-element receiver, signals not received due to diffraction or refraction of the ultrasonic beam are not considered for analysis. The in-phase signals from all received array sites were then summed phase-sensitively. Similarly, the quadrature signals from each array site were summed phase-sensitively. The phase-sensitive power of the received ultrasonic field was subsequently calculated by taking the sum of the squares of the phase-sensitive in-phase and phase-sensitive quadrature signals. We do this for both the reference signals and the signals for the path with the thin woven composite inserted to arrive at an apparent phase-sensitive signal loss.

The apparent phase-insensitive signal loss of the ultrasonic pressure field due to transmission through the thin woven composite was calculated in a similar manner. The primary

difference between the two methods is how the in-phase and quadrature signals received are calculated. Since the phase-insensitive receiver is sensitive to the energy (power) of a pressure field and not the amplitude of a pressure field, the phase-insensitive in-phase power received is calculated by summing the square of the in-phase signal for all received array sites. The phase-insensitive quadrature power is calculated in a similar manner. The phase-insensitive power of the ultrasonic field is then simply the sum of the phase-insensitive in-phase power and the phase-insensitive quadrature power. We do this for both the reference signals and the signals for the path with the thin woven composite inserted to arrive at an apparent phase-insensitive signal loss.

The procedures described above calculate the apparent signal loss for a given composite region at a single frequency. This analysis is then repeated over the frequency range 2 MHz to 9 MHz for each composite region investigated. The 2 MHz to 9 MHz bandwidth was chosen according to the dynamic range measurements of our experimental system described in the previous Progress Report.

C. Results

In this section we discuss the receiver plane images of the experimentally measured in-phase, quadrature, and magnitude of the ultrasonic pressure field for a path through water only and a path with the thin woven composite inserted. We also discuss figures of the reference and composite paths power spectra and apparent signal losses for signals through the composite. Please refer to either the hardcopy figures or the accompanying CD-ROM for viewing of the figures. Note that only a small number of figures of the in-phase and quadrature images are included in the hardcopy version due to the extensive number of figures. In general, figures of pressure field images at the nominal center frequency of the 5 MHz transducer are included in hardcopy.

Table 1 provides an index to the figures of the in-phase and quadrature images. As described in the Data Analysis section, each of the 3 sets are organized into 4 sections. Each set is

composed of 50 figures. The multiple views of the data provide a means of accenting different features of the data. A discussion of the interpretation of these features follows in the next section. The first section of each set consists of the in-phase (quadrature) images for water path and composite path at 3 single frequencies at each of the 4 scanned regions of the composite (24 figures). The second section shows the in-phase and quadrature signals transmitted through the thin woven composite for 3 single frequencies at each of the 4 regions of the composite (12 slides). The third section of each set compares the in-phase (quadrature) images at 3 single frequencies for the 4 regions of the composite (6 slides). The last section compares the in-phase (quadrature) images for the 4 regions at 3 single frequencies (8 slides). Figures included in hardcopy form are for images resulting from analysis performed near the nominal center frequency of each transmitting transducer (i.e., 4.9 MHz, 10.0 MHz , and 14.9 MHz). These figures are chosen as a representative sample of the larger set of figures available in PDF version on the included CD-ROM.

The phase-sensitive and phase-insensitive signal loss analyses are shown in Figures 158 to 175. As mentioned in the Data Analysis section, power spectra for the reference path and composite paths and apparent signal losses due to the thin woven composite are shown only for the 5 MHz transmitting transducer data over the bandwidth 2 MHz to 9 MHz. Reference path and composite path power spectra are compared for both phase-sensitive and phase-insensitive detection. Furthermore, for the case of the composite region 1, phase-sensitive and phase-insensitive power spectra are compared in Figures 160 and 161. Summary figures of both the phase-sensitive and phase-insensitive apparent signal losses for each composite position are shown in Figures 172 and 173.

Figures	Transducer	Brief Description
7 to 30	5 MHz	Compare water path to composite path
31 to 42		Compare I and Q for composite path
43 to 50		Compare different frequencies
51 to 56		Compare different composite positions
57 to 80	10 MHz	Compare water path to composite path
81 to 92		Compare I and Q for composite path
93 to 100		Compare different frequencies
101 to 106		Compare different composite positions
107 to 130	15 MHz	Compare water path to composite path
131 to 142		Compare I and Q for composite path
143 to 150		Compare different frequencies
151 to 156		Compare different composite positions

Table 1. In-phase and quadrature of the pressure field figures.

D. Discussion

This section provides commentary on the Results presented in the previous section. The discussion is separated into three subsections. The first subsection offers qualitative interpretations of the in-phase and quadrature images of the pressure fields for the reference path and composite paths. The second subsection discusses the phase-sensitive and phase-insensitive apparent signal loss analyses. The final subsection addresses transducer alignment and ultrasonic beam profile issues.

D.1 Qualitative Interpretation

D.1a Comparison of Water Path versus Thin Woven Composite Path

Figures 7 to 30, 57 to 80, and 107 to 130 compare the images for reference path and composite paths of in-phase and quadrature parts of the pressure field. Inspection of these figures leads to several general observations. In some of the images for lower frequencies we are able to observe gross features common to both reference path and composite path for different frequencies and different regions of the composite. That is, the same areas of the receiving array appear to detect similar pressures (i.e., similar shapes in the images appear). However, the images appear "mottled" or distorted for the cases of transmission through the inserted thin woven composite. This distortion of the in-phase and quadrature signals, hence the phase, would be expected for transmission through an inhomogeneous and anisotropic material such as our textile composite. Some of this distortion may be attributed to the cross-over regions for which the fill of the woven composite is oriented non-normal to the angle of incidence of our insonifying ultrasonic beam. (See Figure 176.) This angle is referred to as the "crimp angle" and can be used to characterize textile composites.[10] The orientation of the fill within the cross-over regions with respect to the direction of propagation of the insonifying beam may provide a channel for propagation of the energy of the ultrasonic pressure field.[11,12]

We also note that despite the great effort made in alignment of the experimental apparatus, the expected circular symmetry of the in-phase and quadrature parts of the pressure field transmitted through the reference path was not observed. This is most notable at higher frequencies, where we observe a marked increase in mixing of positive (reds) and negative (blues) pressures in the in-phase and quadrature images due in part to transducer misalignment. For pressure fields propagated through only water, we would have expected images of the magnitude, in-phase, and quadrature part of the pressure field similar to Figure 177. These images provide theoretical expectations of a pressure field generated by a 0.5"-diameter, 4" focal length, spherically-focused transducer and propagated 120 mm through water. In our previous Progress

Report we did note that magnitudes of the pressure fields exhibited the expected ring symmetry. We now note, however, that the symmetry is absent in the in-phase and quadrature parts of the pressure field. This undesirable feature of the experimental signals has ramifications that we discuss further in the following subsections regarding phase cancellation at the face of a finite-aperture receiver and alignment of multi-dimensional receiver arrays.

D.1b Comparison of In-Phase and Quadrature of Thin Woven Composite Path

Comparisons of the in-phase and quadrature images of the pressure field propagated through the thin woven composite (Figures 31 to 42, 81 to 92, and 131 to 142) do not appear to provide a simple interpretation with respect to the sample scanned. The images do provide the reader with an idea of the amount of energy of the ultrasonic pressure field found in the in-phase and quadrature parts of the pressure field. However, it should be noted that there are still subtleties even for the apparently simple interpretation of where the energy resides in a pressure field. Appendix B offers a discussion of possible difficulties involved in interpreting in-phase and quadrature images, and in specific, how time shifts in the record of the digitized received pressure data can affect these images.

D.1c Comparison of Insonifying Frequencies for a Thin Woven Composite Path

The reader may immediately observe in Figures 43 to 50, 93 to 100, 143 to 150 that the footprint of the ultrasonic beam decreases as the frequency of insonification is increased. We also observe an increased variability in the features of the in-phase and quadrature images for lower frequencies of insonification (2 MHz to 8 MHz) as compared to higher frequencies of insonification (> 10 MHz) *for a given thin woven composite region.* For the higher frequencies (> 10 MHz), the diameter of the ultrasonic beam is smaller than the large scale features of the thin woven composite (i.e., warp and fill size). Hence, the higher frequencies would be insonifying

the same type of regions of the composite. However, the lower frequencies (2 MHz to 8 MHz) have footprints that will interrogate several warp and fill bundles. It is this variation in region of interrogation by the ultrasonic beam for different frequencies that leads to variation in features of the in-phase and quadrature images.

D.1d Comparison of Thin Woven Composite Paths for a given frequency

Figures 51 to 56, 101 to 106, and 151 to 156 compare the in-phase (quadrature) images of the received pressure field for the 4 different scanned regions of the thin woven composite *for a given frequency of insonification*. In general, the same conclusions of the previous Progress Report regarding the magnitude of the pressure field can be made here for the in-phase and quadrature parts of the pressure field. For lower frequencies, the ultrasonic beam footprint is large enough so that on average approximately the same type of region is insonified. We observe this feature in Figures 51 to 56. There is less variation in these figures than Figures 101 to 106 and 151 to 156 of the higher frequencies of insonification. Due to the smaller footprint of the higher frequencies as describe above, the in-phase and quadrature signals will be highly dependent upon the features of the region scanned as evidenced in the marked variation of the in-phase and quadrature images for the higher frequencies.

D.2 Quantitative Interpretation

D.2a Phase-Sensitive and Phase-Insensitive Apparent Signal Loss

Figures 158 to 175 show the phase-sensitive and phase-insensitive power spectra and apparent signal loss for the 5 MHz transducer data over the bandwidth 2 MHz to 9 MHz for each scanned region of the composite. The power spectra for transmission through the reference path and through water with the thin woven composite inserted are compared for each region of the composite (Figures 158 and 159, 163 and 164, 166 and 167, 169 and 170). In all cases but the

phase-sensitive power spectra for position 1 of the composite (Figure 158) we observe the expected result of greater power in the water path signal compared to the composite path signal. This discrepancy between measured and expected results is discussed further below.

In addition, the phase-sensitive and phase-insensitive power spectra for both reference path and composite path (Figures 160 and 161) are compared for the first scanned region of the composite (position 1). These figures are representative of the other regions of the composite. As expected, the power received at each frequency by the phase-insensitive receiver is greater than or equal to the power received at each frequency by the phase-sensitive receiver. The discrepancy between the two detection methods is most pronounced for higher frequencies. The apparent decrease in power (energy) of the ultrasonic field when detected phase-sensitively is a result of phase cancellation at the face of a finite-aperture piezoelectric receiver.

The phase-sensitive and phase-insensitive apparent signal losses are compared for each region of the composite (Figures 162, 165, 168, and 171) as well as for each detection method (Figures 172 and 173). For the lower half of the bandwidth, the phase-sensitive apparent signal losses exhibit similar frequency behavior as the phase-insensitive apparent signal losses for each composite position. However, for the upper half of the bandwidth, only in the case of position 4 (Figure 171) does the phase-sensitive apparent signal loss exhibit similar frequency behavior the phase-insensitive apparent signal loss. For the other 3 composite positions, the higher frequency behavior of the apparent signal loss measured phase-sensitively seems only to provide similarity in gross features of the phase-insensitive measurements (i.e., local minimum around 8 MHz). Furthermore, there is greater variation in the phase-sensitive apparent signal losses as compared to phase-insensitive apparent signal losses. This is demonstrated in Figure 174 comparing the average phase-sensitive apparent signal loss of the 4 composite positions to the average phase-insensitive apparent signal loss. The large standard deviation error bars of the average phase-sensitive apparent signal loss for higher frequencies illustrate this variation. The strength of phase-insensitive detection versus phase-sensitive detection is the absence of phase cancellation at the face of a finite-aperture receiver. In all phase-sensitive receivers, this phenomenon occurs. Hence, we

would always expect to measure larger signal losses phase-sensitively than phase-insensitively. We note, however, that for composite positions 1 and 3 (Figures 162 and 168) the phase-sensitive apparent signal loss is less than the phase-insensitive apparent signal loss for a portion of the bandwidth. This can be explained by the difference in the reference power spectra for the two cases. In the case of phase-sensitive detection, phase cancellation at the face of the receiver is occurring even for the reference path. For composite position 1, the phase cancellation at the face of the receiver is extensive to the degree we have negative apparent signal loss as the ultrasound is transmitted through the composite. This apparent contradiction between the phase-sensitive and phase-insensitive signal losses for the two case mentioned above is resolved when a common reference power spectrum is used in the calculation of the signal loss. Figure 175 depicts the phase-sensitive and phase-insensitive apparent signal losses with the phase-insensitive reference power spectrum used in both calculations. Now, as expected, the phase-sensitive signal loss is greater than the phase-insensitive signal loss at all frequencies.

A final comment can be offered regarding the signal loss behavior of the composite. It is desirable to have some parameter to characterize the state of the material. In the past, our Laboratory has found the slope of attenuation to be a robust ultrasonic parameter that correlates well with physical properties of the material.[13-16] For the case of this textile composite, a slope of attenuation characterization may not be suitable. Further analysis is required before we might formulate a parameterization method.

D.3 Further Issues

There are some issues that stem from the discussions of the previous subsections. We have observed the lack of symmetry of the in-phase and quadrature images that would be expected for transmission through water. This leads to questions of proper alignment for our two-dimensional pseudo-array. As mentioned in the previous Progress Report, alignment of the experimental apparatus was achieved through optimization of the reference power spectrum for the

case of the receiving hydrophone positioned in the center of the two-dimensional pseudo-array. We would like to believe the hydrophone is on-axis of the transmitting transducer, but there is always the concern of whether or not the transmitting transducer shoots down the geometric axis. In retrospect, our alignment procedure is appropriate for a single-element receiver but is inadequate for the case of a two-dimensional pseudo-array or the case of a true one or two-dimensional array. This is evidenced in Figures 178 and 179. We see that if we only inspect the magnitude (power) of the pressure field we will not observe the possibility of phase cancellation at the face of a finite-aperture phase-sensitive receiver. Figure 178 shows the magnitude, in-phase, and quadrature images of the pressure field at 7 MHz for the reference path. We observe a smoothly varying and symmetric magnitude image and smoothly varying in-phase and quadrature images with some broken symmetry. Figure 179 shows the magnitude, in-phase, and quadrature images of the pressure field at 8 MHz for the reference path. The magnitude of the pressure field image appears smoothly varying. However, the in-phase part of the pressure field exhibits a rapid variation in the center of the ultrasonic beam which we would not expect for an aligned system. Future pseudo-array scans will incorporate monitoring of the in-phase and quadrature images during the alignment of the transmitting transducer and receiving hydrophone.

Knowledge of the volume of insonification is a second issue of concern for evaluation of composites. We have previously described the decrease in footprint of the ultrasonic beam with the increase of insonifying frequency. We further observed how lower frequencies might provide a measure of average quality of a composite region whereas higher frequencies might provide a measure of smaller scale features of the composite. As mentioned in the previous Progress Report, it is a full understanding of the beam profile (focal length, focal depth, beam diameter) as well as knowledge of the material properties of the composite that will permit accurate evaluation of composite viability. Furthermore, with the advances in digital technologies customization of ultrasonic fields is possible through dynamic focusing of one and two-dimensional arrays. Consideration of each of these aspects of an experimental measurement system can lead to advances in quantitative nondestructive evaluation of complex composite materials.

E. References

1. J.G. Miller, "Ultrasonic Nondestructive Evaluation Techniques Applied to Quantitative Characterization of Textile Composite Materials", NASA, Progress Report, Report Number: NAG 1-1848, (December, 1996).

2. J.G. Miller, "Ultrasonic Nondestructive Evaluation Techniques Applied to Quantitative Characterization of Textile Composite Materials", NASA, Progress Report, Report Number: NAG 1-1848, (July, 1997).

3. M.R. Holland and J.G. Miller, "Phase-Insensitive and Phase-Sensitive Quantitative Imaging of Scattered Ultrasound Using a Two-Dimensional Pseudo-Array", Proc. IEEE Ultrasonics Symposium, 815-819 (1988).

4. P.H. Johnston, *Phase-Insensitive Detection and the Method of Moments for Ultrasonic Tissue Characterization*, Doctor of Philosophy Thesis, Washington Univerisity, (1985).

5. P.H. Johnston and J.G. Miller, "A Comparison of Backscatter Measured by Phase-Sensitive and Phase-Insensitive Detection", IEEE Ultrasonics Symposium, 827-831 (1985).

6. P.H. Johnston and A.A. Ananda, "The role of phase cancellation in the ultrasonic NDE of stitched graphite-epoxy composites", Proc. IEEE Ultrasonics Symposium, 845-848 (1991).

7. L.J. Busse and J.G. Miller, "Response Characteristics of a Finite Aperture, Phase Insensitive Ultrasonic Receiver Based Upon the Acoustoelectric Effect," Journal. Acoustical Society of America **70**, 1370-1376 (1981).

8. J.S. Heyman, *Ultrasonic Coupling to Optically Generated Charge Carriers in CdS: Physical Phenomena and Applications*, Doctor of Philosophy Thesis, Washington Univerisity, (1975).

9. J.S. Heyman, "Phase insensitive acoustoelectric transducer," Journal. Acoustical Society of America **64**, 243-9 (1978).

10. B.N. Cox and G. Flanagan, "Handbook of Analytical Methods for Textile Composites", NASA, Report Number: Contractor Report 4750, (March, 1997).

11. S.M. Handley, *Physical Principals Pertaining to Ultrasonic and Mechanical Properties of Anisotropic Media and Their Application to Nondestructive Evaluation of Fiber-Reinforced Composite Materials*, Doctor of Philosophy Thesis, Washington University, (1992).

12. K.W. Hollman, *Phase-Sensitive and Phase-Insensitive Ultrasonic Measurements of Rough Interfaces and Anisotropic Media with Predictions using Angular Spectral Decomposition*, Doctor of Philosophy Thesis, Washington University, (1995).

13. D.K. Hsu and S.M. Nair, "Evaluation of Porosity in Graphite-Epoxy Composite By Frequency Dependence of Ultrasonic Attenuation", Review of Progress in Quantitative NDE, 1185-1193 (1986).

14. S.M. Handley, M.S. Hughes, J.G. Miller, and E.I. Madaras, "Characterization of Porosity in Graphite Epoxy Composite Laminates With Polar Backscatter and Frequency Dependent Attenuation", Proc. IEEE Ultrasonics Symposium, 827-830 (1987).

15. M.S. Hughes, S.M. Handley, J.G. Miller, and E.I. Madaras, "A Relationship Between Frequency Dependent Ultrasonic Attenuation and Porosity in Composite Laminates", Review of Progress in QNDE, 1037-1044 (1987).

16. S.M. Nair, D.K. Hsu, and J.H. Rose, "Porosity estimation using the frequency dependence of the ultrasonic attenuation," Journal of Nondestructive Evaluation **8**, 13-26 (1989).

17. P. Horowitz and W. Hill, *The Art of Electronics* (Press Syndicate of the University of Cambridge, Cambridge, 1989), Second ed.

18. R.N. Bracewell, *The Fourier Transform and Its Applications* (McGraw-Hill, Inc., New York, 1986), Second, Revised ed.

Appendix 1. The Use of In-Phase and Quadrature

In the Data Analysis section, we discuss the choice of referring to the real part of the Fourier transform of the time-domain pressure data as the in-phase part of the pressure field. We also refer to the imaginary part of the Fourier transform of the time-domain pressure data as the quadrature part of the pressure field. This Appendix describes the background for these choices.

We use broadband excitation pulses (short time duration) to initiate the generation of the ultrasonic signal. We can expand our time-domain rf signal (pressure field) received by the pseudo-array as superposition of cosine and sine terms for every frequency:

$$p(t) = \frac{a_0}{2} + \sum_{n=1}^{\infty} a_n \cos(\omega_n t) + \sum_{n=1}^{\infty} b_n \sin(\omega_n t). \tag{A.1}$$

The cosine and sine functions form a set of basis functions that are orthonormal and linearly independent. Because $\sin(\omega_n t + \frac{\pi}{2}) = \cos(\omega_n t)$ at any specific frequency ω_n, the cosine term and sine term are $\pi/2$ or 90° out of phase and are said to be *in quadrature* with each other.[17]

Appendix 2. The Effect of Time Shifts on the In-Phase and Quadrature Signals

In the Discussion section we mentioned the possibility of ambiguities in interpreting the in-phase and quadrature images of the pressure field. A simple exercise that illustrates this is adjustment of a digital delay in the acquisition of the time-domain pressure data. Off-line in software, we are able to apply time shifts to the received time-domain pressure data. The question then is how does the time shift affect the in-phase and quadrature images of the pressure field.

The Fourier Shift Theorem (B.1) addresses this question.[18]

$$P^{shifted}(\omega) = P(\omega) e^{i\omega\Delta t} \tag{B.1}$$

If we shift our time-domain pressure signal by an interval Δt, we see the real and imaginary parts of the Fourier transform of the pressure field are modified by the exponential term. We do note, though, that the magnitude (power) of the shifted pressure field is not affected. The following animation (Movie 1), which only appears in the PDF version on the CD-ROM, illustrates this

effect. Figure 180 shows in-phase and quadrature images for the original pressure field without any time shift and the pressure field shifted by 40 nsec. Each frame of in-phase and quadrature animation has been calculated from a time-domain pressure field that has been shifted forward in time by 40 nsec from the previous in-phase and quadrature images. By inspection of either the Figure 180 or Movie 1, it is apparent that the amount of power (energy) in the in-phase and quadrature parts of the pressure are significantly affected by time shifts in the received time-domain data. Even though the total power in the pressure field remains unchanged, there is a shifting of energy between the in-phase and quadrature parts of the pressure field with time shifting of the received pressure field.

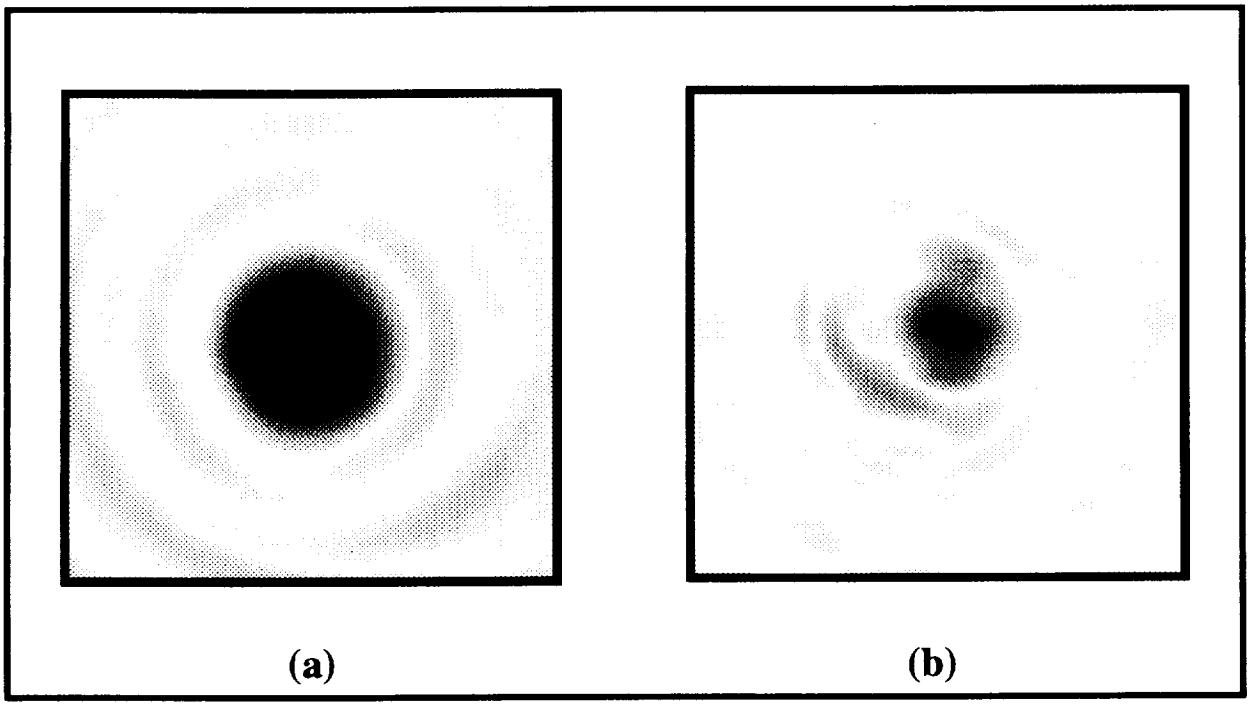

Figure 9. Water path and composite path in-phase images at 4.9 MHz. Receiver plane images for (a) in-phase part of the pressure field for water path only and (b) in-phase part of the pressure field for composite path at Position 1 using the 5 MHz transducer.

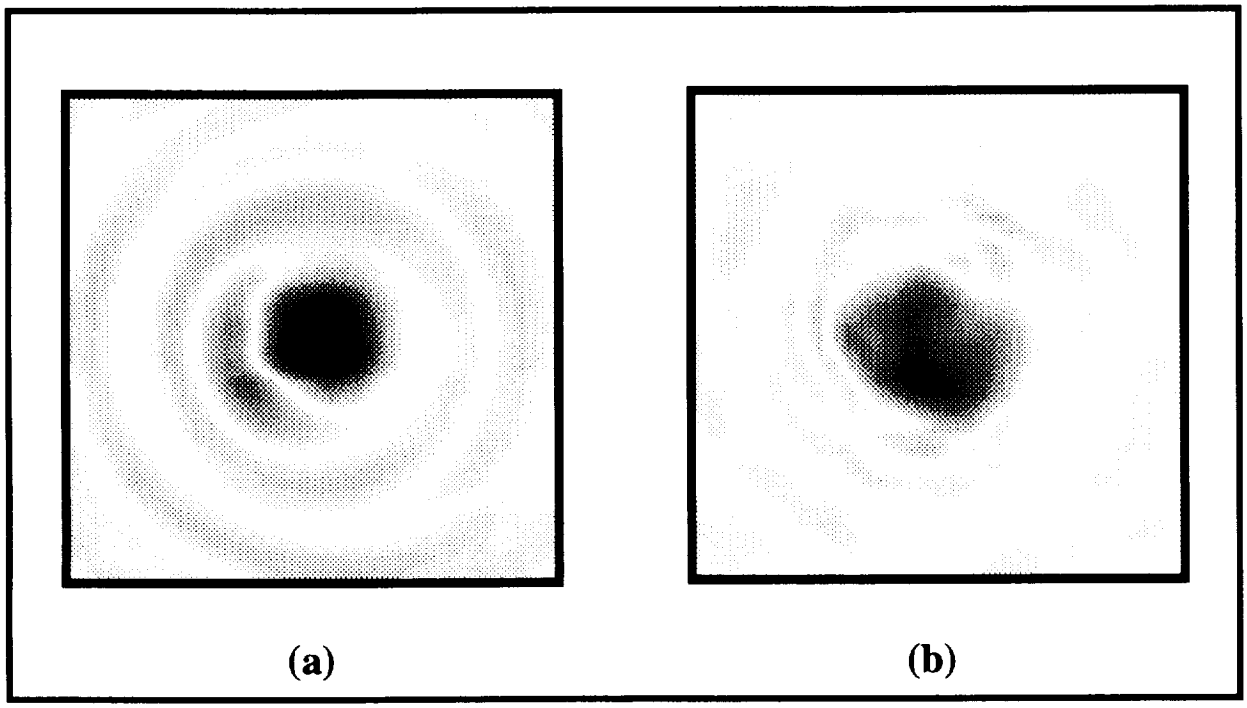

Figure 10. Water path and composite path quadrature images at 4.9 MHz. Receiver plane images for (a) quadrature part of the pressure field for water path only and (b) quadrature part of the pressure field for composite path at Position 1 using the 5 MHz transducer.

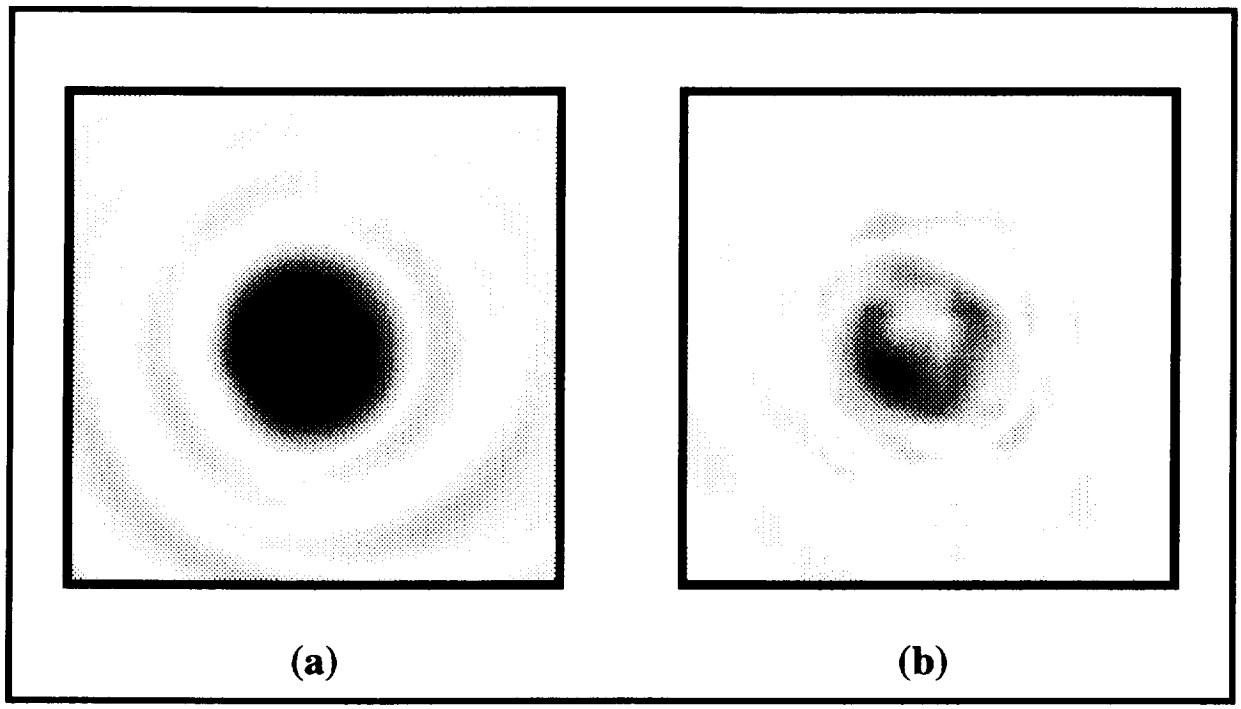

Figure 15. Water path and composite path in-phase images at 4.9 MHz. Receiver plane images for (a) in-phase part of the pressure field for water path only and (b) in-phase part of the pressure field for composite path at Position 2 using the 5 MHz transducer.

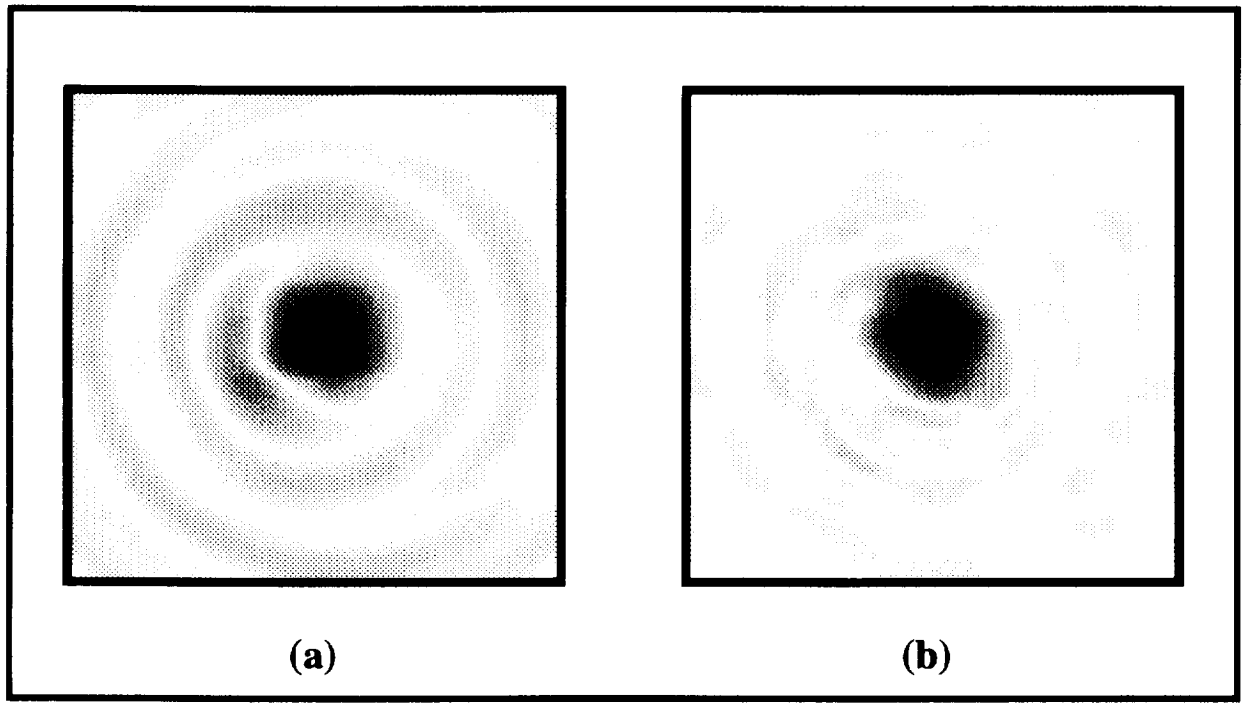

Figure 16. Water path and composite path quadrature images at 4.9 MHz. Receiver plane images for (a) quadrature part of the pressure field for water path only and (b) quadrature part of the pressure field for composite path at Position 2 using the 5 MHz transducer.

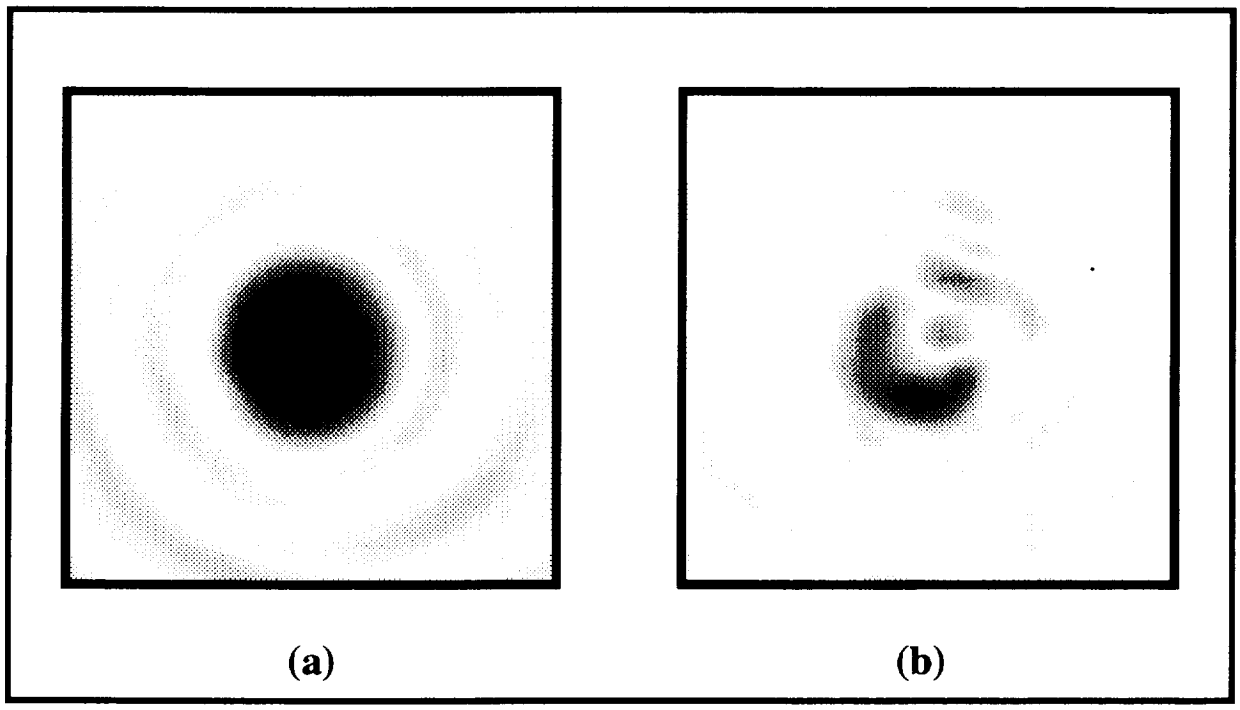

Figure 21. Water path and composite path in-phase images at 4.9 MHz. Receiver plane images for (a) in-phase part of the pressure field for water path only and (b) in-phase part of the pressure field for composite path at Position 3 using the 5 MHz transducer.

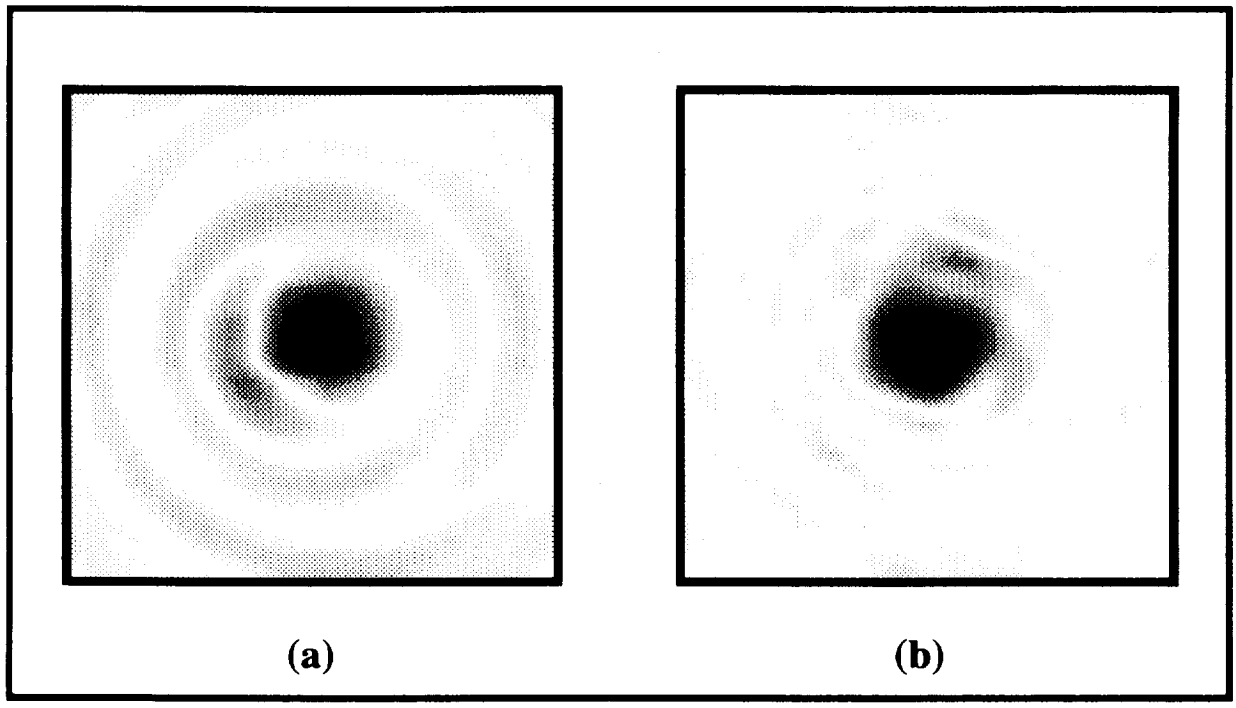

Figure 22. Water path and composite path quadrature images at 4.9 MHz. Receiver plane images for (a) quadrature part of the pressure field for water path only and (b) quadrature part of the pressure field for composite path at Position 3 using the 5 MHz transducer.

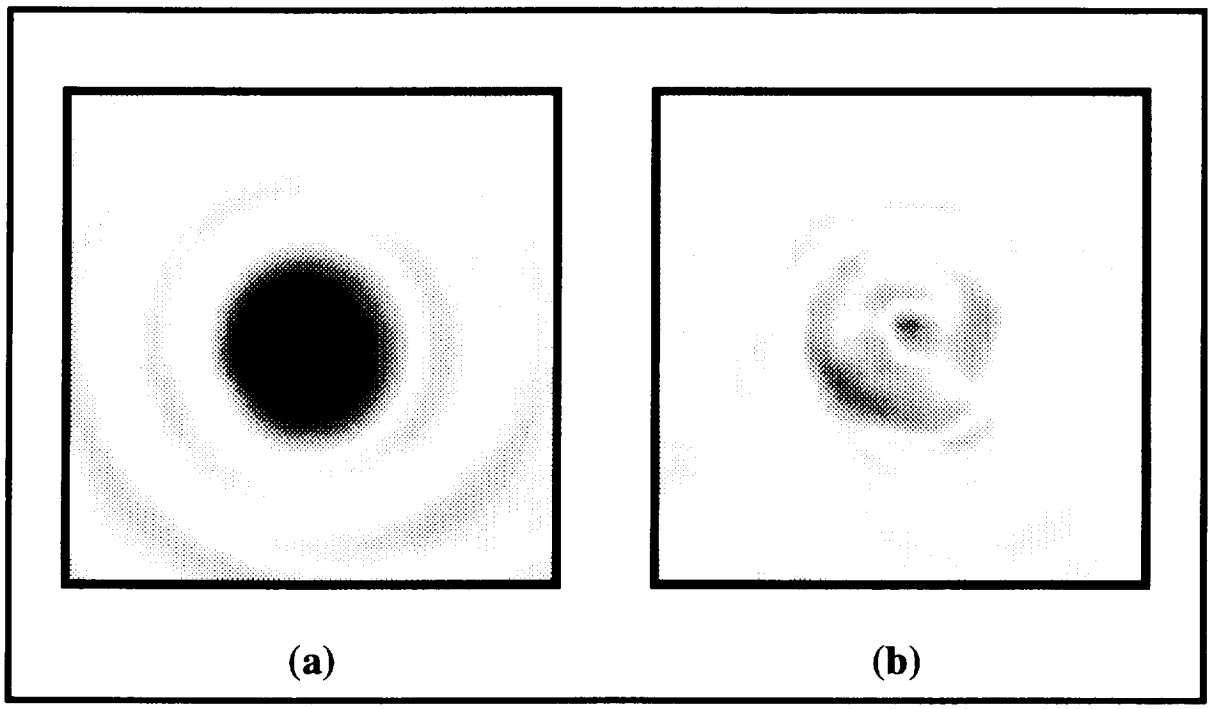

Figure 27. Water path and composite path in-phase images at 4.9 MHz. Receiver plane images for (a) in-phase part of the pressure field for water path only and (b) in-phase part of the pressure field for composite path at Position 4 using the 5 MHz transducer.

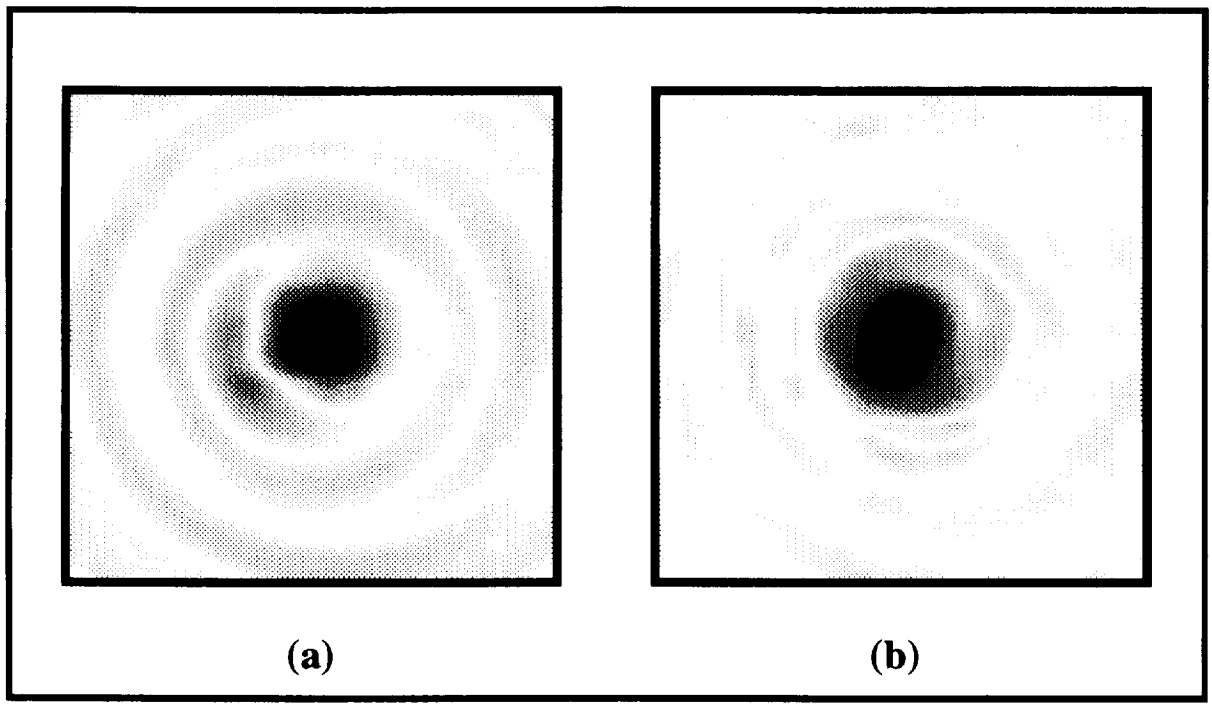

Figure 28. Water path and composite path quadrature images at 4.9 MHz. Receiver plane images for (a) quadrature part of the pressure field for water path only and (b) quadrature part of the pressure field for composite path at Position 4 using the 5 MHz transducer.

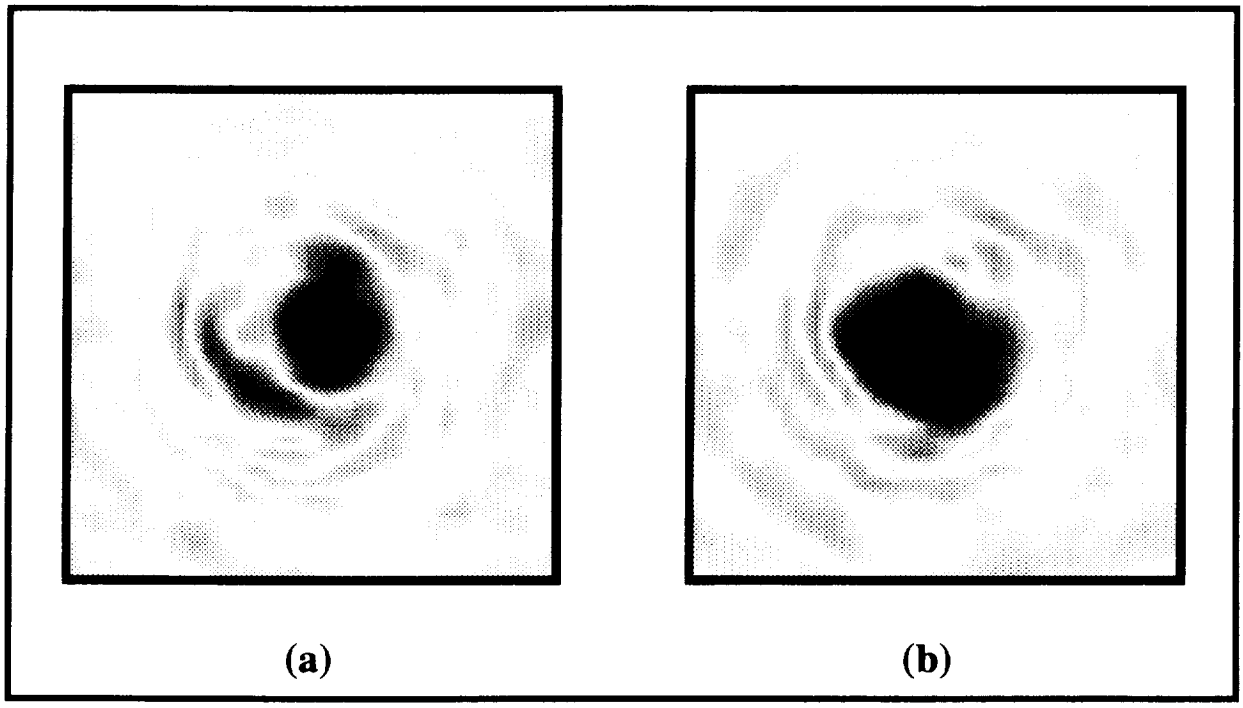

Figure 32. In-phase and quadrature parts of the pressure field at 4.9 MHz. Receiver plane images for composite path at Position 1 using the 5 MHz transducer for the (a) in-phase part of the pressure field and (b) quadrature part of the pressure field.

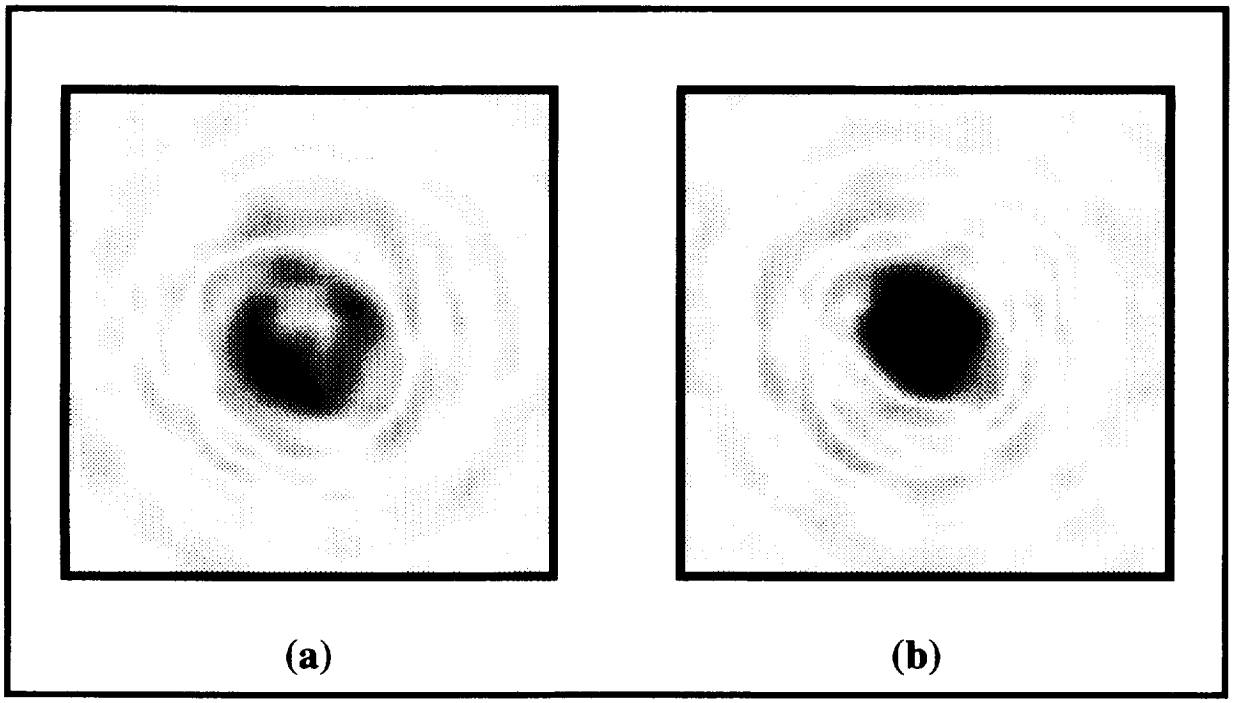

Figure 35. In-phase and quadrature parts of the pressure field at 4.9 MHz. Receiver plane images for composite path at Position 2 using the 5 MHz transducer for the (a) in-phase part of the pressure field and (b) quadrature part of the pressure field.

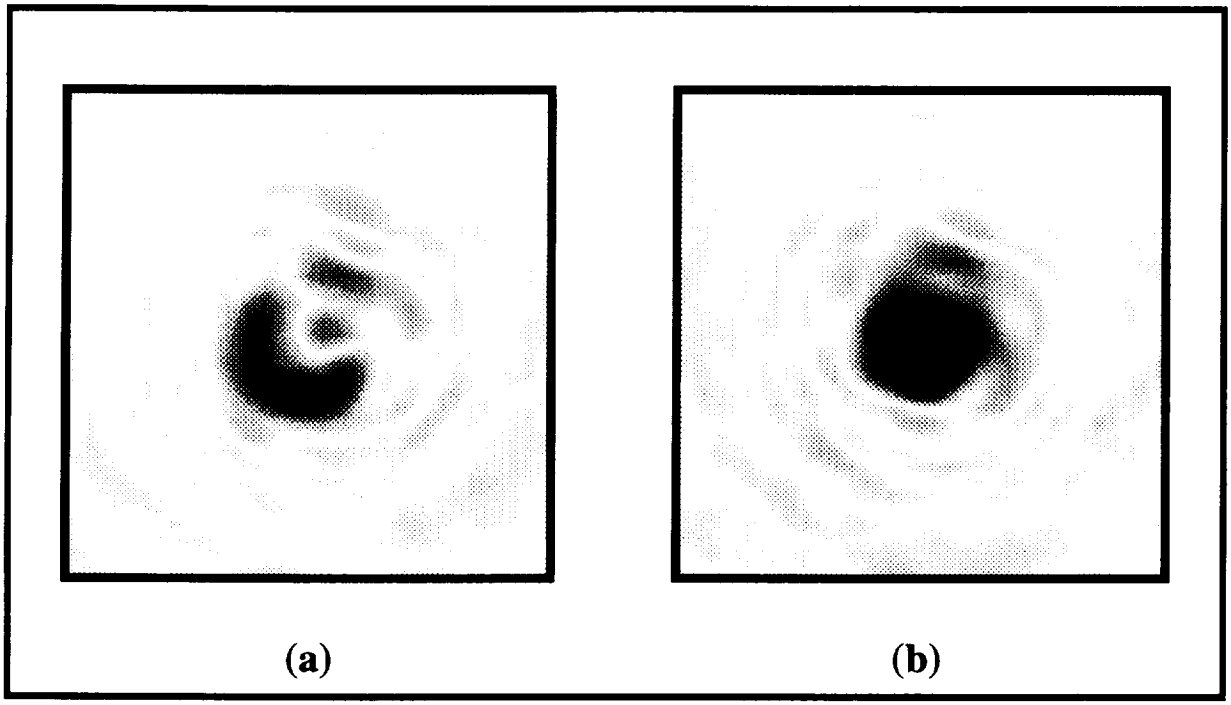

Figure 38. In-phase and quadrature parts of the pressure field at 4.9 MHz. Receiver plane images for composite path at Position 3 using the 5 MHz transducer for the (a) in-phase part of the pressure field and (b) quadrature part of the pressure field.

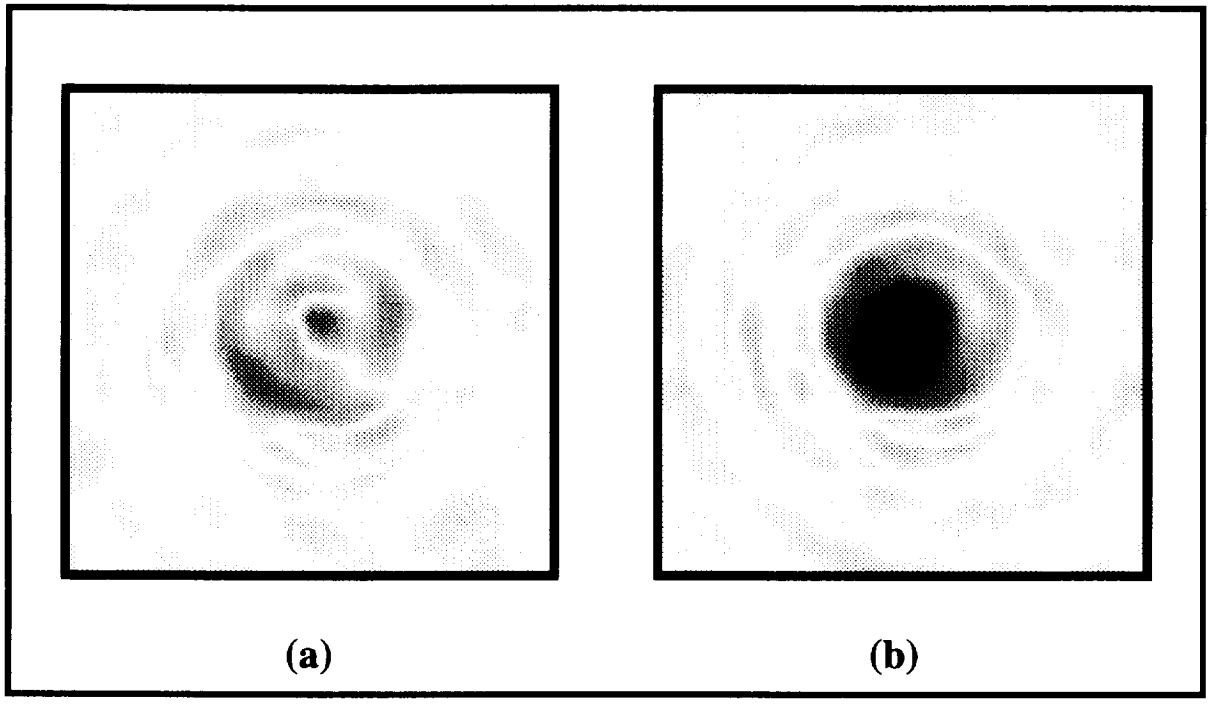

Figure 41. In-phase and quadrature parts of the pressure field at 4.9 MHz. Receiver plane images for composite path at Position 4 using the 5 MHz transducer for the (a) in-phase part of the pressure field and (b) quadrature part of the pressure field.

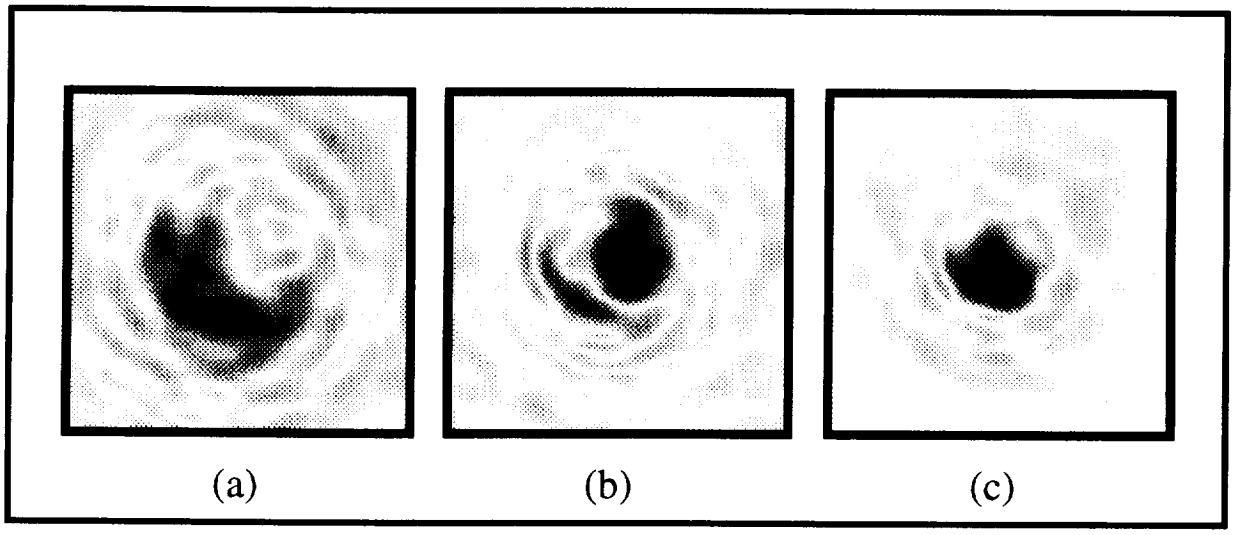

Figure 43. Receiver plane images of the in-phase part of the pressure field at Position 1 of the thin composite using the 5 MHz transducer. Images are shown for the frequencies: (a) 2.9 MHz, (b) 4.9 MHz, and (c) 7.1 MHz.

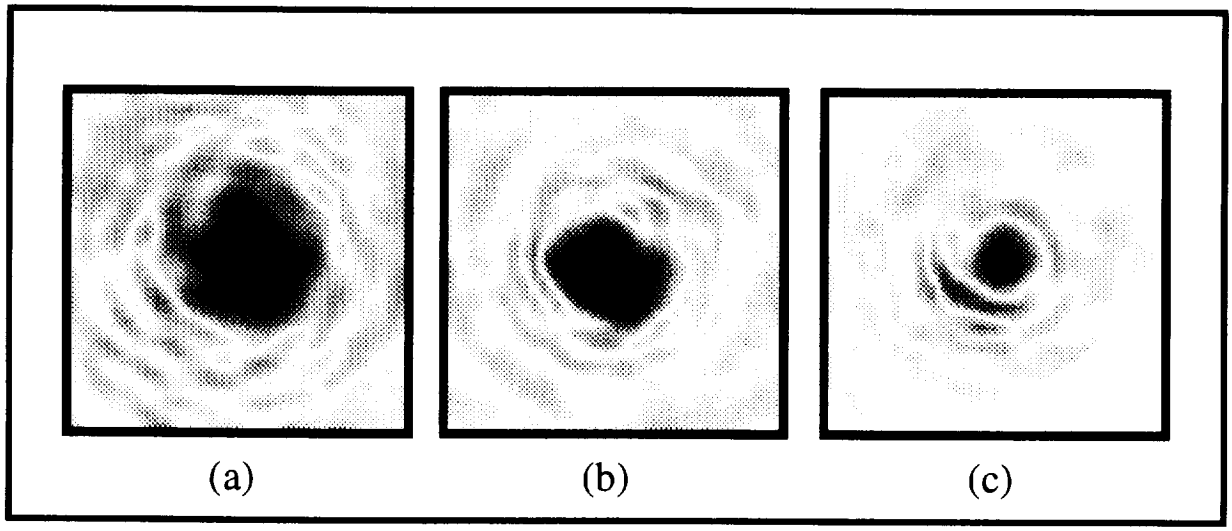

Figure 44. Receiver plane images of the quadrature part of the pressure field at Position 1 of the thin composite using the 5 MHz transducer. Images are shown for the frequencies: (a) 2.9 MHz, (b) 4.9 MHz, and (c) 7.1 MHz.

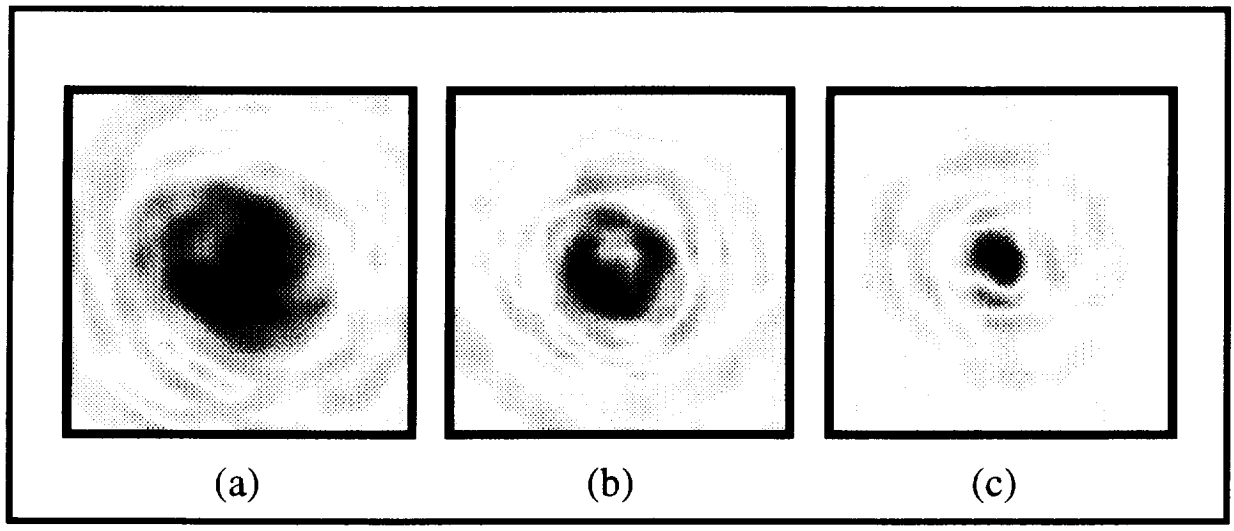

Figure 45. Receiver plane images of the in-phase part of the pressure field at Position 2 of the thin composite using the 5 MHz transducer. Images are shown for the frequencies: (a) 2.9 MHz, (b) 4.9 MHz, and (c) 7.1 MHz.

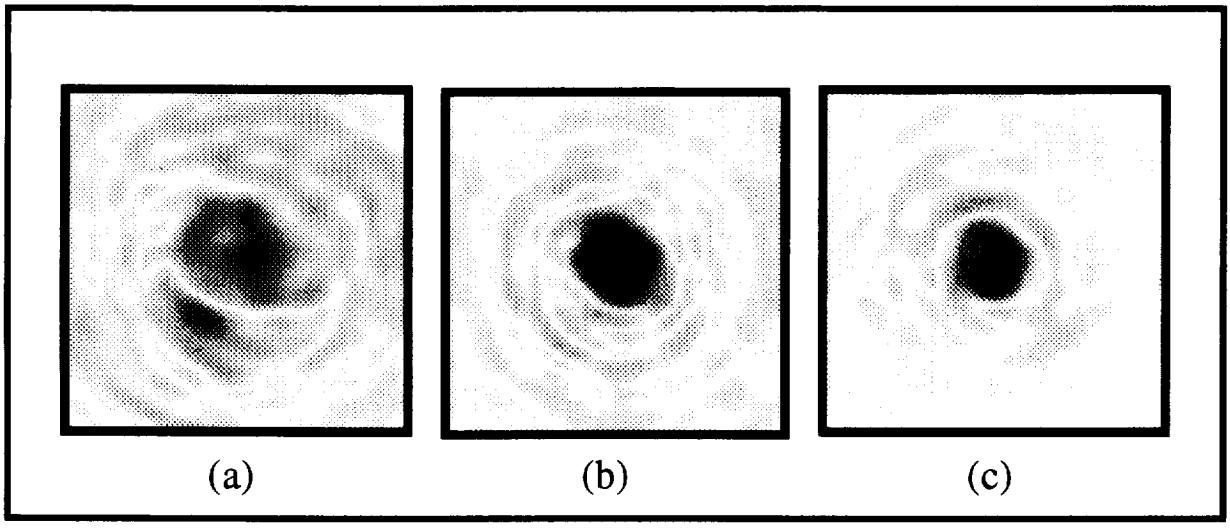

Figure 46. Receiver plane images of the quadrature part of the pressure field at Position 2 of the thin composite using the 5 MHz transducer. Images are shown for the frequencies: (a) 2.9 MHz, (b) 4.9 MHz, and (c) 7.1 MHz.

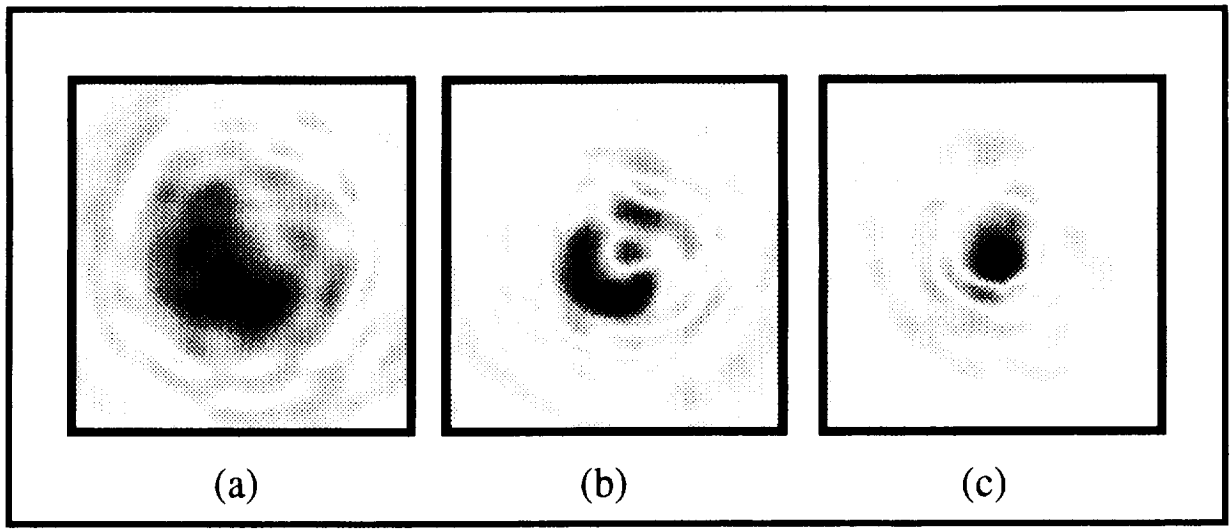

Figure 47. Receiver plane images of the in-phase part of the pressure field at Position 3 of the thin composite using the 5 MHz transducer. Images are shown for the frequencies: (a) 2.9 MHz, (b) 4.9 MHz, and (c) 7.1 MHz.

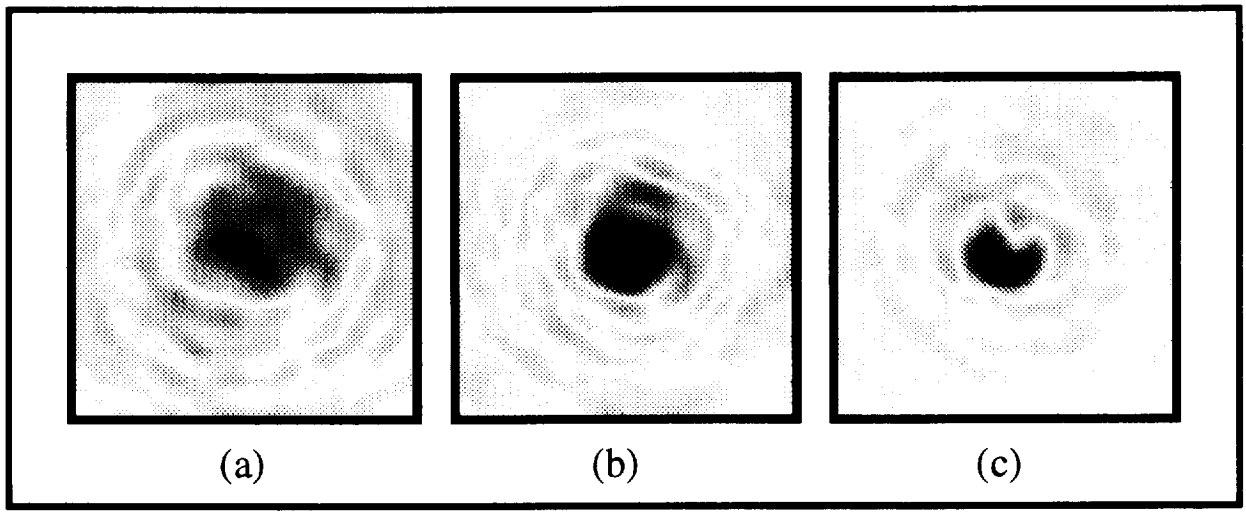

Figure 48. Receiver plane images of the quadrature part of the pressure field at Position 3 of the thin composite using the 5 MHz transducer. Images are shown for the frequencies: (a) 2.9 MHz, (b) 4.9 MHz, and (c) 7.1 MHz.

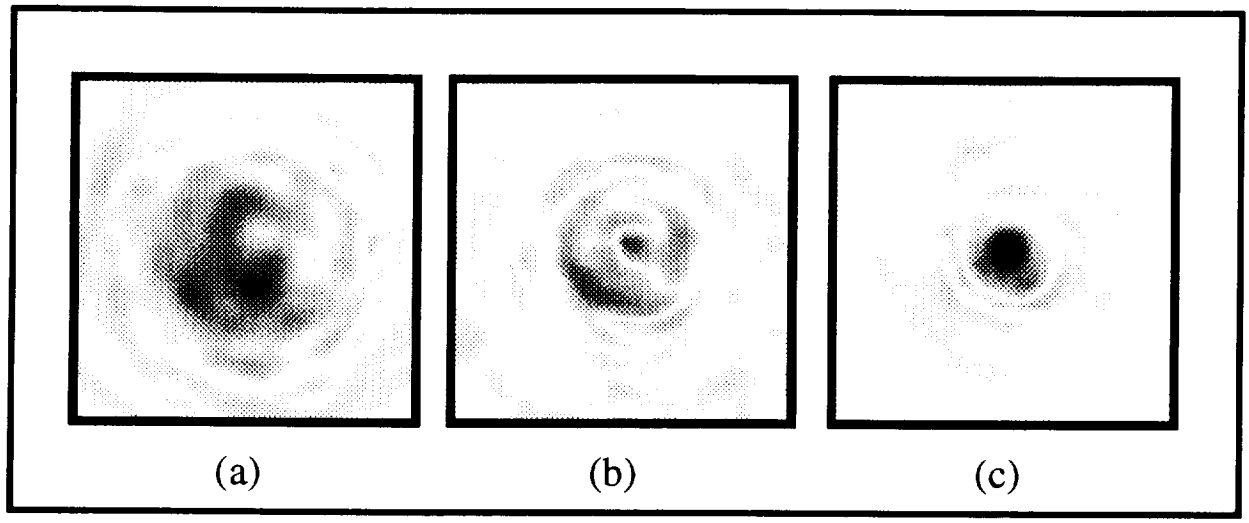

Figure 49. Receiver plane images of the in-phase part of the pressure field at Position 4 of the thin composite using the 5 MHz transducer. Images are shown for the frequencies: (a) 2.9 MHz, (b) 4.9 MHz, and (c) 7.1 MHz.

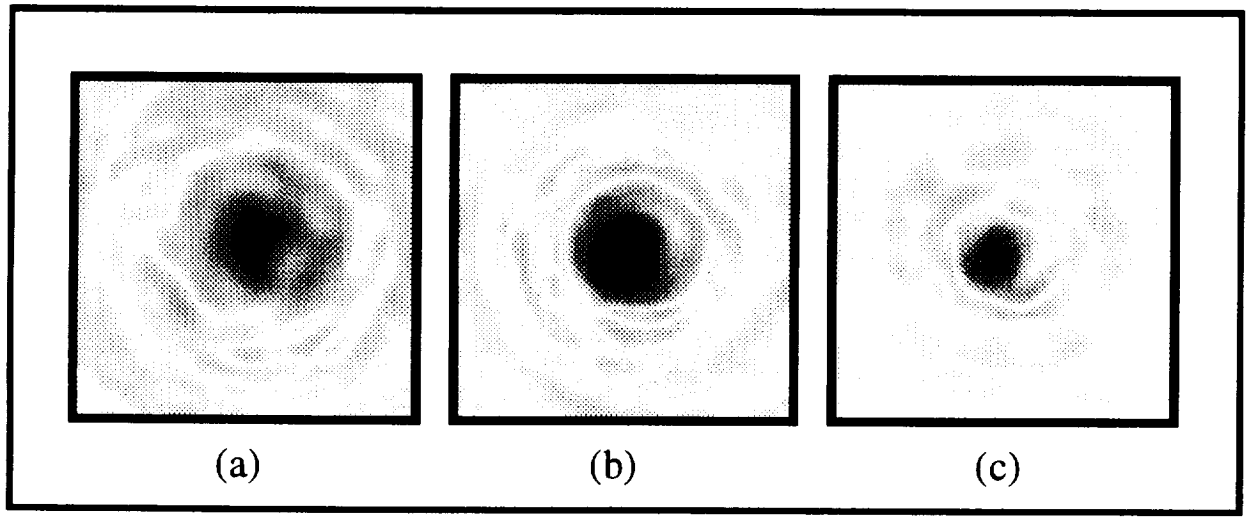

Figure 50. Receiver plane images of the quadrature part of the pressure field at Position 3 of the thin composite using the 5 MHz transducer. Images are shown for the frequencies: (a) 2.9 MHz, (b) 4.9 MHz, and (c) 7.1 MHz.

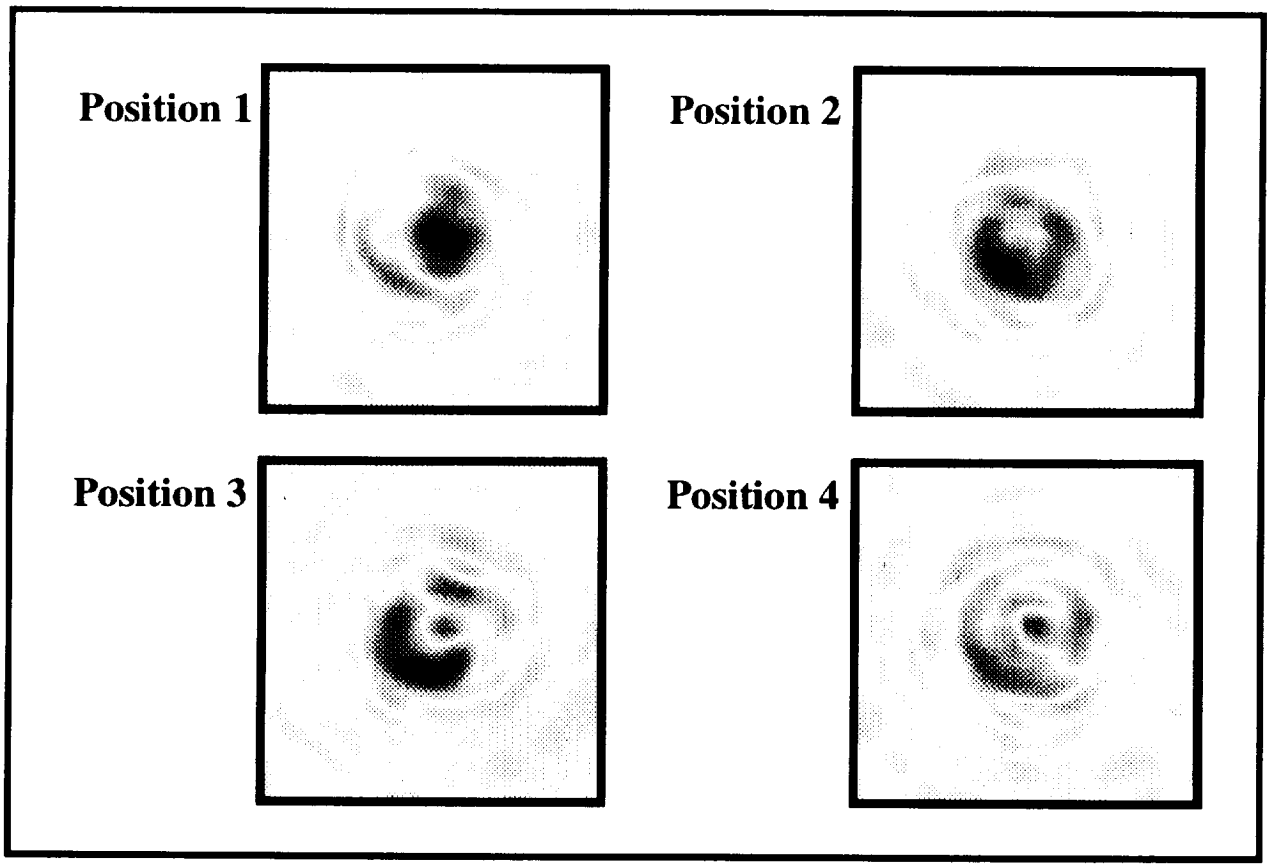

Figure 53. Receiver plane images of the in-phase part of the pressure field at 4.9 MHz are shown for the different scanned regions of the thin composite using the 5 MHz transducer.

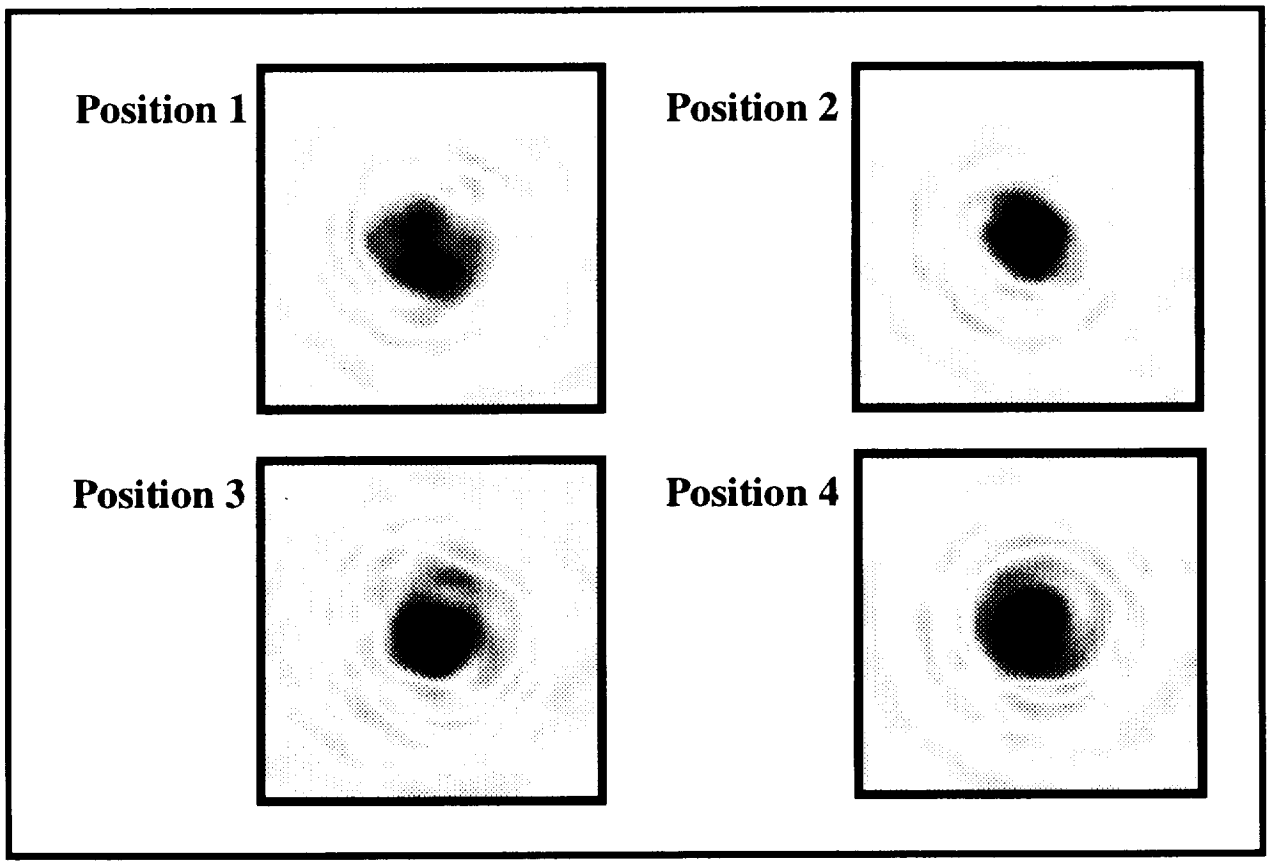

Figure 54. Receiver plane images of the quadrature part of the pressure field at 4.9 MHz are shown for the different scanned regions of the thin composite using the 5 MHz transducer.

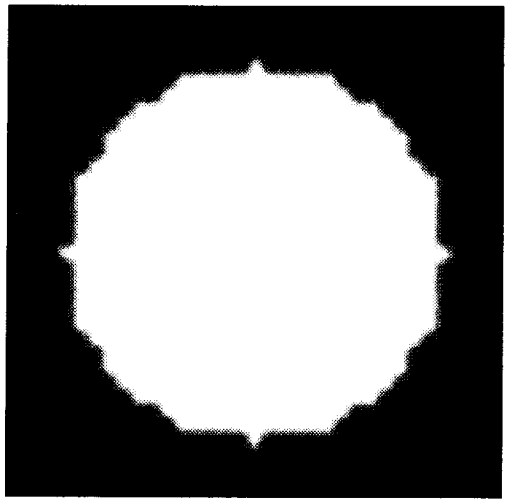

Figure 157. Footprint of simulated 0.5"-diameter receiver used for phase-sensitive and phase-insensitive apparent signal loss measurements.

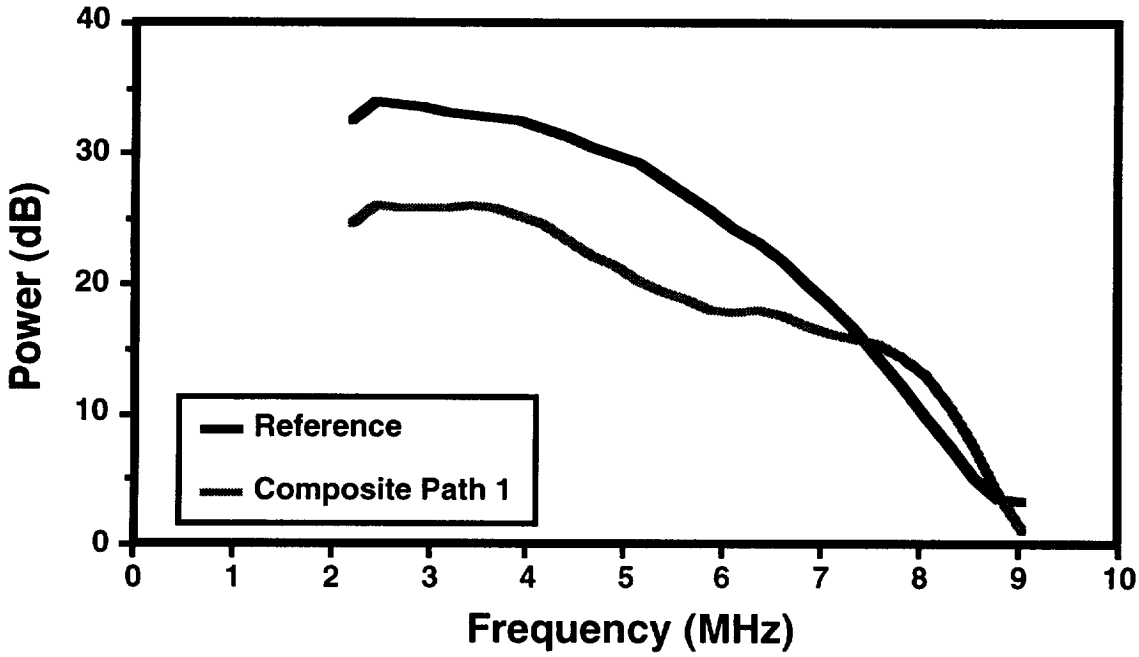

Figure 158. Phase-sensitive power spectra for reference path and region 1 of the thin woven composite using the 5 MHz transmitting transducer. These power spectra were determined by simulating a phase-sensitive receiver of the size shown in Figure 157.

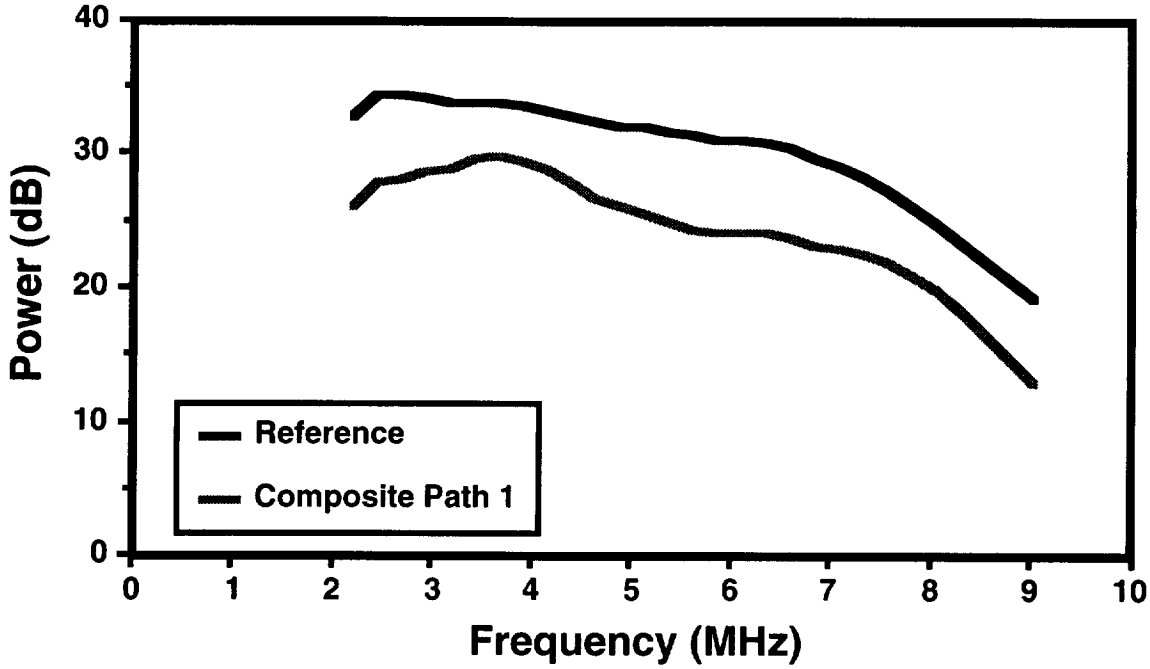

Figure 159. Phase-insensitive power spectra for reference path and region 1 of the thin woven composite using the 5 MHz transmitting transducer. These power spectra were determined by simulating a phase-insensitive receiver of the size shown in Figure 157.

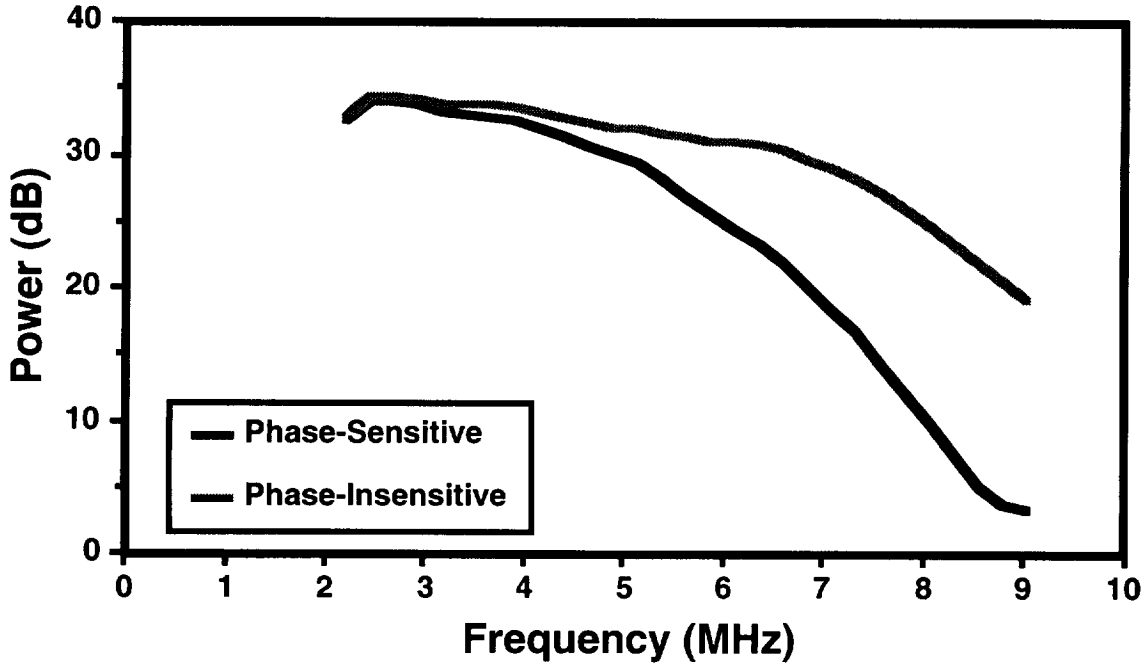

Figure 160. Phase-sensitive and phase-insensitive power spectra for the reference path using the 5 MHz transmitting transducer.

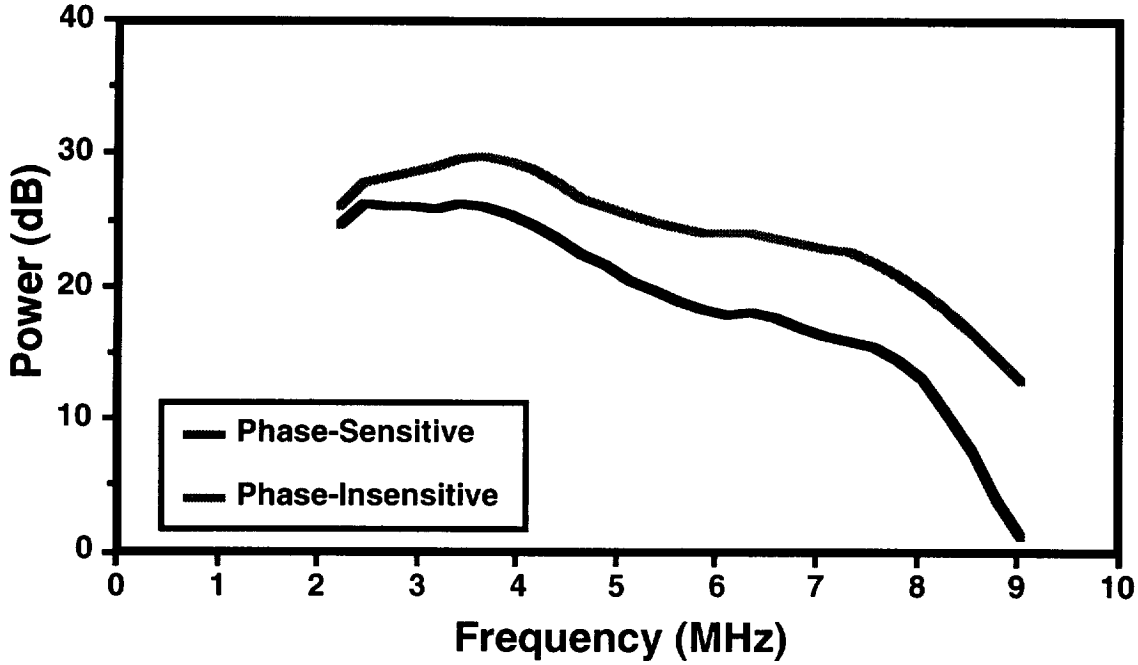

Figure 161. Phase-sensitive and phase-insensitive power spectra for the reference path using the 5 MHz transmitting transducer.

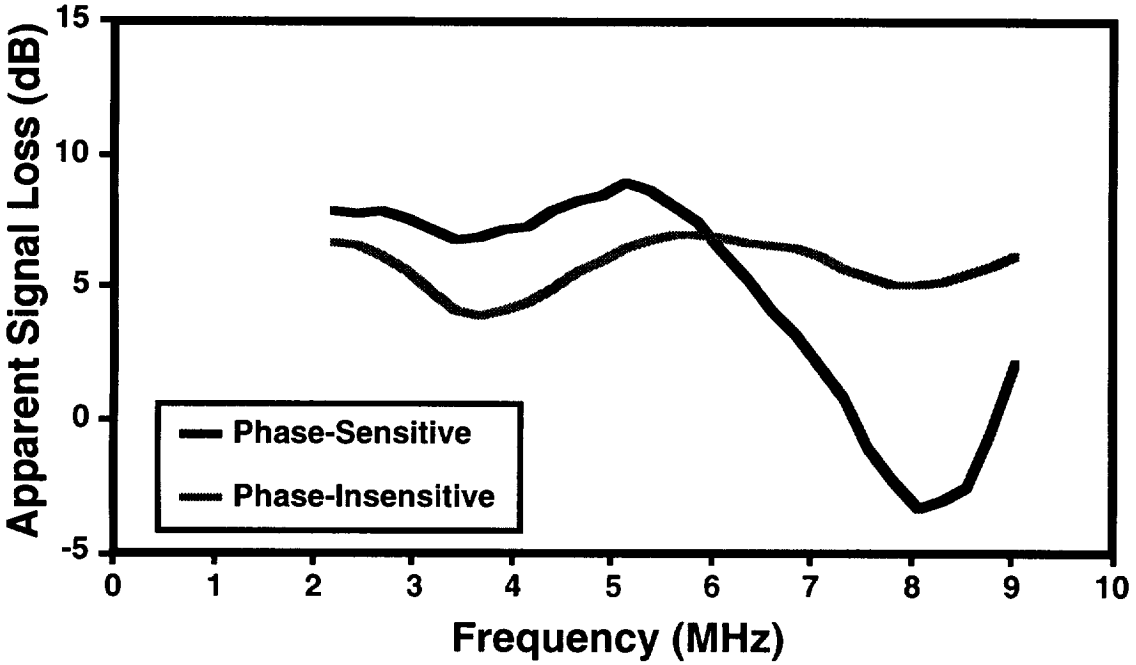

Figure 162. Phase-sensitive and phase-insensitive apparent signal losses for the region 1 of the thin woven composite using the 5 MHz transmitting transducer.

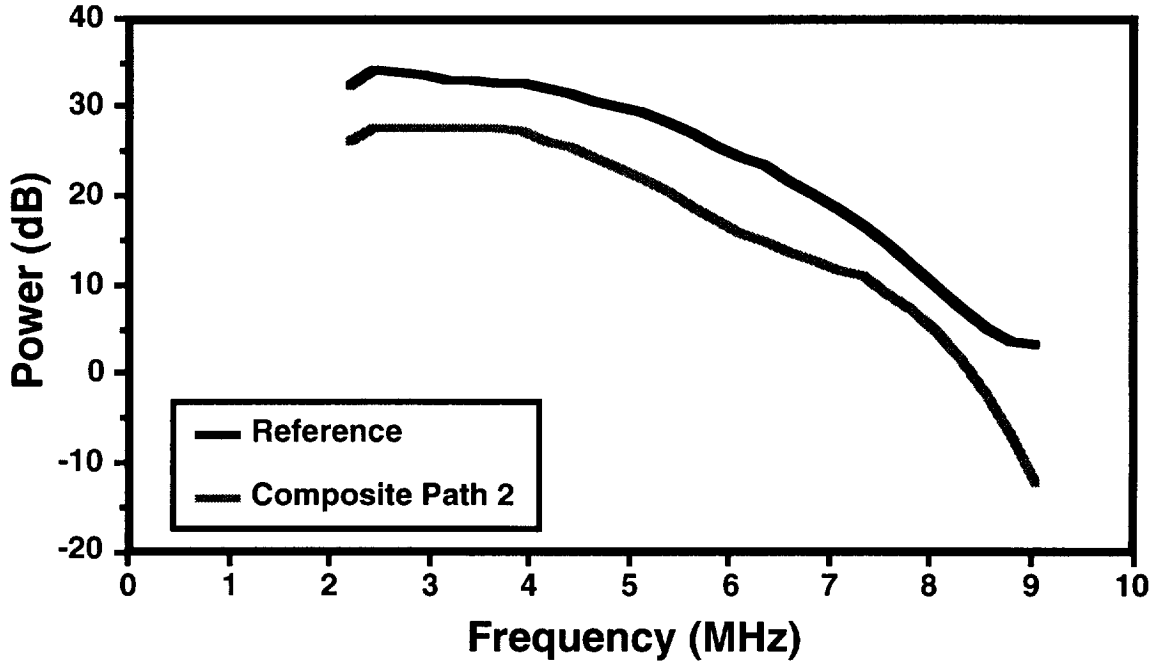

Figure 163. Phase-sensitive power spectra for reference path and region 2 of the thin woven composite using the 5 MHz transmitting transducer. These power spectra were determined by simulating a phase-sensitive receiver of the size shown in Figure 157.

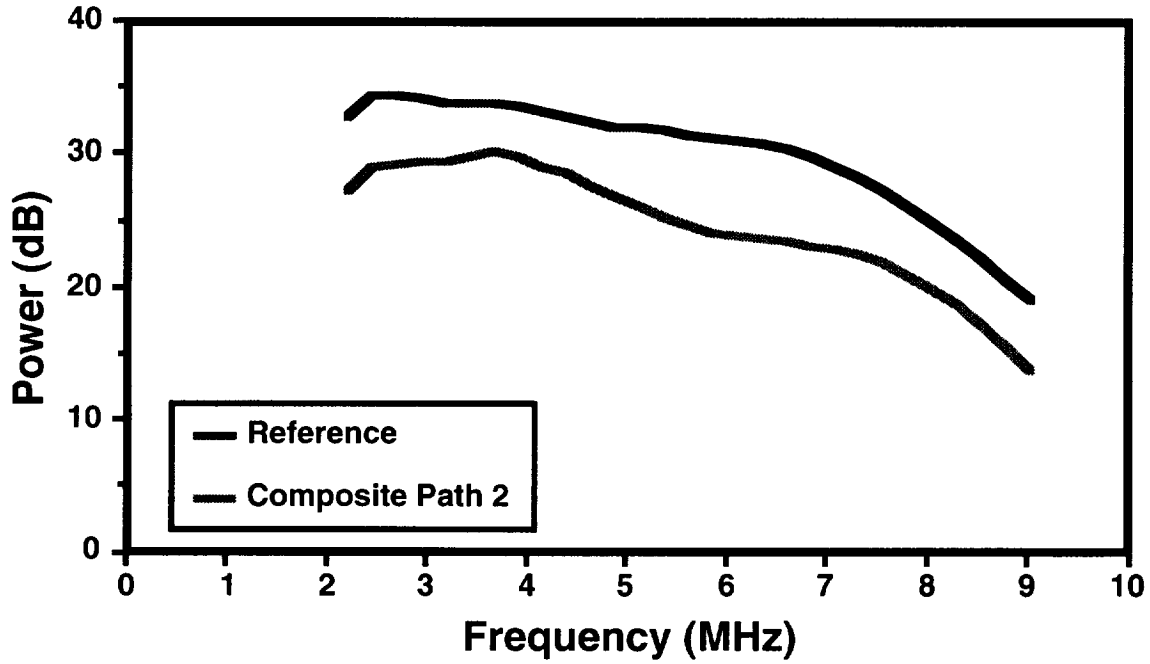

Figure 164. Phase-insensitive power spectra for reference path and region 2 of the thin woven composite using the 5 MHz transmitting transducer. These power spectra were determined by simulating a phase-sensitive receiver of the size shown in Figure 157.

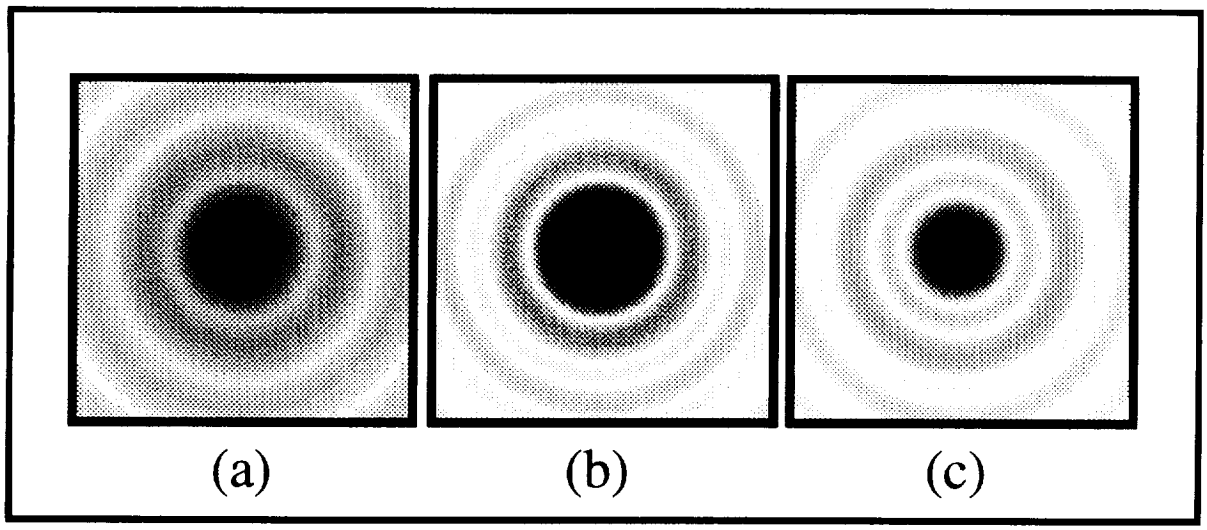

Figure 177. Images of (a) magnitude, (b) in-phase, and (c) quadrature parts of a simulated pressure field at 5 MHz transmitted along the reference path. These simulations illustrate the expected ring symmetry to be found in all images.

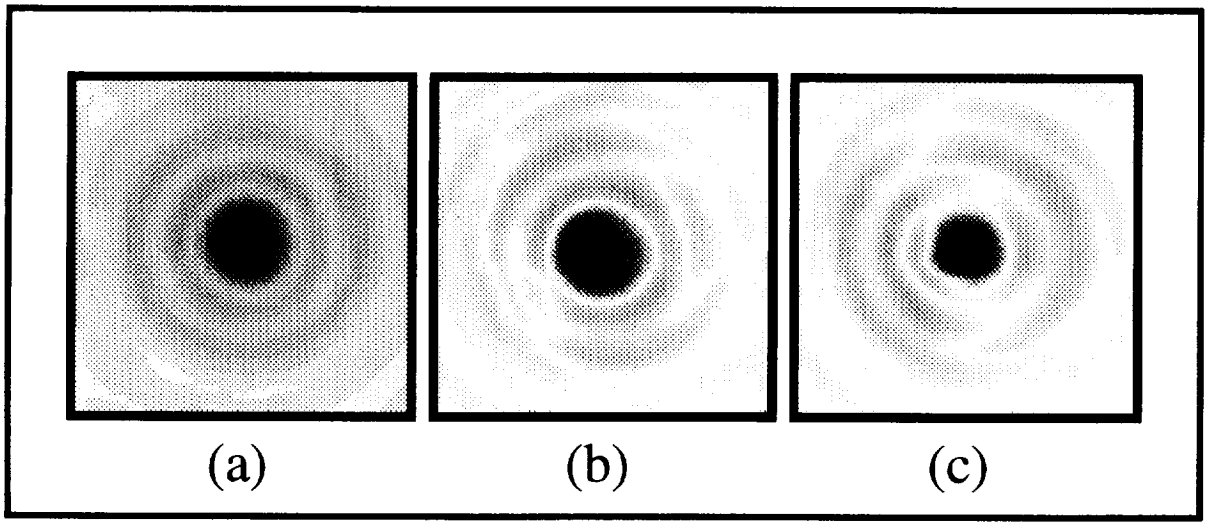

Figure 178. Images of (a) magnitude, (b) in-phase, and (c) quadrature parts of the pressure field at 7 MHz transmitted along the reference path. Note, in general, the expected circular symmetry in each image.

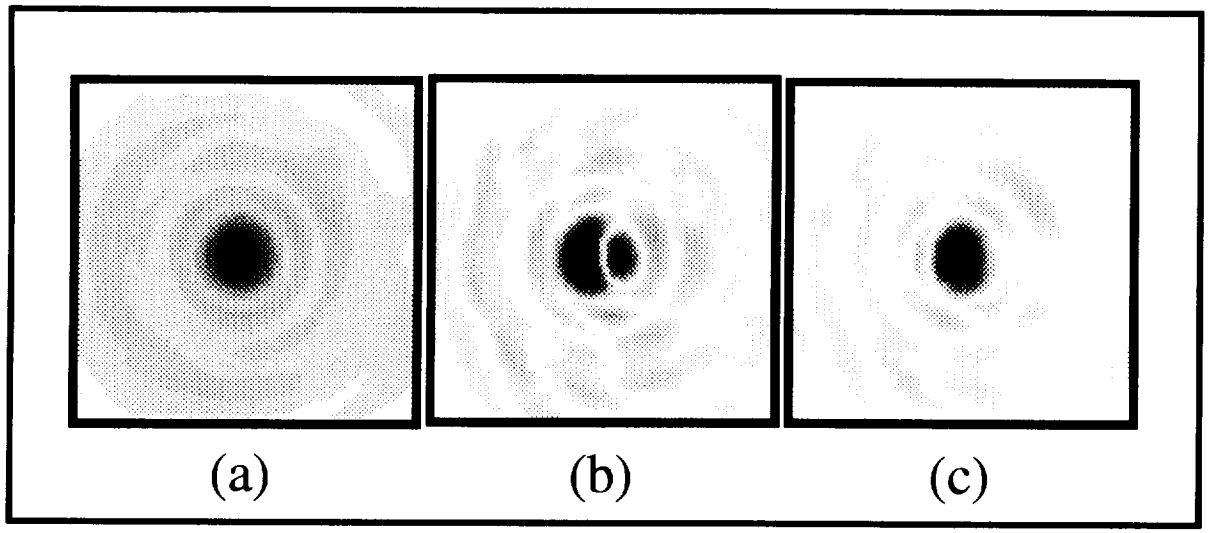

Figure 179. Images of (a) magnitude, (b) in-phase, and (c) quadrature parts of the pressure field at 8 MHz transmitted through the reference path. Note the rapid variation of the in-phase signals within the center of the in-phase image. This asymmetry does not readily appear in the magnitude images.

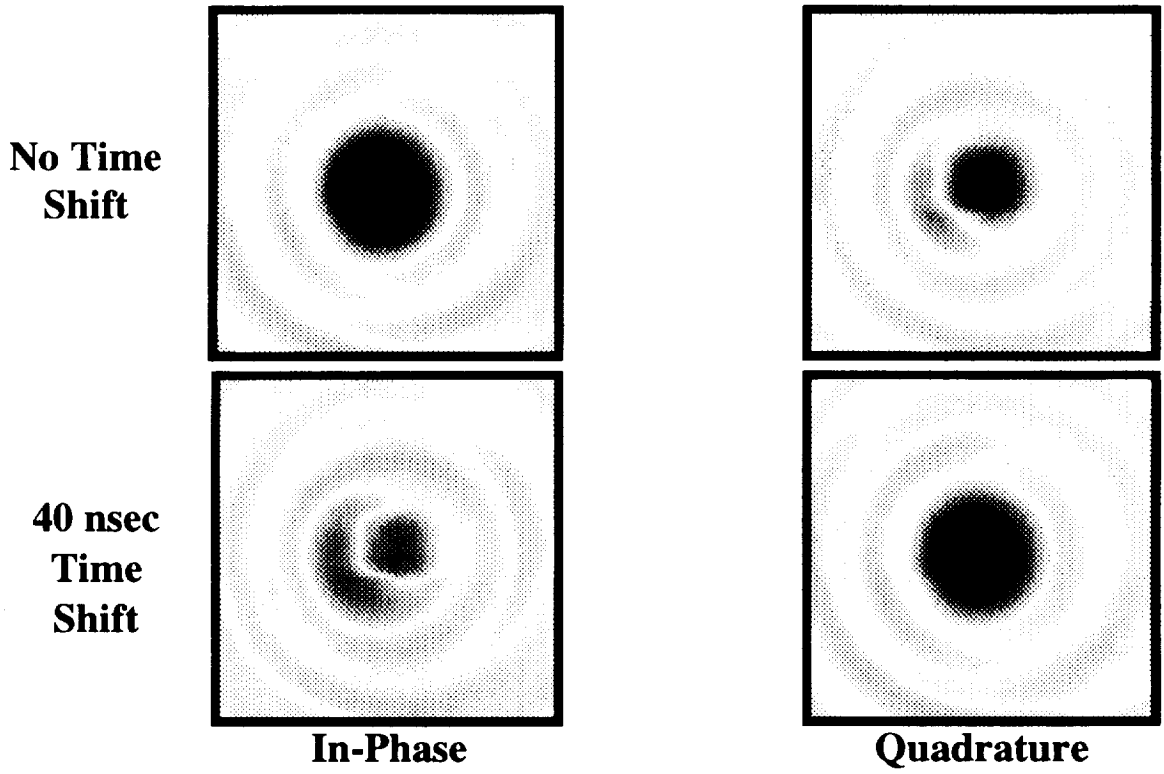

Figure 180. Comparison of in-phase and quadrature images for 5 MHz pressure field for reference path with the original time-domain pressure data (i.e., no time shift) and the time-domain pressure data shifted forward in time by 40 nsec.

V. Dependence of Complex Pressure on Transducer f-number for Ultrasonic Measurements of a Woven Cloth (December 1997 to June 1998)

In this final section, we compare apparent signal loss measurements of the thin woven composite using phase-sensitive and phase-insensitive detection methods. This section presents experimental results that support successful implementation of single element as well as one and two-dimensional ultrasonic array technologies for the inspection of textile composite structures. In previous reports[1-3], we have addressed issues regarding beam profiles of ultrasonic pressure fields transmitted through a water-only path and transmitted through a thin woven composite sample. We presented experimental results of the effect of a thin woven composite on the magnitude and phase (real and imaginary parts) of an insonifying ultrasonic pressure field. In addition, we considered the effect of phase cancellation at the face of a finite-aperture, piezoelectric receiver.

In our continuing effort to understand the effects that variations of physical parameters of the experimental system have on material property measurements, we investigate the role of the f-number (ratio of the focal length to the diameter) of the transmitting transducer in experimental measurements. As in previous reports, we consider issues relevant to the application of single-element, one-dimensional, and two-dimensional array technologies towards probing the mechanical properties of advanced engineering composites and structures. We provide comparisons between phase-sensitive and phase-insensitive detection methods for determination of textile composite structure parameters. We also compare phase-sensitive and phase-insensitive apparent signal loss measurements in an effort to study the phenomenon of phase cancellation at the face of a finite-aperture, single-element, piezoelectric receiver. Furthermore, we extend our work on ultrasonic beam profile issues through investigation of the effects of focusing planar pseudo-array measurements.

In Section V.A of this Progress Report we briefly describe the experimental arrangement and methods for data acquisition of the ultrasonic diffraction patterns upon transmission through a

thin woven composite. Section V.B details the analysis of the experimental data and modeling simulations, and is followed by the experimental and simulation results in Section V.C. Finally, a discussion of the observations and conclusions are found in Section V.D and Section V.E, respectively.

A. Experimental Arrangement and Methods

A.1 Thin Woven Composite

The thin composite studied was a five-harness biaxial weave cloth (a single layer) set in an epoxy. The tow and fill bundles of the cloth were approximately 2 mm in height. Finally, the mean thickness of the cloth was on the order of 0.5 mm.

A.2 Measurement Methods

All measurements in this study were performed in a water tank using two types of piezoelectric transducers with nominal center frequencies of 5 MHz (Panametrics V309) as the transmitting transducer. Either an f/4 (0.5"-diameter, 2" focal length) or an f/8 (0.5"-diameter, 4" focal length) transducer was used for the measurements. The thin woven composite was positioned in the focal plane of the transmitting transducer and oriented normal to the beam axis of the transducer. A lead tape marker was affixed to the composite for position recognition purposes. A 0.5 mm diameter PVDF, broadband, needle hydrophone (Force Institute, Type MI1648) was used as the receiving transducer. A series of scans (C-scan, line scan, pseudo-array scan) were performed on the composite with each transmitting transducer (f/4 and f/8). A corresponding scan of a reference water path was also performed for each measurement of the composite.

A C-scan of the thin woven composite was performed for determination of the region interrogated in the pseudo-array measurements. The positions of the transmitting transducer and

receiving hydrophone were under motion control while the composite remained stationary. For the case of the f/8 transmitting transducer, the receiving hydrophone was positioned on the axis of and 20 mm beyond the focal plane of the transmitting transducer. For the case of the f/4 transmitting transducer, the receiver was again positioned on the axis of the transmitting transducer and 20 mm beyond the composite plane. However, the transmitting transducer was positioned 2.5" from the front face of the composite. (This positioning was chosen for alignment concerns of the pseudo-array measurements in addition to a physical constraint of the gantry apparatus.) In each case, the front side of the composite was positioned in the focal plane of the transmitting transducer. The C-scan consisted of 50 sites by 50 sites with 1 mm site separation to insure coverage of the lead tape marker, portions of the sample mounting apparatus, and the region to be investigated during the pseudo-array measurements. In addition to its position recognition purpose, the C-scan also served as an additional measurement of the apparent signal loss of the thin woven composite.

The experimental setup was modified for the line scan and pseudo-array scan that was performed with each type of transmitting transducer (f/4 and f/8). The transmitting transducer was fixed with respect to the experimental setup while the composite and the receiving hydrophone were under computer control with one degree of motion and three degrees of motion, respectively. It was necessary to perform a line scan of the composite to determine the region of the composite insonified during the pseudo-array measurements. The hydrophone was positioned 20 mm behind the focal plane of the transmitting transducer for both the f/4 and f/8 transmitting transducers. With the positions of the transmitting transducer and receiving hydrophone fixed, the composite was translated in the horizontal direction perpendicular to the transmitter-receiver axis during the line scans. For the pseudo-array measurements, the hydrophone sampled the ultrasonic pressure field in a two-dimensional array composed of 65 sites by 65 sites (4225 total sites) with 0.25 mm separation between adjacent sites for a total sampled area of 16 mm by 16 mm.

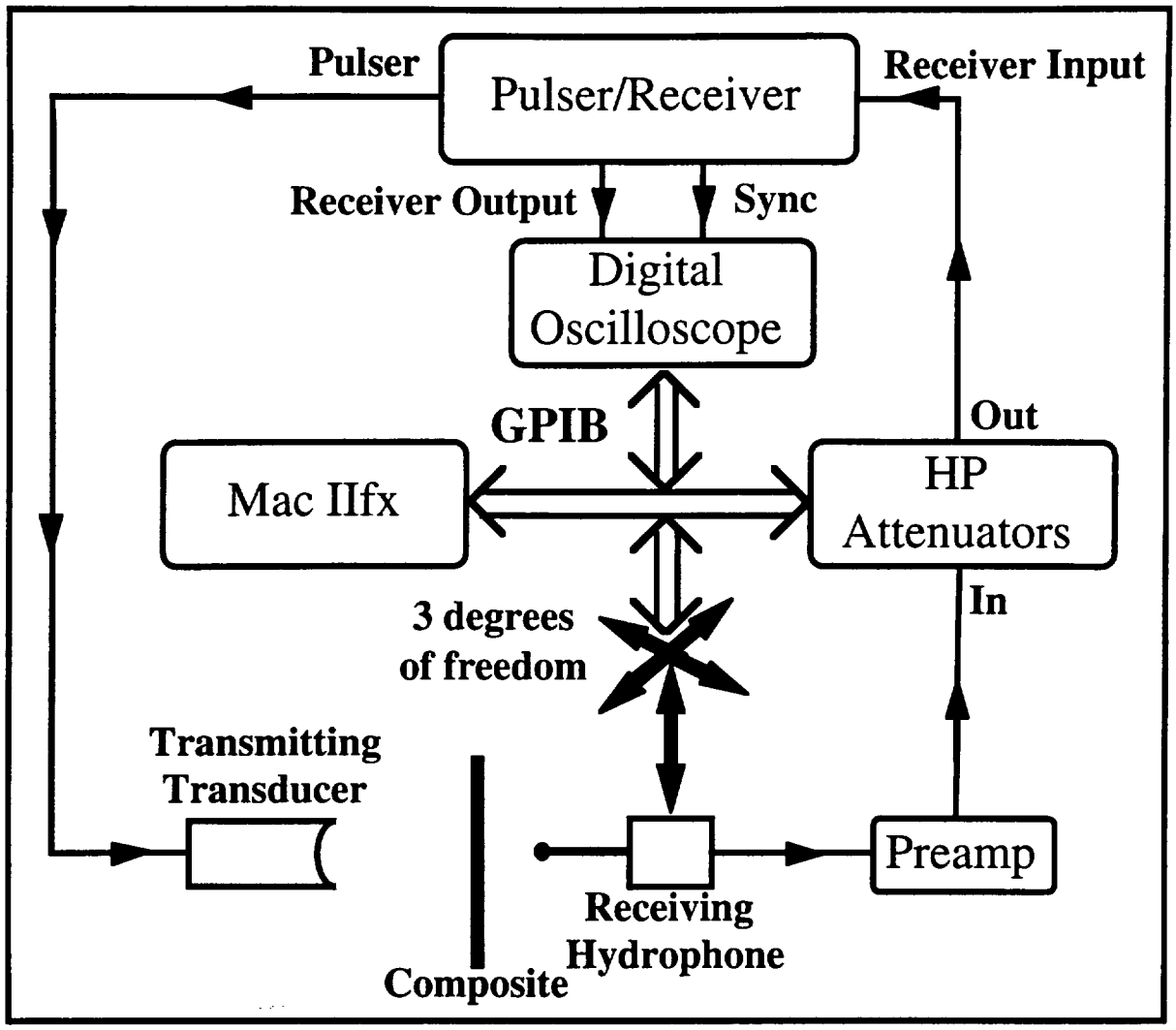

Figure 1. Experimental setup. This figure represents the equipment arrangement for the pseudo-array scans of the thin woven composite. Note that the one degree of freedom for the composite is not detailed. For the C-scan setup, the motions of the transmitter and receiver are synchronized and have three degrees of freedom.

Figure 1 is a schematic diagram showing the data acquisition system used in this investigation. For further details regarding the experimental arrangement and data acquisition protocol please refer to Section II of the previous Progress Reports which are included in the CD-ROM version of this report.

B. Data Analysis and Modeling

Following a brief description of the software utilized, we describe the data reduction techniques for analysis of the C-scan and pseudo-array measurements. We then discuss a model for spherically focusing an ultrasonic field as seen by a two-dimensional planar array. We conclude this section with the procedure for determination of the apparent signal loss due to the composite.

B.1 Software

Data analyses and visualization were performed on a Power Macintosh using in-house custom software written in the C programming language in conjunction with a commercial imaging software package (Transform 3.3, Fortner Software, Sterling, VA), a commercial data management package (Noesys 1.2, Fortner Software, Sterling, VA) and a commercial graphing package (IGOR 3.12, WaveMetrics, Lake Oswego, OR).

B.2 C-Scan Measurement Analysis

For the C-scan measurements, the time-averaged rf trace acquired at each site was Fast Fourier Transformed to determine the spectral content of the time-domain rf trace. The power spectrum was calculated at each site of the two-dimensional C-scan as well as for a water path reference trace. Apparent signal loss was determined using a log spectral subtraction technique. For each transmitting transducer data set, the average apparent signal loss was calculated at three distinct frequencies (3 MHz, 5 MHz, and 7 MHz).

B.3 Pseudo-Array Measurement Analysis

For the two-dimensional pseudo-array scans, the time-averaged rf trace acquired at each pseudo-array site was Fast Fourier Transformed to determine the spectral content of the time-

domain rf trace. Discrete frequency data were extracted from the real and imaginary parts of Fourier transform of the broadband rf trace to provide a single-frequency representation of the respective parts of the pressure field. The magnitude of the Fourier transform was calculated by taking the square root of the sum of the squares of the real and imaginary parts of the Fast Fourier Transform.

For both the f/4 and f/8 transducers, we acquired two sets of data (one water path and one composite path) as mentioned above. For each transmitting transducer data set, single-frequency image analysis was performed at three distinct frequencies. We calculated the magnitude, real, and imaginary parts of the pressure field near 3 MHz, 5 MHz, and 7 MHz.

B.3a Magnitude Image Construction

Image construction of the experimentally measured single-frequency magnitude of the ultrasonic pressure field was performed using Transform 3.3. For the magnitude images, the entire measured region (65 sites by 65 sites, i.e., 16 mm by 16 mm) of the pseudo-array appears. All magnitude of the pressure field images are presented using the grayscale mapping shown in Figure 2. Darker regions correspond to larger relative pressure magnitudes and lighter regions correspond to smaller relative pressure magnitudes. The images were not interpolated as in previous reports due to the improved resolution of the receiving system compared to previous data acquisitions. Figure 3 shows a representative pressure magnitude image with relevant dimensions.

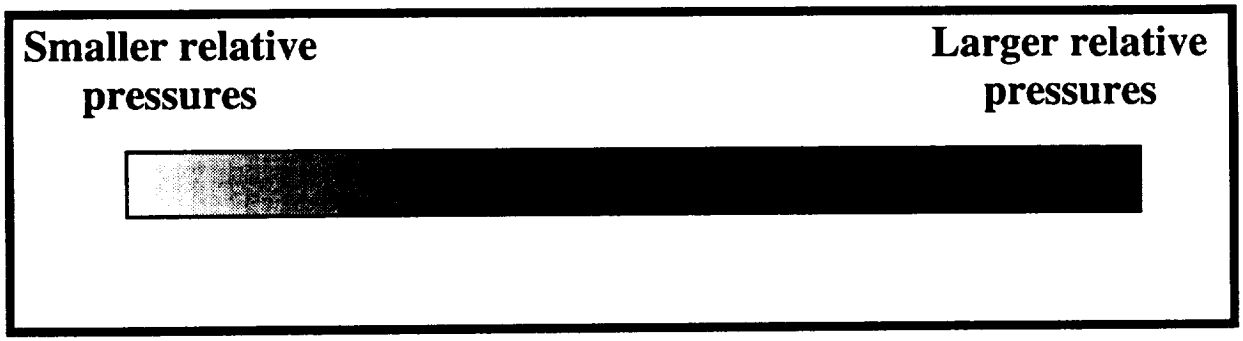

Figure 2. Grayscale mapping used for pressure magnitude images.

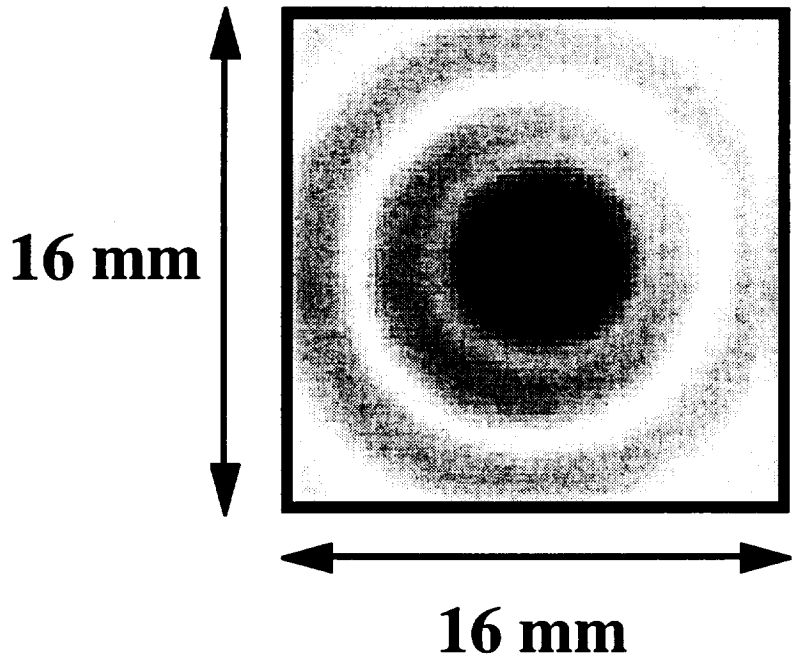

Figure 3. Representative pressure magnitude image of an ultrasonic pressure field propagated along a water path.

B.3b Real and Imaginary Image Construction

Image construction of the experimentally measured single-frequency real and imaginary parts of the ultrasonic pressure field was also performed using Transform 3.3. All images of the real and imaginary parts of the pressure field are presented using the color mapping shown in Figure 4. Red regions correspond to positive values, blue regions correspond to negative values, and white corresponds to neutral values. The particular mapping was chosen so as to emphasize the mixing of positive and negative values of real and imaginary signals over a spatial region. Similar to the pressure magnitude images, the entire region of the pseudo-array appears and no interpolation of the image was performed. Figure 5 shows representative real and imaginary images for a reference path signal. Please note that in previous reports we have referred to the real and imaginary parts of the pressure field as the in-phase and quadrature fields.

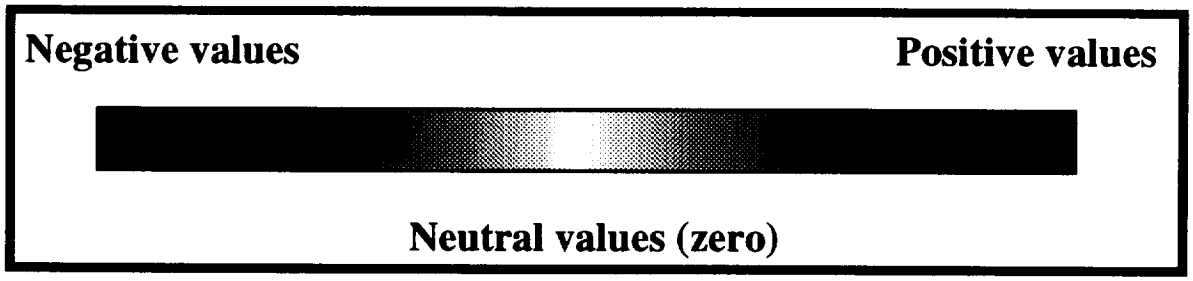

Figure 4. Colorscale mapping used for real and imaginary images.

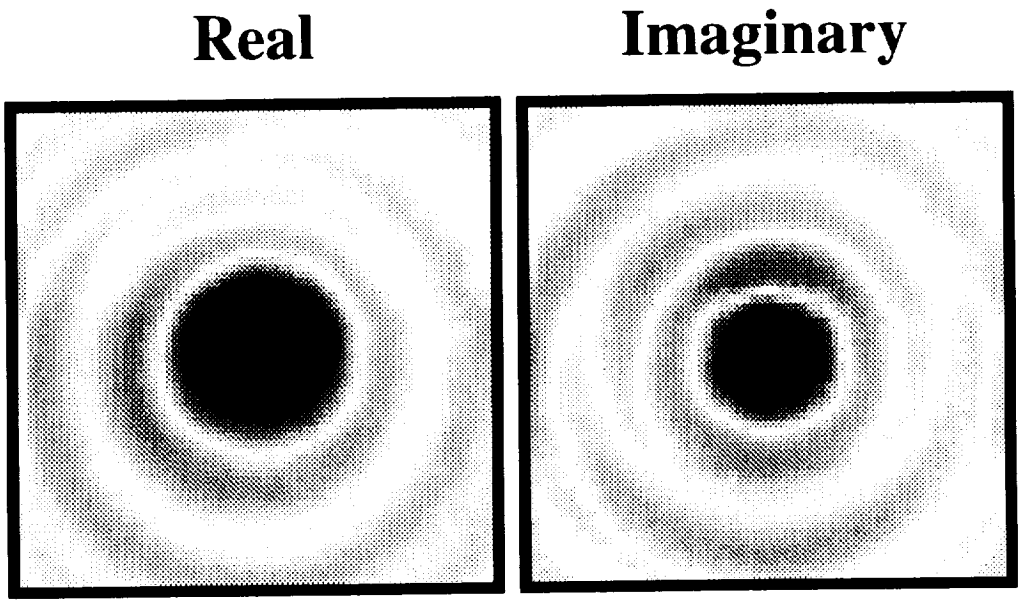

Figure 5. Representative (a) real and (b) imaginary images of an ultrasonic pressure field propagated along a water path.

B.4 Focusing of Planar Array Measurements

In each of the previous reports[1-3], we have measured or modeled ultrasonic fields as seen specifically by a two-dimensional planar array. We extend our investigation of ultrasonic beam profiles through the spherical focusing of modeled ultrasonic fields propagated toward a plane perpendicular to the direction of propagation. As in previous reports[1,2], we model the propagation of ultrasonic fields in water using an angular spectrum-based approach. We examine the 5 MHz ultrasonic field generated by an f/4 (0.5" diameter, 2" focal length) transducer and an f/8 (0.5" diameter, 4" focal length) transducer. In each case, the field is propagated a distance twice the focal length of the transducer. The simulation consisted of a 512 by 512 array with 0.25 mm site separation. The spatial extent of the simulation prevented possible source replication artifacts in the region of interest. The central 63 by 63 array sites (our region of interest) were extracted for

visualization of the real and imaginary parts of the propagated field. This choice of region is comparable to the array size employed during the pseudo-array measurements.

Spherical focusing of the two-dimensional pseudo-array was achieved by applying the appropriate time delays (via the Fourier shift theorem) to the simulated ultrasonic field at each position in the array in order to focus at a point a distance of one focal length from the center position of the array on a line perpendicular to the plane of the array. These time delays were determined by calculating the difference between the time-of-flight of an ultrasonic field in water from each element in the array to the focal point and the time-of-flight of an ultrasonic wave from the center array element position to the focal point. Figure 6 schematically illustrates the geometry used in the determination of the appropriate time shifts used for spherical focusing. In this figure, D represents the distance between the center position in the array and the desired focal point along a line perpendicular to the plane of the array (D = 2" for the f/4 simulation, D = 4" for the f/8 simulation). The distance between the (m, n) position in the array and the center position is represented by r_{mn}.. The distance between the (m, n) position in the array and the focal point, represented by R_{mn}, is determined from

$$R_{mn} = \sqrt{r_{mn}^2 + D^2}\,. \tag{1}$$

The difference, Δd_{mn}, in the distance between the (m, n) array position and the focal point and the center array position and the focal point is found from

$$\Delta d_{mn} = R_{mn} - D = \sqrt{r_{mn}^2 + D^2} - D\,. \tag{2}$$

The time shift, Δt_{mn}, required to focus an ultrasonic field at a given array element (m, n) at the desired focal point is expressed as

$$\Delta t_{mn} = \frac{\Delta d_{mn}}{c} = \frac{\sqrt{r_{mn}^2 + D^2} - D}{c}, \tag{3}$$

where c is the velocity of ultrasound in water. The shifts applied to spherically focus the two-dimensional array are graphically represented in Figure 7.

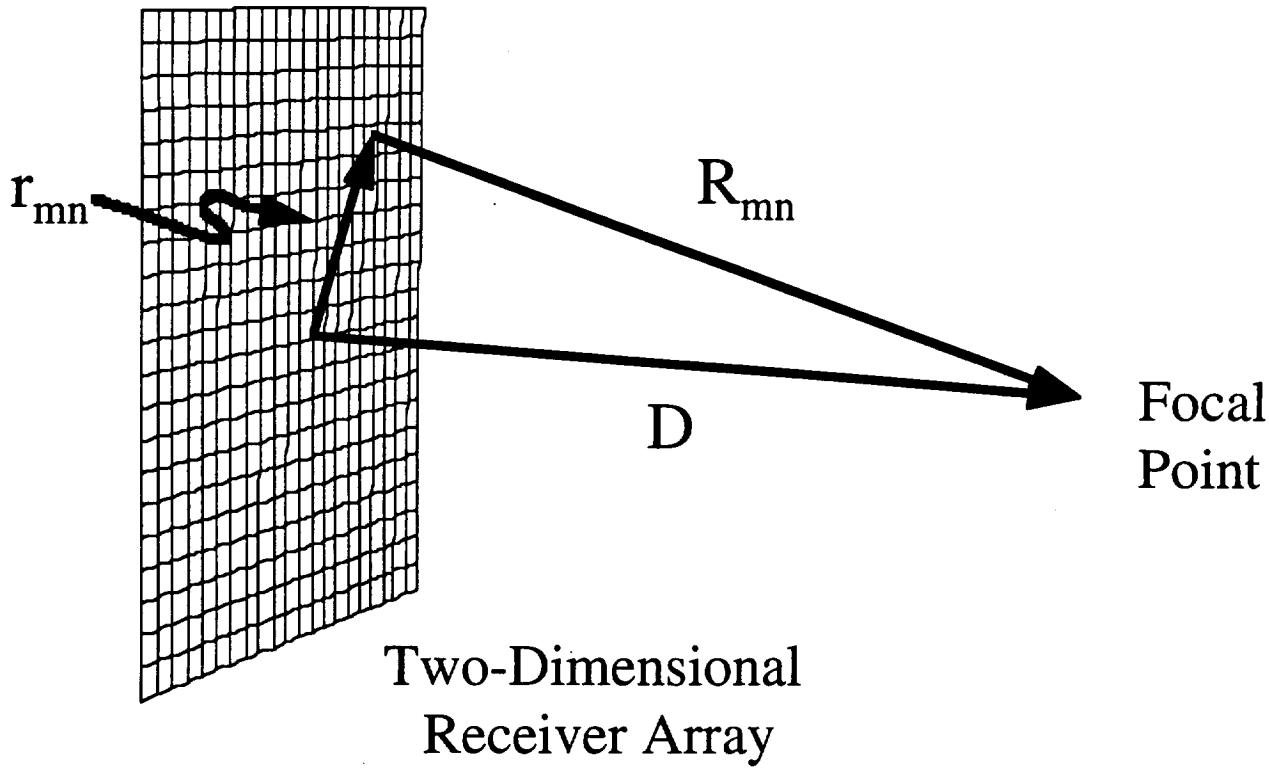

Figure 6. Geometry used in the determination of the time shifts to be used for spherical focusing.

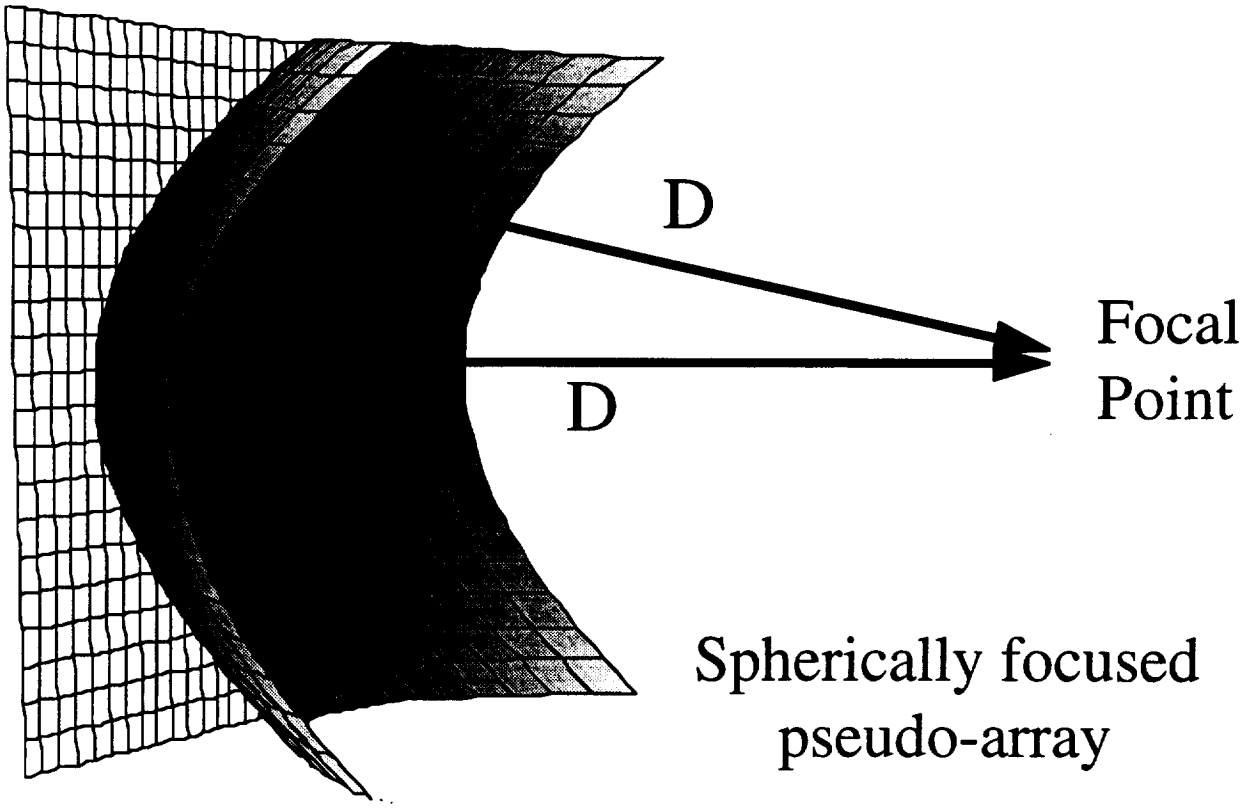

Figure 7. Three dimensional graphical representation of time shifts for spherical focusing.

B.5 Apparent Signal Loss Analysis

Extending our qualitative analysis of the magnitude, real, and imaginary images constructed from the pseudo-array measurements, we calculate the apparent signal loss of the ultrasonic pressure field due to transmission through the thin woven composite. The apparent signal loss calculations have not taken into account diffraction corrections or transmission losses.

We calculate the apparent signal loss by two approaches.[4-10] The first method simulates the two-dimensional pseudo-array as a 0.5"-diameter *phase-sensitive* planar receiver. In this case, the receiver is sensitive to the phase of the pressure field. The second method uses the pseudo-array to simulate a 0.5"-diameter *phase-insensitive* planar receiver. In contrast to a phase-sensitive receiver, a phase-insensitive receiver is not sensitive to the phase of the pressure field but instead is sensitive to the magnitude or energy of the pressure field. For the present case,

we will always be considering a phase-insensitive receiver that is sensitive to the energy (power) of the pressure field (i.e., an acoustoelectric-like receiver[6,11,12]). For further details of the apparent signal loss calculation, please refer to the previous report.

C. Results

The organization of the C-scan and pseudo-array receiver plane images generally follows the outline of the Data Analysis and Modeling section. Figure 8 and Figure 9 compare the C-scan measured apparent signal losses at 3 MHz, 5 MHz, and 7 MHz for both the f/4 and f/8 transmitting transducers, respectively. Figure 10 depicts a typical region interrogated during the hydrophone pseudo-array measurements. We compare the magnitude, real, and imaginary parts of the ultrasonic fields (3 MHz, 5 MHz, and 7 MHz) measured by the hydrophone pseudo-array when propagated through a water path only and a water path with the thin woven composite inserted (composite path). Figure 11 through Figure 13 are the comparisons for the f/4 transducer data, and Figure 14 through Figure 16 are the comparisons for the f/8 transducer data. We next compare the magnitude, real, and imaginary parts of the ultrasonic fields (3 MHz, 5 MHz, and 7 MHz) propagated through a water path or a composite path and measured by the hydrophone pseudo-array when excited by the f/4 transducer and the f/8 transducer. Figure 17 through Figure 19 compare the water path data for the two transducers, and Figure 20 through Figure 22 compare the composite path data for the f/4 and f/8 transducers.

For each of the six-panel figures (Figure 11 through Figure 22) images are displayed using a common data floor and data ceiling to calculate the grayscale (magnitude) or colorscale (real and imaginary) bin size. Therefore, the same data values are mapped to the same gray or color value for the images within each figure (i.e., bin sizes are the same). The use of this grayscale and colorscale mapping technique permits direct comparison of magnitude images and real (imaginary) images, respectively, within each figure. The grayscale and colorscale are noted for each figure.

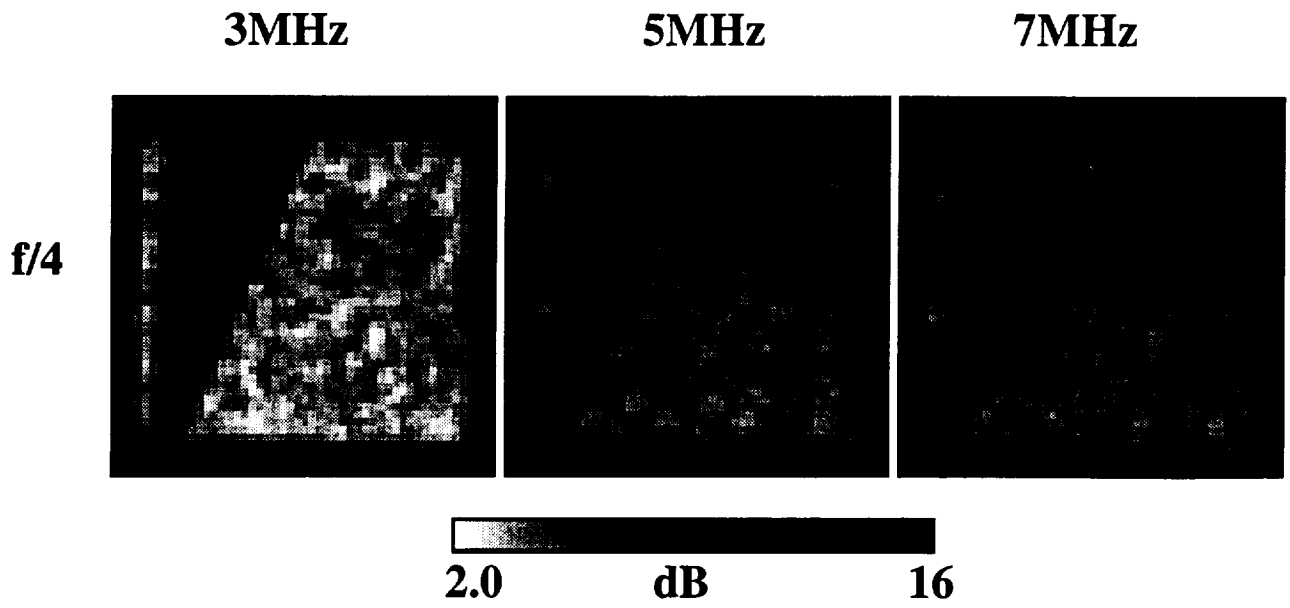

Figure 8. Apparent signal loss determined by through-transmission C-scan measurements with the f/4 transmitting transducer. The signal losses of the lead tape marker and outer steel frame were significantly greater than the signal loss of the composite. A value of 16 dB was chosen to threshold these larger values of signal loss.

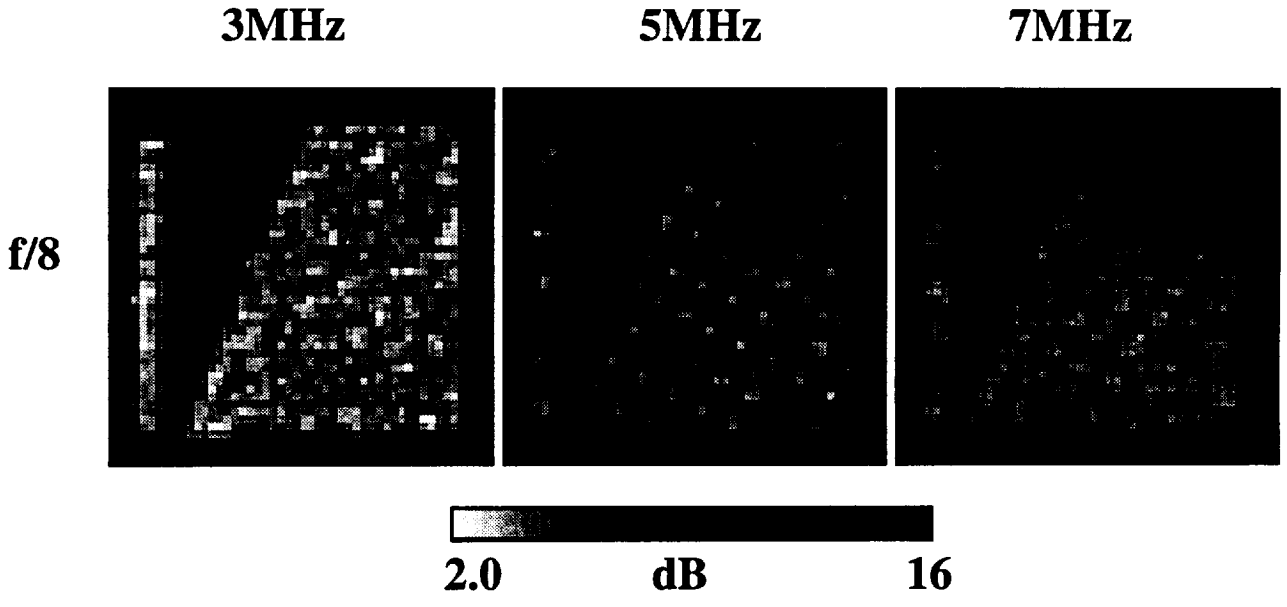

Figure 9. Apparent signal loss determined by through-transmission C-scan measurements with the f/8 transmitting transducer. The signal losses of the lead tape marker and outer steel frame were significantly greater than the signal loss of the composite. A value of 16 dB was chosen to threshold these larger values of signal loss.

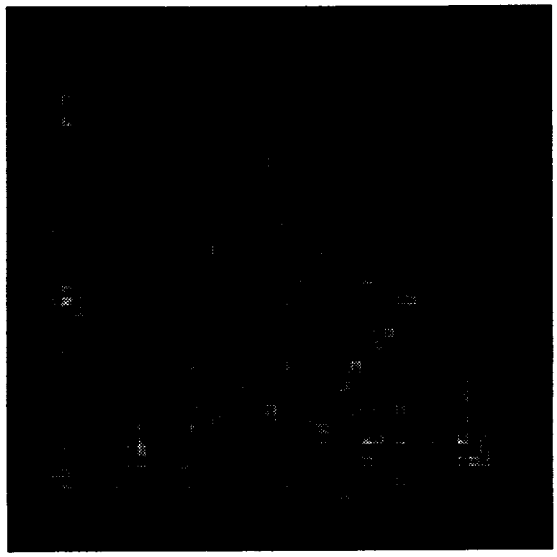

Figure 10. Apparent signal loss C-scan image with a representative footprint of the hydrophone pseudo-array depicted by the dark square outline.

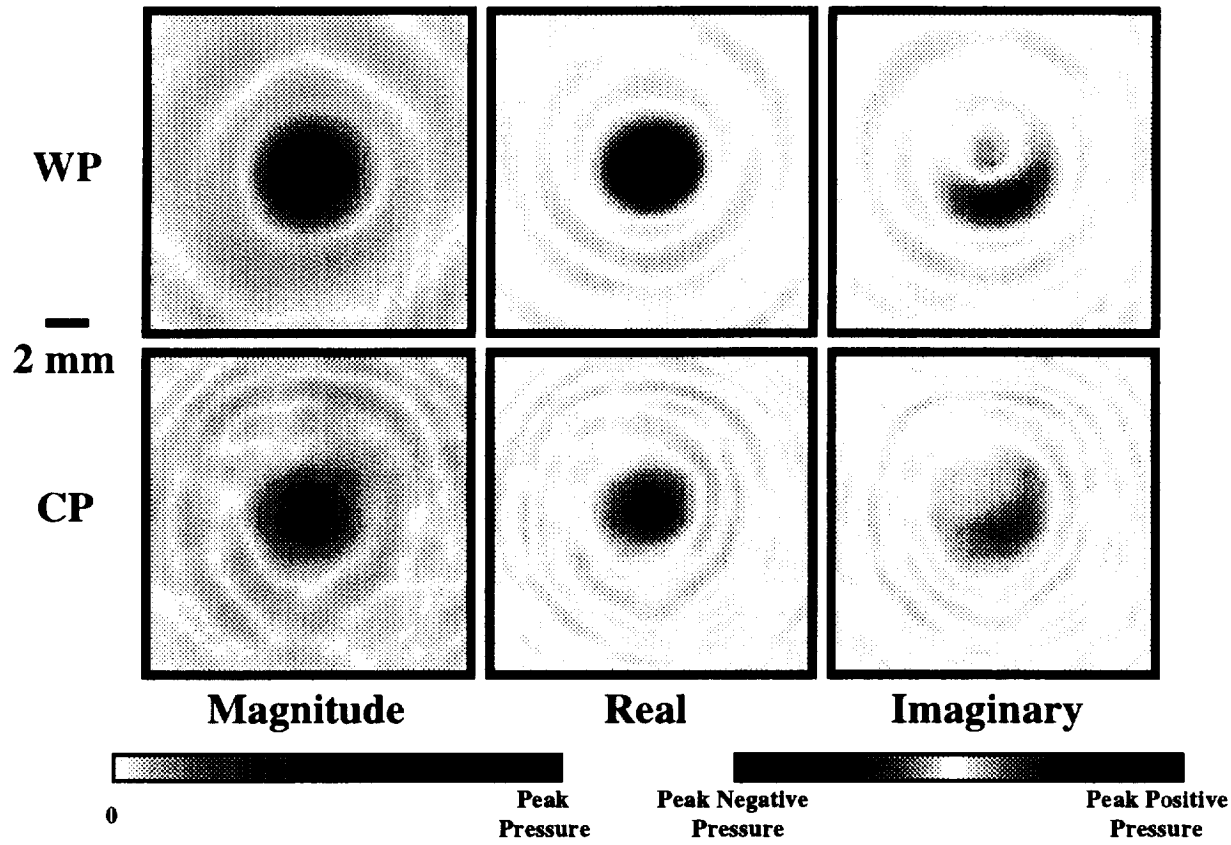

Figure 11. Comparison of magnitude, real, and imaginary receiver plane images of the measured 3 MHz ultrasonic field generated by the f/4 transducer along a water path and a composite path. The hydrophone scanning plane was positioned about 20 mm beyond the nominal focal plane (2") of the transmitting transducer (~70 mm total).

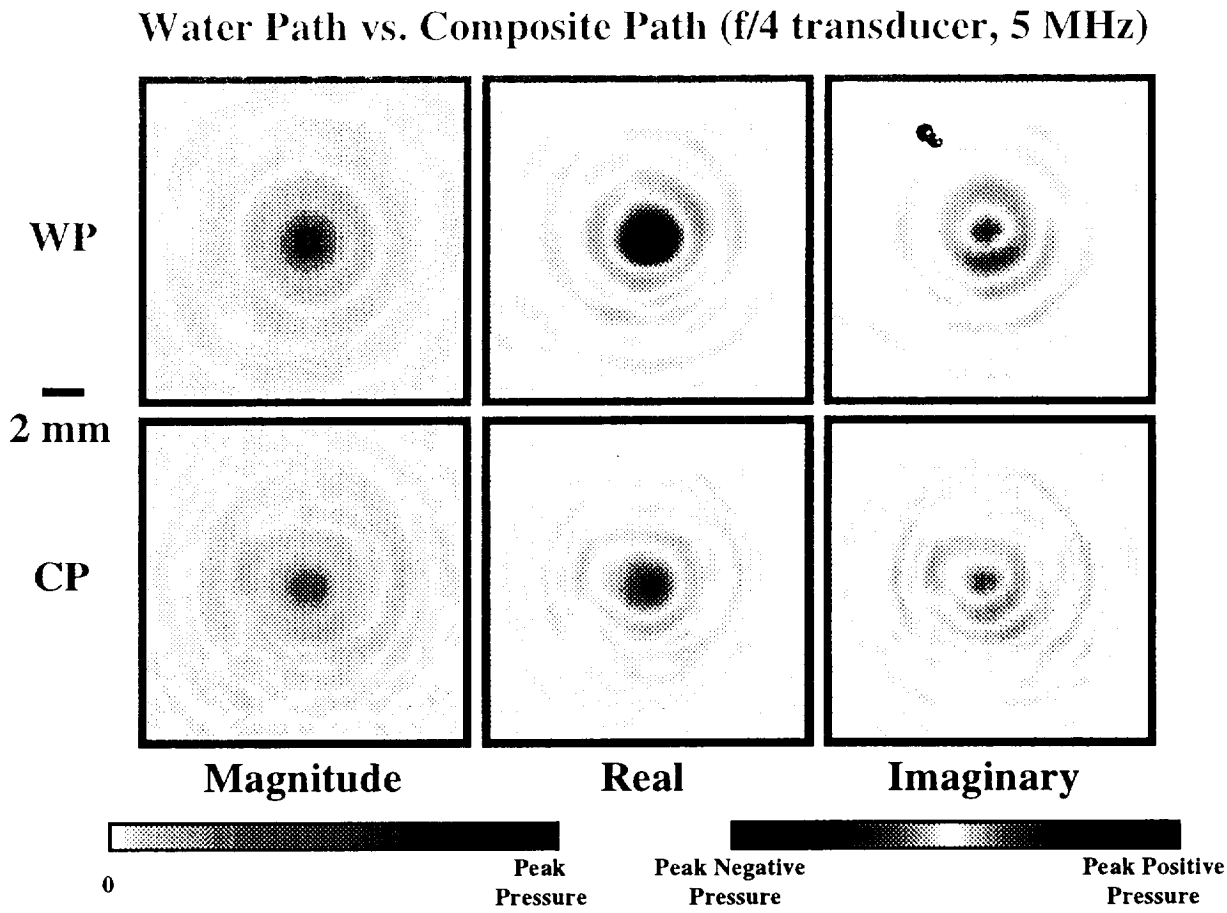

Figure 12. Comparison of magnitude, real, and imaginary receiver plane images of the measured 5 MHz ultrasonic field generated by the f/4 transducer along a water path and a composite path. The hydrophone scanning plane was positioned about 20 mm beyond the nominal focal plane (2") of the transmitting transducer (~70 mm total).

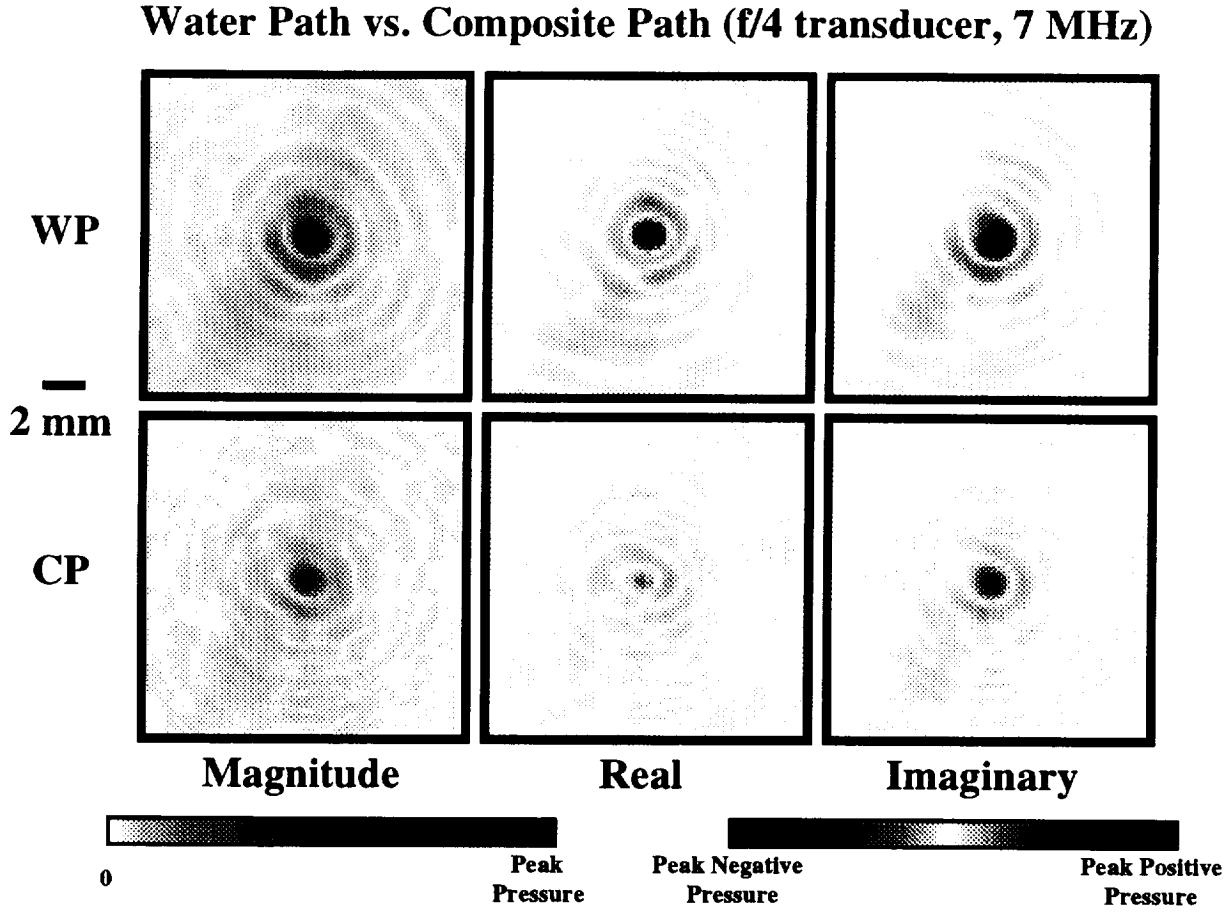

Figure 13. Comparison of magnitude, real, and imaginary receiver plane images of the measured 7 MHz ultrasonic field generated by the f/4 transducer along a water path and a composite path. The hydrophone scanning plane was positioned about 20 mm beyond the nominal focal plane (2") of the transmitting transducer (~70 mm total).

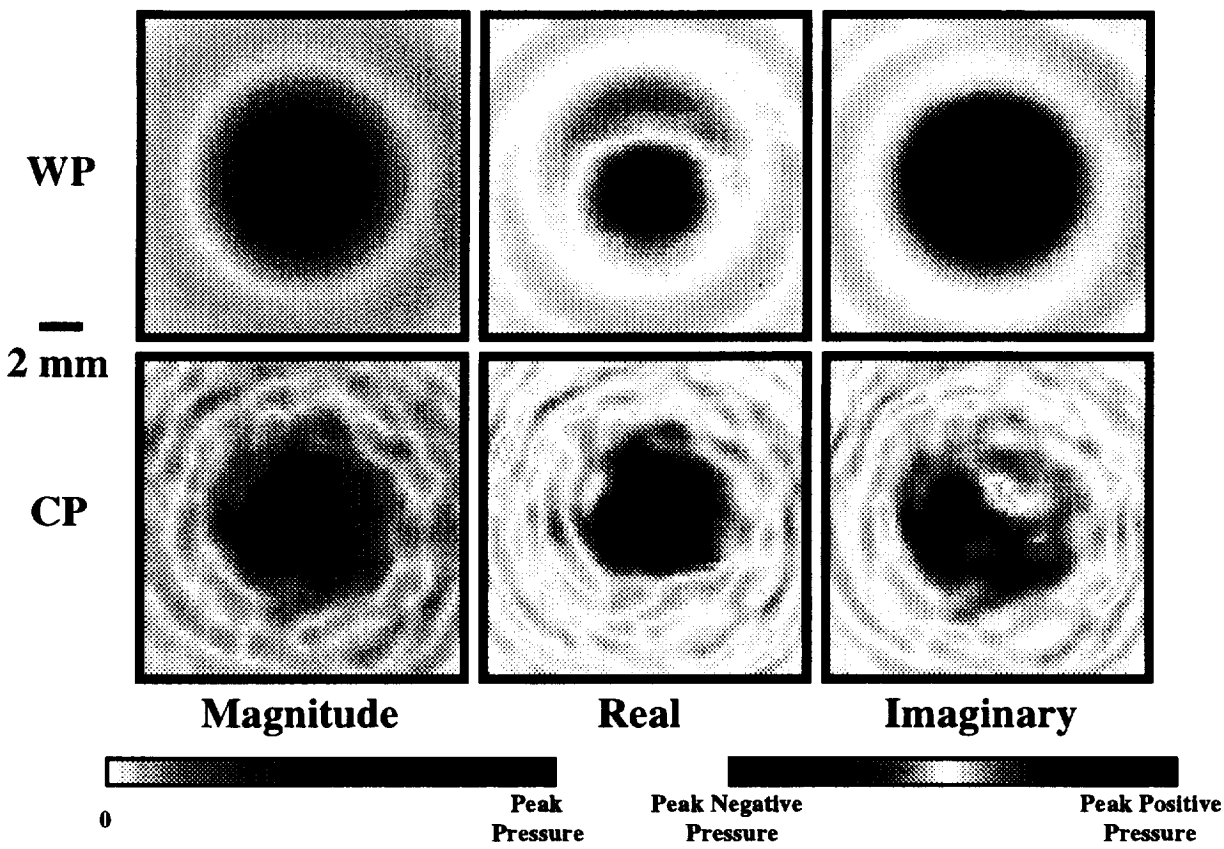

Figure 14. Comparison of magnitude, real, and imaginary receiver plane images of the measured 3 MHz ultrasonic field generated by the f/8 transducer along a water path and a composite path. The hydrophone scanning plane was positioned about 20 mm beyond the nominal focal plane (4") of the transmitting transducer (~121 mm total).

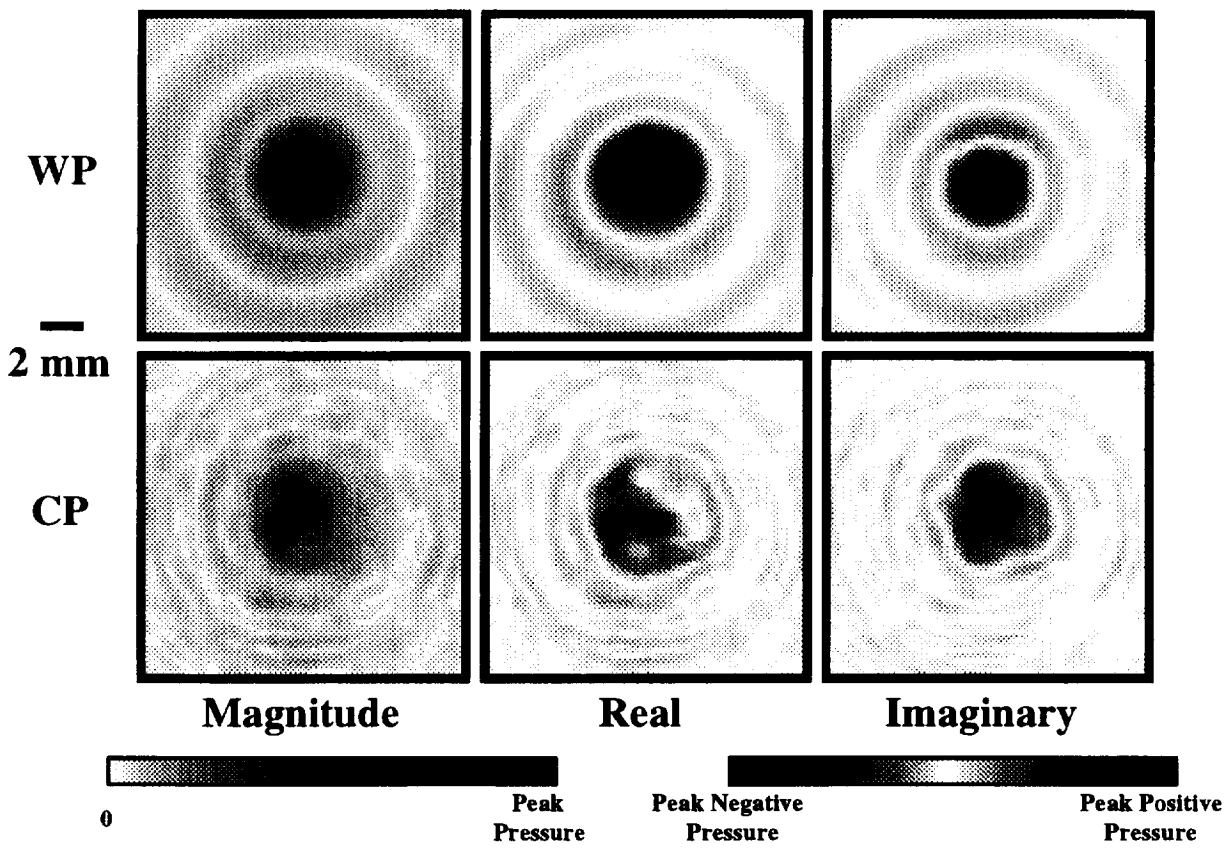

Figure 15. Comparison of magnitude, real, and imaginary receiver plane images of the measured 5 MHz ultrasonic field generated by the f/8 transducer along a water path and a composite path. The hydrophone scanning plane was positioned about 20 mm beyond the nominal focal plane (4") of the transmitting transducer (~121 mm total).

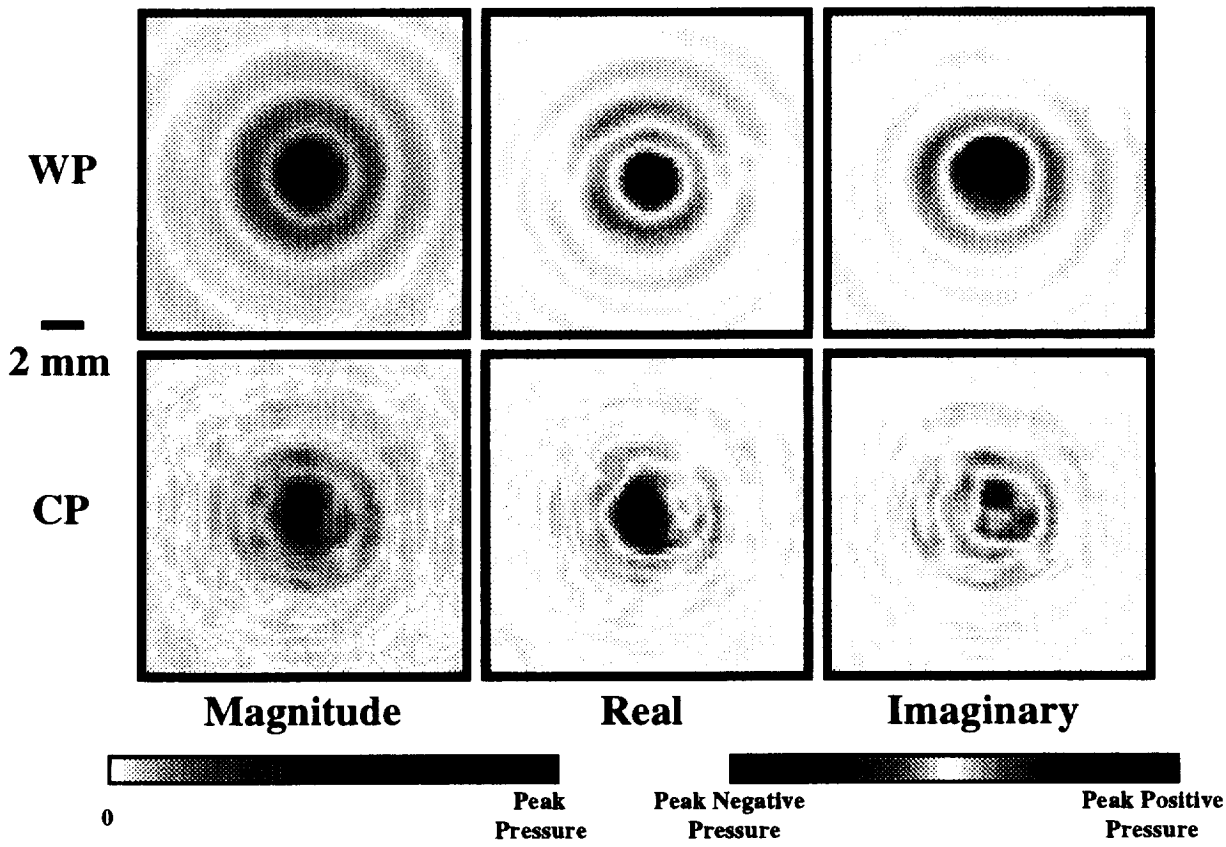

Figure 16. Comparison of magnitude, real, and imaginary receiver plane images of the measured 7 MHz ultrasonic field generated by the f/8 transducer along a water path and a composite path. The hydrophone scanning plane was positioned about 20 mm beyond the nominal focal plane (4") of the transmitting transducer (~121 mm total).

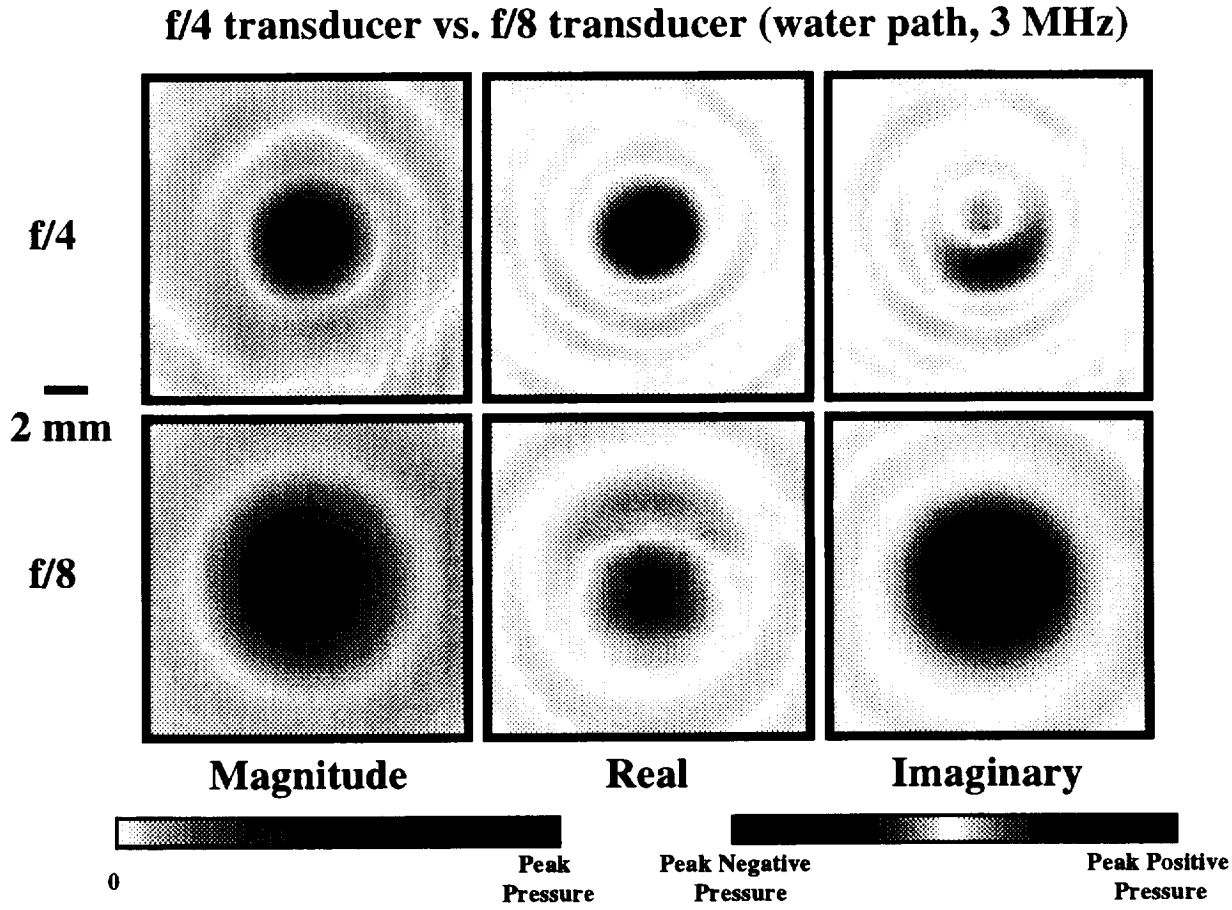

Figure 17. Comparison of magnitude, real, and imaginary receiver plane images of the measured 3 MHz ultrasonic field generated by the f/4 and f/8 transducers along a water path. The hydrophone scanning plane was positioned about 20 mm beyond the nominal focal plane (2" or 4") of the transmitting transducer (f/4 or f/8).

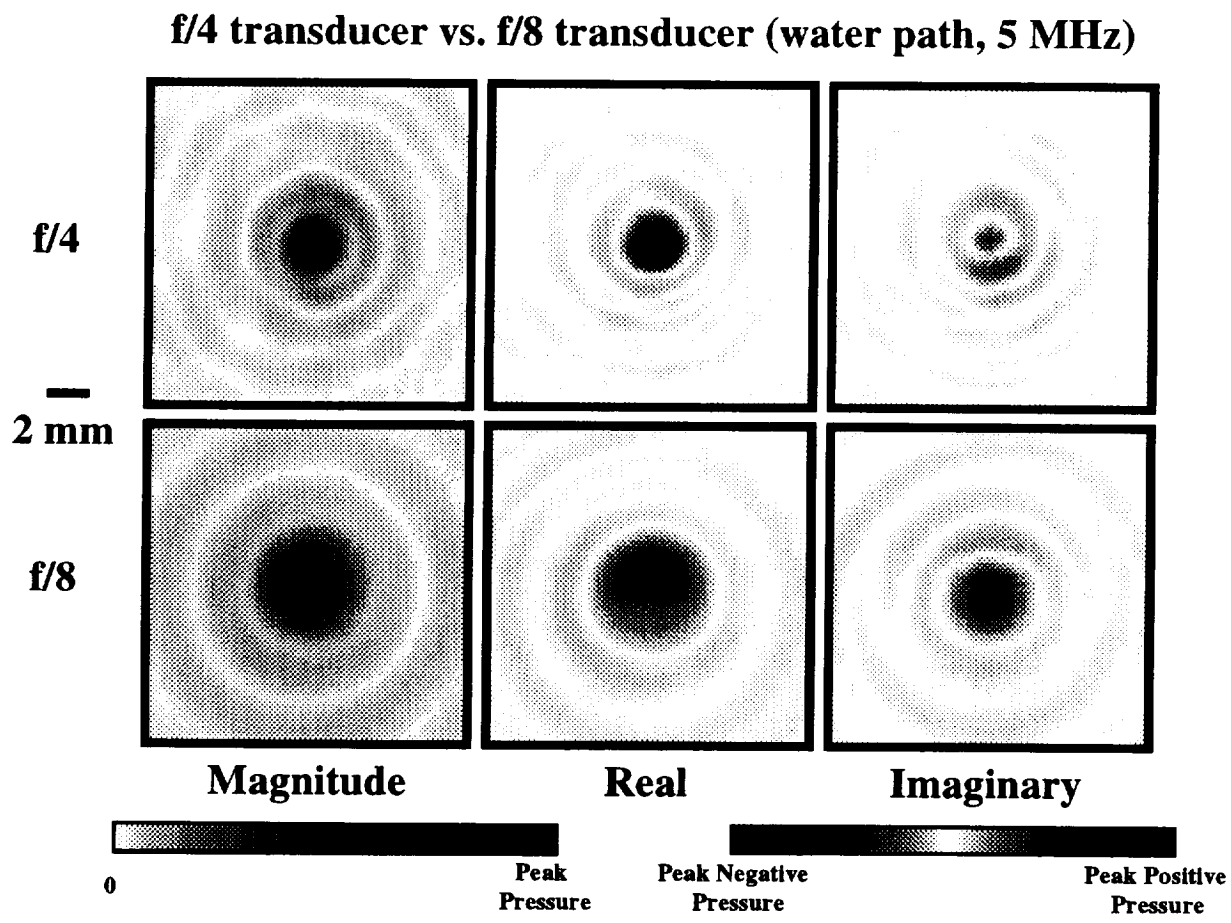

Figure 18. Comparison of magnitude, real, and imaginary receiver plane images of the measured 5 MHz ultrasonic field generated by the f/4 and f/8 transducers along a water path. The hydrophone scanning plane was positioned about 20 mm beyond the nominal focal plane (2" or 4") of the transmitting transducer (f/4 or f/8).

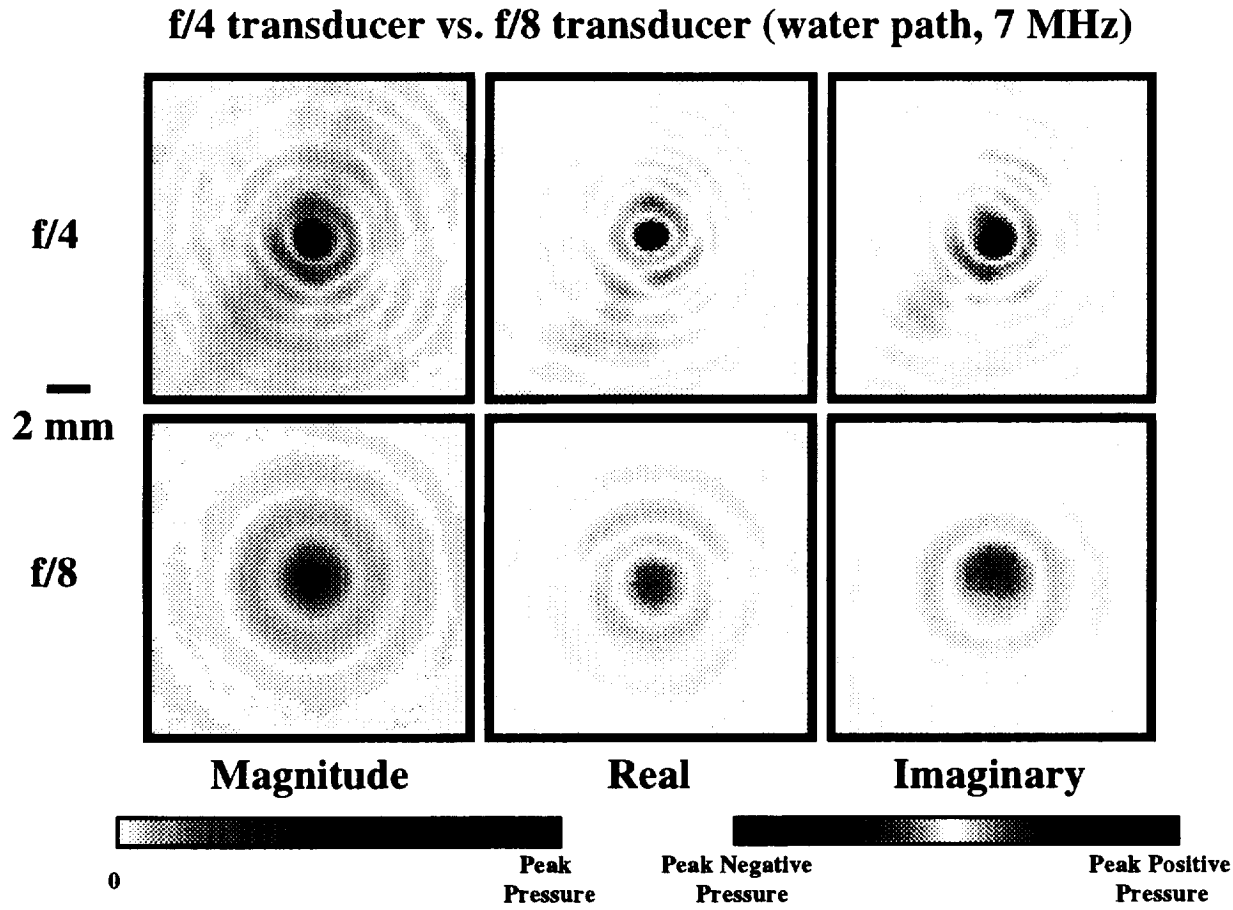

Figure 19. Comparison of magnitude, real, and imaginary receiver plane images of the measured 7 MHz ultrasonic field generated by the f/4 and f/8 transducers along a water path. The hydrophone scanning plane was positioned about 20 mm beyond the nominal focal plane (2" or 4") of the transmitting transducer (f/4 or f/8).

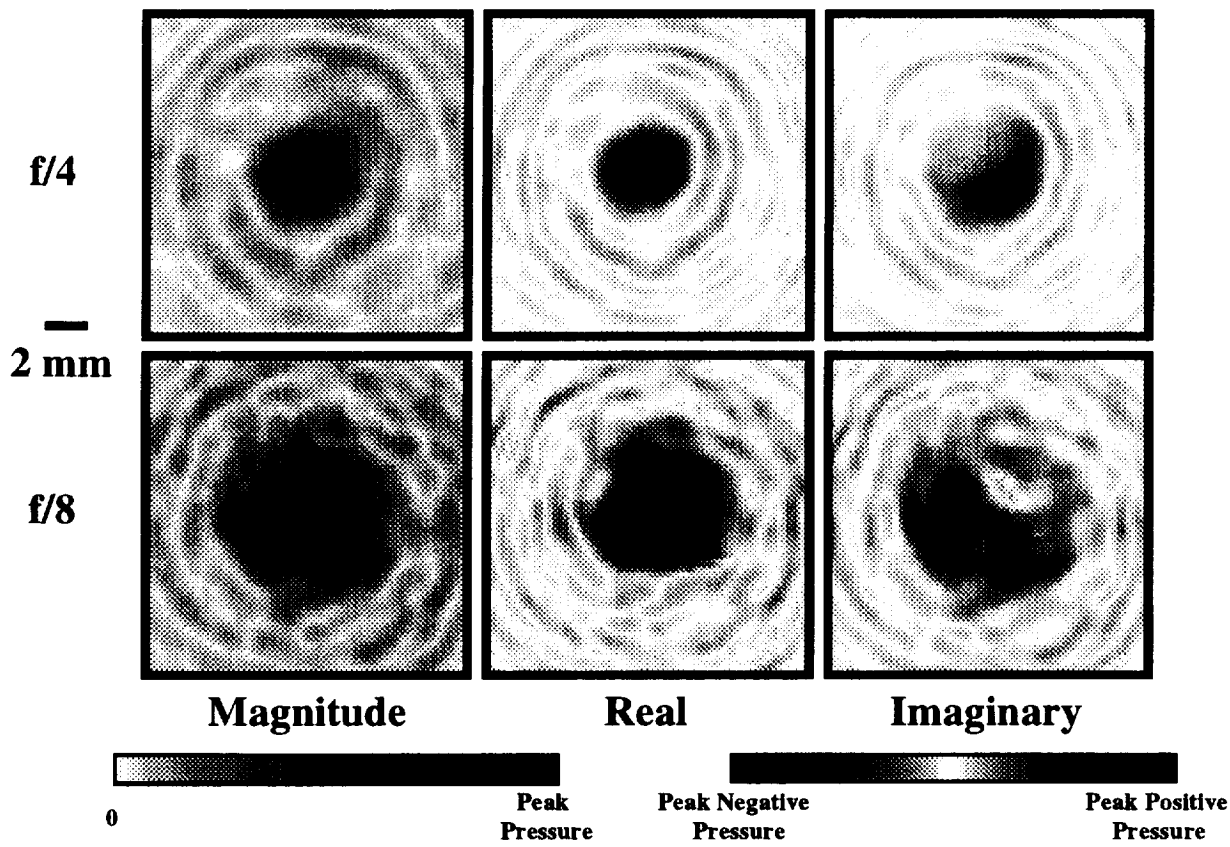

Figure 20. Comparison of magnitude, real, and imaginary receiver plane images of the measured 3 MHz ultrasonic field generated by the f/4 and f/8 transducers along a composite path. The hydrophone scanning plane was positioned about 20 mm beyond the nominal focal plane (2" or 4") of the transmitting transducer (f/4 or f/8).

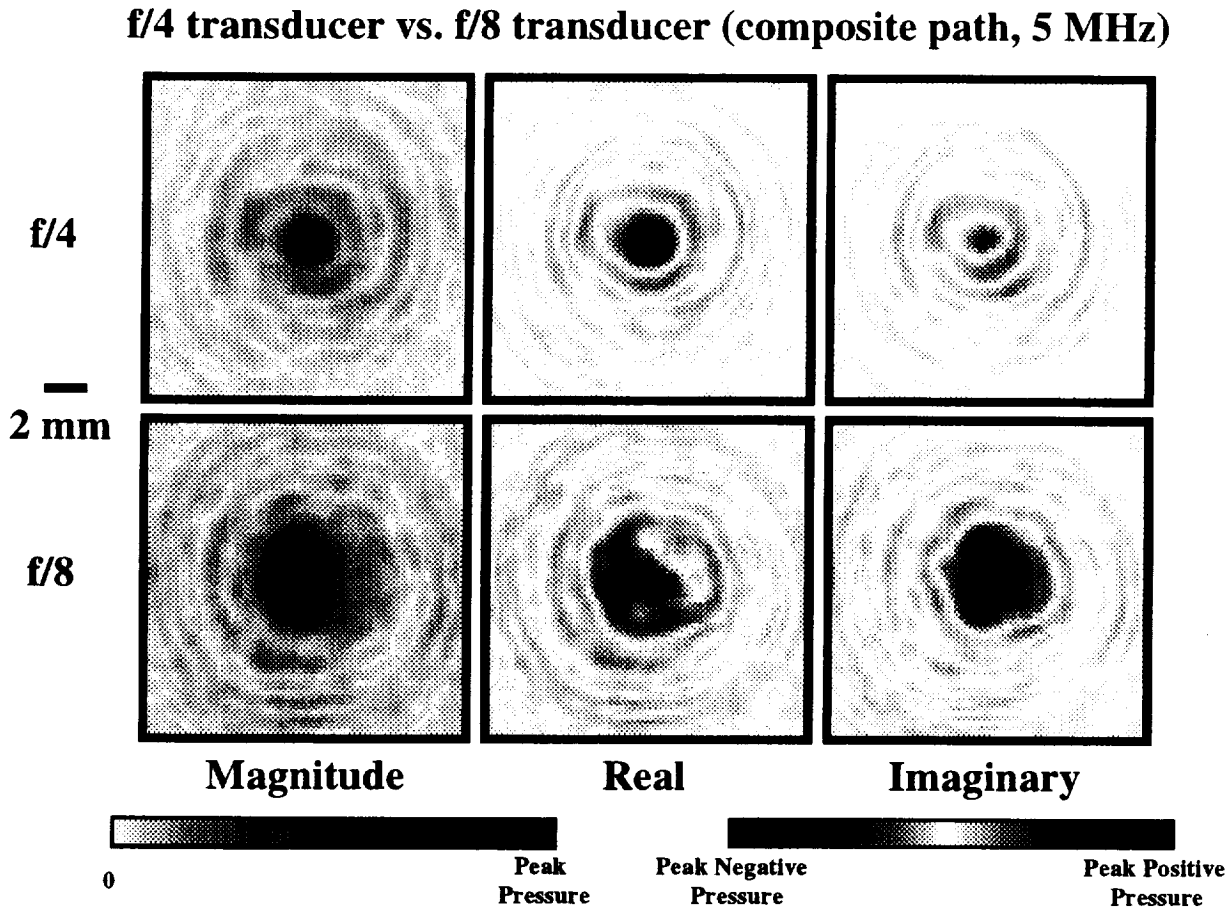

Figure 21. Comparison of magnitude, real, and imaginary receiver plane images of the measured 5 MHz ultrasonic field generated by the f/4 and f/8 transducers along a composite path. The hydrophone scanning plane was positioned about 20 mm beyond the nominal focal plane (2" or 4") of the transmitting transducer (f/4 or f/8).

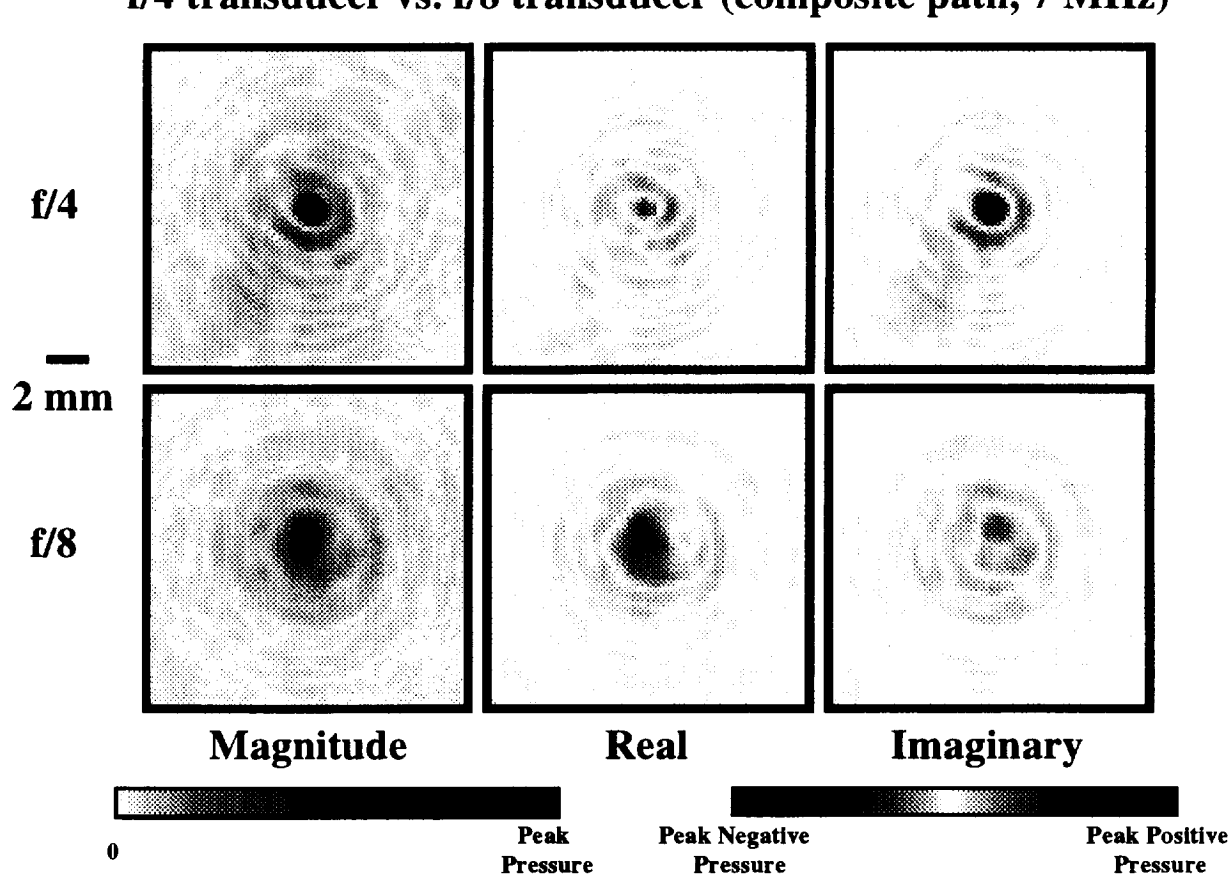

Figure 22. Comparison of magnitude, real, and imaginary receiver plane images of the measured 7 MHz ultrasonic field generated by the f/4 and f/8 transducers along a composite path. The hydrophone scanning plane was positioned about 20 mm beyond the nominal focal plane (2" or 4") of the transmitting transducer (f/4 or f/8).

We now demonstrate the effect of spherical focusing of a simulated pressure field by investigation of the real and imaginary parts of the field. Figure 23 shows the planar and spherically-focused real and imaginary parts of a 5 MHz ultrasonic field propagated to twice the nominal focal length of an f/4 transducer (4"). Figure 24, similarly, compares the planar and spherically-focused real and imaginary parts of a 5 MHz ultrasonic field propagated to twice the nominal focal length of an f/8 transducer (8").

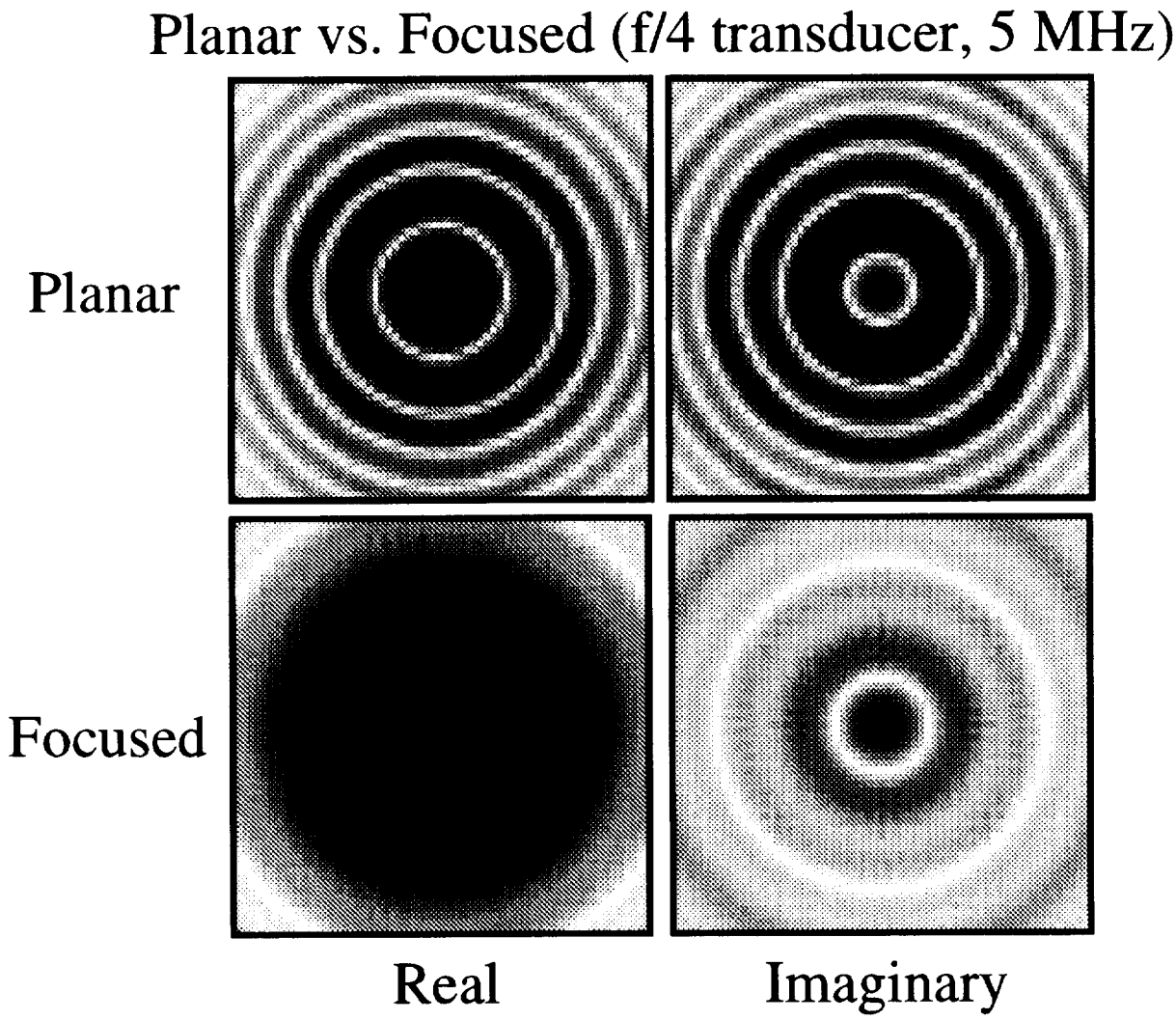

Figure 23. Comparison of the real and imaginary parts of planar and focused ultrasonic fields for an f/4 transducer (0.5" diameter, 2" focal length). The field is propagated to twice the focal length (4") of the transducer. These images are 63 by 63 arrays with 0.25 site separation for a total area of 15.5 mm by 15.5 mm. The focused fields have a 2" focal length.

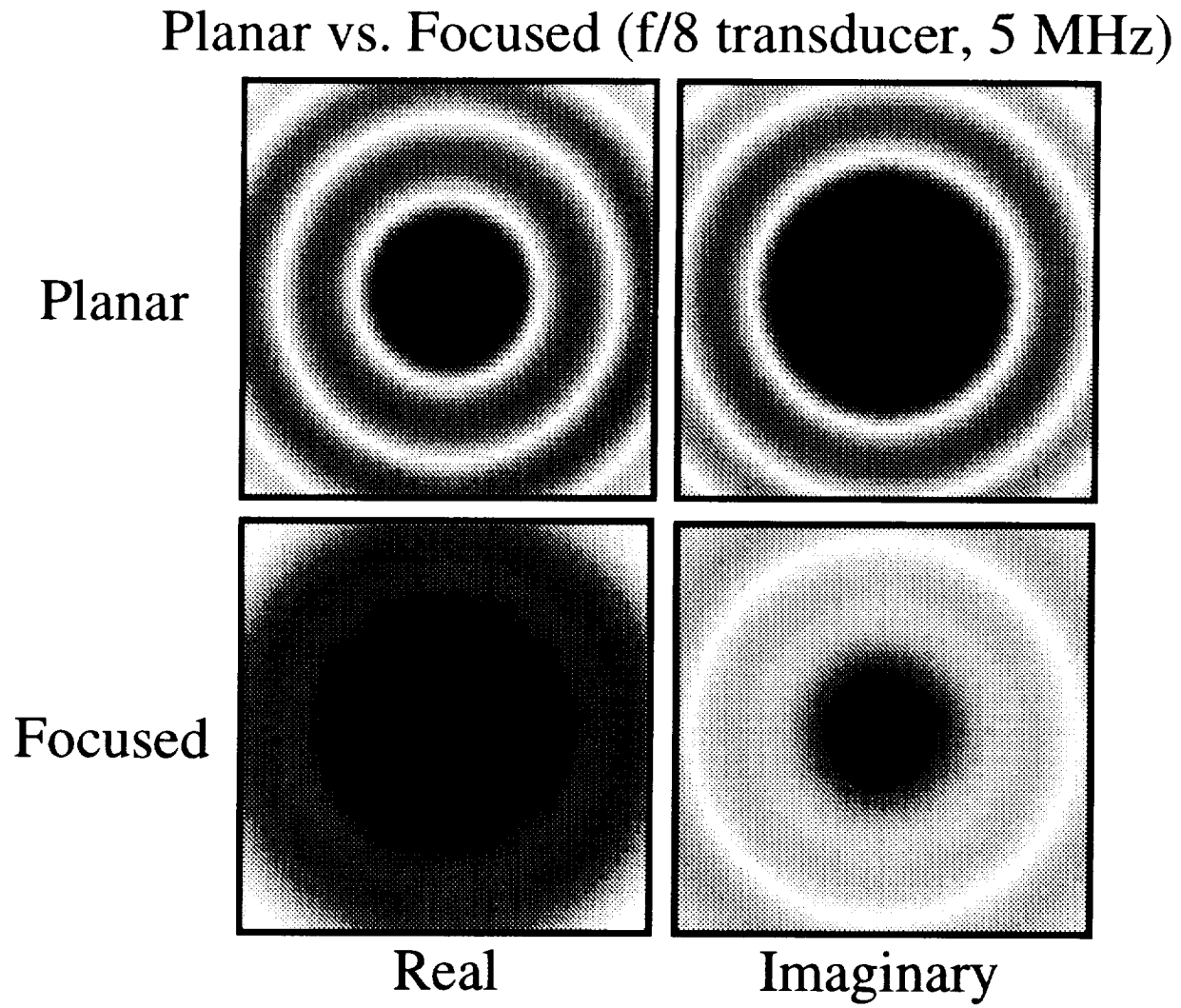

Figure 24. Comparison of the real and imaginary parts of planar and focused ultrasonic fields for an f/8 transducer (0.5" diameter, 4" focal length). The field is propagated to twice the focal length (8") of the transducer. These images are 63 by 63 arrays with 0.25 site separation for a total area of 15.5 mm by 15.5 mm. The focused fields have a 4" focal length.

Figure 25 compares the average apparent signal losses for the C-scan measurements using the f/4 and f/8 transmitting transducers. The apparent signal losses are averaged in the linear domain for those sites that are within the footprint of the hydrophone pseudo-array (see Figure 10).

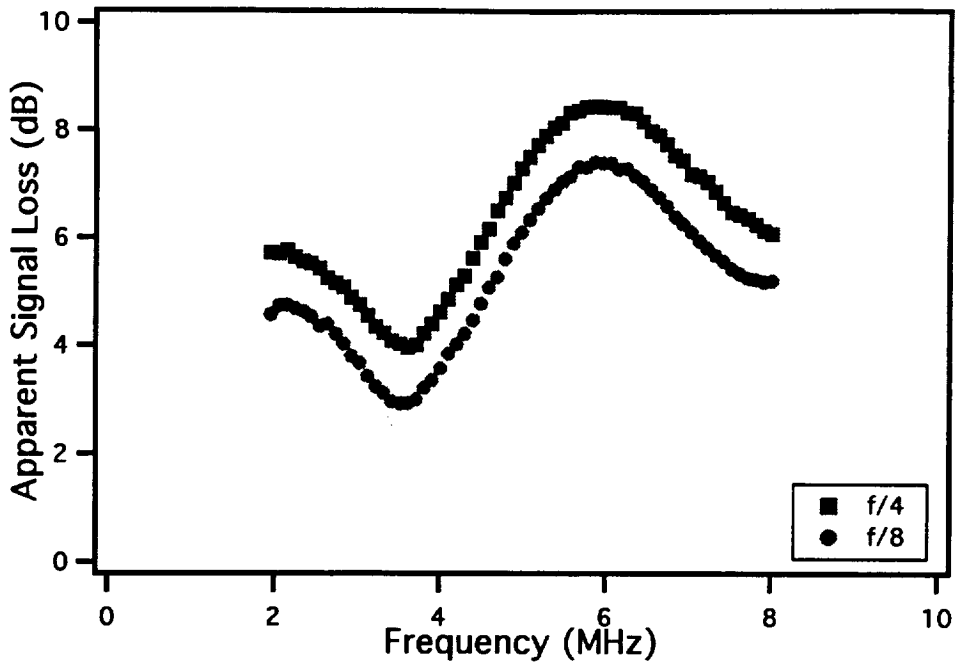

Figure 25. Comparison of average apparent signal losses for the C-scan measurements over a 17 mm by 17 mm area using the f/4 and f/8 transmitting transducers.

The phase-sensitive and phase-insensitive pseudo-array receiver analyses are shown in Figure 26 through Figure 34. The phase-sensitive and phase-insensitive power spectra for the water path and composite path using the f/4 transducer are shown in Figure 26 and Figure 27, respectively. The phase-sensitive and phase-insensitive apparent signal losses are shown in Figure 28. In addition, Figure 29 provides the phase-sensitive and phase-insensitive apparent signal losses for the case where the phase-insensitive water-path power spectrum is used for both apparent signal loss calculations. The use of the phase-insensitive water-path power spectrum with the phase-sensitive composite-path power spectrum, while not technically a valid comparison, is intended to emphasize the phase cancellation at the face of the phase-sensitive pseudo-array receiver for the composite path. Figure 30 through Figure 33 shows the analogous power spectra and apparent signal losses for the f/8 transducer. Lastly, Figure 34 compares the phase-insensitive apparent signal loss for the f/4 and f/8 transducers.

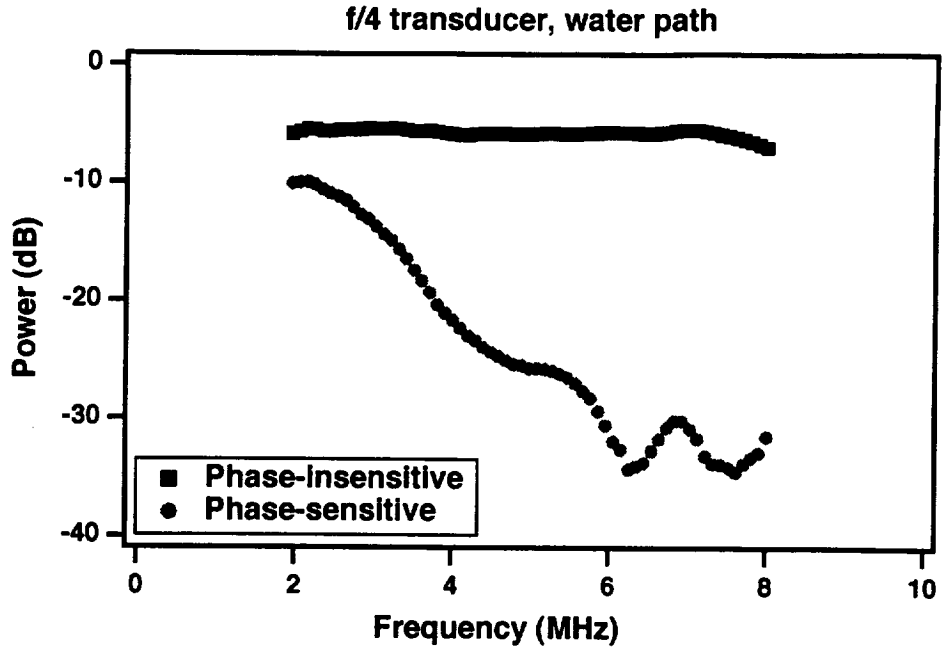

Figure 26. Comparison of phase-sensitive and phase-insensitive water path power spectra calculated for a 0.5"-diameter pseudo-array receiver. The scanning plane of the hydrophone pseudo-array was positioned 20 mm beyond the nominal focal plane of the f/4 transmitting transducer.

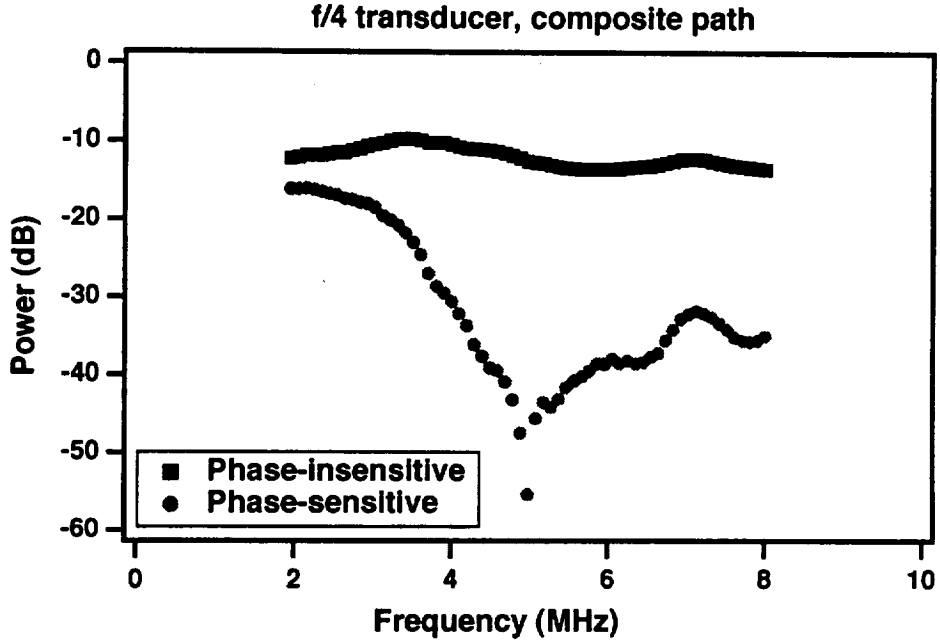

Figure 27. Comparison of phase-sensitive and phase-insensitive composite path power spectra calculated for a 0.5"-diameter pseudo-array receiver. The scanning plane of the hydrophone pseudo-array was positioned 20 mm beyond the nominal focal plane of the f/4 transmitting transducer.

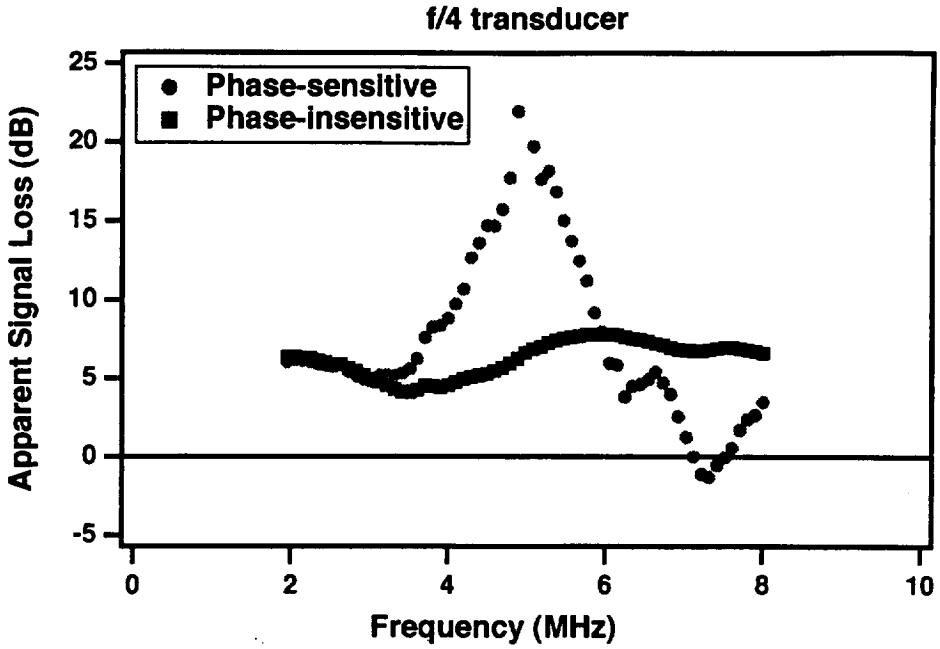

Figure 28. Comparison of phase-sensitive and phase-insensitive apparent signal loss due to the thin woven composite, calculated for a 0.5"-diameter pseudo-array receiver. The scanning plane of the hydrophone pseudo-array was positioned 20 mm beyond the nominal focal plane of the f/4 transmitting transducer.

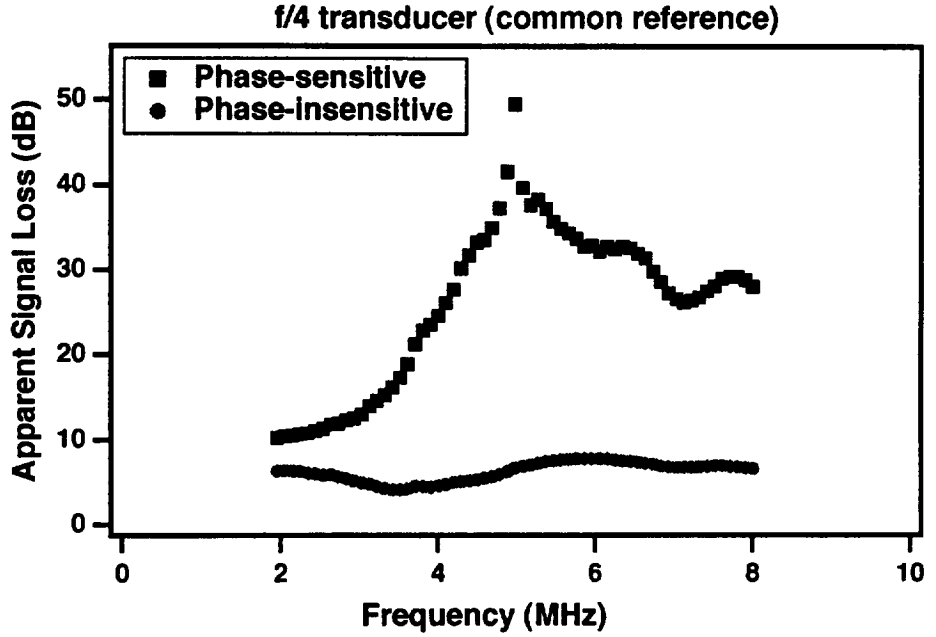

Figure 29. Comparison of phase-sensitive and phase-insensitive apparent signal loss (using the phase-insensitive water path power spectrum as a common reference) due to the thin woven composite, calculated for a 0.5"-diameter pseudo-array receiver. The scanning plane of the hydrophone pseudo-array was positioned 20 mm beyond the nominal focal plane of the f/4 transmitting transducer.

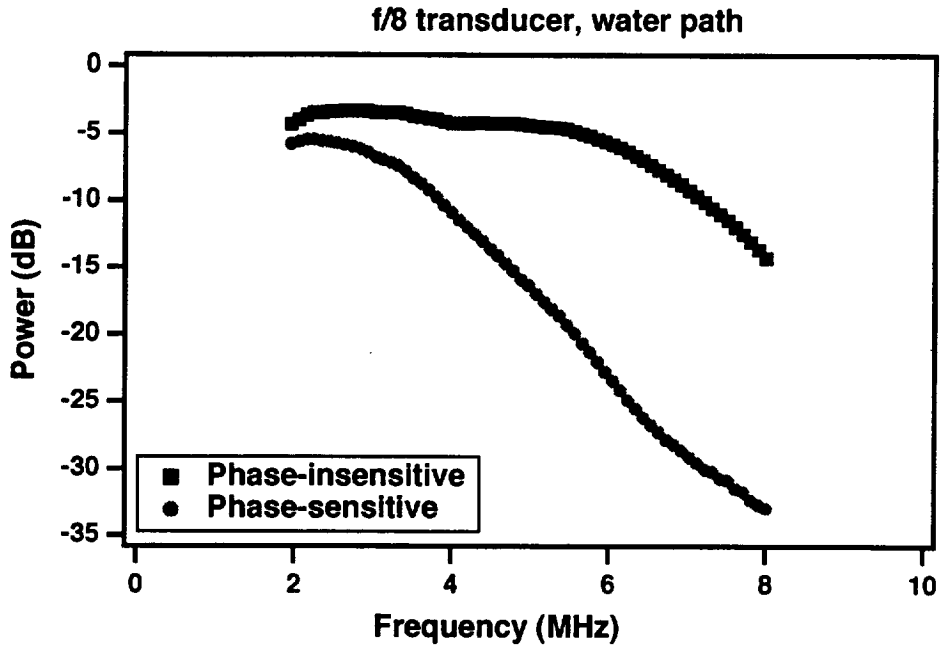

Figure 30. Comparison of phase-sensitive and phase-insensitive water path power spectra calculated for a 0.5"-diameter pseudo-array receiver. The scanning plane of the hydrophone pseudo-array was positioned 20 mm beyond the nominal focal plane of the f/8 transmitting transducer.

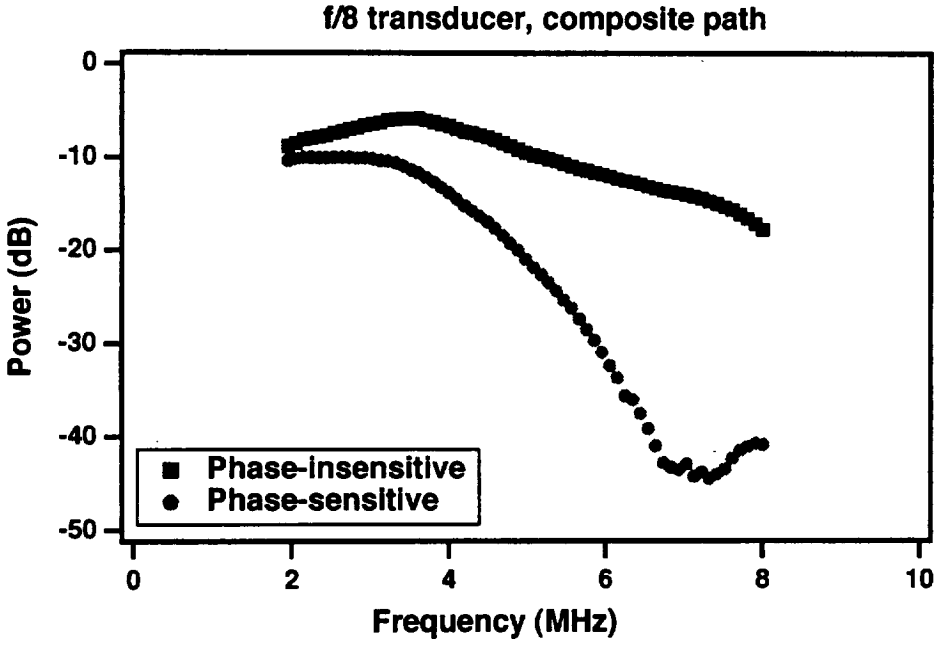

Figure 31. Comparison of phase-sensitive and phase-insensitive composite path power spectra calculated for a 0.5"-diameter pseudo-array receiver. The scanning plane of the hydrophone pseudo-array was positioned 20 mm beyond the nominal focal plane of the f/8 transmitting transducer.

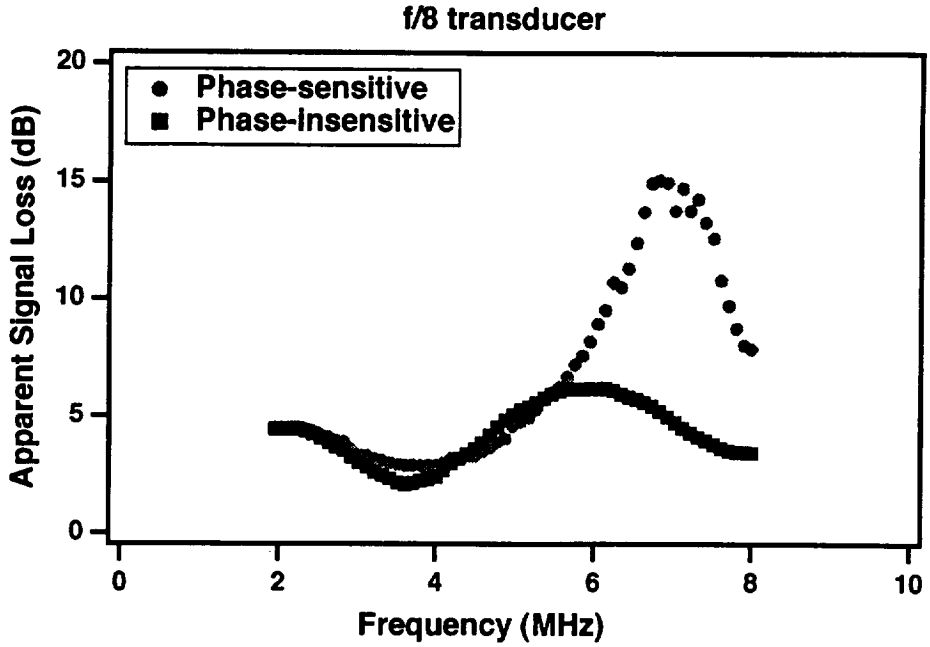

Figure 32. Comparison of phase-sensitive and phase-insensitive apparent signal loss due to the thin woven composite, calculated for a 0.5"-diameter pseudo-array receiver. The scanning plane of the hydrophone pseudo-array was positioned 20 mm beyond the nominal focal plane of the f/8 transmitting transducer.

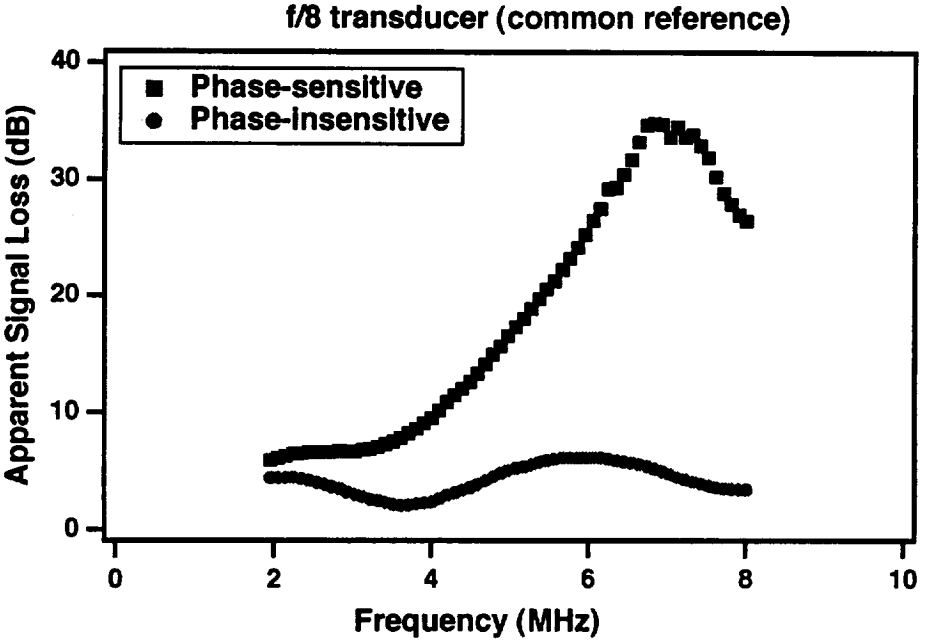

Figure 33. Comparison of phase-sensitive and phase-insensitive apparent signal loss (using the phase-insensitive water path power spectrum as a common reference) due to the thin woven composite, calculated for a 0.5"-diameter pseudo-array receiver. The scanning plane of the hydrophone pseudo-array was positioned 20 mm beyond the nominal focal plane of the f/8 transmitting transducer.

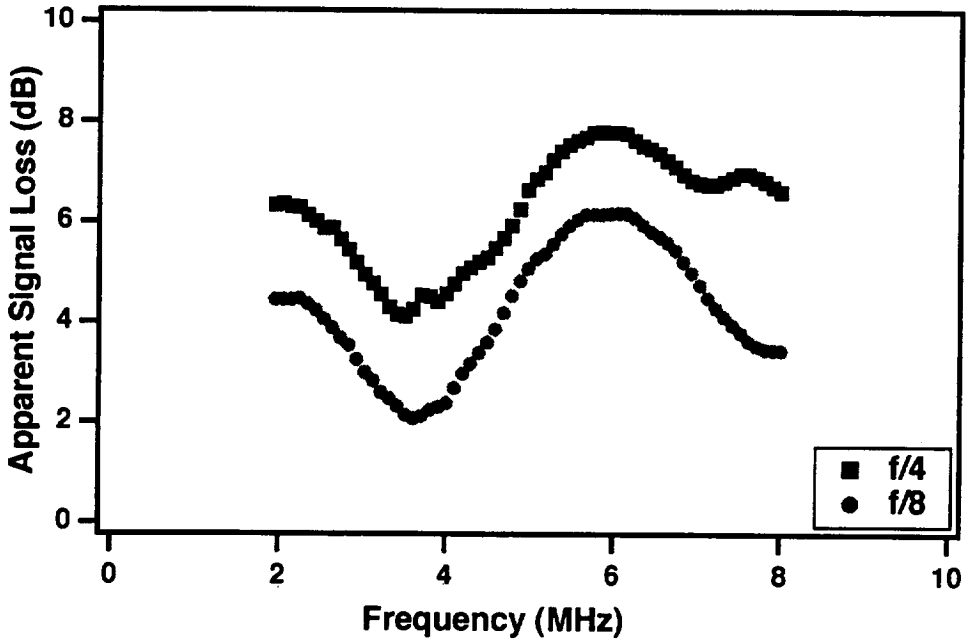

Figure 34. Comparison of the f/4 and f/8 phase-insensitive apparent signal loss due to the thin woven composite, calculated for a 0.5"-diameter pseudo-array receiver. The scanning plane of the hydrophone pseudo-array was positioned 20 mm beyond the nominal focal plane of the f/4 or f/8 transmitting transducer, respectively.

D. Discussion

This section provides commentary on the Results presented in the previous section. Initial comments concern qualitative interpretations of the receiver plane images, and follow with a discussion of the quantitative results. The final part of this section considers issues that have not been fully addressed in previous reports.

D.1 Qualitative Interpretation

D.1a Apparent Signal Loss C-Scan Measurement

Figure 8 and Figure 9 compare apparent signal loss images at three distinct frequencies derived from through-transmission C-scan measurements of the thin woven composite using both the f/4 and f/8 transmitting transducers, respectively. In each image, the dark outer border represents the stainless steel frame used to mount the composite sample. The large, dark triangular region in each panel is a lead tape marker that provides position recognition for the pseudo-array scans as depicted in Figure 10. We observe finer detail resolution with increasing frequency in addition to increased signal loss, as would be expected.

D.1b Pressure fields of the f/4 and f/8 transducers

Of primary interest for this report is a comparison of the measured ultrasonic fields of the f/4 and f/8 transmitting transducers (Figure 17 through Figure 22). For discussions concerning comparison of water path and composite path receiver plane images (Figure 11 through Figure 16) for a given transmitting transducer, please refer to previous Progress Reports[1,3]. The conclusions of previous experimental measurements are valid for these current measurements as well for comparison of water path and composite path receiver plane images.

A comparison of the measured ultrasonic pressure fields of the different f-number transducers indicates that the differences in beam diameter (as defined by the 6-dB down region for the pressure magnitude) is a significant feature. For circular-aperture transmitters, the 6-dB beam diameter in the focal zone is linearly proportional to the f-number of the transmitting transducer.[13,14] The choice of the f-number for the transmitter can play a role when *a priori* information is available regarding typical flaw dimensions for a given material. With available one- and two-dimensional ultrasonic arrays, it is conceivable that f-numbers can be tailored for optimal interrogation of a given composite.

D.1c Spherical focusing of fields

The issue of phase cancellation across the face of a finite-aperture, piezoelectric receiver has been of continuing interest as part of this grant. Previously, we have only concerned ourselves with the ultrasonic fields as measured by a planar pseudo-array. Here, we extend this work to consider the effect on phase (real and imaginary parts) of ultrasonic fields by focusing. Figure 23 and Figure 24 demonstrate the effect spherical focusing has on the real and imaginary parts of the ultrasonic field for simulations with a transmitting transducer (f/4 or f/8) and a two-dimensional planar receive array separated a distance twice the focal length of the transmit transducer along a water path. In each case, the planar receive array is spherically focused at the focal point of the transmitting transducer. If we were to then simulate a finite-aperture, piezoelectric receiver, the amount of phase cancellation across the face of the finite-aperture, piezoelectric receiver would be greatly reduced, and virtually eliminated for the case of an f/8 receiver of the type considered within this report. This observation can be significant for material property measurements which rely upon ultrasonic parameters that are concerned with the energy of the received ultrasonic field.

D.2 Quantitative Interpretation

D.2a C-Scan Apparent Signal Loss Measurements

We achieve results for the C-scan measurements that are consistent with previous and current phase-insensitive receiver simulations from the experimental hydrophone pseudo-array measurements. One possible explanation for the ~1 dB discrepancy between the apparent signal losses for the C-scan measurements using the f/4 and f/8 transmitting transducers could be the positioning of the thin woven composite with respect to the transmitting transducer for the case of the f/4 transducer. The physical constraints of the C-scan apparatus did not permit positioning the thin composite in the focal plane of the f/4 transducer.

D.2b Phase-Sensitive and Phase-Insensitive Apparent Signal Loss

Phase-sensitive results compared with phase-insensitive results are consistent with results of the previous Progress Report. Phase-insensitive results, comparing signal loss for the f/4 and f/8 transmitting transducers, have the same frequency dependence, but the absolute level of the f/4 data lies about 2 dB above the f/8 data. In addition to the absolute level of signal loss, the frequency dependence of the apparent signal loss is also of interest. It is not immediately intuitive why we do not measure a monotonically increasing apparent signal loss as has been done for other types of composites, such as graphite/epoxy laminate composites.[15] This behavior, upon further investigation, is most likely accounted for by a frequency-dependent transmission loss due to a thin sample. We discuss this in more detail below.

D.3 Continuing Issues: Alignment and Signal Loss

There are issues that arise from the current investigation as well as previous investigations of ultrasonic beam profiles that have not been fully addressed. We have observed a lack of symmetry in the real and imaginary images of the ultrasonic field that would not be expected for transmission through only a water path. This lack of symmetry leads to questions of proper alignment of our two-dimensional planar pseudo-array. We have previously commented that alignment procedures that rely only upon an optimization of a reference power spectrum may not be adequate for alignment of two-dimensional arrays. Figure 35 demonstrates the effect a slight misalignment (~0.5°) of the receiving plane with respect to the direction of propagation of the transmitted field can have on the received ultrasonic field. Previously[1], we suggested that a monitoring of the real and imaginary parts of the pressure field at a given frequency may provide an improved alignment protocol. In this effort of improving alignment of our transmitting transducer and receiving pseudo-array, we have chosen to indirectly monitor the real and imaginary parts of the pressure field by observing shifts in time-of-flights of ultrasonic signals across the two-dimensional pseudo-array in addition to observing the reference power spectrum. Through an

iterative technique of minimizing shifts in time-of-flights of pulse/echoes off an adjustable stainless steel plate, we can improve the alignment of the transducer with respect to the scanning receive plane. The phenomenon of phase cancellation across the face of a finite-aperture, piezoelectric receiver is sensitive to even modest changes in path lengths. What can readily be detected as misalignment in the real and imaginary images is not apparent in the magnitude (or power) images, as demonstrated in Figure 35. In addition to alignment benefits, we have found this technique to be sensitive enough to observe accuracy limits of our computer-controlled motion controller positioning.

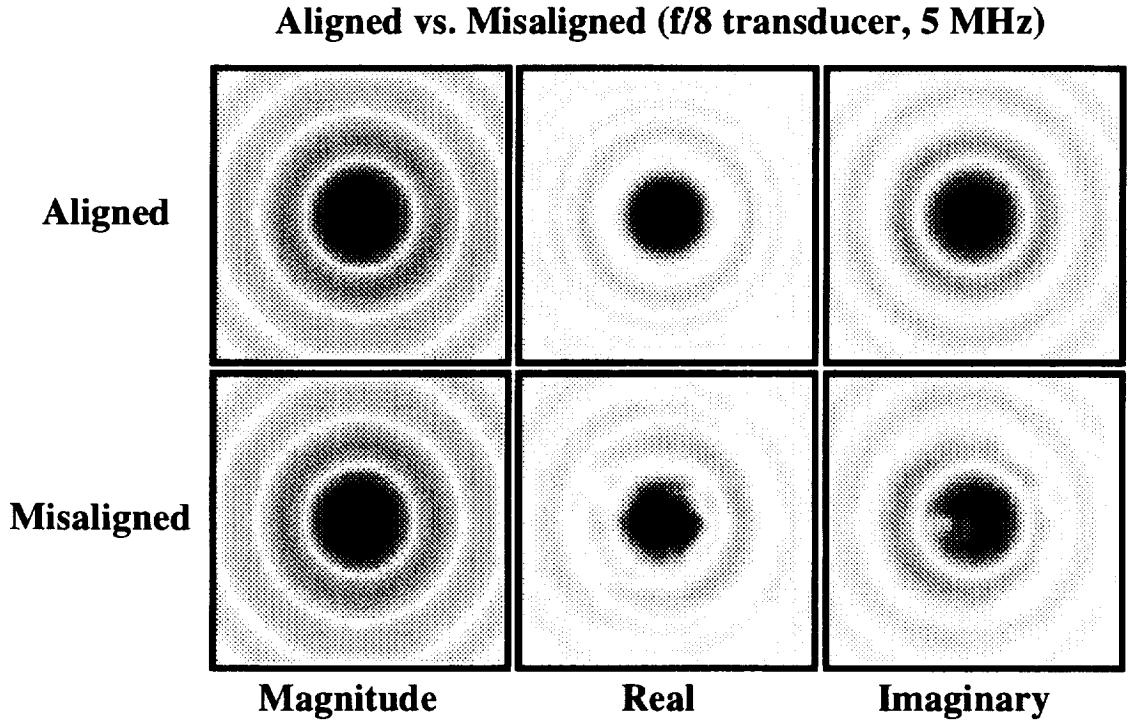

Figure 35. Comparison of simulated 5 MHz ultrasonic fields propagated along a water path (~120 mm). The top row of images is for the case of ideal alignment of a two-dimensional array with respect to a transmitting transducer (0.5" diameter, 4" focal length). The bottom row of images indicates the effect a slight misalignment (~0.5°) can have on the received ultrasonic field.

As mentioned above, the non-monotonic behavior of the apparent signal loss may be partially explained by consideration of the transmission loss due to the thin woven composite acting as a thin interface. According to a simple transmission line model[16], selective frequencies of ultrasound can be passed through the thin sample with only negligible transmission losses, while other frequencies suffer *relatively* large losses. In principle, the apparent signal loss that we measure could be compensated for the transmission loss due to a thin interface. However, a difficulty in applying the transmission line model to the thin composite we have investigated is the non-uniform thickness of the composite. The thickness of the thin sample plays a significant role in the selection of which frequencies of ultrasound are transmitted through the thin interface with negligible losses, and which are attenuated.

E. Conclusions

An overall goal of this research has been to enhance our understanding of the scientific principles necessary to develop advanced ultrasonic nondestructive techniques for the quantitative characterization of advanced composite structures. To this end, we have investigated a thin woven composite (5-harness biaxial weave). We have studied the effects that variations of the physical parameters of the experimental setup can have on the ultrasonic determination of the material properties for this thin composite. In particular, we have considered the variation of the nominal center frequency and the f-number of the transmitting transducer which in turn address issues such as focusing and beam spread of ultrasonic fields.

This study has employed a planar, two-dimensional, receiving pseudo-array that has permitted investigation of the diffraction patterns of ultrasonic fields. Distortion of the ultrasonic field due to the spatial anisotropy of the thin composite has prompted investigation of the phenomenon of phase cancellation at the face of a finite-aperture, piezoelectric receiver. We have

performed phase-sensitive and phase-insensitive analyses to provide a measure of the amount of phase cancellation at the face of a finite-aperture, piezoelectric receiver. The pursuit of robust measurements of received energy (i.e., those not susceptible to phase cancellation at the face of a finite-aperture, piezoelectric receiver) supports the development of robust techniques to determine material properties from measured ultrasonic parameters.

During this grant period we have achieved a majority of the goals we set in the proposal. Namely, we have investigated the effects of the f-number and nominal center frequency (i.e., focal zone parameters) of the transmitting transducer on estimates of signal loss of the thin woven composite, as well as compared phase-sensitive and phase-insensitive estimates of the signal loss. Our study has also led to new avenues of investigation, such as the aforementioned alignment issues, that were not initially foreseen but were nonetheless of substantial merit. In addition, the research has provided a basis for designing future investigations. One such extension would be the application of observations from measurements using a two-dimensional *pseudo*-array to measurements using a *true* two-dimensional array.

F. References

1. James G. Miller, "Ultrasonic Nondestructive Evaluation Techniques Applied to Quantitative Characterization of Textile Composite Materials", NASA, Progress Report, Report Number: NAG 1-1848, (December, 1997).

2. James G. Miller, "Ultrasonic Nondestructive Evaluation Techniques Applied to Quantitative Characterization of Textile Composite Materials", NASA, Progress Report, Report Number: NAG 1-1848, (December, 1996).

3. James G. Miller, "Ultrasonic Nondestructive Evaluation Techniques Applied to Quantitative Characterization of Textile Composite Materials", NASA, Progress Report, Report Number: NAG 1-1848, (June, 1997).

4. Lawrence J. Busse, *Electron-Phonon Interactions in Piezoelectric Semiconductors for the Phase Insensitive Detection of Ultrasound*, Doctor of Philosophy Thesis, Washington University, (1979).

5. L.J. Busse and J.G. Miller, "A comparison of finite aperture phase sensitive and phase insensitive detection in the near field of inhomogeneous material"(Published 1981), pp. 617-626.

6. L.J. Busse and J.G. Miller, "Response Characteristics of a Finite Aperture, Phase Insensitive Ultrasonic Receiver Based Upon the Acoustoelectric Effect", *Journal. Acoustical Society of America*, Vol. 70, pp. 1370-1376, (1981).

7. Mark R. Holland and J.G. Miller, "Phase-Insensitive and Phase-Sensitive Quantitative Imaging of Scattered Ultrasound Using a Two-Dimensional Pseudo-Array"(Chicago, Published 1988), Vol. 88 CH 2578-3, pp. 815-819.

8. Patrick H. Johnston, *Phase-Insensitive Detection and the Method of Moments for Ultrasonic Tissue Characterization*, Doctor of Philosophy Thesis, Washington University, (1985).

9. Patrick H. Johnston and J.G. Miller, "A Comparison of Backscatter Measured by Phase-Sensitive and Phase-Insensitive Detection"(Published 1985), pp. 827-831.

10. Patrick H. Johnston and Agus A. Ananda, "The role of phase cancellation in the ultrasonic NDE of stitched graphite-epoxy composites"(Orlando, Published 1991), Vol. 91CH3079-1, pp. 845-848.

11. Joseph S. Heyman, *Ultrasonic Coupling to Optically Generated Charge Carriers in CdS: Physical Phenomena and Applications*, Doctor of Philosophy Thesis, Washington University, (1975).

12. J. S. Heyman, "Phase insensitive acoustoelectric transducer", *Journal. Acoustical Society of America*, Vol. 64, pp. 243-9, (1978).

13. J. Krautkrämer and H. Krautkrämer, *Ultrasonic testing of materials*, 4th fully rev. ed., (Springer-Verlag, Berlin, 1990).

14. Panametrics Inc., "Technical Notes: Ultrasonic Transducers", Publication P393, (Waltham, MA, 1993).

15. S.M. Handley, M.S. Hughes, J.G. Miller, and E.I. Madaras, "Characterization of Porosity in Graphite Epoxy Composite Laminates With Polar Backscatter and Frequency Dependent Attenuation"(Denver, Published 1987), Vol. 87CH2492-7, pp. 827-830.

16. Jack Blitz, *Fundamentals of ultrasonics*, 2nd ed., (Butterworths, London, 1967).